

1999

# Validating the use of Airborne Remote Sensing in the Coastal Zone and its Application to Suspended Sediment Flux Estimation

ROBINSON, MARIE-CLAIRE

<http://hdl.handle.net/10026.1/1930>

---

<http://dx.doi.org/10.24382/4698>

University of Plymouth

---

*All content in PEARL is protected by copyright law. Author manuscripts are made available in accordance with publisher policies. Please cite only the published version using the details provided on the item record or document. In the absence of an open licence (e.g. Creative Commons), permissions for further reuse of content should be sought from the publisher or author.*

# **Validating the use of Airborne Remote Sensing in the Coastal Zone and its Application to Suspended Sediment Flux Estimation**

by

**MARIE-CLAIRE ROBINSON**

A thesis submitted to the University of Plymouth  
in partial fulfilment for the degree of

**DOCTOR OF PHILOSOPHY**

Institute of Marine Studies  
Faculty of Science

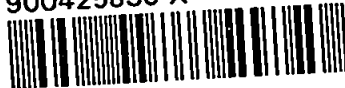
In collaboration with  
Centre for Coastal and Marine Science,  
Plymouth Marine Laboratory

**July 1999**

BK DSC thesis no. DX239516

UNIVERSITY OF PLYMOUTH	
Item No.	900425830X
Date	10 MAY 2000 S
Class No.	T 551.460028 Kob
Contl. No.	X704064269
LIBRARY SERVICES	

900425830 X



REFERENCE ONLY

LIBRARY STORE

for  
my mother

— ♦ —

*No estuary is as headstrong, as wild and treacherous, or as breathtakingly spacious, as the Humber.*

C.J. Stone

*Nature cannot be ordered about, except by obeying her.*

Francis Bacon

*If Earth's Children ever forget who provides for them, we may wake up someday and find we don't have a home.*

Jean M. Auel

## Abstract

Coastal and estuarine environments are dynamic yet highly sensitive which makes them particularly susceptible to any changes dictated by external forces. The interaction between environmental forces and those imposed by humans who live and work in the area is a very delicate one and needs to be considered through an holistic management approach to ensure the maintenance of a sustainable equilibrium. The use of airborne remote sensing in the coastal zone has been employed and validated for the specific aims of suspended particulate matter (SPM) concentration and flux quantification in the Humber Estuary and sea-surface temperature and salinity determination in the Tweed Estuary. Routines for the effective radiometric, atmospheric, thermal and geometric correction of Compact Airborne Spectrographic Imager (CASI) and Airborne Thematic Mapper (ATM) data were tested and enhanced. Validations at all stages were executed through comparison with sea-based optical data acquired coincident with the images. The data acquired from the sea-surface also yielded important information regarding the nature and content of the waters. Water classification techniques were addressed and a new algorithm for use in case II waters based on the Austin & Petzold (1981)  $K_d(490)$  routine derived. A new algorithm to determine SPM concentration in the Humber Estuary from CASI images was successfully determined and validated. SPM flux estimates were ascertained through the incorporation of image data, hydrodynamic models and depth profiles determined from hydrographic charts. In the Tweed Estuary, ATM images were used to determine sea-surface temperature and salinity using thermal image calibration and comparison with surface monitoring. The results provide an hitherto unseen insight into the dynamics of the Humber and the Tweed Estuaries. In particular, information regarding SPM concentration and fluxes in the Humber supports the so far unproved hypothesis that most of the SPM moves into and out of the mouth in elongated streaks. The use of the width of a streak (or patch) to predict the SPM concentration and / or flux and so eliminate the necessity for surface-based monitoring was addressed. Algorithms to determine SPM concentration and flux were devised using patch size and within-patch water depth alone. A model to apply these algorithms to all data was unsuccessful due to the sparse temporal coverage of the image data. The analyses exemplified in this study give an invaluable insight into the forces at play in coastal and estuarine environments and would provide key information sources for hydrodynamic modellers and coastal zone managers.

# Contents

<b>Abstract .....</b>	<b>i</b>
<b>Contents .....</b>	<b>ii</b>
<b>List of Figures .....</b>	<b>v</b>
<b>List of Tables .....</b>	<b>xi</b>
<b>Acknowledgements .....</b>	<b>xiii</b>
<b>Author's Declaration .....</b>	<b>xiv</b>
<b>Chapter 1 : Introduction .....</b>	<b>1</b>
1.1 Aims and objectives .....	2
1.2 The Land-Ocean Interaction Study .....	3
1.3 Thesis overview .....	3
<b>Chapter 2 : Optical Theory .....</b>	<b>5</b>
2.1 Properties of the radiation field .....	5
2.2 Properties of aquatic media .....	6
2.2.1 Inherent optical properties .....	6
2.2.2 Apparent optical properties .....	8
2.3 The air-water interface .....	12
2.4 Classification of water types .....	14
<b>Chapter 3 : Instrumentation and Fieldwork .....</b>	<b>16</b>
3.1 Study area .....	16
3.1.1 The Humber Estuary .....	16
3.1.2 The Tweed Estuary .....	19
3.2 Airborne instrumentation .....	20
3.2.1 Compact Airborne Spectrographic Imager .....	21
3.2.2 Airborne Thematic Mapper .....	24
3.3 Sea-based instrumentation .....	25
3.3.1 PML-Satlantic profiling system .....	26
3.3.2 Core data collection and underway instrumentation .....	27
3.3.3 Moored instrumentation .....	28

3.4 Fieldwork campaign .....	29
3.4.1 <i>Sea Vigil</i> cruises .....	29
3.4.2 <i>Challenger</i> cruises .....	31
3.4.3 Time series .....	32
<b>Chapter 4 : Data Calibration and Processing .....</b>	<b>33</b>
4.1 <i>In-situ</i> optical profiles .....	34
4.2 Airborne images .....	38
4.2.1 Radiometric calibration .....	38
4.2.1.1 Compact Airborne Spectrographic Imager .....	38
4.2.1.2 Airborne Thematic Mapper .....	42
4.2.1.2.1 Thermal calibration .....	42
4.2.2 Atmospheric correction .....	44
4.2.3 Algorithm development .....	55
4.2.3.1 Suspended Particulate Matter .....	55
4.2.3.2 Temperature and Salinity .....	61
4.2.4 Geometric correction .....	63
<b>Chapter 5 : Optics and Airborne Remote Sensing in .....</b>	<b>67</b>
<b>the Humber Estuary</b>	
5.1 Classification of water types .....	67
5.2 Diffuse attenuation and $K_d(490)$ .....	70
5.3 SPM concentration from CASI images .....	74
5.3.1 Two-dimensional Fourier Transforms of image data .....	74
5.3.2 SPM concentration distributions .....	76
5.3.3 One-dimensional Fourier Transforms of SPM .....	89
concentration data	
5.4 SPM flux .....	91
5.4.1 Calculation of SPM flux .....	92
5.4.2 Possible errors in SPM flux calculation .....	104
5.4.3 SPM fluxes in the Humber Estuary .....	106

<b>Chapter 6 : Discussion</b>	<b>108</b>
6.1 Water classification and $K_d(490)$	109
6.2 Possible errors in the data processing	110
6.3 Verification of the flux estimates	112
6.4 SPM concentration and flux distributions across the Humber mouth	114
<b>Chapter 7 : Summary and Recommendations for Future Work</b>	<b>133</b>
7.1 The achievements of the original aims of study	133
7.2 Recommendations for future work	136
<b>References</b>	<b>138</b>
<b>Appendix A : Acronyms</b>	<b>145</b>
<b>Appendix B : Proof that <math>Q = \pi</math> for a Lambertian reflector</b>	<b>147</b>
<b>Appendix C : Optical profile results from datasets acquired</b>	<b>148</b>
during CH118a, CH118b, SV23 and SV24	
<b>Appendix D : Results from optical profiles acquired</b>	<b>168</b>
coincident with airborne data	
<b>Appendix E : Pearson's correlation coefficients describing within-</b>	<b>184</b>
patch parameters in the Humber Estuary	
<b>Appendix F : Published papers</b>	<b>197</b>



## List of Figures

Figure		Page
2.1	Simplified diagram to show the fate of a ray of light hitting the water's surface	5
2.2	The relationship between surface spectral reflectance with varying SPM concentrations (Han & Rundquist, 1994)	11
2.3	Graphical representation of $K_d(\lambda)$ ( $m^{-1}$ ) and its relation to $K_d(475)$ ( $m^{-1}$ ) for different water masses (Jerlov, 1976)	15
3.1	The LOIS RACS(C) coastal sampling grid stations	17
3.2	The Humber Estuary	18
3.3	The Tweed Estuary	20
3.4	The Integrated Data System onboard the NERC aircraft (Wilson, 1995)	21
3.5	The CASI imaging concept (Wilson, 1995)	22
3.6	a) CASI spatial mode configuration (Wilson, 1995) b) CASI spectral mode configuration (Wilson, 1995)	23
3.7	Optics and detector layout within the ATM (Wilson, 1995)	25
3.8	The PML-Satlantic profiling system	26
3.9	The <i>flux curtain</i> moorings and their relation to the transaxial flightlines	28
3.10	The <i>Sea Vigil</i> cruise track. The VP vertical profiling stations span the outer estuary cruise track and the MC vertical profiling stations coincide with the transaxial flightpaths across the inner estuary.	31
4.1	CASI image calibration and correction procedures	33
4.2	ATM image calibration and correction procedures	33
4.3	Relationship between log calibrated upwelling radiance at 510 nm and depth	36
4.4	NERC ARSF processing strategy for CASI and ATM data. The HDF file output and product definitions at each stage and for each sensor are detailed (Wilson <i>et al.</i> , 1997).	40
4.5	Radiometrically corrected CASI image acquired on 15 August 1995 at LW - 2.7h over the mouth of the Humber Estuary. The image is a false colour composite with band 7 (669 nm) represented in red, band 5 (554 nm) in green and band 3 (490 nm) in blue.	41
4.6	The influence of the atmosphere on the signal received at the sensor	44
4.7	The variability of the target-sensor path length	45
4.8	a) Rayleigh corrected (left) & b) Fully COAST corrected (right), land-masked CASI images acquired on 15 August 1995 (LW - 2.7h) over the Humber Estuary. The images are false colour composites where red depicts band 7 (669 nm), green band 5 (554 nm) and blue band 3 (490 nm).	47
4.9	Measured water-leaving radiance (from in-water optical profiles) and the comparative results from radiometrically, Rayleigh and fully atmospherically (COAST) corrected CASI image data	48 - 51
4.10	The Rayleigh correction of a CASI image with no land-masking	52

4.11	a) The across-track constants (from the subtraction of fig. 4.8a from fig. 4.5) used to correct a CASI image for Rayleigh scattering (left) & b) The Rayleigh corrected (no land masking) equivalent (right) for an example image acquired on 15 August 1995 (LW - 2.7h). Red = band 7 (669 nm), green = band 5 (554 nm) & blue = band 3 (490 nm).	54
4.12	Relationship between SPM concentration and reflectance in clear water (left) and in algae-laden water (right) (Han, 1997)	55
4.13	Relationship between SPM concentration ( $\text{mg m}^{-3}$ ) as measured from the Bull Light Float and as derived from CASI images. The error bars represent one standard deviation away from the mean values as derived from image pixel averaging and from the averaging of a series of surface measurements spanning a few seconds.	59
4.14	Two examples of SPM images derived from CASI data acquired over the Humber Estuary on 10 August 1995 at LW + 2.07h (left) and LW + 3.08h (right)	60
4.15	Relationship between temperature ( $^{\circ}\text{C}$ ) measured at the sea's surface and as derived from ATM images. The error bars represent one standard deviation away from the mean values as derived from image pixel averaging.	61
4.16	Geometrically correct ATM images depicting a) temperature in $^{\circ}\text{C}$ (top) & b) salinity in psu (bottom) acquired at LW + 4h on 4 May 1995 over the Tweed Estuary	62
4.17	SPM concentration ( $\text{mg m}^{-3}$ ) derived from a mosaic of six CASI images acquired over the Humber Estuary on 22 August 1995	66
5.1	a (top) & b (bottom) : $K_d(\lambda)$ ( $\text{m}^{-1}$ ) and its relation to $K_d(490)$ for the water masses of the Humber Estuary and the North Sea. Also detailed are the boundary limits for Jerlov's (1976) oceanic water type III and coastal water types 1, 3, 5, 7 and 9.	68
5.2	Transmittance per metre of downward irradiance in the surface layer for optical water types - oceanic water types I, II, III and coastal water types 1, 3, 5, 7, 9 (Jerlov, 1976)	69
5.3	SeaWiFS $K_d(490)$ values acquired from a variety of oceanic cruises compared with calculated values as derived from equation 5-2 (Mueller & Trees, 1996)	71
5.4	$K_d(490)$ algorithms as devised by Austin & Petzold (1981) and Mueller & Trees (1986). Their relation to the newly quantified case II algorithm and the measured $K_d(490)$ results are shown.	72
5.5	Data transformation from "real space" (left) to Fourier space (right). The solid line depicts information taken from an image across which the DN values vary slowly (left). In this case the Fourier spectrum is narrow (right). Where DN values vary rapidly across a scene, as exemplified by the dashed line (left), the Fourier spectrum is much broader (right).	75

- 5.6  $|D(\omega_x, \omega_y)|$  values for 1024 x 2048 subsets of example SPM images 77  
from each of the five days of survey. The central axes define  $\omega_x$  and  $\omega_y$  and the solid lines depict the actual transect across the estuary mouth chosen for further analysis; the plots are orientated with north at the top.
- 5.7 SPM concentrations ( $\text{kg m}^{-3}$ ) derived from CASI images (left) 78  
acquired on 29 June 1995 during spring tide conditions. SPM concentrations ( $\text{kg m}^{-3}$ ) procured from a transect taken across the Humber mouth in accordance with the solid lines shown on the images (left) are detailed to the right. The x-axis corresponds to distance from Spurn Head with zero representing Spurn Head itself and 6825 m Tetney Haven.
- 5.8 SPM concentrations ( $\text{kg m}^{-3}$ ) derived from CASI images (left) 79 - 81  
acquired on 10 August 1995 one day before springs. SPM concentrations ( $\text{kg m}^{-3}$ ) procured from a transect taken across the Humber mouth in accordance with the solid lines shown on the images (left) are detailed to the right. The x-axis corresponds to distance from Spurn Head with zero representing Spurn Head itself and 6825 m Tetney Haven.
- 5.9 SPM concentrations ( $\text{kg m}^{-3}$ ) derived from CASI images (left) 82  
acquired on 11 August 1995 during spring tidal conditions. SPM concentrations ( $\text{kg m}^{-3}$ ) procured from a transect taken across the Humber mouth in accordance with the solid lines shown on the images (left) are detailed to the right. The x-axis corresponds to distance from Spurn Head with zero representing Spurn Head itself and 6825 m Tetney Haven.
- 5.10 SPM concentrations ( $\text{kg m}^{-3}$ ) derived from CASI images (left) 83 - 84  
acquired on 15 August 1995 four days after springs. SPM concentrations ( $\text{kg m}^{-3}$ ) procured from a transect taken across the Humber mouth in accordance with the solid lines shown on the images (left) are detailed to the right. The x-axis corresponds to distance from Spurn Head with zero representing Spurn Head itself and 6825 m Tetney Haven.
- 5.11 SPM concentrations ( $\text{kg m}^{-3}$ ) derived from CASI images (left) 85 - 87  
acquired on 21 August 1995 during neap tide conditions. SPM concentrations ( $\text{kg m}^{-3}$ ) procured from a transect taken across the Humber mouth in accordance with the solid lines shown on the images (left) are detailed to the right. The x-axis corresponds to distance from Spurn Head with zero representing Spurn Head itself and 6825 m Tetney Haven.
- 5.12 Bathymetry across the Humber mouth derived from hydrographic 88  
charts and corresponding to the transects shown in figs. 5.7 - 5.11

5.13	Most frequently occurring SPM concentration patch size across each image related to the averaged surface velocity ( $\text{m sec}^{-1}$ ) into the estuary. The solid line represents a polynomial trendline fit to the data with the highest power of 5 for the independent variable. Data acquired during spring tidal conditions are represented in red, one day after springs in pink, four days after springs in green, and during neaps in blue.	91
5.14	The derivation of depth-averaged velocity vectors perpendicular to the transect across the Humber mouth	92
5.15	SPM fluxes ( $\text{kg m}^{-1} \text{s}^{-1}$ ) into the Humber Estuary along each transect as derived from CASI images acquired on 29 June 1995. Positive values indicate flux into the estuary and negative out into the North Sea.	94
5.16	SPM fluxes ( $\text{kg m}^{-1} \text{s}^{-1}$ ) into the Humber Estuary along each transect as derived from CASI images acquired on 10 August 1995. Positive values indicate flux into the estuary and negative out into the North Sea.	95 - 97
5.17	SPM fluxes ( $\text{kg m}^{-1} \text{s}^{-1}$ ) into the Humber Estuary along each transect as derived from CASI images acquired on 11 August 1995. Positive values indicate flux into the estuary and negative out into the North Sea.	98
5.18	SPM fluxes ( $\text{kg m}^{-1} \text{s}^{-1}$ ) into the Humber Estuary along each transect as derived from CASI images acquired on 15 August 1995. Positive values indicate flux into the estuary and negative out into the North Sea.	99 - 100
5.19	SPM fluxes ( $\text{kg m}^{-1} \text{s}^{-1}$ ) into the Humber Estuary along each transect as derived from CASI images acquired on 21 August 1995. Positive values indicate flux into the estuary and negative out into the North Sea.	101 - 103
5.20	a) A typical depth profile of SPM concentrations acquired approximately 600 m to the west of Spurn Head at Hawke (Uncles, R.J., <i>pers. comm.</i> ) b) Van-Veen profile showing the variation of water velocity with depth (e.g. Uncles and Jordan, 1994)	105
5.21	Surface velocities ( $\text{m sec}^{-1}$ ), derived from the DIVAST model, averaged across the Humber mouth transect for each of the 27 datasets. Data acquired during spring tidal conditions are represented in red, one day after springs in pink, four days after springs in green, and during neaps in blue.	106
5.22	Total SPM flux into the estuary ( $\text{kg m}^{-1} \text{s}^{-1}$ ) for each dataset covering the five days of survey. Data acquired during spring tidal conditions are represented in red, one day after springs in pink, four days after springs in green, and during neaps in blue. The error bars represent the $\pm 33\%$ uncertainty in the flux calculations.	107
5.23	Total SPM flux into the estuary ( $\text{kg m}^{-1} \text{s}^{-1}$ ) for each dataset covering the five days of survey. The total flux integrated for each survey has been calculated as the area under the curve and is specified in the related text boxes.	107

6.1	An example of patch delineation using the transect data acquired across the Humber mouth from CASI images (figs. 5.7 - 5.11). The data has been smoothed with an averaging filter and the patch is defined as a section between two troughs in the concentration distribution. Total SPM concentration and flux within the patch is calculated as the area under the curve; averaged depth and velocity as mean values across the patch.	115
6.2	The percentage of total SPM flux moving into or out of the Humber Estuary contained within patch sizes < 50 m, 50 m - 100 m and > 100 m for each image transect. The results are related to averaged surface velocities into the estuary. The first 50% of SPM flux is not shown as in all cases this is transported in patches less than 50 m wide.	117
6.3	Pearson's correlation coefficients describing the relationship between patch size and within-patch total SPM concentration. The coefficients for each dataset are plotted against the averaged surface velocity into the estuary for the survey.	119
6.4	Pearson's correlation coefficients describing the relationship between $\ln(\text{patch size})$ and $\ln(\text{within-patch total SPM concentration})$ . The coefficients for each dataset are plotted against the averaged surface velocity into the estuary for the survey.	119
6.5	Pearson's correlation coefficients describing the relationship between within-patch averaged surface velocity and $\ln(\text{within-patch averaged water depth})$ . The coefficients for each dataset are plotted against the averaged surface velocity into the estuary for the survey.	121
6.6	Pearson's correlation coefficients describing the relationship between within-patch averaged velocity and $\ln(\text{within-patch total SPM concentration})$ . The coefficients for each dataset are plotted against the averaged surface velocity into the estuary for the survey.	121
6.7	Pearson's correlation coefficients describing the relationship between patch size and within-patch total SPM flux. The coefficients for each dataset are plotted against the averaged surface velocity into the estuary for the survey.	123
6.8	Pearson's correlation coefficients describing the relationship between within-patch total SPM concentration and within-patch total SPM flux. The coefficients for each dataset are plotted against the averaged surface velocity into the estuary for the survey.	123
6.9	$R^2$ values describing the goodness of fit of equation 6-1 (to derive within-patch total SPM concentration) to the 27 surveyed datasets. The dotted line represents the threshold where $R^2$ is 0.95.	128
6.10	$R^2$ values describing the goodness of fit of equation 6-2 (to derive within-patch total SPM flux) to the 27 surveyed datasets. The dotted line represents the threshold where $R^2$ is 0.95.	128
6.11	The coefficient $a$ from equation 6-1 for 26 of the datasets. The trendline describes the distribution of the coefficient in relation to the averaged surface velocity for the survey.	129

6.12	The coefficient $b$ from equation 6-1 for 26 of the datasets. The trendline describes the distribution of the coefficient in relation to the averaged surface velocity for the survey.	129
6.13	The coefficient $c$ from equation 6-1 for 26 of the datasets. The trendline describes the distribution of the coefficient in relation to the averaged surface velocity for the survey.	130
6.14	The coefficient $d$ from equation 6-1 for 26 of the datasets. The trendline describes the distribution of the coefficient in relation to the averaged surface velocity for the survey.	130
6.15	The coefficient $a$ from equation 6-2 for 26 of the datasets. The trendline describes the distribution of the coefficient in relation to the averaged surface velocity for the survey.	131
6.16	The coefficient $b$ from equation 6-2 for 26 of the datasets. The trendline describes the distribution of the coefficient in relation to the averaged surface velocity for the survey.	131
6.17	The coefficient $c$ from equation 6-2 for 26 of the datasets. The trendline describes the distribution of the coefficient in relation to the averaged surface velocity for the survey.	132
6.18	The coefficient $d$ from equation 6-2 for 26 of the datasets. The trendline describes the distribution of the coefficient in relation to the averaged surface velocity for the survey.	132

## List of Tables

Table		Page
2.1	$K_d(\lambda)$ ( $\text{m}^{-1}$ ) for different water masses (adapted from Jerlov, 1976)	15
3.1	CASI bandset and its relation to SeaWiFS	24
3.2	ATM bandset and its relation to Landsat TM	25
3.3	<i>Challenger &amp; Sea Vigil</i> cruise and airborne image data obtained as part of the 1994 and 1995 fieldwork campaigns. The sampling grid abbreviations refer to those depicted in figure 3.1 where H is the Humber grid, H-T the Humber-Tweed grid and H-W the Humber-Wash grid. For completeness, data acquired using a Profiling Reflectance Radiometer (PRR) and an Undulating Oceanographic Recorder (UOR) are also detailed. The data acquired using these instruments were not used for further study and their use and application are not reported in this thesis.	30
3.4	Time series of CASI and ATM image data acquired in 1995 coincident with sea-based measurements obtained from the <i>flux curtain</i> in the Humber Estuary and from a survey vessel in the Tweed Estuary	32
4.1	The effects of ship shadow on the definition of water-leaving radiance, just below the water's surface (at 510 nm), through regression analysis	37
4.2	$R^2$ values from the regression of radiometrically corrected CASI image band ratios [band (x) / band (y)] against SPM concentration ( $R^2 > 0.9$ in bold)	58
4.3	$R^2$ values from the regression of Rayleigh corrected CASI image band ratios [band (x) / band (y)] against SPM concentration ( $R^2 > 0.9$ in bold)	58
4.4	$R^2$ values from the regression of fully atmospherically corrected (COAST) CASI image band ratios [band (x) / band (y)] against SPM concentration	58
5.1	Classification of water "types" according to Jerlov (1976) and "cases" according to Morel & Prieur (1977) for each profile. The maximum depth from which 90% of the original optical signal reached the surface, $z_{90}$ , is also shown.	69
5.2	Standardised coefficients and the coefficient of determination from the multiple regression of results from three $K_d(490)$ algorithms and in-water constituents for twenty datasets	73
6.1	The mean, maximum and minimum percentages of the total flux transported across the Humber mouth transect in the different patch sizes of < 50 m, 50 - 100 m and > 100 m considering all 27 image datasets	116

6.2	Summary of the significant relationships suggested for use in the derivation of within-patch total SPM concentration from the known quantities of patch size and within-patch averaged water depth. $x$ = patch size, $s$ = within-patch total SPM concentration, $v$ = within-patch averaged surface velocity, and $z$ = within-patch averaged water depth.	120
6.3	Summary of the significant relationships suggested for use in the derivation of within-patch total SPM flux from the known quantities of patch size and within-patch total SPM concentration. $x$ = patch size, $s$ = within-patch total SPM concentration, and $f$ = within-patch total SPM flux.	122
6.4	The coefficients $a$ , $b$ , $c$ and $d$ corresponding to equation 6-1, their $R^2$ values and the averaged surface velocity during survey.	125
6.5	The coefficients $a$ , $b$ , $c$ and $d$ corresponding to equation 6-2, their $R^2$ values and the averaged surface velocity during survey.	126



## Acknowledgements

I would like to express my heartfelt gratitude to all those who have helped and supported me throughout this period of study.

In particular, I owe much to the steadfast support, advice and guidance given freely by my supervisors Professor Keith Dyer (University of Plymouth), Dr. Jim Aiken and Dr. Kevin Morris (both of Plymouth Marine Laboratory). Without their encouragement and confidence in me I would not have been able to conclude this study so satisfactorily.

I am indebted to Mr. Andrew Wilson (Institute of Terrestrial Ecology) for giving me the opportunity to work with him to overcome some of the hurdles placed in my way, and also to Mr. Bill Mockridge (Azimuth Systems) for his help and advice.

I am also much appreciative of the general advice, help and discussion afforded to me throughout my studies by Dr. Richard Murphy, Dr. Reg Uncles, Mr. Matthew Pinkerton, Mr. Gerald Moore, Dr. Samantha Lavender, Mr. Steve Gibson and Mr. Tony Moore.

I would like to thank the NERC Airborne Remote Sensing Facility for the use of the airborne image data, the pilots and crew of the NERC Piper Chieftain, the masters, crew and technical staff of the EA's *Sea Vigil* and of the RRS *Challenger*, and Dr. Howard Bottrell for the use of the COAST software.

Special thanks go to Miss. Bekkqi King and Dr. Axel Miller for making my ventures at sea more bearable and for their unerring support on dry land. I would also like to thank Dr. Carl Rawling and Mr. Mark Williams for being there when I needed a pint or a sofa to sleep on.

I would like to acknowledge the support of my family and in particular my mother and David for putting up with me and giving me the space to write up, and my father and Chris for their constant encouragement.

Finally I would like to express my fondest thanks to Oliver for keeping me on track and for always being there for me.

## Author's Declaration

At no time during the registration for the degree of Doctor of Philosophy has the author been registered for any other University award.

This study was financed with the aid of a studentship from the Natural Environment Research Council, and carried out in collaboration with the Plymouth Marine Laboratory.

A programme of advanced study was undertaken which included participation on

- BODC database course, 15-16 January 1996, British Oceanographic Data Centre, Bidston, Liverpool, UK
- Writing and publishing course, 13 November 1995, University of Plymouth
- MAST Advanced Study course, *Advanced European Training course on remote sensing for marine applications*, held at ITC Enschede, The Netherlands, 18-29 September 1995
- RRS *Challenger* cruises CH118a, CH118b, CH119a in 1995
- NRA *Sea Vigil* cruises SV23, SV24 in 1995
- NRA *Sea Vigil* cruises SV7, SV8, SV9, SV10, SV12 in 1994
- NRA *Water Guardian* cruise SV11 in 1994

## Publications:

Dyer, K.R., Aiken, J., Morris, K.P., Youngs, K.J. & Robinson, M-C., 1997, *Processing and Interpretation of remote sensed data*, LOIS Second annual meeting, 18-20 March 1997, Hull, LOIS publication No. 323, 82-83

Morris, K.P., Robinson, M-C., Youngs, K.J., Lavender, S.H., & Murphy, R.J., 1996, *Integration of CASI data and Sea-truth Measurements in the Coastal Zone*, Proceedings of the Second International Airborne Remote Sensing Conference and Exhibition : Technology, Measurement and Analysis, 24-27 June 1996, San Francisco, California, USA, ERIM, Michigan, vol. 1, I-74-I-82

Robinson, M., 1996, *LOIS Airborne Remote Sensing Research Report*, SeaWiFS Technical Report Series: Proceedings of the First SeaWiFS Exploitation Initiative (SEI) Team Meeting, Moore, G.F. & Hooker, S.B. (eds.), NASA Technical Memorandum 104566, vol. 33, 33-34

- Robinson, M-C. & Dyer, K.R., 1997, *The Assessment of the Estuarine and Coastal Waters of the East Coast of England through Airborne Remote Sensing*, Proceedings of the Third International Airborne Remote Sensing Conference and Exhibition, 7-10 July 1997, Copenhagen, Denmark, ERIM, Michigan, vol. 1, I-26-I-133
- Robinson, M-C. & Morris, K.P., 1997, *The Validation of Atmospheric Correction Algorithms for the CASI in the Coastal Zone*, Proceedings of the Third International Airborne Remote Sensing Conference and Exhibition, 7-10 July 1997, Copenhagen, Denmark, ERIM, Michigan, vol. 2, II-455-II-462
- Robinson, M-C., Morris, K.P. & Dyer, K.R., 1998, *Deriving Fluxes of Suspended Particulate Matter in the Humber Estuary using Airborne Remote Sensing*, Marine Pollution Bulletin, **37(3-7)**, 155-163
- Robinson, M-C., Morris, K.P. & Dyer, K.R., 1998, *A New Approach to the Derivation of Fluxes of Suspended Particulate Matter using Airborne Remote Sensing*, Proceedings of the 24th Annual Conference and Exhibition of the Remote Sensing Society, 9-11 September 1998, The University of Greenwich, UK, 492-498
- Robinson, M-C., Morris, K., Dyer, K. & Hardisty, J., 1998, *Deriving Fluxes of Suspended Particulate Matter in the Humber Estuary using Airborne Remote Sensing*, LOIS Final Annual Meeting, University of East Anglia, 24-26 March 1998, NERC LOIS publication no. 447, 59
- Uncles, R.J., Morris, K.P., Stephens, J.A., Robinson, M-C. & Murphy, R.J., 1999, *Aircraft and Sea-truth Observations of Salinity and Temperature within the Tweed Estuary and Coastal-zone Frontal System*, International Journal of Remote Sensing, **20(3)**, 609-625
- Uncles, R.J., Morris, K.P., Stephens, J.A., Robinson, M-C. & Murphy, R.J., 1999, *Cover*, International Journal of Remote Sensing, **20(3)**, 481
- Wilson, A.K., Mockridge, W. & Robinson, M-C., 1997, *Post-processing to Achieve Radiometric and Geometric Correction of ATM and CASI Data*, Proceedings of the Third International Airborne Remote Sensing Conference and Exhibition, 7-10 July 1997, Copenhagen, Denmark, ERIM, Michigan, vol. 1, I-447-I-454

### **Presentations given and conferences attended :**

- 24th Annual Conference and Exhibition of the Remote Sensing Society, 9-11 September 1998, The University of Greenwich, UK (Oral presentation)
- LOIS Final Annual Meeting, 24-26 March 1998, University of East Anglia, UK (Oral & poster presentations)
- ECSA '98, 1-5 September 1997, University of St. Andrews, Scotland, UK
- Third International Airborne Remote Sensing Conference and Exhibition, 7-10 July 1997, Copenhagen, Denmark (Oral & two poster presentations)

Land-Ocean Interaction Study, Second Annual Meeting, 18-20 March 1997, University of Hull, UK (Poster presentation)

Second International Airborne Remote Sensing Conference and Exhibition : Technology, Measurement and Analysis, 24-27 June 1996, San Francisco, California, USA (Poster presentation)


Land-Ocean Interaction Study, First Annual Meeting, 26-28 March 1996, University of Plymouth, UK

20th Annual Conference and Exhibition of the Remote Sensing Society, 11-13 September 1995, University of Southampton, UK

SeaWiFS Exploitation Initiative Science Team Meeting, First Annual Meeting of the SEI Science Team, 24 January 1995, James Renell Centre, University of Southampton, UK

Remote Sensing Society Student Meeting, 20-21 December 1994, University of Nottingham, UK

First International Airborne Remote Sensing Conference and Exhibition : Applications, Technology and Science, 12-15 September 1994, Strasbourg, France

Signed.....

## 1 Introduction

The United Kingdom boasts an extensive coastline approximately 12 000 km in length (Turner, *et al.*, 1998). It comprises a series of physically and ecologically diverse stretches which are highly dynamic, environmentally sensitive regions and are thus greatly influenced by the impact of those humans who live and work there. The physical, social and economic processes affecting these active environments must be addressed to enable their effective enhancement, protection and management. The adoption of an holistic approach to the coastal system is thus necessary.

The north-eastern coast of England is a particularly striking example of a coastal stretch where an integrated management approach is essential. Key inputs into such a management approach are the understanding of the underlying processes driving and maintaining the coastline and its environs. A major factor influencing the coastal zone of north-eastern England is the erosion, transport and accretion of the fine sediments. The characterisation, monitoring and modelling of fluxes within the coastal zone also provides insight into the impact of the disposal of toxic pollutants in this region, another key input into the integrated management system.

Traditional approaches of oceanographic, estuarine and riverine monitoring projects incorporate *in-situ* point measurements. As Allan (1983) observed, 'the worst place from which to study the sea is the sea surface'. Monitoring through single point measurements does not provide a synoptic view of the area in question and may in fact be misleading in cases where a localised anomaly occurs, or where the properties change quickly in space and time. Jay *et al.* (1997) suggest that estimates of flux derived from direct measurements are generally inadequate and prone to error and further that fluxes should be estimated using consideration of two-dimensional spatial distributions, in conjunction with variations in depth and time. A more multi-dimensional approach to survey is thus necessary with the incorporation of hydrodynamic modelling to fill in any gaps in the measurements.

This study attempts to approach the question of suspended sediment movement and flux estimation multi-dimensionally. Remote sensing provides a two-dimensional synoptic coverage of an area and, by repeatedly flying an aircraft across a target, a unique and invaluable time series of image data is generated. The measurement of in-water parameters with depth introduces a third dimension and, when incorporated with information gained through hydrodynamic modelling, provides a comprehensive multi-dimensional description of an area.

### **1.1 Aims and objectives**

The aims and objectives of this study were devised in response to the requirements of the airborne remote sensing section of the Land-Ocean Interaction Study (whose role is discussed in section 1.2). The overall aim of this work was to provide an assessment of the practical use of airborne remote sensing in coastal and estuarine studies and to investigate the more technical aspects of image processing and manipulation. More specifically the stated aims and objectives were:

1. To explore the practical use of airborne remote sensing in the coastal zone for the quantification of suspended particulate matter (SPM) concentration, SPM flux, sea-surface temperature and salinity,
2. To develop a protocol for the sea-truthing of remotely sensed airborne data acquired using the Compact Airborne Spectrographic Imager (CASI) and the Airborne Thematic Mapper (ATM) and to generate a comprehensive dataset as part of the core Land-Ocean Interaction Study (LOIS) field programme,
3. To assess the optical characteristics of the waters surveyed and to develop a  $K_d(490)$  algorithm for use in the coastal zone,
4. To utilise and enhance the processing routines used to correct the CASI and ATM,
5. To test atmospheric correction routines developed for use with the CASI,
6. To develop and substantiate algorithms to quantify SPM concentration in the Humber Estuary using CASI data and sea-surface temperature and salinity in the Tweed Estuary using ATM data, and
7. To develop a methodology for the estimation of SPM flux in the Humber Estuary through the incorporation of SPM concentration information derived from CASI images and hydrodynamically modelled flows.

## **1.2 The Land-Ocean Interaction Study**

The Land-Ocean Interaction Study (LOIS) was a 6 year UK community research project undertaken during the period 1992 - 1998. LOIS was funded by the Natural Environment Research Council (NERC) and involved 11 NERC institutes and 27 Universities. The project aimed to quantify the exchange, transformation and storage of materials at the land-ocean boundary, and to determine how these parameters vary in space and time. At the heart of LOIS was the Rivers, Atmospheres, Estuaries and Coasts Study (RACS) component. The work undertaken for this thesis was executed as part of the LOIS RACS(C) component, the coasts and estuaries section of RACS, which aimed to specifically determine the fluxes from estuary to sea, together with their controlling factors. More expressly some of the stated aims were:

- To estimate the contemporary fluxes of momentum and materials (sediments, nutrients, contaminants into and out of the coastal zone),
- To characterise the key physical and biogeochemical processes that govern coastal morphodynamics and the functioning of coastal ecosystems, and
- To simulate the transport, transformation and fate of materials in the coastal zone.

(Natural Environment Research Council, 1992)

## **1.3 Thesis overview**

Before launching on a study investigating the use of optically sensitive instrumentation within an aquatic environment, it is important to have a firm understanding of the processes and interactions of the water itself, the constituents held within the medium, and the atmosphere which the remotely sensed signal passes through to reach the airborne (or satellite) sensor. Chapter 2 introduces the theory of water optics and in particular the complex interactions the medium has with the constituents held within its mass. Classification of water types is addressed through the use of in-water optical theory. This is an important aid to identifying the likely in-water processes affecting the remotely sensed signal received at the airborne (or satellite) sensor from the target water medium.

The areas of study and the acquisition of data is discussed in chapter 3. The main area under investigation is the north-east coast of England, one of the principal LOIS RACS(C) study sites, which is an extremely dynamic, environmentally sensitive and economically

important stretch of coastline. The contrasting environmental regimes of the Humber and Tweed estuaries are the foci for the study. Data acquisition from the air and from the sea are discussed and the instrumentation described. Chapter 4 embraces the calibration and processing of this data in two main sections. The first component (section 4.1) addresses the data acquired from the sea-surface (in-water optical profiles) and the second (section 4.2) the airborne data (CASI and ATM images). Each processing stage is discussed and new algorithms developed and evaluated.

Chapter 5 takes the use of in-water optical monitoring and of airborne remote sensing a stage further by utilising the calibrated and processed datasets to investigate the waters of the Humber Estuary. Using theory described in earlier chapters (chapters 2 and 4), in-water optical measurements are used to characterise the estuarine environment. SPM concentration is derived using the algorithms developed for the CASI (chapter 4) and used to assess a series of images acquired across the Humber mouth at a variety of tidal states and under different spring and neap conditions. Fourier transforms are used to evaluate SPM distributions throughout the images and to interrogate transects taken from the image data across a line which spans the Humber mouth. The question of SPM flux evaluation is addressed and estimates derived from the transects. Possible errors are discussed and total flux estimates for the five survey periods determined.

Discussion of the results from chapter 5 reveal that there may be a relationship between the patterns and quantities of SPM flux and the SPM concentration which is shown to move into and out of the estuary in elongated streaks or patches (chapter 6). This is investigated further and the findings reveal that it is possible to use the size of the patches and the averaged water depth within the patch as a surrogate for SPM concentration and for SPM flux. This would eliminate some of the costly time and effort involved in fieldwork and data processing and the data would provide a key input into the development of more accurate hydrodynamic models of the Humber estuary.

A summary of the results is provided in chapter 7. Suggestions for future work are made which carry on from the techniques developed and evaluated in this study and which propose the utilisation of the vast archive of LOIS data now available.



## 2 Optical Theory

The electromagnetic spectrum comprises a variety of radiation types which differ only in wavelength. Visible radiation covers that part of the spectrum lying between 390 nm (violet) and 740 nm (dark red). These wavelengths are fundamental in the study of water colour and water quality. The selective absorption and scattering by constituents within the water such as sediments, phytoplankton and dissolved organic compounds, and the interaction of light at the water's surface, determine its colour.

### 2.1 Properties of the radiation field

Light falling onto a parcel of water may be reflected from the surface, absorbed into the water and augmented by light upwelling through the surface from the water column below (fig. 2.1). Hence, the radiant field is complex and its form is dictated by the nature of the target. In order to quantify the angular structure of the radiant field, upwelling and downwelling light, radiance and irradiance, need to be defined.

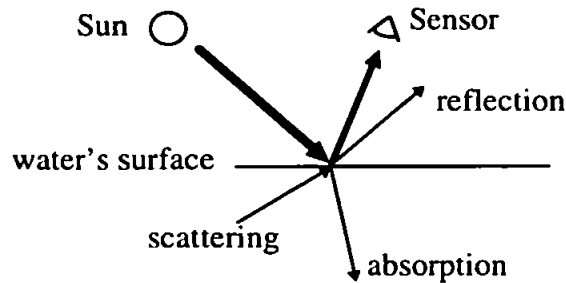


Figure 2.1 : Simplified diagram to show the fate of a ray of light hitting the water's surface

*Radiant flux*,  $\phi(\lambda)$  (Watts, W), is fundamental to optical theory and is the rate of flow of radiant energy with respect to time:

$$\phi(\lambda) = \frac{dF(\lambda)}{dt} \quad (2-1)$$

where  $F$  is the radiant energy (Joules, J),

$t$  is time (seconds), and

$\lambda$  is the wavelength (nanometres, nm).

*Radiant intensity*,  $I(\lambda)$  ( $\text{W sr}^{-1}$ ), provides a measure of the radiant flux per unit solid angle in a specified direction and is defined as:

$$I(\lambda) = \frac{d\phi(\lambda)}{d\Omega} = \frac{d^2 F(\lambda)}{d\Omega dt} \quad (2-2)$$

where  $\Omega$  is the solid angle subtended on a cone.

*Radiance*,  $L(\lambda)$  ( $\text{W m}^{-2} \text{sr}^{-1}$ ), considers radiant flux per unit solid angle per unit area of a plane at right angles to the direction of flow (Kirk, 1983). Radiance can thus be expressed as:

$$L(\lambda) = \frac{d^2 \phi(\lambda)}{dA d\Omega} = \frac{dI(\lambda)}{dA} \quad (2-3)$$

where  $A$  is the area perpendicular to the direction of photon propagation.

*Irradiance*,  $E(\lambda)$  ( $\text{W m}^{-2}$ ), is the radiant flux per unit area impinging upon the selected surface within the radiative field. Irradiance can be expressed as:

$$E(\lambda) = \frac{d\phi}{dS} \quad (2-4)$$

where  $S$  is the surface area upon which the radiant flux impinges.

## 2.2 Properties of aquatic media

The optical properties of aquatic media are classified into two main groups, inherent and apparent. Inherent optical properties do not alter according to any change in the radiant distribution whereas apparent properties are affected.

### 2.2.1 Inherent optical properties

Inherent optical properties are optical descriptors of the constituents within the medium and not of the ambient light field. The fundamental inherent optical properties of absorption and scattering within an aquatic medium are defined by the volume absorption coefficient and the volume scattering coefficient. These functions carry information about the material present within the body of water.

The *volume absorption coefficient*,  $a(\lambda, z)$ , is the fraction of the incident flux which is absorbed, divided by the thickness of the layer  $dz$  (Kirk, 1983) and is defined as:

$$a(\lambda, z) = -\frac{d}{dz} \ln[1 - A] \quad (2-5)$$

where  $z$  is the depth relative to the water's surface and

where  $A = \frac{\phi_a}{\phi_0}$ ,  $\phi_a$  is the radiant flux absorbed and  $\phi_0$  the radiant flux incident in the form of a parallel beam (Kirk, 1983).

The *volume scattering coefficient*,  $\beta(\lambda, z, \sigma)$ , is a measure of the radiant flux which is scattered in a specific direction within the medium:

$$\beta(\lambda, z, \sigma) = -\frac{d}{dz} \ln[1 - B] \quad (2-6)$$

where  $\sigma$  is the specified direction of scattering, and

where  $B = \frac{\phi_b}{\phi_0}$  and  $\phi_b$  is the radiant flux scattered (Kirk, 1983).

As  $\beta(\lambda, z, \sigma)$  is a measure of scattering in one direction only, it is necessary to define a *total volume scattering coefficient*,  $b(\lambda, z)$ . This describes the proportion of incident intensity which is scattered in all directions from the medium and is thus defined as:

$$b(\lambda, z) = \int_0^{4\pi} \beta(\lambda, z, \sigma) d\Omega \quad (2-7)$$

$b(\lambda, z)$  is often considered as comprising two distinct coefficients, forward scattering,  $b_f(\lambda, z)$ , and backscattering,  $b_b(\lambda, z)$ , where:

$$b(\lambda, z) = b_f(\lambda, z) + b_b(\lambda, z) \quad (2-8)$$

The effects of absorption and scattering are additive:

$$a(\lambda) = a_w + a_y + a_{ch} + a_s \quad (2-9)$$

$$b_b(\lambda) = 0.5b_w + b_{bch} + b_{bs} \quad (2-10)$$

where  $w$  is the water component,  
 $y$  is the yellow substance component,  
 $ch$  is the chlorophyll component, and  
 $s$  is the SPM component.

The coefficient 0.5 is necessary in equation 2-10 to convert the water scattering values to backscattering quantities and can be applied due to the symmetry of the volume scattering function for water molecules (Morel, 1974).

The optical properties of a water body are determined by any material contained within it. If a water mass has a low mineral SPM content, the backscattered part of the signal is weak and  $b_b(\lambda) \ll a(\lambda)$ . In this case, the optical penetration depth is mainly determined by the absorption properties of water itself (Nanu & Robertson, 1993). Conversely, where the SPM concentration within an aquatic medium is high, backscattering dominates (Viollier & Sturm, 1984).

### 2.2.2 Apparent optical properties

Apparent optical properties are attributes of the medium in the ambient light field as well as of the material present within the water. The attenuation coefficient is a measure of these properties and evaluates the combined effect of absorption and scattering of the water. Attenuation is at a minimum in the blue and green and rises rapidly with wavelength due to the wavelength dependence of the absorption and scattering functions.

The irradiance, or *diffuse attenuation coefficient*,  $K(\lambda, z)$ , defines the attenuation of light as a function of depth and can be used as a measure of water quality, to predict the depth of the euphotic zone (the uppermost part of the water where enough light is received for photosynthesis to take place) and ultimately the depth of maximum primary production (Austin & Petzold, 1981; Stumpf & Pennock, 1991). The diffuse attenuation coefficient is the logarithmic depth derivative of spectral irradiance found at a depth  $z$ :

$$K(\lambda, z) = -\frac{d}{dz} \ln[E(\lambda, z)] \quad (2-11)$$

The *optical depth*,  $\zeta(\lambda, z)$ , of an aquatic medium is a dimensionless quantity and is useful in defining the attenuation coefficient of downwelling irradiance at a particular depth. Attenuation is thus defined as a percentage of the original subsurface irradiance remaining at the optical depth. Mathematically, the optical depth is expressed as the integration of the downwelling irradiance attenuation coefficient,  $K_d(\lambda, z)$ , over the subsurface depth  $z$ :

$$\zeta(\lambda, z) = \int_0^z K_d(\lambda, z) dz \quad (2-12)$$

If  $K_d(\lambda, z)$  is the average value of the irradiance attenuation coefficient over the depth interval 0 to  $z$  then:

$$\zeta(\lambda, z) = K_d z \quad (2-13)$$

As the propagation of light within an aquatic medium is characterised by its inherent optical properties, so these determine the optical depth:

$$\zeta(\lambda, z) = \frac{1}{\mu_0 (a^2 + G\mu_0 ab)^{0.5}} \quad (2-14)$$

where:  $\mu_0$  is the cosine of the refracted solar photons just below the surface and  $G$  is approximately 0.323 and varies as a function of  $\mu_0$  (Kirk, 1994).

The depth from which 90% of irradiance originates is known as the penetration depth,  $z_{90}$  (Gordon & McCluney, 1975), and is defined as:

$$z_{90}(\lambda) = \frac{1}{K_d(\lambda)} \quad (2-15)$$

The ratio of upwelling irradiance at a point due to the stream of upwelling light, to the downwelling irradiance due to the downwelling light stream defines the *volume reflectance*,  $R(\lambda, z)$ , of a medium:

$$R(\lambda, z) = \frac{E_u(\lambda, z)}{E_d(\lambda, z)} \quad (2-16)$$

where  $u$  and  $d$  denote upwelling and downwelling.

Remote sensing instrumentation mounted on airborne or spaceborne platforms measures radiance rather than irradiance, having a fixed field-of-view which does not extend to the full cosine response. The available reflectance quantity from remote sensors,  $R_L(\lambda, z)$ , is thus the ratio of upwelling radiance to downwelling irradiance:

$$R_L(\lambda, z) = \frac{L_u(\lambda, z)}{E_d(\lambda, z)} \quad (2-17)$$

Differential attenuation of sunlight penetrating the water column changes the reflectance spectrum with depth. The reflectance of water is also variable in response to the properties of any absorbing and scattering materials within. This relationship approximates to:

$$R(\lambda, 0^-) = Y \frac{b_b(\lambda)}{a(\lambda) + b_b(\lambda)} \quad (2-18)$$

where  $R(\lambda, 0^-)$  is the irradiance reflectance just below the water's surface, and

$Y$  is approximately 0.33 and depends on the light field (Gordon *et al.*, 1975).

Reflectance is a function of any environmental influences acting upon the water mass (Curran & Novo, 1988). In coastal regions the terrigenous component is extremely important and is the determining influence on the water body's optical response to incoming light. In the coastal zone, SPM concentration and the properties of individual particles present are the dominant force dictating the shape of the spectral response (Novo *et al.*, 1989; Bhargava & Mariam, 1990; Ferrier, 1995). Thus, in turbid (coastal) waters the reflectance spectrum is dominated by the backscatter component:

$$R(\lambda) = Y' \frac{b_{bs}^*(\lambda)}{s^*(\lambda) + \frac{a_x(\lambda)}{n_s}} \quad (2-19)$$

(Stumpf & Pennock, 1989; 1991)

where  $n_s$  is SPM concentration,

$a_x$  is the absorption coefficient for water, chlorophyll & dissolved pigments,

$b_{bs}^*$  is the specific backscatter coefficient for SPM such that  $b_{bs}^* = \frac{b_{bs}}{n_s}$ ,

$s^* = b_{bs}^* + a_s^*$  and  $a_s^*$  is the specific SPM absorption coefficient ( $a_s^* = \frac{a_s}{n_s}$ ), and

$Y'$  is a constant of proportionality equal to 0.178 (Gordon *et al.*, 1975) and includes components relating to surface refraction and reflection effects.

The magnitude and spectral distribution of reflected light from surface waters changes as the concentration of suspended solids increases (Ritchie *et al.*, 1983). Morel & Prieur (1977) found the relationship between SPM concentration and reflectance to be linear for a

narrow range of concentrations. Where the range of concentrations are broader, this relationship becomes logarithmic (Munday & Alföldi, 1979).

In clear offshore waters SPM concentrations are zero and the maximum radiant intensity is located in the blue wavelengths. Within the coastal zone, where SPM concentrations are generally higher, the reflected solar radiation between 500 nm and 950 nm increases (Bartolucci *et al.*, 1977) and the region of maximum reflection shifts from approximately 550 nm at low concentrations to over 600 nm at higher concentrations (fig. 2.2; Ritchie *et al.*, 1976). Between 700 nm and 900 nm this increase is generally uniform (fig. 2.2) making it an ideal part of the spectrum to use in SPM concentration quantification.

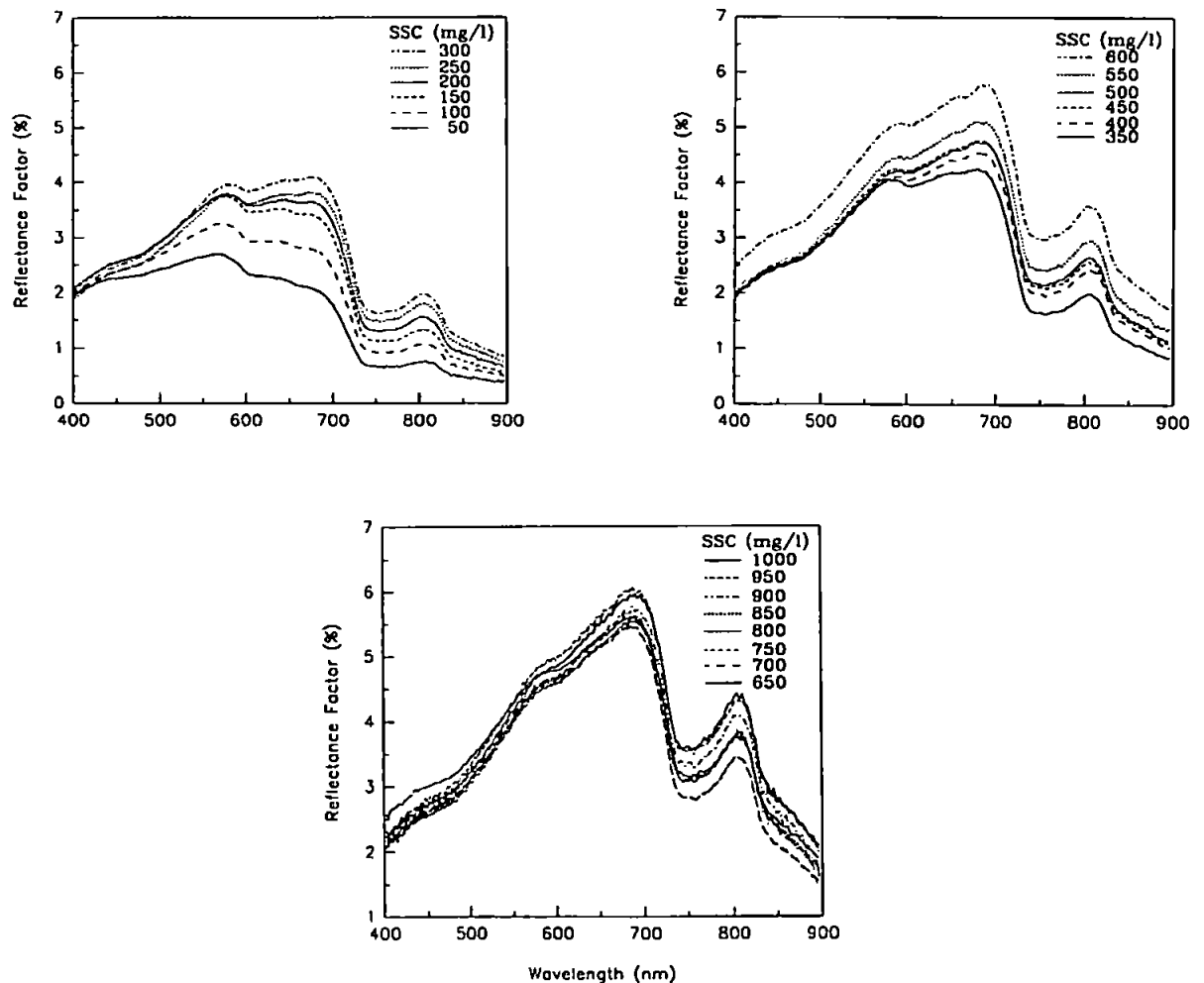


Figure 2.2 : The relationship between surface spectral reflectance with varying SPM concentrations (Han & Rundquist, 1994)

Bhargava & Mariam (1990) found a high coefficient of correlation and low standard error in the response between 700 nm and 900 nm for a variety of particulates studied in suspension. In addition they found that, between 550 nm and 750 nm, particulates with an high organic content exhibited a lower reflectance than those with a lower organic content. Remote sensing, therefore, needs to consider the properties of the individual suspended particles as well as the bulk properties of the sediment (Bhargava & Mariam, 1991).

### 2.3 The air-water interface

The signal returned upward by a water mass is the value which, after propagation up through the surface, becomes the inherent radiance of that medium, expressed as the *water-leaving radiance*. As radiation enters the water it is refracted, according to Snell's law (e.g. Bukata *et al.*, 1995). Water-leaving radiance is accordingly defined as:

$$L_u(\lambda, 0^+) = \frac{1 - \rho(\lambda, \theta)}{n_w(\lambda)^2} L_u(\lambda, 0^-) \quad (2-20)$$

(Mueller & Austin, 1995)

where  $0^+$  denotes a point just above the water's surface and  $0^-$  a point just below,

$\rho(\lambda, \theta)$  is the Fresnel reflectance which is assumed to be 0.021 over the visible spectrum (Gordon *et al.*, 1988), and

$n_w(\lambda)^2$  is the refractive index of sea water according to:

$$1.325 + \frac{6.610}{\lambda - 137.192}$$

(Mueller & Austin, 1992)

The roughness of the air-water boundary influences  $L_u(\lambda, 0^+)$ . In addition, any sunglint on the water's surface will increase  $L_u(\lambda, 0^+)$ , particularly at low solar zenith angles. This latter relationship is particularly strong where the surface waves are orthogonal to the look direction of the sensor. It is therefore necessary to normalise  $L_u(\lambda, 0^+)$  to a value that would have been obtained under theoretically ideal conditions, i.e. at a solar zenith angle of  $0^\circ$ , located at a mean distance between the earth and sun and minus any atmospheric effects contaminating the signal. *Normalised water-leaving radiance*,  $L_{wN}(\lambda)$ , is defined as:



$$L_{wn}(\lambda) = \frac{(1 - \rho(\theta))(1 - \bar{\rho})F_0(\lambda)R(\lambda, 0^-)}{n_w(\lambda)^2 Q(1 - rR(\lambda, 0^-))} \quad (2-21)$$

Gordon *et al.* (1988)

where  $\bar{\rho}$  is the Fresnel reflectance albedo of the sea surface for normal incidence and is averaged at 0.043 (Gordon *et al.*, 1988),

$F_0(\lambda)$  is the mean extraterrestrial solar irradiance derived from tables (Gregg *et al.*, 1993),

$$Q = \frac{E_u(\lambda)}{L_u(\lambda)} \text{ towards the zenith, and}$$

$r$  is the water-air reflectance for totally diffuse irradiance which is assumed to be 0.48 (Gordon *et al.*, 1988).

To provide a comparison between reflectance measured from the water's surface and image derived values it was necessary to redefine equation 2-21 to enable the propagation of  $R_L(\lambda, 0^-)$  quantities up through the water's surface to calculate  $R_L(\lambda, 0^+)$ . Equation 2-17 can be expressed as:

$$R_L(\lambda, 0^-) = \frac{R(\lambda, 0^-)}{Q} \quad (2-22)$$

Mueller & Austin (1995) specify that:

$$L_{wn}(\lambda) = \frac{F_0(\lambda)}{E_d(\lambda)} \cdot L(\lambda, 0^+) \quad (2-23)$$

Using equations 2-22 and 2-23 redefines equation 2-21 as:

$$\frac{F_0(\lambda)}{E_d(\lambda)} \cdot L_u(\lambda, 0^+) = \frac{(1 - \rho(\theta))(1 - \bar{\rho})F_0(\lambda)}{n_w(\lambda)^2 (1 - rR(\lambda, 0^-))} \cdot R_L(\lambda, 0^-) \quad (2-24)$$

From Mueller & Austin (1995):

$$R_L(\lambda, 0^+) = \frac{L_u(\lambda, 0^+)}{E_d(\lambda, 0^+)} \quad (2-25)$$

Incorporating equations 2-25 and 2-22 into equation 2-24 removes all remaining radiance parameters:

$$R_L(\lambda, 0^+) = \frac{(1 - \rho(\theta))(1 - \bar{\rho})}{n_w(\lambda)^2(1 - r \cdot Q \cdot R_L(\lambda, 0^-))} \cdot R_L(\lambda, 0^-) \quad (2-26)$$

Underwater, in  $Q$  equation 2-21 is often replaced by  $\pi$ .  $Q$  is only weakly dependent on wavelength (Morel & Gentilli, 1991) and would be  $\pi$  for a Lambertian reflector (see appendix B for proof). As most surfaces are not pure Lambertian reflectors, and studies by Bricaud & Morel (1987) have shown that the value of  $Q$  may actually be closer to 4.5, replacing  $Q$  by  $\pi$  is a potential source for error if the sea surface is not completely flat. However, in the absence of any field measurements for the value of  $Q$ , it was assumed that that  $Q$  equates to  $\pi$  (appendix B) as is commonly found in the literature. Substituting all known quantities into equation 2-26 and assuming that  $Q$  equates to  $\pi$  defines:

$$R_L(\lambda, 0^+) = \frac{0.521771}{1 - 2.16 \cdot R_L(\lambda, 0^-)} \cdot R_L(\lambda, 0^-) \quad (2-27)$$

Equation 2-27 thus allows the propagation of  $R_L(\lambda, 0^-)$ , which is derived from in-water optical measurements, up through the water's surface to quantify  $R_L(\lambda, 0^+)$ . This is the available reflectance quantity from remote sensors and can thus be used to compare and validate coincident digital images.

## 2.4 Classification of water types

The classification of water types yields information about the nature and content of the aquatic medium. Morel & Prieur (1977) categorised waters by their optical properties and identified two broad water types, case *I* and case *II*. Case *I* are clear, open oceanic waters and are those dominated by light absorption due to the presence of phytoplankton and their by-products. Case *II* waters refer to near-shore and estuarine waters whose optical properties are determined by resuspended inorganic and / or organic sediments, terrigenous particles and / or yellow substance.

Jerlov (1976) identified a more empirical approach to water type classification. Jerlov's (1976) theory is based on the spectral transmittance and  $K_d(\lambda)$  of a water body with respect to a reference wavelength of 475 nm. From earlier work using spectral transmittance to categorise two distinct water types (I and II) and using the  $K_d(\lambda)$

relationships, Jerlov (1976) classified three distinct and two intermediary water types (I, IA, IB, II and III). He went on to further categorise five types of coastal waters (types 1, 3, 5, 7 and 9) derived from observations in the type III waters off the coast of Scandinavia and western North America. A section of his results is shown in table 2.1 and figure 2.3 and are used later to categorise the water types under investigation for this study (section 5.1).

Water type	Wavelength (nm)						
	400	450	475	500	550	675	700
<b>I</b>	0.028	0.019	0.018	0.027	0.063	0.420	0.560
<b>IA</b>	0.038	0.026	0.025	0.032	0.067	0.430	0.570
<b>IB</b>	0.051	0.036	0.033	0.042	0.072	0.435	0.580
<b>II</b>	0.096	0.068	0.062	0.070	0.089	0.465	0.610
<b>III</b>	0.185	0.135	0.116	0.115	0.120	0.520	0.660
<b>1</b>	0.510	0.250	0.170	0.140	0.120	0.510	0.650
<b>3</b>	0.780	0.390	0.290	0.220	0.190	0.560	0.710
<b>5</b>	1.100	0.560	0.430	0.360	0.300	0.650	0.800
<b>7</b>	1.600	0.890	0.710	0.580	0.460	0.780	0.920
<b>9</b>	2.400	1.600	1.230	0.990	0.630	0.920	0.110

Table 2.1 :  $K_d(\lambda)$  ( $\text{m}^{-1}$ ) for different water masses (adapted from Jerlov, 1976)

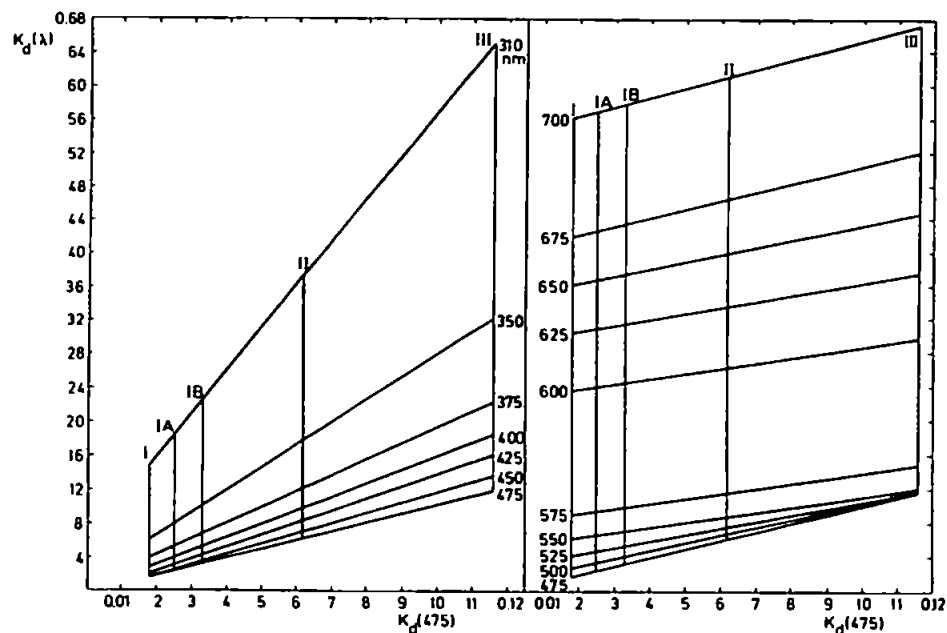


Figure 2.3 : Graphical representation of  $K_d(\lambda)$  ( $\text{m}^{-1}$ ) and its relation to  $K_d(475)$  ( $\text{m}^{-1}$ ) for different water masses (Jerlov, 1976)

### **3 Instrumentation and Fieldwork**

A fundamental problem when working in the marine environment is that, from a sea-going vessel, one can obtain only a single point measurement at the time of an overflight. As water is constantly moving, only one sea-truth measurement may be directly compared to the image. In terms of a sampling strategy for validation purposes this is not very satisfactory, although repeat overflights of the ship help to improve this somewhat. This problem can be partially overcome through the use of fixed moorings which continuously record a number of relevant parameters and allow the flight programmes to be more flexible.

#### **3.1 Study area**

The study area was contained within the LOIS RACS(C) coastal sampling grid which comprised a set of sites routinely revisited during the LOIS cruises (fig. 3.1). This included a section of the east coast of England extending from Great Yarmouth to Berwick-upon-Tweed (fig. 3.1). This area is highly dynamic and susceptible to change, particularly in response to any rise in sea level.

##### **3.1.1 The Humber Estuary**

The Humber Estuary (fig. 3.2) is one of the UK's largest and most economically influential estuaries with a catchment area spanning one fifth of the surface area of England. Its ports handle 15,000 ship movements and 500,000 passengers every year. The Estuary has to be constantly dredged to maintain the shipping lanes that are so important to the economy of the region. Sediment fluxes into and out of the Humber Estuary, therefore, have great economic as well as environmental influence and importance. The monitoring and understanding of the sediment dynamics are thus very important for an effective estuarine and coastal zone management strategy.

Along the Holderness coast, erosion is prevalent with an average land loss of 1.75 m p.a. (Hardisty, 1996) over a stretch of coastline extending 60 km from Spurn Head at the mouth of the Humber Estuary to Flamborough Head in the north (fig. 3.1). The Holderness coastline's soft boulder clay is constantly attacked by the sea augmented by storms. The

eroded silts and clays which dominate the coastline are carried offshore and any sand is moved alongshore due to wave action and strong tidal currents. Approximately 1,400,000 tonnes p.a. are contributed to the North Sea from cliff erosion along the Holderness coast (Pethick, 1988). The offshore silts and clays are carried southerly forming part of the Humber sediment plume and feeding the Humber Estuary and the Wash further to the south.

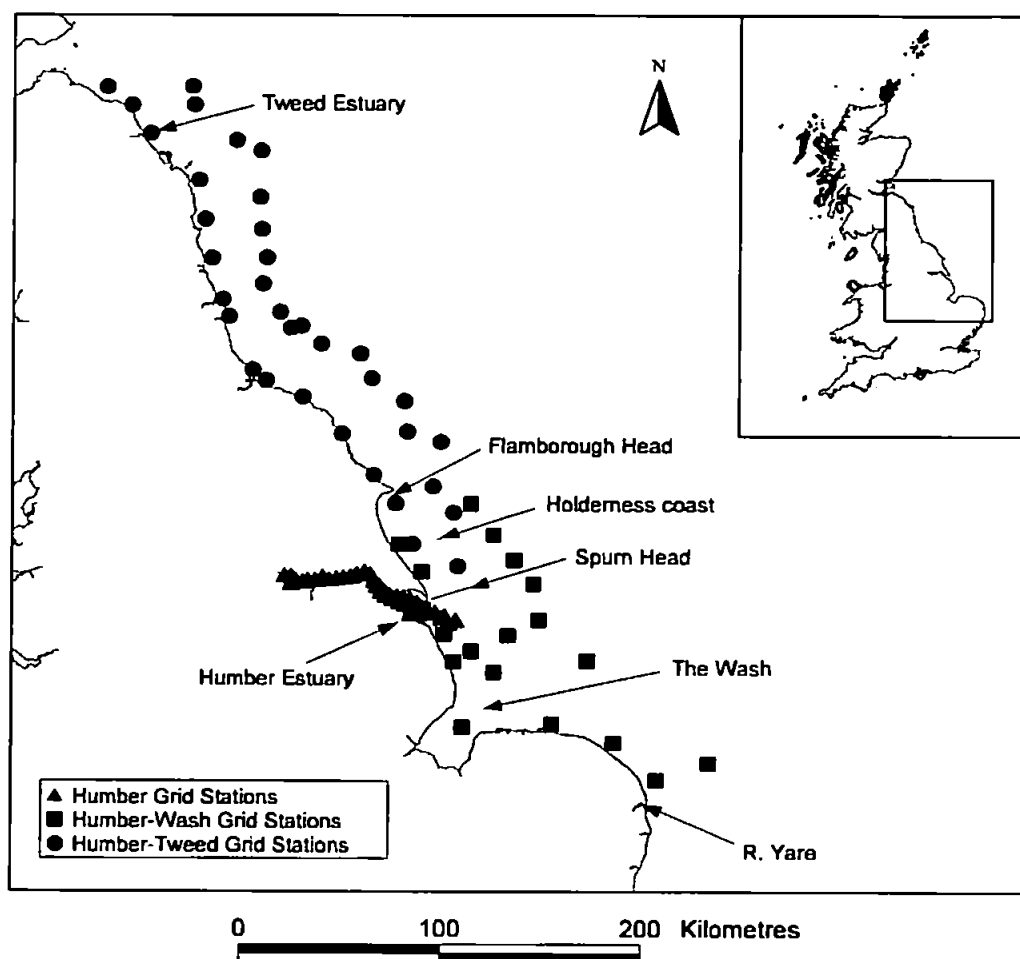


Figure 3.1: The LOIS RACS(C) coastal sampling grid stations

The Humber is a wide (15 km at its widest point) well mixed macrotidal estuary with a tidal length of 120 km and a tidal range in excess of 4 m (Pethick, 1988). Its large tidal range brings approximately  $1.2 \text{ km}^3$  of water into the estuary during the flood tide (Hardisty & Rouse, 1996). This cuts the deep channels at Immingham and Kingston-upon-Hull (fig. 3.2) upon which the majority of the region's trade is based. Due to the estuary's macrotidal nature, the tidal wave is deformed as it propagates upstream and the currents experienced during the flood are much greater than those experienced during the ebb

(Dyer, 1986). As a consequence, SPM is carried into the estuary on the flood, but is not removed in the same quantities on the ebb. Approximately 63,400 tonnes of sediment are deposited in the Humber every year. Over the past 6,000 years the estuary has accumulated enormous quantities of sands and muds and a deposit from 2 - 20 m thick has accumulated (Pethick, 1988). This has caused an overall smoothing of the estuary bed and banks into a trumpet shaped channel (Pethick, 1988).

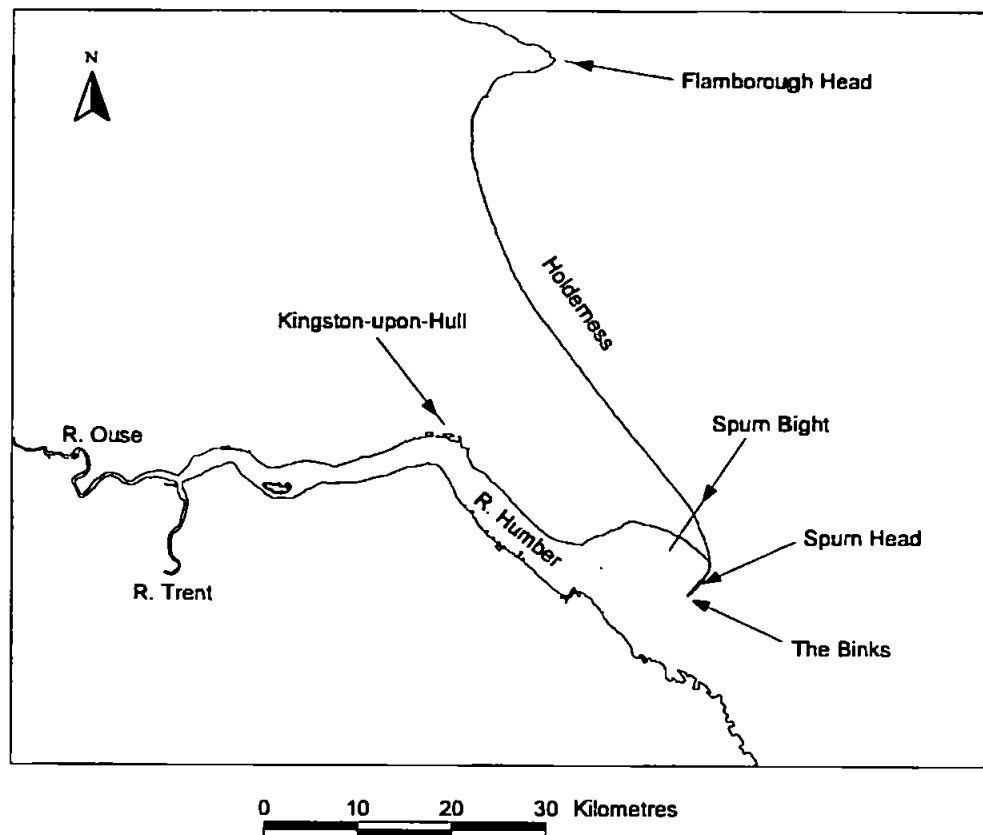


Figure 3.2 : The Humber Estuary

Approximately 200,000 tonnes p.a. of sediment are carried into the Humber by river flow (Pethick, 1988). The Rivers Ouse and Trent which flow into the Humber Estuary drain some 25,000 km<sup>2</sup> of central and eastern England (Arnett, 1991). The sediment content of the Humber itself, therefore, reflects the drainage across a variety of geological and superficial deposits. The tidal asymmetry of the estuary causes a net landward movement of sediment entering the estuary from the sea; the fluvial-derived particulates tend to be transported offshore due to the fresher water floating on the surface (National Rivers Authority, 1993). Most of the sediments found in the Humber, however, are not riverine-derived, rather they were transported from the North Sea through tidal power. The riverine-derived sediments are mainly found in the upper part of the Ouse, only 20 - 30 km

from its tidal limit at Naburn Weir (Uncles, *et al.*, 1997a). Below this the sediments are mostly derived from the sea. The ratio of Holderness cliff-derived sediments to those fluvial sediments derived from the Humber Estuary and further south in the Wash is of the order of 7:1 (McCave, 1987).

Vast quantities of material have been transported down the Holderness coast and into the breaker zone of the Humber Estuary. This has been the sediment source for the formation of Spurn Head, a spit which lies across the mouth of the estuary (fig. 3.2). A spit is formed by an accumulation of material until a point is reached where its physical presence across the estuary mouth causes such an increase in velocities that the currents erode as much material as is deposited (Dyer, 1986). Thus, they are highly mobile landforms and Spurn Head migrates inland as the Holderness coastline erodes. The channel through which the River Humber follows was carved during the last glacial period but the shape of the outer estuary seen today (i.e. from Kingston-upon-Hull to the sea) is largely controlled by the infill of Spurn Bight (fig. 3.2). This infill lies below high tide and continues seaward of Spurn Head to the Binks (fig. 3.2). The Binks form the northern shoulder of the glacial channel and project 5 km into the North Sea. The whole feature forms a 15 km long, 5 km wide platform and is an integral part of the estuary.

### 3.1.2 The Tweed Estuary

Located in the far northern section of the LOIS RACS(C) study area lies the Tweed Estuary (figs. 3.1 & 3.3). The Tweed is a shallow estuary and is particularly important for trout and salmon. It is a rapidly flushed, highly stratified estuary in which frontal systems are ubiquitous (Uncles & Stephens, 1996; Uncles *et al.*, 1997b). The Tweed has a tidal limit about 13 km from the estuary mouth at Horncliffe Island. Tides at Berwick-upon-Tweed are semidiurnal with mean springs of 4.1 m and mean neaps of 2.5 m. There is strong variability in water velocity and salt intrusion between springs and neaps (Uncles & Stephens, 1996). The estuary drains the Rivers Tweed and Whiteadder; the long term monthly-averaged inflows to the lower reaches of the Tweed in July approach  $30 \text{ m}^3 \text{ s}^{-1}$  and rise to  $140 \text{ m}^3 \text{ s}^{-1}$  in January (Uncles & Stephens, 1997). The higher inflows associated with the winter months mean that higher SPM concentrations than in the summer months are experienced during this time (Uncles & Stephens, 1997). Even during the winter months, however, the concentrations of SPM in the Tweed are low.

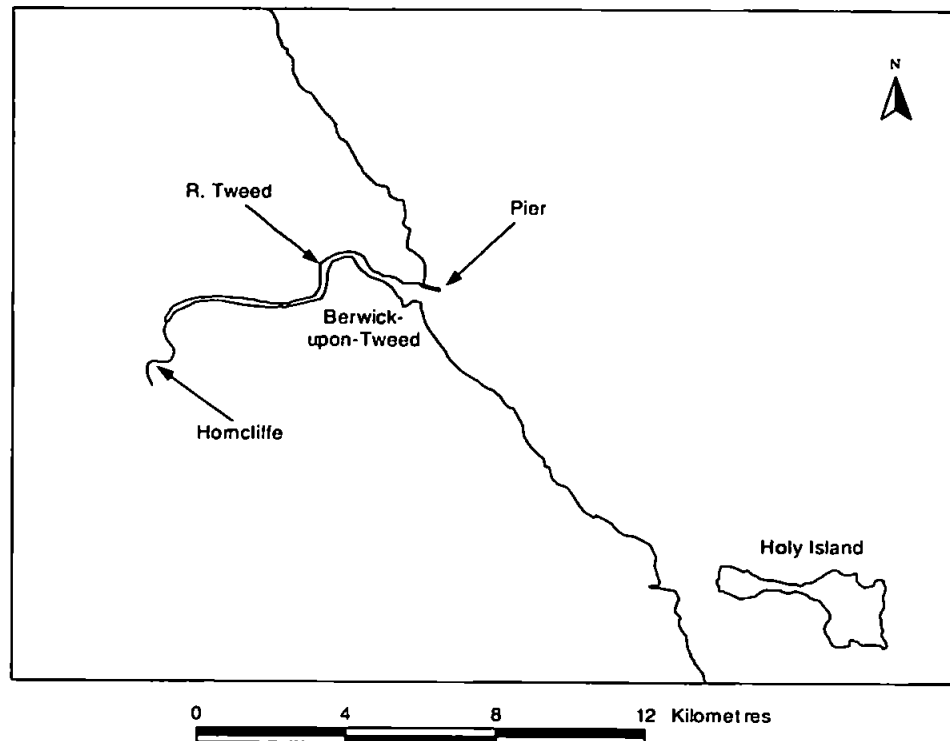


Figure 3.3 : The Tweed Estuary

In such an highly stratified system, the forces determining estuarine circulation can be assessed by looking at surface salinity and temperature distributions. These parameters delineate frontal phenomena and plumes, and by studying a time series of data, covering particular sections of the tidal cycle, it would be possible to gain a greater understanding of the forces at work in the estuary.

### 3.2 Airborne instrumentation

The remote sensing platform used in this study was a Piper Navajo Chieftain aircraft maintained by the NERC Airborne Remote Sensing Facility (ARSF). On board was an ITRES Compact Airborne Spectrographic Imager (CASI), alongside a Daedalus AADS-1268 Airborne Thematic Mapper (ATM) and a Wild RC-10 metric survey camera (not used in this study). A downwelling Incident Light Sensor (ILS) was installed on the roof of the aircraft at the beginning of the LOIS campaign. Attitude and position of the aircraft was obtained from a differential Global Positioning System (GPS). The GPS information was combined with output from a laser ring gyro Attitude and Heading Reference System (AHRS), also housed onboard, to accurately detail the aircraft's location in three-dimensional space. The output from the equipment onboard the NERC aircraft was



combined through custom designed hardware known as the Integrated Data System (IDS) (fig. 3.4).

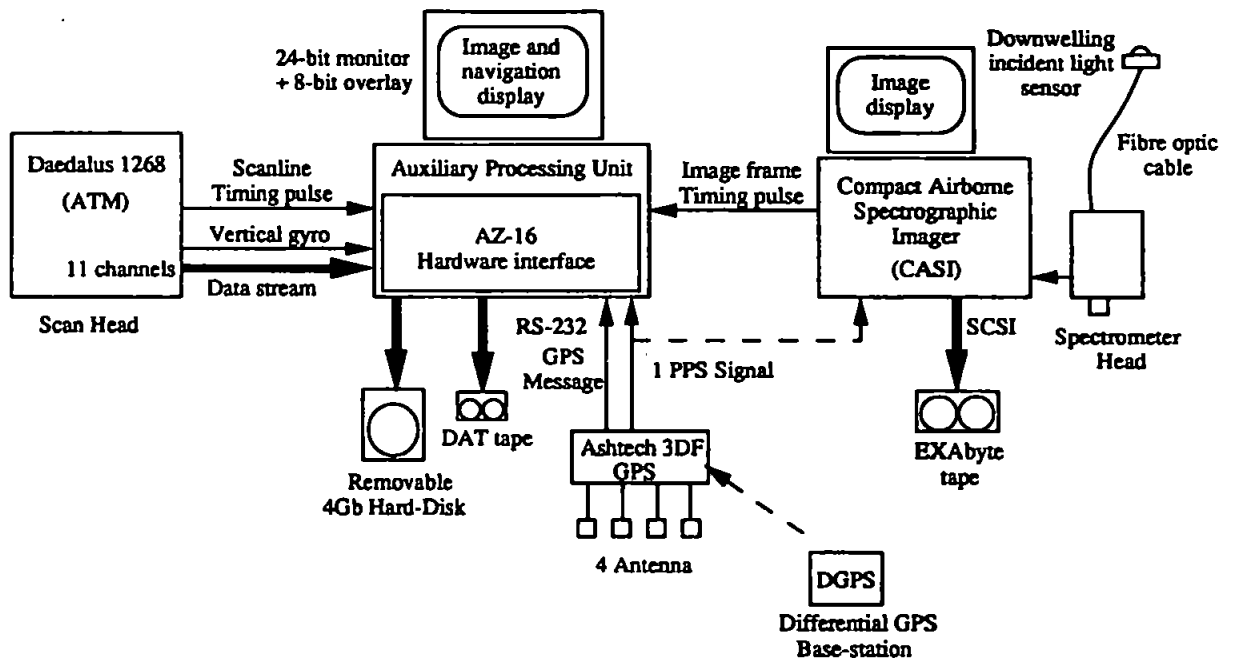


Figure 3.4 : The Integrated Data System onboard the NERC aircraft (Wilson, 1995)

### 3.2.1 Compact Airborne Spectrographic Imager

The CASI is a programmable high spectral and spatial resolution imaging spectrometer with a wide dynamic range and low noise on high quality data (Anger *et al.*, 1990). The CASI is a pushbroom type imager operating through the use of a two-dimensional CCD array (fig. 3.5) coated with lumogen to improve blue response. This improves the sensitivity for the identification of subtle variations in water-leaving radiance arising from spatial variations in SPM, plant pigments and dissolved organic matter (also known as yellow substance or gelbstoff). It has a field-of-view of 42° thereby covering a swathwidth of 2.303 km at an altitude of 3.048 km. The along-track resolution is dependent on the scan rate and aircraft speed.

The CASI has the analytical potential of a spectrometer with the ability to record up to 288 spectral channels in the visible and near-infrared. Its spectral range lies between 400 nm and 915 nm with a nominal bandwidth of 1.8 nm, spectrally separated by a reflectance grating. The CASI has very high data acquisition rates (typically a terabyte per hour) thereby limiting the amount of data that can be recorded at any one time and necessitating

subsampling of the data through alteration of the mode of operation. This can be done in one of three ways:

- Spatial (or imaging) mode (fig. 3.6a),
- Spectral (or multispectral) mode (fig. 3.6b), or
- Full frame (hyperspectral) mode.

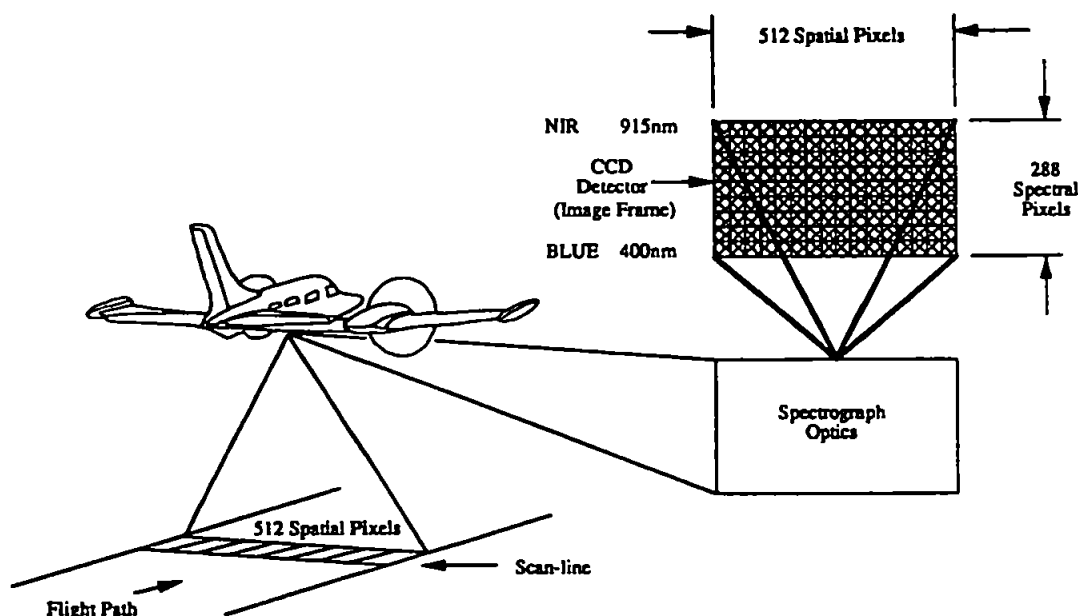


Figure 3.5 : The CASI imaging concept (Wilson, 1995)

This study utilises the CASI in its spatial mode of operation (fig. 3.6a). In spatial mode the full amount of information from the scene line (512 pixels plus 66 columns of information within the CCD's hidden zone, fig. 3.6a) is collected. This information is, however, restricted in the spectral dimension through the selection of a limited number of wavelength bands (up to eighteen). Fourteen wavelength ranges were chosen here to match the specific scientific interests of water quality and atmospheric parameters and to include those ranges covered by NASA's Sea Wide Field-of-view Spectrometer (SeaWiFS) (table 3.1). SeaWiFS is a satellite-based sensor, housed onboard ORBIMAGE-2, which became operational in 1997. It was launched to provide vital oceanographic information the likes of which have not been seen since the Coastal Zone Color Scanner (CZCS) ceased operation in 1986. The launch of ORBIMAGE-2 was originally planned for a date much earlier than September 1997 and it was hoped that the data generated

during this study would be analysed in concert with SeaWiFS images. The delayed launch of the satellite prevented this.

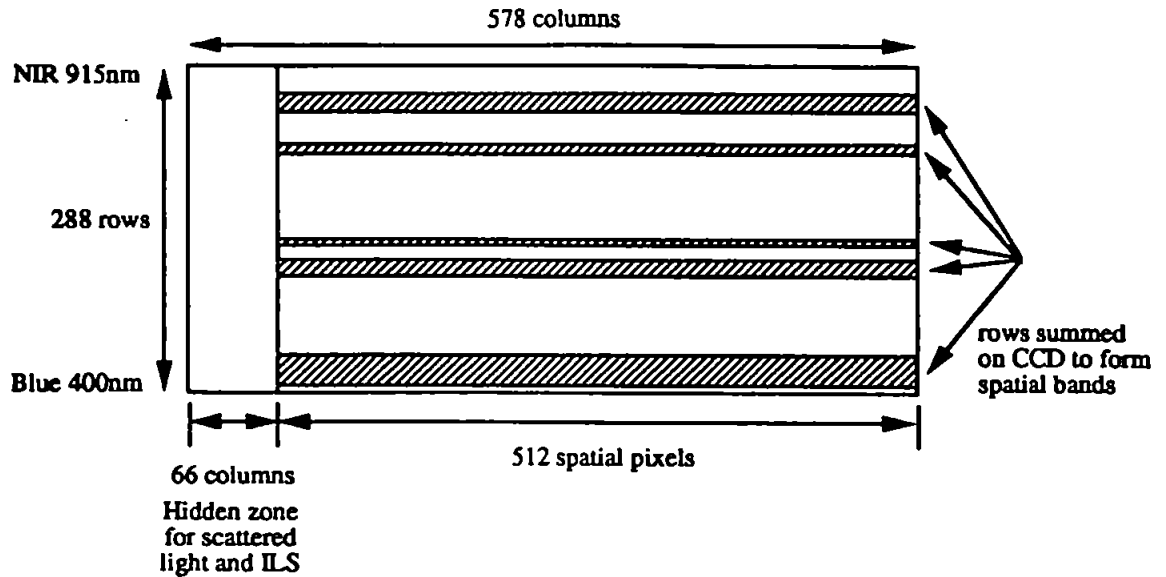


Figure 3.6a : CASI spatial mode configuration (Wilson, 1995)

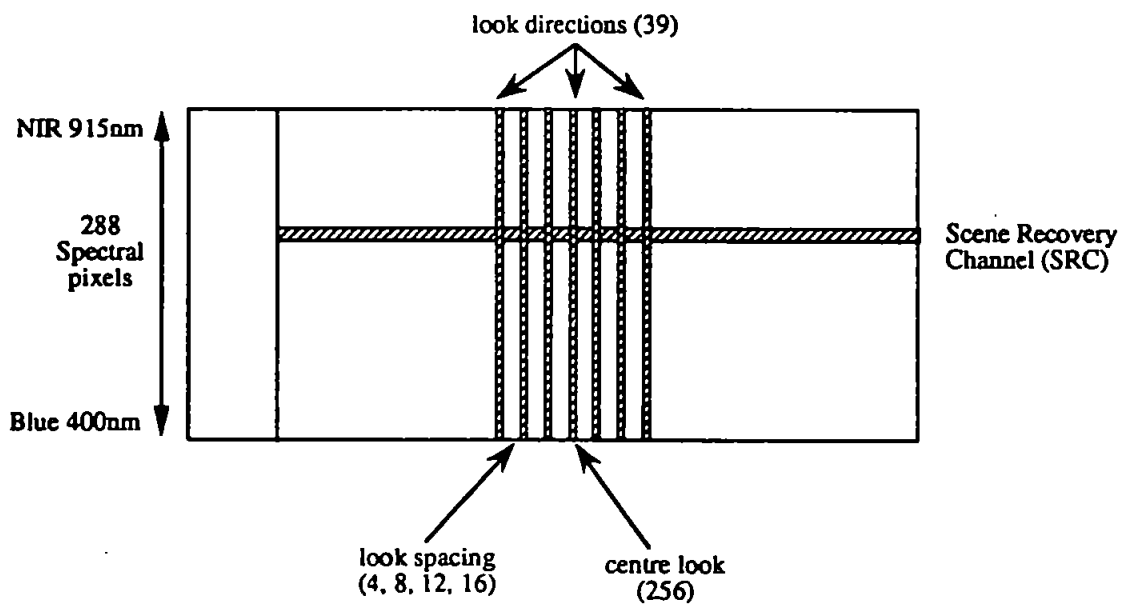


Figure 3.6b : CASI spectral mode configuration (Wilson, 1995)

CASI Band Number	Min. (nm)	Wavelength Max. (nm)	Centre (nm)	SeaWiFS Band & Wavelengths
1	408.08	422.15	412.13	1 (402 - 422 nm)
2	438.00	453.87	443.51	2 (433 - 453 nm)
3	483.91	490.02	490.02	3 (480 - 500 nm)
4	503.38	509.68	501.68	4 (500 - 520 nm)
5	547.74	563.75	554.31	5 (545 -565 nm)
6	611.89	631.55	620.37	
7	661.99	678.13	668.64	6 (660 - 680 nm)
8	679.92	687.10	682.06	
9	706.86	717.66	710.75	
10	748.27	755.49	750.28	7 (745 - 785 nm)
11	757.29	784.37	769.21	
12	816.94	831.43	822.55	
13	847.75	884.03	864.40	8 (845 - 885 nm)
14	887.71	902.27	893.63	

Table 3.1 : CASI bandset and its relation to SeaWiFS

### 3.2.2 Airborne Thematic Mapper

The ATM is a twelve channel multi-spectral scanner. Its wavelength range spans the visible to the thermal-infrared and includes channels that closely match those of the Landsat Thematic Mapper (TM), a satellite-based sensor mainly used in terrestrial studies (table 3.2). The visible and near-infrared light is split by a prism before being imaged by an array of silicon detectors (fig. 3.7). Middle- and thermal- infrared light is split, imaged and recorded on single, nitrogen cooled detector elements. The inclusion of the thermal-infrared channels complements the CASI whose sensitivity does not reach as far into the electromagnetic spectrum. Between the two sensors, a clear picture of the content and nature of the target waters can be built up by using image information spanning from visible to thermal-infrared wavelengths.

ATM Band Number	Wavelength		Landsat TM Band & Wavelengths
	Min. (nm)	Max. (nm)	
1	424	448	
2	469	518	1 (450 - 520 nm)
3	522	601	2 (520 - 600 nm)
4	594	635	
5	627	694	3 (630 - 690 nm)
6	691	761	
7	754	924	4 (760 - 900 nm)
8	897	1027	
9	1600	1785	5 (1550 - 1750 nm)
10	2097	2391	7 (2080 - 2350 nm)
11	8400	11500	6 (10400 - 12500 nm)
12	8400	11500	

Table 3.2 : ATM bandset and its relation to Landsat TM

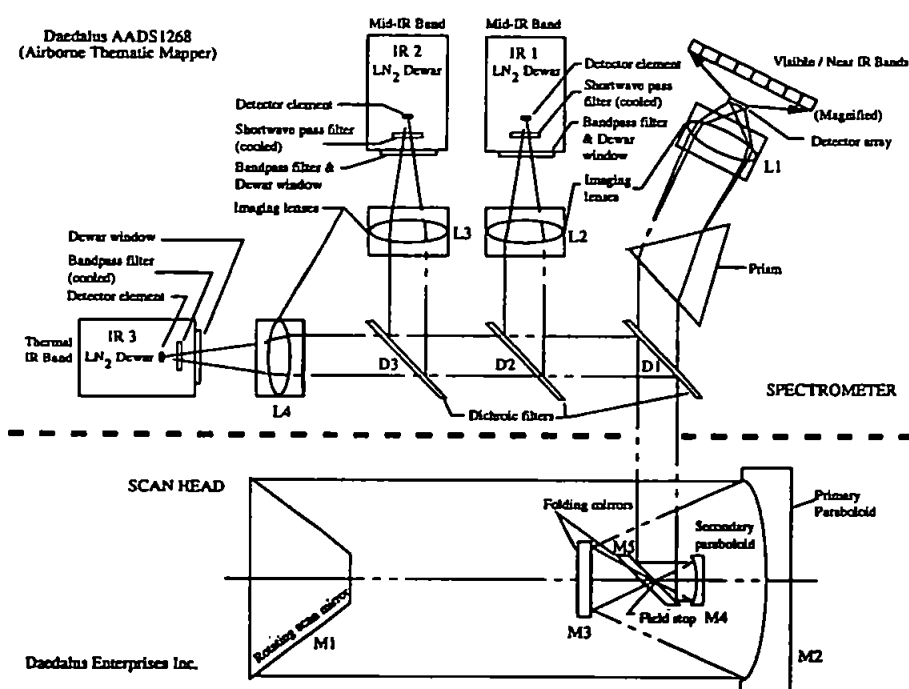


Figure 3.7 Optics and detector layout within the ATM (Wilson, 1995)

### 3.3 Sea-based instrumentation

Sea-based instrumentation was deployed from a series of cruises executed over two years (1994 - 1995) from the *Sea Vigil*, maintained by the National Rivers Authority (now the Environment Agency), and the Royal Research Ship *Challenger*. The inner and outer

estuary work in the Humber was executed from the former and the offshore and coastal work from the *Challenger*.

### 3.3.1 PML-Satlantic profiling system

The PML-Satlantic profiling system consists of a seven-band radiance and a seven-band irradiance Satlantic sensor head (both set to conform to SeaWiFS specification and covering the same wavelengths, except in the seventh channels where radiance is set to 683 nm and irradiance 700 nm), a logger and a battery pack mounted on a T-shaped frame painted matte black to reduce interference from the upwelling light field (fig. 3.8). When profiling, the equipment was suspended on a taut wire with a weight suspended a distance of 3 - 4 m from the bottom of the frame. The weight kept the profiler vertical and was held at a distance sufficient to minimise interference from the weight itself on the upwelling radiance field. The battery pack was manually connected to the logger to commence operation and data were acquired and stored internally. Logging stopped when the battery pack was disconnected. Data were subsequently downloaded from the logger onto a PC.

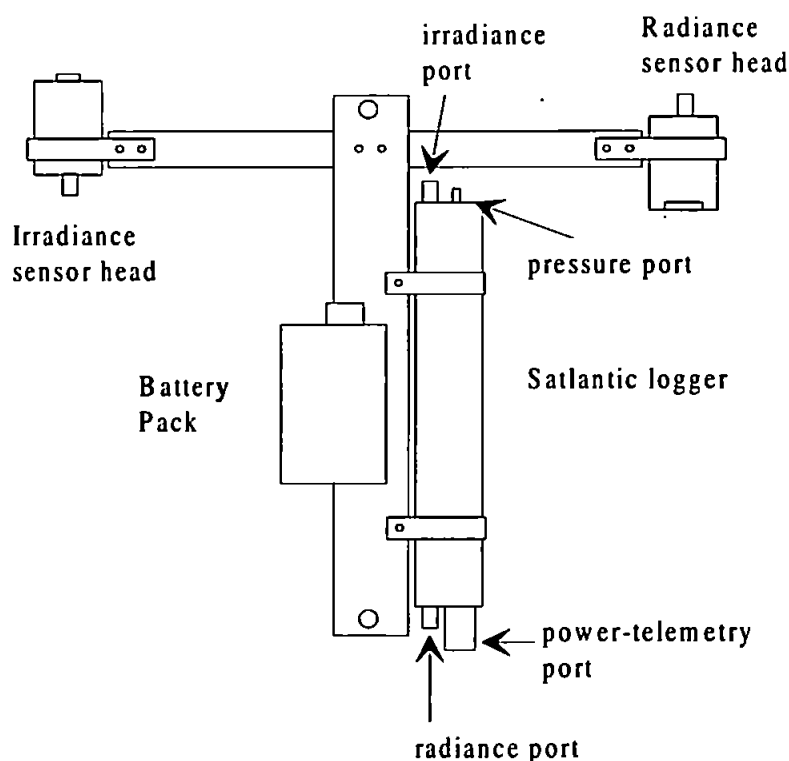


Figure 3.8 : The PML-Satlantic profiling system

SeaWiFS protocols state that optical profiles should be acquired from the stern of the ship facing into the sun and from a point as far away from the ship as possible (Mueller & Austin, 1995). This ensures that the amount of shading by the ship itself is kept to a minimum and within acceptable limits. The PML-Satlantic was deployed from a telescopic jib crane into a position facing into the sun and located as far away from the ship as possible.

### **3.3.2 Core data collection and underway instrumentation**

The data acquired by the underway instrumentation operational during the *Sea Vigil* and *Challenger* cruises was calibrated through comparison with discrete samples collected throughout the monitoring period. The resulting data included information on temperature, salinity, dissolved oxygen, SPM, chlorophyll, phaeopigments and water depth. Navigational information, acquired through differential GPS, was used to geolocate each sampled point.

The following discrete sample data were obtained as part of the core LOIS data collection campaign:

- Chlorophyll by filtration through 0.2 $\mu$  nucleopore filters and then extraction in 90% acetone. The total chlorophyll was assessed by fluorescence measurements using a Turner fluorometer.
- Total suspended particulate matter by filtration through pre-ashed and pre-weighed GFF (Glass fibre Filter F) filters (0.7 $\mu$ ).

The underway instrumentation onboard the *Sea Vigil* was controlled by a *Qubit* system which logs data from a variety of instrumentation including navigational information. Those used in this study operated on a flow through pumped system which obtained water at a set depth. The instrumentation included:

- WS Oceans CTD,
- Omnidatas Hydrolab,
- Turner Electronics Fluorometer, and
- Partech 7000i Transmissometer (40 mm cell).

The underway instrumentation operational during the *Challenger* cruises included:

- EA-500 echo sounder,
- Decca Mark 53G differential GPS, and
- Fluorometer, transmissometer and thermosalinograph operated on a flow through pumped system which obtained water at a set depth.

### 3.3.3 Moored instrumentation

It is a great advantage to have instrumentation permanently moored and recording at strategic locations to ensure that, should particularly favourable conditions prevail for flying, any image data acquired could be compared to sea-based information. The presence of permanently moored instrumentation eliminates some of the time-consuming and costly efforts involved with field work. To this end, a *flux curtain* consisting of five permanent moorings monitoring the dynamics of the estuary were put in place across the mouth of the Humber Estuary (fig. 3.9) by the University of Hull (Hardisty, *et al.*, 1995).

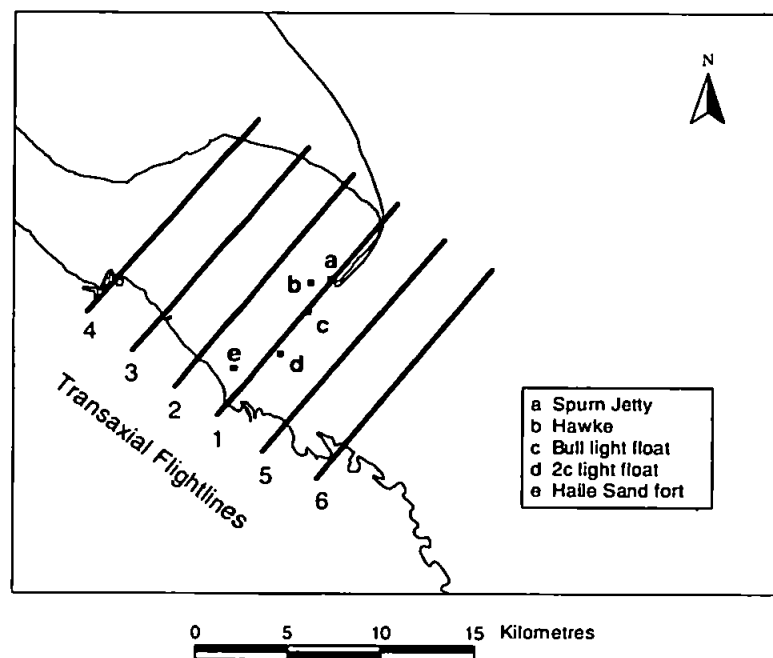


Figure 3.9 : The *flux curtain* moorings and their relation to the transaxial flightlines

Development and installation of the *flux curtain* took place in 1994 and it became fully operational towards the end of that year. For the 1995 field campaign the Bull Light Float mooring (fig. 3.9, mooring c) generated data sampled from the top 0.2 m of the water for



SPM, tidal velocity, temperature and salinity at hourly intervals. The sampling rate was increased to 15 minute intervals during some of the overflights. The data were telemetered to the University of Hull where it were calibrated and archived.

### **3.4 Fieldwork campaign**

The objective of the field campaign throughout 1994 and 1995 was to acquire coincident airborne and sea-truth data for comparison and for algorithm development and validation. There were several technical problems encountered during the 1994 campaign concerning the airborne data system. These included the delay of the introduction of an interim positioning system and the postponement of the fully Integrated Data System (IDS), both of which were designed to provide accurate position and attitude information (Mockridge *et al.*, 1997). As a result, the images that were acquired in 1994 cannot be accurately geometrically corrected (neither for position nor attitude). There were also a few problems during 1994 that resulted in the CASI being sent back to ITRES in Canada due to poor performance. This coincided with a major data gathering campaign. As a result of the technical difficulties, and due to the scarcity of those images coincident with sea-based monitoring, this study focuses on data acquired during the 1995 campaign which was more successful in terms of acquisition of image data of an acceptable quality and quantity (table 3.3).

#### **3.4.1 *Sea Vigil* cruises**

Monthly campaigns in the Humber Estuary were planned throughout the summer of 1994 and 1995 with simultaneous acquisition of airborne and sea-based data. These were executed from the *Sea Vigil* (cruises SV23 & SV24) as part of the core LOIS fieldwork programme in the Humber Estuary (table 3.3). The vessel track followed a predetermined course extending out from the mouth of the Humber into the North Sea (fig. 3.10).

The flight campaign was organised into a series of discrete blocks across and down the estuary. These were predetermined and the *Sea Vigil*'s track designed to encompass the flightpaths (fig. 3.10). The cruise track spanned the heavily SPM laden waters inside the estuary and extended into the clearer waters of the North Sea. Profiling stations were identified along the cruise track (fig. 3.10). Vertical profile stations VP (VP1 - 10) and

MC (MC1 - 6) stations were devised to span the outer estuary waters and to coincide with the transaxial flightpaths across the estuary respectively. The PML-Satlantic was deployed at the profiling stations VP1 - 10, and occasionally MC1 - 6 when communication by air-band radio signalled that the aircraft was overhead the vessel.

Cruise	Date	Sampling Grid	Underway data	Sea-based data acquired			Discrete samples	Coincident overflights of ship
				PRR profiles	Satlantic profiles	UOR		
1994								
SV7	26 April	H	*				*	
	27 April	H	*			*	*	
	28 April	H	*				*	
SV8	11 May	H	*	*		*	*	
SV9	18 May	H	*	*		*	*	
	19 May	H	*	*		*	*	
SV10	28 June	H	*	*		*	*	1
	29 June	H	*				*	
	30 June	H	*	*		*	*	
SV11	26 July	H	*	*		*	*	
	27 July	H	*				*	
	28 July	H	*				*	
SV12	09 August	H	*			*	*	
	10 August	H	*				*	
1995								
CH118a	06 April	H-T	*		*	*	*	4
	10 April	H-T	*		*	*	*	1
	11 April	H-W	*			*	*	
	12 April	H-W	*		*	*	*	4
CH118b	21 April	H-T	*		*	*	*	3
	23 April	H-T	*		*		*	2
CH119c	07 July	H	*		*		*	
SV23	19 July	H	*		*	*	*	
SV24	22 August	H	*		*		*	2
	23 August	H	*		*	*	*	

Table 3.3 : *Challenger & Sea Vigil* cruise and airborne image data obtained as part of the 1994 and 1995 fieldwork campaigns. The sampling grid abbreviations refer to those depicted in figure 3.1 where H is the Humber grid, H-T the Humber-Tweed grid and H-W the Humber-Wash grid. For completeness, data acquired using a Profiling Reflectance Radiometer (PRR) and an Undulating Oceanographic Recorder (UOR) are also detailed. The data acquired using these instruments were not used for further study and their use and application are not reported in this thesis.

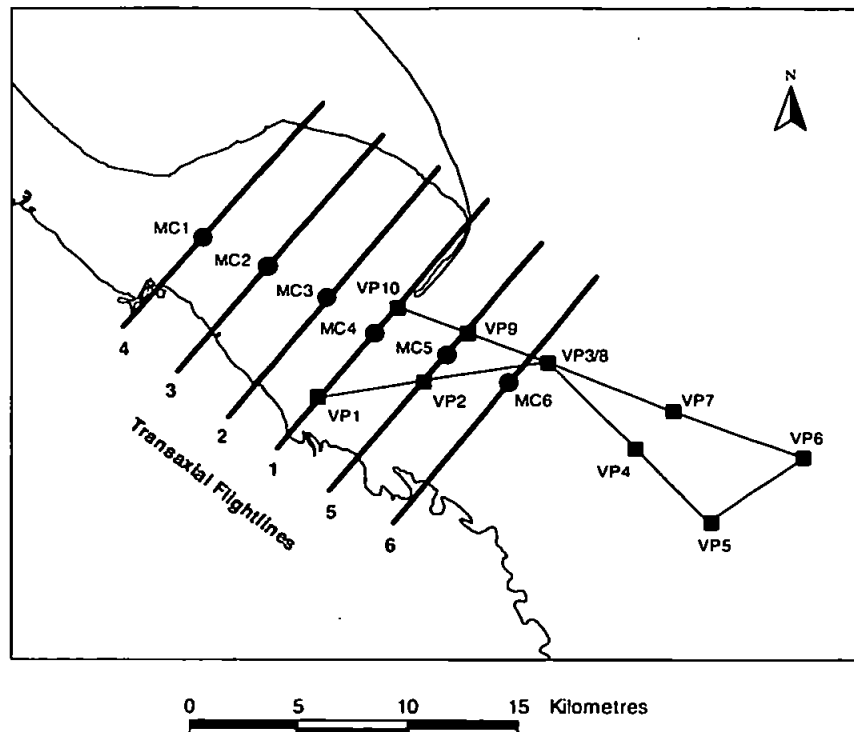


Figure 3.10 : The *Sea Vigil* cruise track. The VP vertical profiling stations span the outer estuary cruise track and the MC vertical profiling stations coincide with the transaxial flightpaths across the inner estuary.

### 3.4.2 Challenger cruises

Field data were acquired from three *Challenger* cruises during 1995, CH118a, CH118b and CH119c (table 3.3). The ship's track encompassed the core sampling stations on the Humber-Wash and Humber-Tweed grids (fig. 3.1). Airborne data were acquired over the *Challenger* to enable direct comparison with measurements taken from the vessel. Communication between the ship and plane was maintained by the use of air-band radio to ascertain the exact location of the ship.

A predetermined protocol for flightline delimitation from the air was followed throughout the *Challenger* cruises (CH118a, CH118b & CH119a). This consisted of a preliminary run over the ship followed by lines to the east and to the west thereby building up a grid of flightpaths around the ship and finishing with a final run over the vessel. In the presence of sunglint, the flightlines were reoriented to minimise these effects but to still pass over the ship. Whilst this was being executed, the ship remained stationary in most cases and PML-Satlantic optical profiles were acquired.

### 3.4.3 Time series

As well as for the acquisition of comparative sea- and air-based data, the objective behind the overflights of the Humber and Tweed Estuaries during 1995 was the acquisition of sequential data time series. This type of exercise enables the synoptic study of a region's dynamics over certain sections of the tidal cycle. A number of imaged time series were acquired during 1995 for significant fractions of the tide (table 3.4). Time series were acquired over both the Humber and the Tweed Estuaries. In the Humber Estuary, transaxial flightline 1 was devised and repeat flights undertaken to target the cross-section of the estuary mouth monitored by the *flux curtain* (fig. 3.9).

	Date	Time in hours relative to low water (LW)	Tidal state	Number of images
Humber	29 June	LW - 0.23h to LW + 0.1h	springs	3
	10 August	LW + 1.38h to LW + 3.33h	1 day before springs	9
	11 August	LW - 0.15h to LW + 0.08h	springs	2
	15 August	LW - 3.33h to LW - 2.17h	4 days after springs	6
	21 August	LW + 3.27h to LW + 4.7h	neaps	7
Tweed	4 May	LW - 0.125h to LW + 4.1h	5 days after springs	19

Table 3.4 : Time series of CASI and ATM image data acquired in 1995 coincident with sea-based measurements obtained from the *flux curtain* in the Humber Estuary and from a survey vessel in the Tweed Estuary

## 4 Data Calibration and Processing

There are a number of image calibration and correction steps that need to be followed in order to accurately relate image radiance values to sea-surface measurements with sub-pixel accuracy. These include radiometric calibration, thermal calibration (for thermal-infrared channels), atmospheric correction and geometric correction (figs. 4.1 & 4.2). Providing each stage can be attained with sufficient accuracy, the development of algorithms to quantify in-water parameters can be achieved. Ideally, an algorithm should be portable, both in time and space, and not require *in-situ* measurements for its operative use. Here, measurements taken from the sea surface are used to develop algorithms. Examples of CASI image calibration and processing form the focus for this chapter. Procedures relating to the ATM are also addressed but are more fully exemplified in Appendix F : Uncles *et al.*, 1999.

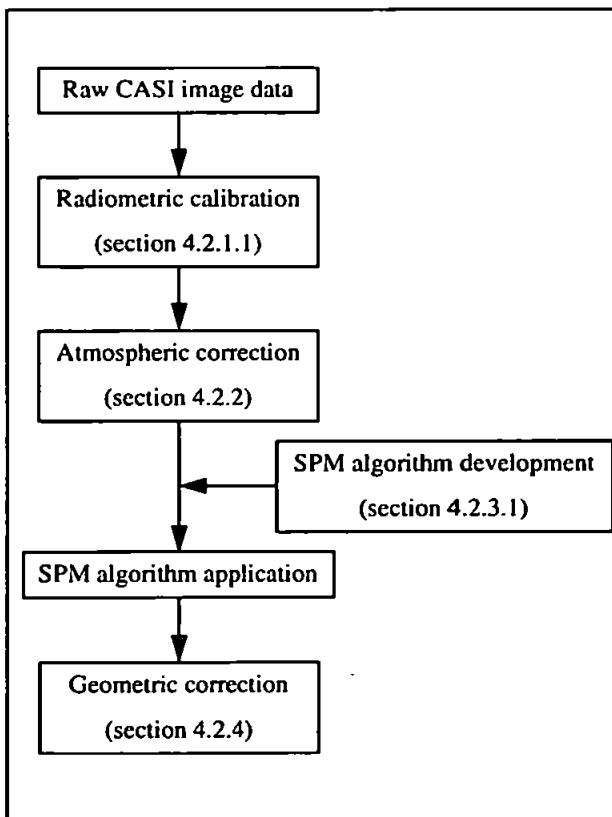


Figure 4.1 : CASI image calibration and correction procedures

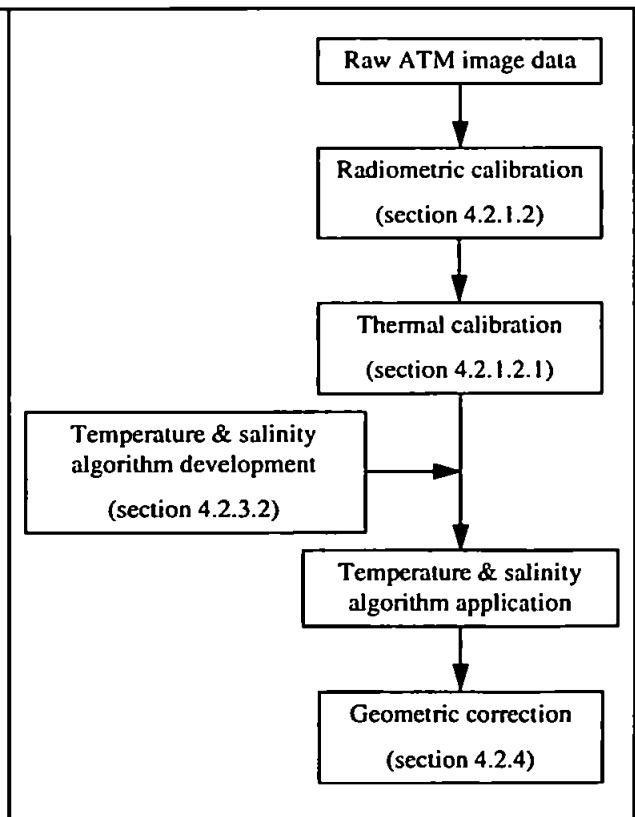


Figure 4.2 : ATM image calibration and correction procedures

To verify the image calibration stages, optical profile data acquired coincident with the images were used.

#### **4.1 *In-situ* optical profiles**

An in-water optical profile sensor detects the upwelling light field with an exponentially decreasing magnitude with depth. Austin & Petzold (1981) executed a study over waters with low SPM concentrations which involved measurements taken from an in-water optical sensor and from the spaceborne sensor the Coastal Zone Color Scanner (CZCS). They found that, at 520 nm, 87% of the upwelling radiance signal at the surface was returned from the first 20 m or less and 50% of the signal originated from the upper 7 m of the water column. Therefore, the properties most relevant from the remotely sensed signal are contained within the upper surface waters.

In order to quantify SPM using remote sensing techniques, the characteristics of the water are specified by direct measurements of the optical properties and their variation with depth. Here, this was achieved through the acquisition of twenty PML-Satlantic optical depth profiles (see section 3.3.1) which spanned the waters of the North Sea and the Humber Estuary.

The raw data files from the PML-Satlantic profiler were downloaded from the internal logger onto a PC immediately following profiling. Each channel was calibrated according to a set of calibration coefficients as supplied by the manufacturers, Satlantic Inc. (Nova Scotia, Canada). This yielded calibrated upwelling radiance ( $L_u$ ) values at 412 nm, 443 nm, 490 nm, 510 nm, 555 nm, 670 nm and 683 nm, and calibrated downwelling irradiance ( $E_d$ ) values at 412 nm, 443 nm, 490 nm, 510 nm, 555 nm, 670 nm and 700 nm.

The data files contain information as a time series from the moment the unit is switched on. Using detailed logs, consisting of accurately monitored and recorded times, it was possible to time stamp the data for the entire profile. Depth was also recorded during profiling via a pressure sensor on the rig.

Errors will be incurred at many stages in data acquisition and processing. The PML-Satlantic was rigorously calibrated on the bench both by Satlantic Inc. (Nova Scotia) and also at PML. However it must be recognised that would still be is at least a 1% uncertainty in the calibration of the instrument. Measurements are also affected by the instantaneous depth of the underwater sensor, its attitude, the location of any ship shadow, the refractive effects of waves and swell (Austin & Petzold, 1981) and self-shading by the instrument itself (Gordon & Ding, 1992). Aas & Korsbø (1997) estimated that under normal conditions in coastal areas, the error in radiance readings close to the surface is seldom less than 20% due to the influence of waves and the ship's movement. Such effects were kept to a minimum in this study by profiling at a distance from the ship to minimise ship shadow, by attaching a weight to the bottom of the rig to keep it near-vertical and by only acquiring data under favourable weather conditions (i.e. under clear or totally cloud covered skies and calm sea conditions). The PML-Satlantic and the frame upon which the instrument is mounted was constructed with the SeaWiFS protocols (Mueller & Austin, 1995) in mind. Thus the effects of self-shading on the measurements is kept to a minimum although it should be recognised that the error due to self-shading may be as much as 5% in more turbid waters (Gordon & Ding, 1992).

The profiles were examined in log space where the relationship of radiance and irradiance with depth is a linear one above the maximum depth of light penetration (Mueller & Austin, 1995). Linear regression analyses were performed on the log plots of the radiance and irradiance profiles. The resulting regression equations derived the  $L_u$  and  $E_d$  values for that profile at a point just below the air-water interface,  $L_u(\lambda, 0^-)$  and  $E_d(\lambda, 0^-)$ .

It was necessary to ascertain whether the profile's upcast or the downcast alone or an average of the two were the most relevant for analysis. In some cases the upcast and downcast differed significantly. These differences may have been due to changes in the water structure during profiling or due to external environmental effects such as changing lighting conditions (e.g. scattered cloud). In the absence of any evidence for making a decision regarding which section of the profile is the most relevant for use, an average of the up and downcasts was sought for each dataset. Where the up and downcast differed

significantly, the upcast alone was chosen or that section of the data most relevant for comparison with a coincident flightline.

In an attempt to ascertain the most reliable methodology to adopt in linear regression analysis to achieve subsurface downwelling radiance and upwelling irradiance, a profile was selected as the test subject. One acquired in clear case I waters was chosen as these conditions support relatively deep optical penetration depths for all wavelengths and so the test dataset provides a clear visualisation of the nature and distribution of the light field with depth. Those profiles acquired in case II waters reflected similar trends seen in the test dataset but were not as clearly apparent on visual scrutiny due to the shallower maximum penetration depth of the light field. The 510 nm upwelling radiance channel was selected as an example of a characteristic dataset (fig. 4.3) and regression analyses on its log derivative, to achieve  $L_u(510,0^-)$ , were performed.

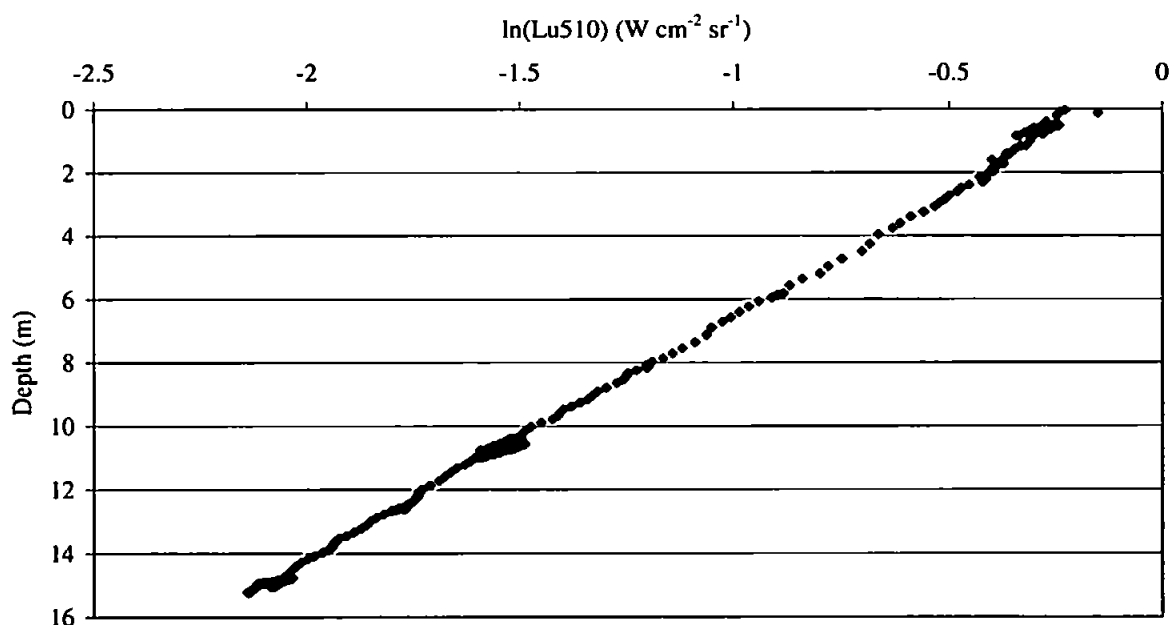


Figure 4.3 : Relationship between log calibrated upwelling radiance at 510 nm and depth

Two linear regression analyses were performed on the test dataset. The preliminary situation used the entire set of readings, the second scenario used those readings deemed entirely free from ship shading. The proportion of the 510 nm upwelling radiance profile



free from ship shading was identified as that lying at a depth of 2.5 m or below through visual scrutiny of the profile (fig. 4.3).

$L_u(510,0^-)$  for the entire profile was found to be lower than that calculated from the 2.5 - 15 m section of the profile (table 4.1). Ship shadow would lower the overall value for  $L_u(510,0^-)$  and is likely to be the primary factor influencing this result. Assuming that the 0.863 result is the more accurate due to less probable shading contamination, the error introduced by using the entire profile is -2.8%.

	$R^2$	$L_u(510,0^-)$
0 - 15m section of profile	0.999	0.839
2.5 - 15m section of profile	0.998	0.863

Table 4.1 : The effects of ship shadow on the definition of water-leaving radiance, just below the water's surface (at 510 nm), through regression analysis

Through comparison of these results with the other datasets acquired for this study, a similar technique to that described above was adopted in the profile analysis. This consisted of the visual selection of the best section of the profile to use (thereby eliminating any contamination in the surface layers by ship shading) followed by regression analysis to achieve  $L_u(\lambda,0^-)$  and  $E_d(\lambda,0^-)$ . Once  $L_u(\lambda,0^-)$  values were ascertained for each profile, it was necessary to propagate  $L_u(\lambda,0^-)$  up through the air-water interface by deriving  $L_u(\lambda,0^+)$  according to equation 2-20. Equation 2-27 was then used to calculate  $R_L(\lambda,0^+)$  for twenty complete datasets acquired during the cruises CH118a, CH118b, SV23 and SV24 (all results for the twenty datasets appear in Appendix C). The results shown in Appendix C detail the general water characteristics at the time of profiling and represent an averaged analysis of each site throughout the time of survey. This data is used later (sections 5.1 and 5.2) to investigate the nature of these waters and to classify them based on their optical properties.

To compare sea-based optically profiled information with airborne (or satellite) image data, both must be truly coincident in space and time. From the profiles acquired during

the *Challenger* and *Sea Vigil* cruises, reduced sections of the complete datasets were selected which coincided exactly with image data. Sixteen images were identified and married with profiled datasets; the exact location of the ship at the time of survey was known and could be identified on the images due to the accurate georectification information available with each image (see later in section 4.2.4). Appendix D details the profile results from the sixteen reduced datasets. The optically profiled water-leaving radiance spectra were used for the verification of the calibration, processing and analysis of the image data (section 4.2).

## **4.2 Airborne images**

A greater number of image calibration and correction procedures are required for airborne images than for those acquired from a satellite. This is due to the fact that an aircraft is a less stable platform upon which to mount a sensor and its position within the earth's atmosphere constantly varies. Thus, a satellite does not require coincident, per pixel location measurements in three-dimensional (3D) space as these quantities are relatively easy to calculate from its orbit parameters. Spaceborne images do not need as complex an atmospheric correction given the satellite's location above the entire atmospheric column. An aircraft, on the other hand, has a constantly varying 3D position which makes the atmospheric correction procedures much more complex.

### **4.2.1 Radiometric calibration**

#### **4.2.1.1 Compact Airborne Spectrographic Imager**

The light levels entering the optics of the CASI through the lens can be controlled using the iris in response to external lighting conditions. Prior to and after a flightline, the iris closes up completely to allow a dark-current reading to be taken. This information is used in post-processing to relate and then calibrate each sensor in a 288 charge coupled detector (CCD) array (fig. 3.5) and hence radiometrically calibrate the datastream. Light enters the CASI through a 15 $\mu$ m wide spectrographic reflectance slit and then passes through a reflectance grating which disperses the light over the 400 - 915 nm spectral range. The signal is recorded by the CCD array which has a nominal spectral sampling of 1.8 nm. In addition to this, the signal from an incident light sensor (ILS), housed on the roof of the aircraft, is directed through the CASI optics and onto the CCD (fig. 3.4). The ILS

information is recorded alongside the imaged datastream which thus allows the direct comparison of the two.

Spectral calibration of the CCD array was carried out on the bench at regular intervals throughout the flight campaigns and provided, at best, a 2% accuracy to sensor radiance. This information was used to calibrate each spectral band (table 3.1) and applied to the dataset on a per pixel basis through the use of a suite of software developed for the NERC ARSF (fig. 4.4; Wilson *et al.*, 1997). The software also appends ancillary information, including position and attitude data, to each radiometrically correct image scanline and stores it all in a single hierarchical data format (HDF) file (fig. 4.4). An example of a radiometrically corrected CASI image acquired over the Humber Estuary is shown in figure 4.5.

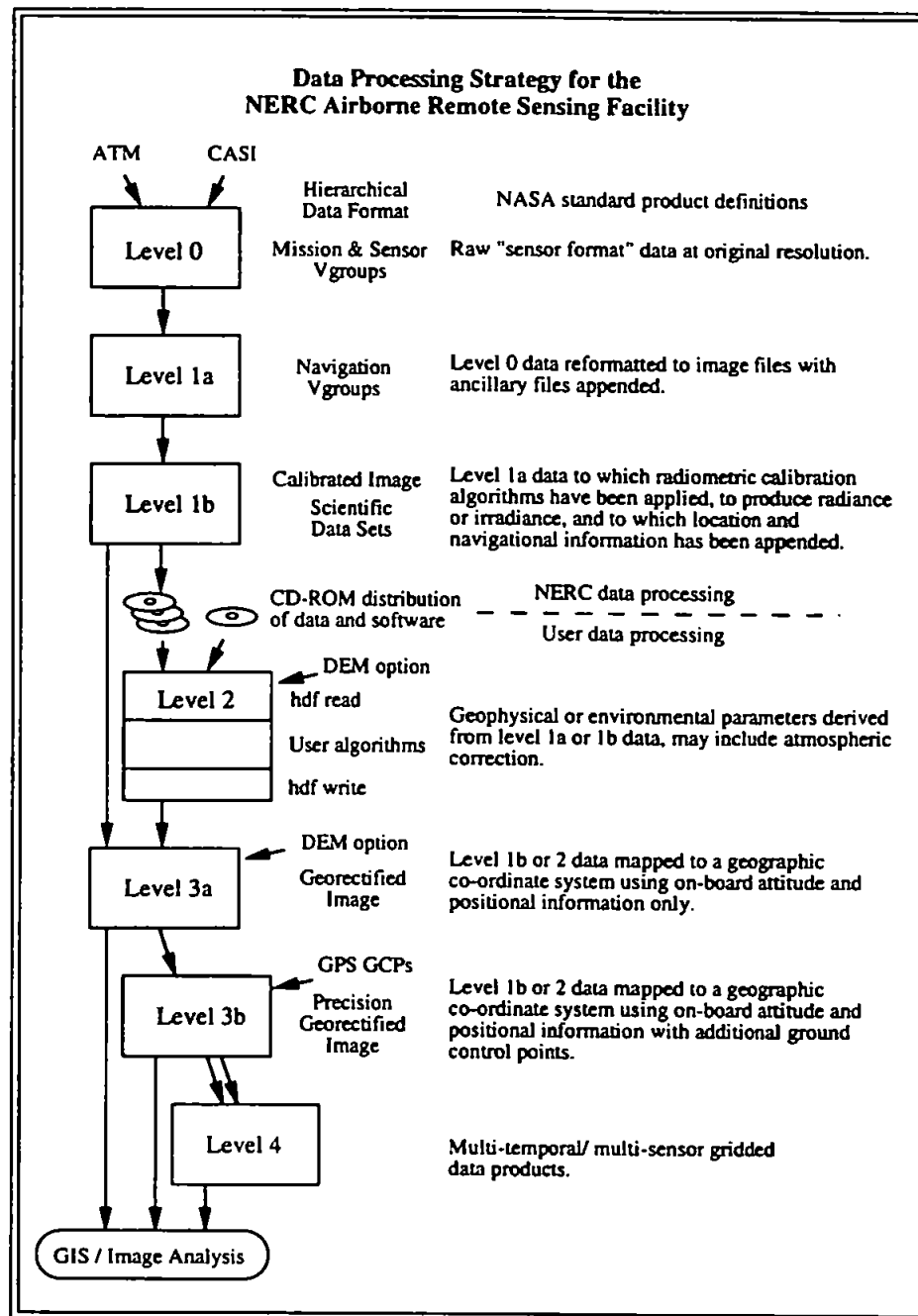


Figure 4.4 : NERC ARSF processing strategy for CASI and ATM data. The HDF file output and product definitions at each stage and for each sensor are detailed (Wilson *et al.*, 1997).

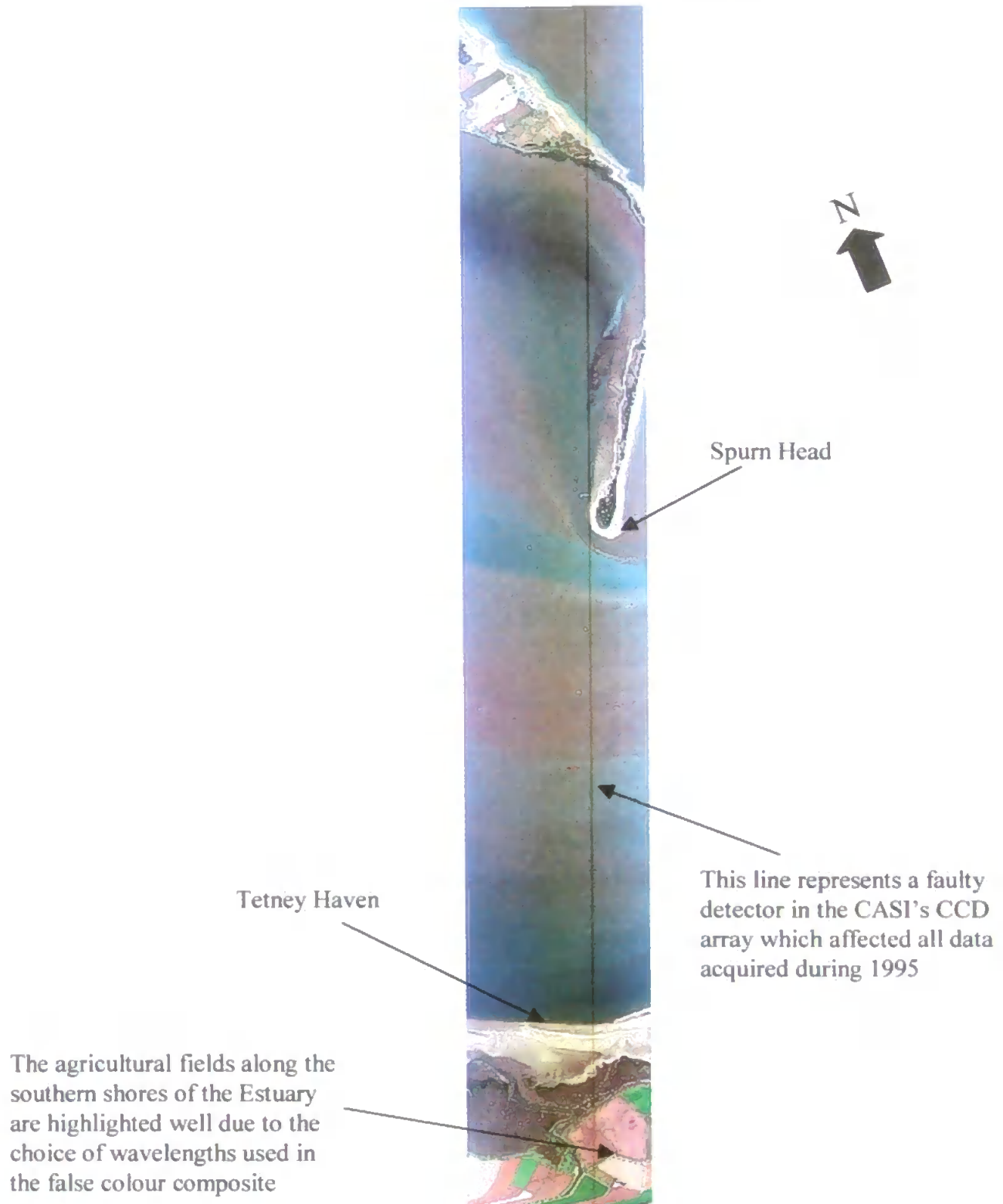


Figure 4.5 : Radiometrically corrected CASI image acquired on 15 August 1995 at LW - 2.7h over the mouth of the Humber Estuary. The image is a false colour composite with band 7 (669 nm) represented in red, band 5 (554 nm) in green and band 3 (490 nm) in blue.

### 4.2.1.2 Airborne Thematic Mapper

The ATM is sensitive to those parts of the electromagnetic spectrum ranging from the visible to the near-infrared (NIR), shortwave-infrared (SWIR) and thermal-infrared (TIR) (table 3.2). A rotating mirror directs the incoming light onto dichroic filters which split it into the separate fractions of the electromagnetic spectrum (fig. 3.7). The visible and NIR fractions are further split by a prism before being imaged onto an array of silicon detectors (fig. 3.7). Those wavelengths beyond the NIR (SWIR to TIR) are split and imaged onto single detector elements which are housed in individual Dewars (fig. 3.7) cooled with liquid nitrogen. On the bench, spectral calibration was executed at regular intervals throughout the flight campaigns. This provided a sensor radiance accuracy of between 5% and 10% for the visible channels and to within 0.3°K brightness temperature for the thermal-infrared. As with the CASI data, the radiometric calibration of the ATM dataset is applied on a per pixel basis and output as an HDF file using the NERC ARSF routines (fig. 4.4; Wilson *et al.*, 1997).

#### 4.2.1.2.1 Thermal calibration

Thermal-infrared data from channels 11 and 12 (both 8400 - 11500nm; channel 12 records at half the standard gain, i.e. at 0.5, and is particularly useful if channel 11 becomes unexpectedly saturated) require initial calibration to 'at sensor' radiance (to derive the brightness or apparent temperature) before conversion to sea-surface temperature. The calibration procedure utilises two controllable blackbodies whose temperatures are set to the minimum and maximum temperatures expected across the target scene. The blackbodies are imaged before and after each scanline, the direction of the signal through the optics being controlled by a rotating mirror (fig. 3.7). The blackbody temperature and the emitted radiation have a nonlinear relationship which is defined by the Planck radiation law:

$$R(\lambda) = \frac{C_1}{\lambda^5 \left( \exp\left(\frac{C_2}{\lambda T}\right) - 1 \right)} \quad 4-1$$

(Wilson, 1988)

where  $R(\lambda)$  is the spectral radiant emittance ( $\text{W m}^{-2} \mu\text{m}^{-1}$ ),

$\lambda$  is the radiation wavelength ( $\mu\text{m}$ ),

$T$  is the absolute temperature (K),

$$C_1 = 2\pi hc^2 = 3.74151 \times 10^8 \text{ Wm}^{-2} \mu\text{m}^4,$$

$$C_2 = \frac{ch}{k} = 1.43879 \times 10^4 \mu\text{m K},$$

and:  $h$  is Planck's constant =  $6.6256 \times 10^{-34} \text{ W s}^2$ ,

$c$  is the velocity of light =  $2.9979 \times 10^8 \text{ m s}^{-1}$ , and

$k$  is Boltzmann's constant =  $1.38054 \times 10^{-23} \text{ W s}^{-1} \text{ K}^{-1}$ .

The detector response of the ATM was determined by "on the bench" calibration. The response curve was used, together with knowledge of the Planck function, to determine the effective radiance for each of the two blackbodies by:

$$R_x = \epsilon_x \int_{8400}^{11500} \left( \frac{\phi_\lambda C_1}{\lambda^5 \left( \exp\left(\frac{C_2}{\lambda T_x}\right) - 1 \right)} \right) d\lambda \quad 4-2$$

(Wilson, 1988)

where  $x$  is blackbody 1 or 2,

$R$  is the effective radiance at the sensor when viewing the blackbody at  $T$ ,

$\epsilon$  is the emissivity of the blackbody (assumed to be constant), and

$\phi_\lambda$  is the detector response function.

$R_x$  is assumed to be a linear function of the sensor response thus providing a two point calibration and enabling the determination of the apparent temperature for all digital number (DN) values. A further step of atmospheric correction would be required to derive actual sea-surface temperature (Callison *et al.*, 1987). However, this was not possible within the atmospheric correction software available to the author. Thus, sea-surface temperature was approximated from the apparent temperature images by ignoring any atmospheric errors and by assuming a constant emissivity of the water of 0.965 in the case of the Humber Estuary and of 0.98 for the Tweed (A. K. Wilson, *pers. comm.*). The possible errors remaining within the images as a result of the omission of an atmospheric correction could lie between 5% - 10%. When the additional possible errors within the data from the radiometric calibration of the ATM are recalled, these figures become quite considerable. Thus, to reduce any remaining atmospheric effects and error within the

images, they were further calibrated through comparison with coincident surface-based measurements.

### 4.2.2 Atmospheric correction

The useful remotely sensed information about an area of sea is contained within the physical properties of the radiation leaving the target, *i.e.* the water-leaving radiance. The signal is difficult to quantify due to complex interactions between absorption, scattering and reflection of light by any in-water constituents. This is a considerable problem in coastal waters whose optical properties are determined by resuspended organic and / or inorganic sediments and terrigenous particles (Gordon & Morel, 1983). Compounding this problem is the fact that radiative flux arriving at the sensor has travelled some distance through the atmosphere and has therefore suffered scattering, attenuation and possibly augmentation from surrounding light fields (fig. 4.6). The atmospheric contribution to remotely sensed data at optical wavelengths is over 50% and may approach 80 - 90% of the radiance received at the sensor towards the blue end of the spectrum (Cracknell & Hayes, 1991). Atmospheric correction is therefore imperative.

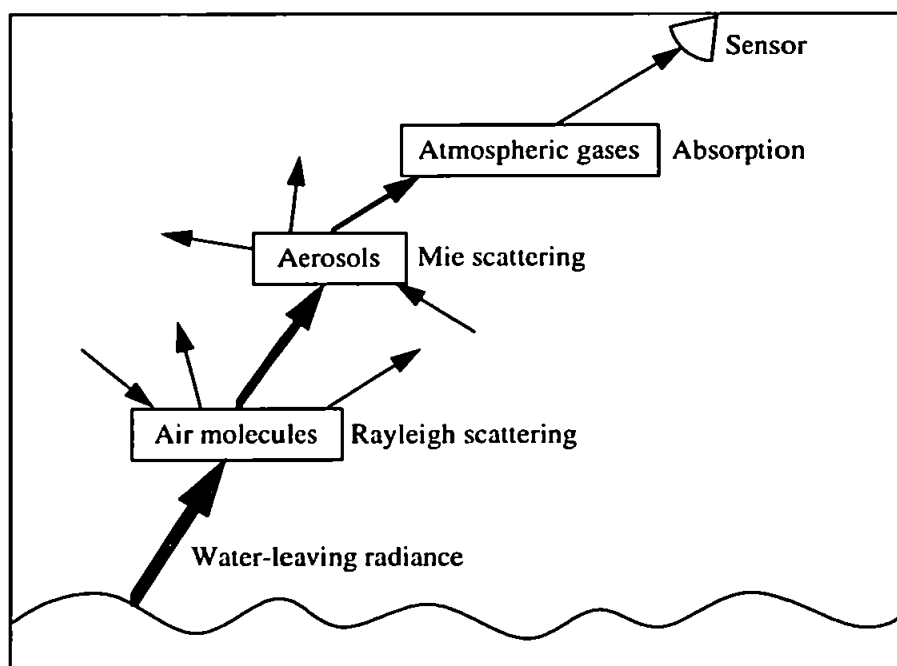
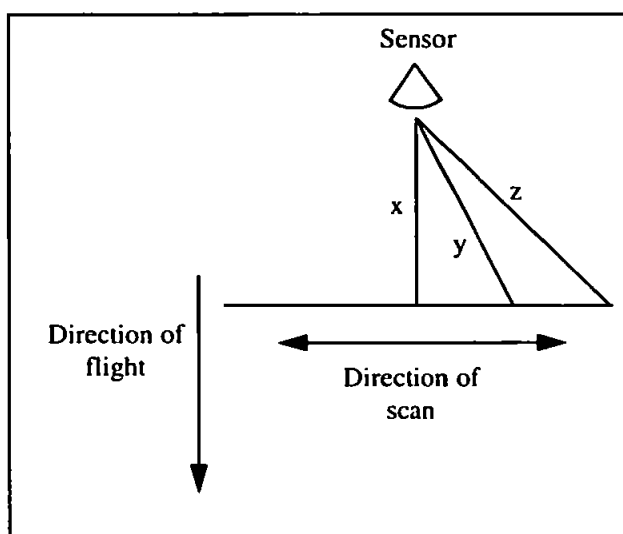


Fig 4.6 : The influence of the atmosphere on the signal received at the sensor

The atmospheric component is not constant throughout an image, particularly in airborne data where the target-sensor path length is variable (fig. 4.7). The CASI bandset (table 3.1)



was chosen to target wavelengths which would enable the detection and quantification of important atmospheric parameters as well as surface water characteristics. In particular, some wavebands were chosen to highlight atmospheric aerosols which represent a key input to the atmospheric correction procedure over coastal, SPM dominated waters.



$x$ ,  $y$  and  $z$  represent the distances between the target and the remote sensor as the instrument scans across a scene. The target-sensor path length at nadir ( $x$ ) is smaller than when viewing off-nadir ( $y$ ). At the edge of the scanline the path length between sensor and target increases to  $z$ , a distance possibly much greater than that found at nadir ( $x$ ).

Figure 4.7 : The variability of the target-sensor path length

The atmospheric correction algorithms used in this study were devised at Plymouth Marine Laboratory (Moore *et al.*, 1999) and were applied to the image datasets through the Coastal Earth Observation Application for Sediment Transport (COAST) software (Bottrell & Matthews, 1994). The atmospheric correction routines assume that in waters with a significant SPM concentration, as is the case in the Humber Estuary, there is significant water-leaving radiance at NIR wavelengths. Such areas are flagged within the atmospheric correction procedure and an iterative approach is employed. Iterations are based upon information contained within look-up tables and use a constrained fit of aerosol optical thickness values in the NIR and water-leaving reflectance against sediment concentrations. In clearer waters it is assumed that all radiance in the NIR has originated from the atmosphere because water absorbs all energy at these wavelengths (Gordon and Wang, 1994). Values from the NIR are then used to correct bands in the visible part of the spectrum.

The COAST software outputs Rayleigh (e.g. fig. 4.8a) and fully (Rayleigh and aerosol; e.g. fig. 4.8b) atmospherically corrected, land-masked images (the latter will hereafter be

referred to as COAST images). An assessment of the accuracy of the atmospheric corrections were required. The results from known comparative points on sixteen Rayleigh and COAST images, and on their radiometrically correct companion, were related to the water-leaving radiance spectra calculated from PML-Satlantic optical profiles (Appendix D). The profiles were acquired from the side of the ship facing towards the sun. This could easily be visually identified on the (nongeometrically corrected) radiometrically, Rayleigh and COAST corrected images once the ship had been located. An area of interest was delineated on each of the images which represented that section of water whose optical properties were measured from the sea's surface. The mean and standard deviation values were obtained from these groups of pixels and were compared with the exact water-leaving radiance as derived from the sea-based profiles. The results from the sixteen sets of images were compared to measured water-leaving radiances and are shown in figures 4.9a - 4.9p.

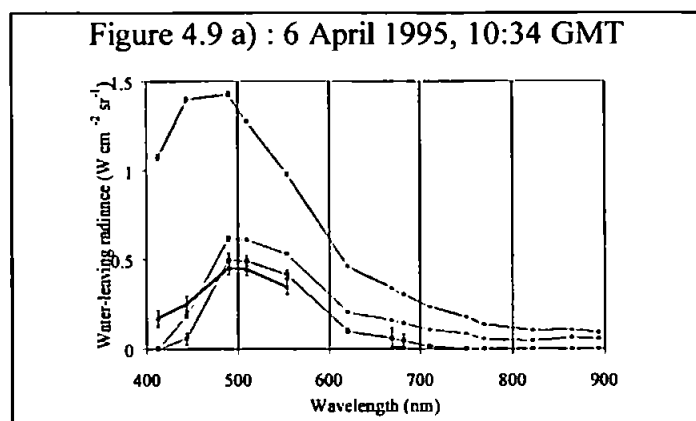
The comparisons of the image and profiled  $L_u(\lambda, 0^+)$  results are limited to the seven wavelengths measured by the PML-Satlantic which constrains the assessment somewhat. However, the overall trend of the spectra can be assessed from figures 4.9a - 4.9p and the comparison highlights some of the strengths and weaknesses of the COAST routines. The representative spectra for each image have very similar shapes and characteristics with the exception of figures 4.9o and 4.9p. These two images were acquired over extreme case // waters in the upper reaches of the River Humber where SPM concentrations are very high. The image spectra do not reflect the measured radiances and possibly highlight the weaknesses of the COAST routines in extremely SPM laden waters.

In general, all the images sustain values much higher than expected given the sea-based water-leaving radiance results. Considering the lower wavelengths in particular, the shape of the spectra suggest an over-correction for Rayleigh scattering. An over-correction would have the greatest impact at lower wavelengths due to a steep exponential relationship with wavelength. This appears to be the case in all sixteen samples as the 412 nm image values for all the COAST images are zero. With the exception of figures 4.9b, 4.9i and 4.9k, the 412 nm value in the Rayleigh images also reach zero.

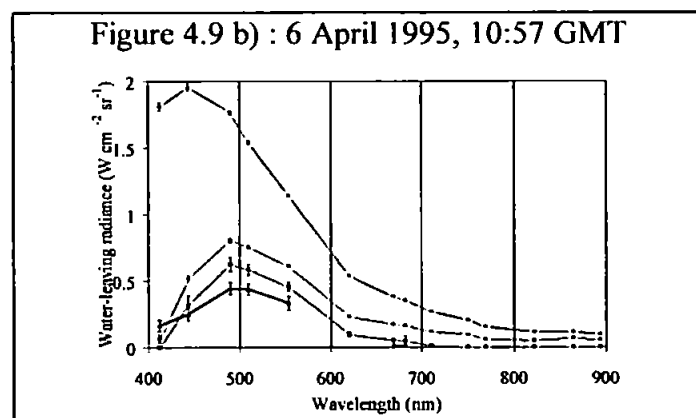


Figure 4.8 a) Rayleigh corrected (left) & b) Fully COAST corrected (right), land-masked CASI images acquired on 15 August 1995 (LW - 2.7h) over the Humber Estuary. The images are false colour composites where red depicts band 7 (669 nm), green band 5 (554 nm) and blue band 3 (490 nm).

Figure 4.9 : Measured water-leaving radiance (from in-water optical profiles) and the comparative results from radiometrically, Rayleigh and fully atmospherically (COAST) corrected CASI image data

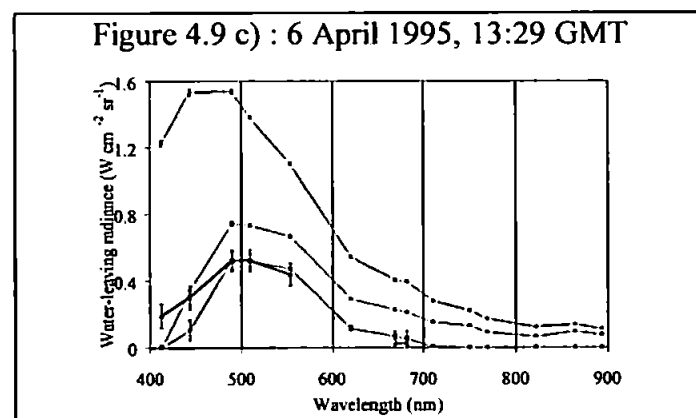


The error bars relating to the image-derived results represent one standard deviation away from the mean value as derived from pixel averaging. For the optical profiles, the error bounds are quantified as the standard error from the regression analyses.



Water-leaving radiance derived from in-water optical profiles

Water-leaving radiance derived from radiometrically corrected CASI image data



Water-leaving radiance derived from Rayleigh corrected CASI image data

Water-leaving radiance derived from fully atmospherically corrected (COAST) CASI image data

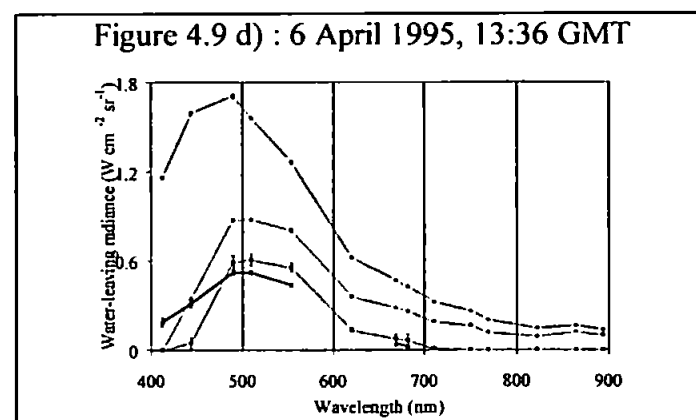


Figure 4.9 e) : 10 April 1995, 10:41 GMT

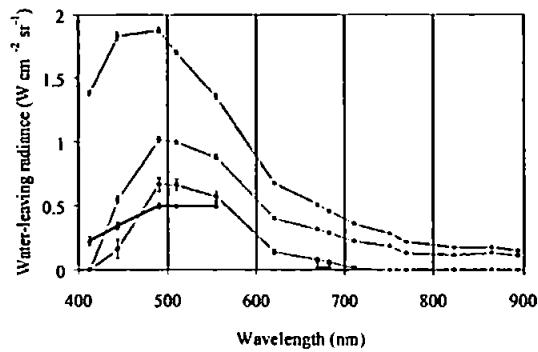
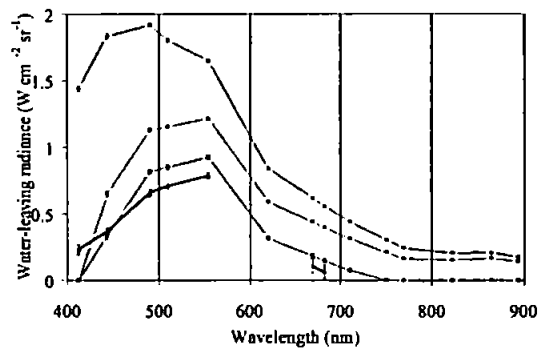


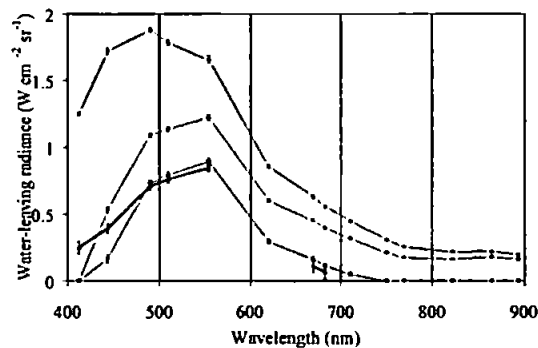
Figure 4.9 f) : 12 April 1995, 09:53 GMT



Water-leaving radiance  
derived from in-water  
optical profiles

Water-leaving radiance  
derived from radiometrically  
corrected CASI image data

Figure 4.9 g) : 12 April 1995, 10:02 GMT



Water-leaving radiance  
derived from Rayleigh  
corrected CASI image data

Water-leaving radiance  
derived from fully  
atmospherically corrected  
(COAST) CASI image data

Figure 4.9 h) : 12 April 1995, 10:11 GMT

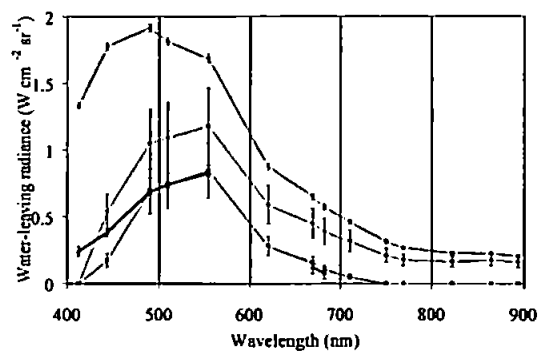


Figure 4.9 i) : 12 April 1995, 10:20 GMT

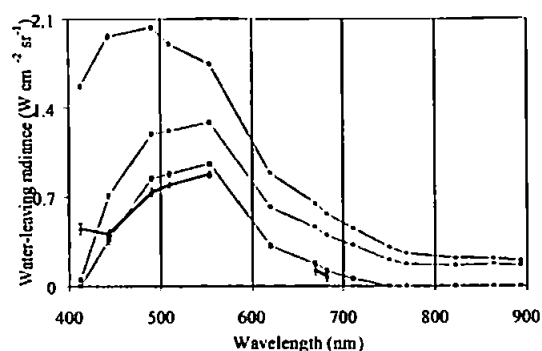
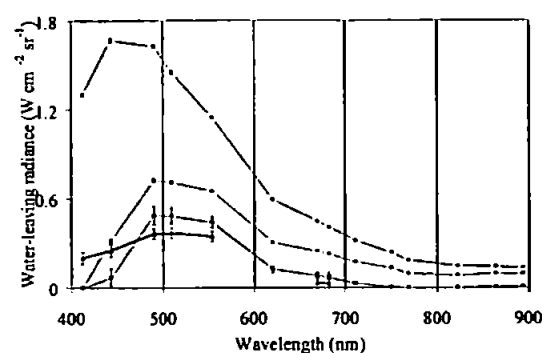


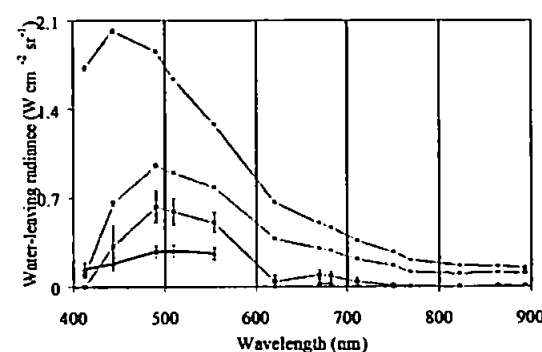
Figure 4.9 j) : 21 April 1995, 09:55 GMT



Water-leaving radiance  
derived from in-water  
optical profiles

Water-leaving radiance  
derived from radiometrically  
corrected CASI image data

Figure 4.9 k) : 21 April 1995, 10:14 GMT



Water-leaving radiance  
derived from Rayleigh  
corrected CASI image data

Water-leaving radiance  
derived from fully  
atmospherically corrected  
(COAST) CASI image data

Figure 4.9 l) : 21 April 1995, 10:22 GMT

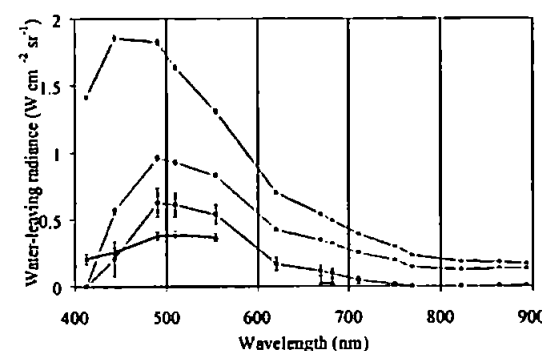


Figure 4.9 m) : 23 April 1995, 10:36 GMT

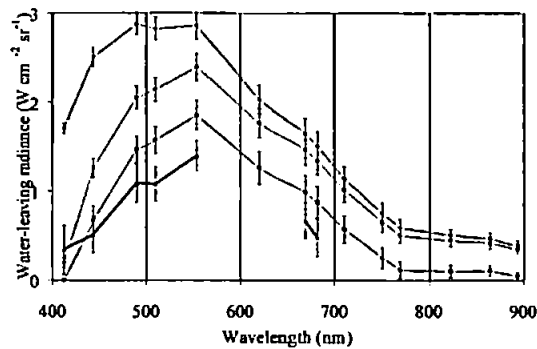
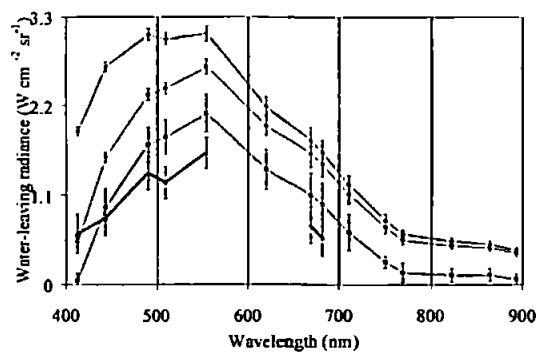


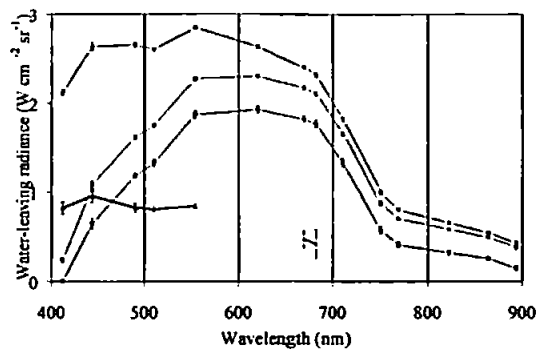
Figure 4.9 n) : 23 April 1995, 10:42 GMT



Water-leaving radiance  
derived from in-water  
optical profiles

Water-leaving radiance  
derived from radiometrically  
corrected CASI image data

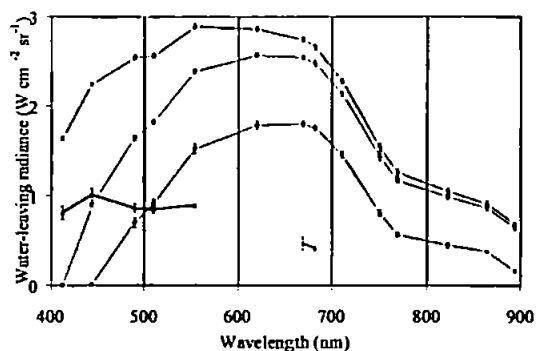
Figure 4.9 o) : 22 August 1995, 13:31 GMT



Water-leaving radiance  
derived from Rayleigh  
corrected CASI image data

Water-leaving radiance  
derived from fully  
atmospherically corrected  
(COAST) CASI image data

Figure 4.9 p) : 22 August 1995, 13:57 GMT



While the gradient between the radiances from the Rayleigh and COAST images and the “true” water-leaving radiance can be attributed to Rayleigh scattering correction, the offset between the two is likely to be due to an under-correction for aerosol and, to a lesser extent, gaseous atmospheric absorption. This theory is supported in all images at wavelengths above 555 nm where the COAST image spectra and the measured water-leaving radiance spectra are all displaced with the latter spectra sustaining the lower values.

The COAST software contains a land-masking routine and this came into conflict in areas with exceptionally high SPM concentrations, such as large sections of the Humber Estuary and, in particular, the upper reaches. In the extreme case // scenario, the COAST routines tended to erroneously mask out large sections of the image which represented waters with particularly high SPM concentrations. The incorrectly masked out areas contained regions of specific scientific interest. To recover this information, the Rayleigh and COAST images needed to be recreated with no land-masking. This had to be done externally from the COAST software (fig. 4.10).

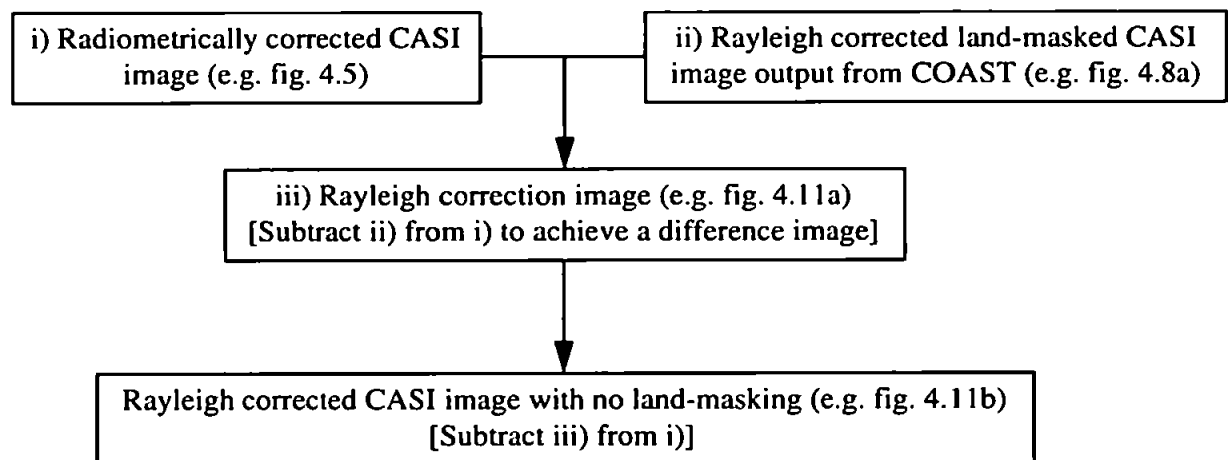


Figure 4.10 : The Rayleigh correction of a CASI image with no land-masking

The Rayleigh correction of an image is a relatively straightforward procedure although the orientation of the flightline with respect to the sun has to be assumed to be constant throughout the flight. Constant offset values for each column of pixels (along-track) in the image are applied to correct for Rayleigh scattering. These constants were calculated by the routines within COAST. The results were quantified by subtracting the Rayleigh



corrected image from the radiometrically corrected one (fig. 4.10). This gave the 512 specific constants used to correct a particular image for Rayleigh scattering (an example taken from 15 August 1995 is expressed as a digital image in figure 4.11a). These values were then reapplied to the radiometrically corrected image and a new Rayleigh corrected one produced with no land-masking (e.g. fig. 4.11b).

The distribution of aerosols across an image is not a constant and varies along-track as well as across-track. It was thus impossible to determine what the digital number (DN) values should be in those sections of the fully atmospherically corrected images which were erroneously masked out as land without complete knowledge of COAST's underlying routines and / or more flexibility within the software. These were not available. Together with the results from the initial tests on COAST's reliability (fig. 4.9; Robinson & Morris, 1997), it was concluded that the Rayleigh corrected image (with no land-masking) alone would probably be adequate given that any further analysis (such as the use of algorithms to determine in-water parameters) incorporated band ratios. The use of Rayleigh corrected images would therefore be sufficient as any residual atmospheric component within the image (primarily due to the effects of aerosols which have an exponentially decreasing impact with increasing wavelength) would be cancelled out in the band ratio particularly if longer wavelengths were chosen for analysis.



Figure 4.11 a) The across-track constants (from the subtraction of fig. 4.8a from fig. 4.5) used to correct a CASI image for Rayleigh scattering (left) & b) The Rayleigh corrected (no land masking) equivalent (right) for an example image acquired on 15 August 1995 (LW - 2.7h). Red = band 7 (669 nm), green = band 5 (554 nm) & blue = band 3 (490 nm).

## 4.2.3 Algorithm development

### 4.2.3.1 Suspended Particulate Matter

The effectiveness of an algorithm to derive SPM concentration from digital image data is largely determined by knowledge of the correlation between SPM and any chlorophyll present in the water (Tassan, 1993). In case *I* waters, this relationship is stable and well defined. However, in case *II* coastal waters, the relationship may vary significantly across both spatial and temporal scales. The contributions of chlorophyll and dissolved organic matter to absorption can be neglected when considering river plumes which are dominated by SPM (Tassan, 1997). The study area, the Humber Estuary, is one such region where SPM dominates and chlorophyll concentrations are extremely low or commonly zero. The effect of chlorophyll on the SPM concentration - reflectance relationship is at a minimum between 700 nm and 900 nm (fig. 4.12). Therefore, these wavelengths could be confidently used in an SPM retrieval algorithm for use over the Humber Estuary without the necessity of the addition of a chlorophyll term.

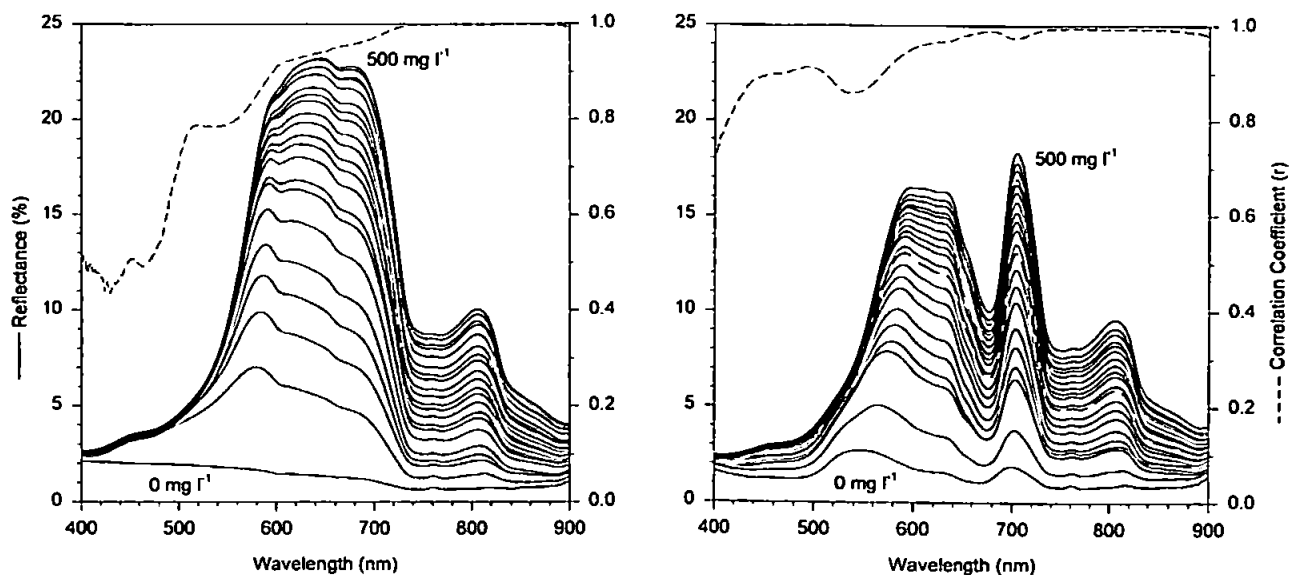


Figure 4.12 : Relationship between SPM concentration and reflectance in clear water (left) and in algae-laden water (right) (Han, 1997)

Waters with high SPM concentrations generally exhibit a greater overall reflectance than those at lower concentrations (Viollier & Sturm, 1984). This is due to an increase in scattering by the SPM particles in the water. In one of the first studies on the topic, Ritchie *et al.* (1976) investigated the nature of the relationship between reflectance and SPM concentration. They found that reflectance between 450 nm and 900 nm increased as SPM concentration values rose (fig. 2.2 depicts this same relationship as gleaned from a later study by Han & Rundquist, 1994). They also discovered that the maximum peak moved from approximately 550 nm at low SPM concentrations to over 600 nm at high concentrations (fig. 2.2). Their conclusion was that the best spectral region for assessing SPM concentration from reflectance lies between 700 nm and 800 nm. This region was adjusted to the 700 - 900 nm wavelength range in a later study (Ritchie *et al.*, 1983). The applicability of this wavelength region for SPM concentration determination is similarly echoed throughout the literature (e.g. Han & Rundquist, 1994; Mayo *et al.*, 1993; Xia, 1993; Dekker *et al.*, 1991; Bhargava & Mariam, 1990).

SPM concentration and reflectance have a positive correlation (Curran *et al.*, 1987). This relationship is linear at low SPM concentrations and nonlinear at high concentrations (Han & Rundquist, 1994). Thus, in general, when considering sediment plumes, the relationship is linear for a narrow range of SPM concentrations (Morel & Prieur, 1977) and logarithmic for a wider range (Munday & Alföldi, 1979). The logarithmic relationship is widely used in the literature (e.g. Tassan, 1993; Doerffer *et al.*, 1989; Tassan & Sturm, 1986; Gordon & Morel, 1983) and takes the form:

$$\ln(S) = i + j \ln(X) \quad 4-3$$

where  $S$  is the SPM concentration,

$X$  is the sediment retrieval term and

$i$  and  $j$  are constants derived from least squares regression between  $\ln(S)$  and  $\ln(X)$ .

Due to the limitations of the atmospheric correction available for the CASI, it was necessary that for this study  $X$  should be a ratio of two, Rayleigh corrected, wavebands. This would ensure the reduction of any remaining atmospheric effects in the Rayleigh corrected data. Comparative CASI image and sea-surface SPM concentration data were

available for use in the determination of an effective SPM algorithm for seventeen images acquired over 3 days in August 1995, the 10<sup>th</sup>, 11<sup>th</sup> and 15<sup>th</sup>. The sea-based measurements of SPM were acquired from the Bull Light Float, one of the *flux curtain* moorings (fig. 3.9, mooring c), and concentrations for this period ranged from 20 mg m<sup>-3</sup> to 305 mg m<sup>-3</sup>.

For a band ratio algorithm to be effective, two bands must be chosen that, when ratioed, highlight the concentrations in the water well. All fourteen bands from the seventeen radiometrically, Rayleigh and COAST corrected images were ratioed against each other. A least squares regression of each against coincident SPM concentration as derived from the Bull Light Float was then performed. The coefficient of determination (R<sup>2</sup>) in each case was used as the indicator of the strength of the relationship and hence their potential for use in an effective SPM algorithm (tables 4.2 - 4.4).

In all cases, the R<sup>2</sup> results from the COAST image ratios never exceeded 0.8 (table 4.4). This further highlights the ineffectiveness of the full atmospheric correction routines within COAST for this group of images. The results from the radiometrically (table 4.2) and Rayleigh (table 4.3) corrected images exhibit a similar pattern. In their study of inland lake systems using MSS data, Dekker *et al.* (1991) found that the best wavebands to use for the retrieval of SPM concentration were a ratio of wavebands 6 (673.14 - 687.46 nm) and 7 (708 - 714.76 nm). Similarly in this study, one of the best ratios of Rayleigh corrected CASI image wavebands incorporate bands 8 (679.92 - 687.10 nm) and 9 (706.86 - 717.66 nm) (table 4.3).

Based on equation 4-3,  $X$  was taken as  $\frac{band8}{band9}$ . Constants  $i$  and  $j$  (equation 4-3) were determined by regression of the Rayleigh corrected image band ratios with *in-situ* SPM concentration measurements. The resultant relationship has an R<sup>2</sup> of 0.952 (table 4.3, fig. 4.13) and is defined as:

$$SPM = \exp(7.1) \times \left( \frac{band8}{band9} \right)^{-13.104} \quad 4-4$$

where SPM has the units mg m<sup>-3</sup>.

		band (x)													
		1	2	3	4	5	6	7	8	9	10	11	12	13	14
band (y)	1														
	2	0.209													
	3	0.209	0.192												
	4	0.216	0.207	0.196											
	5	0.176	0.109	0.012	0.126										
	6	0.477	0.537	0.581	0.574	0.792									
	7	0.311	0.256	0.192	0.172	0.219	0.003								
	8	0.624	0.687	0.75	0.753	0.836	0.856	0.145							
	9	0.775	0.826	0.871	0.873	0.919	0.953	0.486	0.948						
	10	0.807	0.863	0.913	0.919	0.92	0.892	0.797	0.857	0.743					
	11	0.814	0.868	0.918	0.923	0.924	0.897	0.811	0.864	0.758	0.185				
	12	0.875	0.917	0.947	0.951	0.96	0.947	0.856	0.918	0.876	0.002	0.001			
	13	0.816	0.866	0.909	0.914	0.912	0.871	0.821	0.82	0.716	0.382	0.348	0.149		
	14	0.812	0.86	0.9	0.904	0.903	0.849	0.799	0.774	0.646	0.03	0.016	0.015	0.305	

Table 4.2 :  $R^2$  values from the regression of radiometrically corrected CASI image band ratios [band (x) / band (y)] against SPM concentration ( $R^2 > 0.9$  in bold)

		band (x)													
		1	2	3	4	5	6	7	8	9	10	11	12	13	14
band (y)	1														
	2	0.014													
	3	0.01	0.001												
	4	0.011	0.004	0.021											
	5	0.036	0.097	0.219	0.294										
	6	0.002	0.095	0.192	0.263	0.75									
	7	0.057	0.373	0.549	0.613	0.826	0.856								
	8	0.069	0.403	0.567	0.624	0.824	0.86	0.577							
	9	0.232	0.67	0.78	0.812	0.912	0.954	0.937	0.952						
	10	0.577	0.878	0.936	0.937	0.925	0.89	0.864	0.854	0.742					
	11	0.594	0.885	0.939	0.94	0.928	0.895	0.87	0.861	0.758	0.404				
	12	0.604	0.903	0.947	0.954	0.965	0.951	0.928	0.924	0.884	0.002	0.022			
	13	0.621	0.894	0.938	0.938	0.922	0.873	0.829	0.818	0.71	0.202	0.115	0.1		
	14	0.616	0.891	0.928	0.927	0.913	0.849	0.784	0.771	0.639	0.001	0.005	0.004	0.259	

Table 4.3 :  $R^2$  values from the regression of Rayleigh corrected CASI image band ratios [band (x) / band (y)] against SPM concentration ( $R^2 > 0.9$  in bold)

		band (x)													
		1	2	3	4	5	6	7	8	9	10	11	12	13	14
band (y)	1														
	2	0.132													
	3	0.15	0.397												
	4	0.15	0.355	0.06											
	5	0.151	0.314	0.023	0.007										
	6	0.175	0.513	0.372	0.394	0.602									
	7	0.195	0.626	0.585	0.604	0.694	0.736								
	8	0.198	0.634	0.581	0.593	0.68	0.721	0.253							
	9	0.22	0.683	0.614	0.616	0.682	0.719	0.587	0.624						
	10	0.285	0.771	0.789	0.782	0.753	0.719	0.7	0.692	0.582					
	11	0.3	0.74	0.729	0.721	0.699	0.675	0.659	0.655	0.582	0.245				
	12	0.291	0.682	0.618	0.615	0.632	0.628	0.592	0.596	0.567	0.005	0.091			
	13	0.297	0.777	0.792	0.784	0.755	0.723	0.706	0.699	0.607	0.728	0.006	0.054		
	14	0.303	0.774	0.757	0.746	0.726	0.708	0.694	0.691	0.624	0.092	0.085	0.054	0.023	

Table 4.4 :  $R^2$  values from the regression of fully atmospherically corrected (COAST) CASI image band ratios [band (x) / band (y)] against SPM concentration

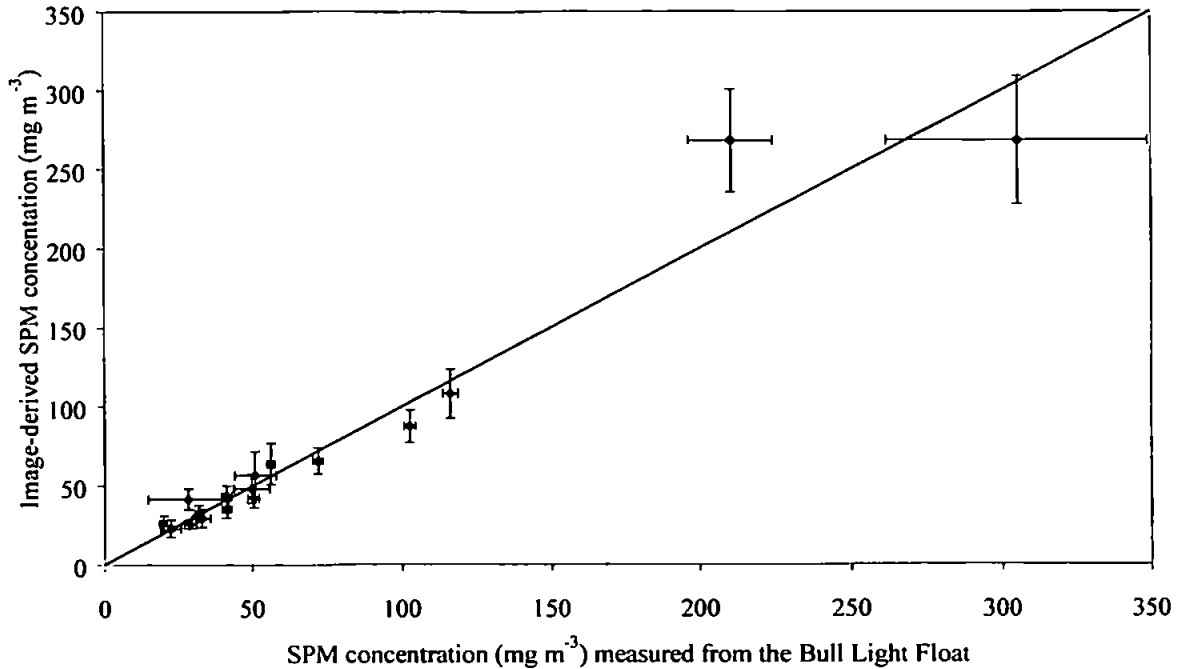


Figure 4.13 : Relationship between SPM concentration ( $\text{mg m}^{-3}$ ) as measured from the Bull Light Float and as derived from CASI images. The error bars represent one standard deviation away from the mean values as derived from image pixel averaging and from the averaging of a series of surface measurements spanning a few seconds.

Figure 4.14 shows two examples of SPM images derived from CASI data using equation 4-4. The portability of the algorithm is, however, limited both spatially and temporally as the data used in its derivation were acquired over three days in August 1995 and over the same location. Also, there were no independent datasets to test equation 4-4 thoroughly and so its use with other similar datasets may not be justified. With the incorporation of similar images and coincident *in-situ* measurements (e.g. from the vast quantity of data acquired during the LOIS), the procedure described here could reliably be replicated and fully temporally portable algorithms for key sections of the Humber Estuary derived.

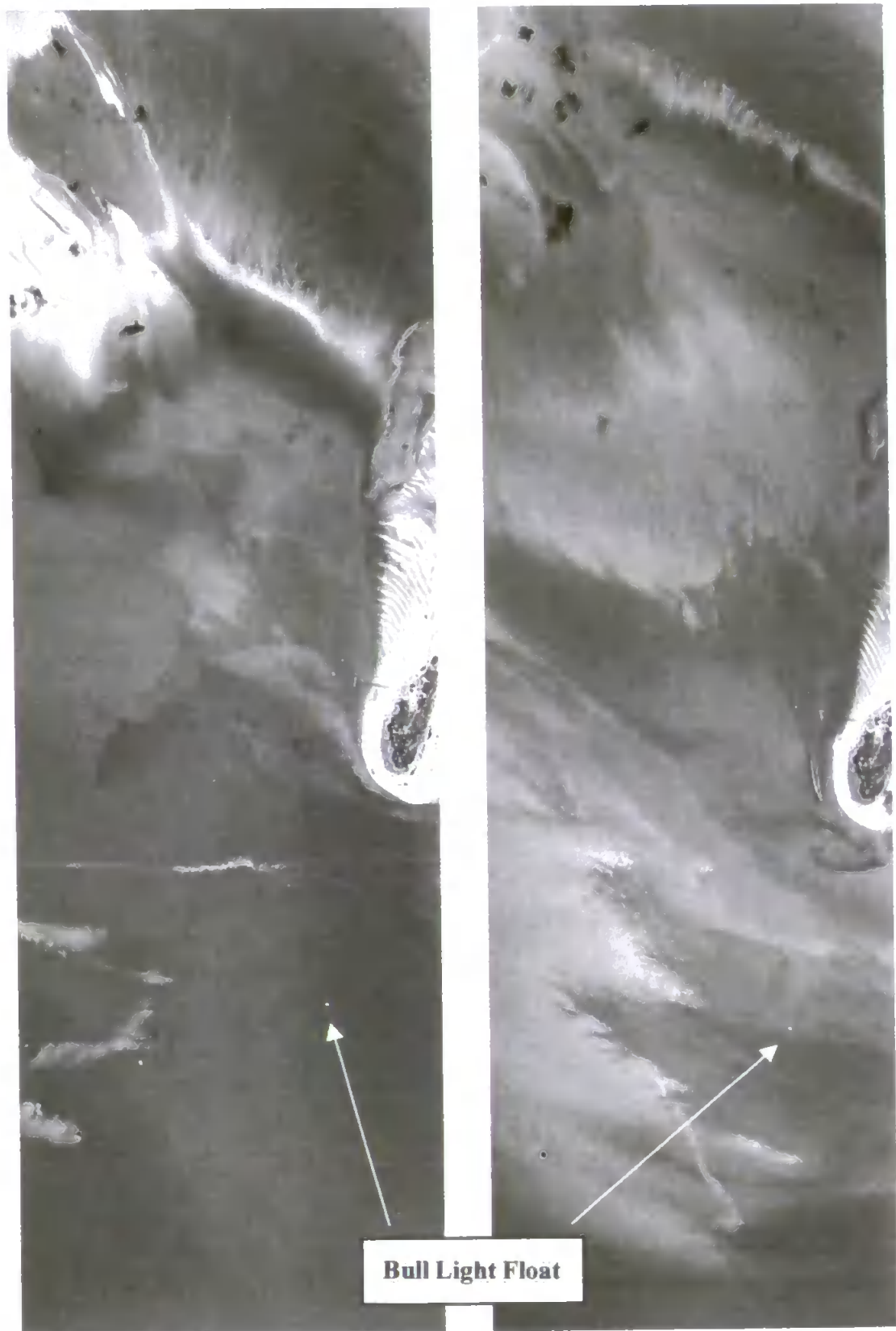


Figure 4.14 : Two examples of SPM images derived from CASI data acquired over the Humber Estuary on 10 August 1995 at LW + 2.07h (left) and LW + 3.08h (right)



### 4.2.3.2 Temperature and Salinity

Temperature was quantified from a series of twelve ATM images (see section 4.2.1.2.1) acquired on 4 May 1995 over the Tweed Estuary. In those images where there were coincident sea-surface measurements of temperature, the boat was identified and the relevant pixels interrogated. These were compared to the sea-truth data (fig. 4.15) by least squares regression, the fit yielding a 0.952 coefficient of determination. This relationship was used to ‘fine tune’ the temperature images and to reduce the effects of any remaining atmospheric errors within the data. Figure 4.16a shows an example sea-surface temperature image as derived from the ATM.

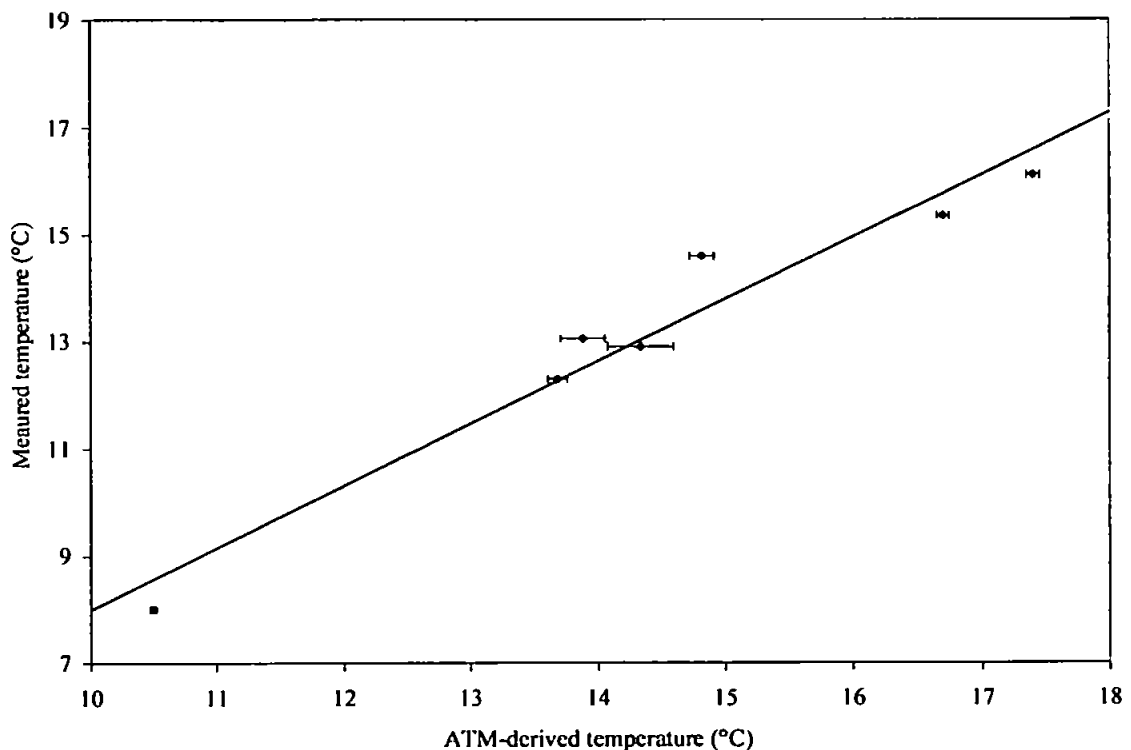


Figure 4.15 : Relationship between temperature (°C) measured at the sea's surface and as derived from ATM images. The error bars represent one standard deviation away from the mean values as derived from image pixel averaging.

The strong linear relationship between temperature and salinity renders the derivation of the latter, from a temperature image, relatively straightforward given knowledge of the particular water body's characteristics. The comparison of sea-based measurements of temperature and salinity at the water's surface enabled the determination of the relationship between the two by least-squares regression analysis which supported a 0.911 coefficient of

determination (Appendix F: Uncles *et al.*, 1999). The same relationship was then applied to the temperature image (e.g. fig. 4.16a) to enable the derivation of salinity (e.g. fig. 4.16b). More complete results from this study are detailed Appendix F: Uncles *et al.*, 1999.

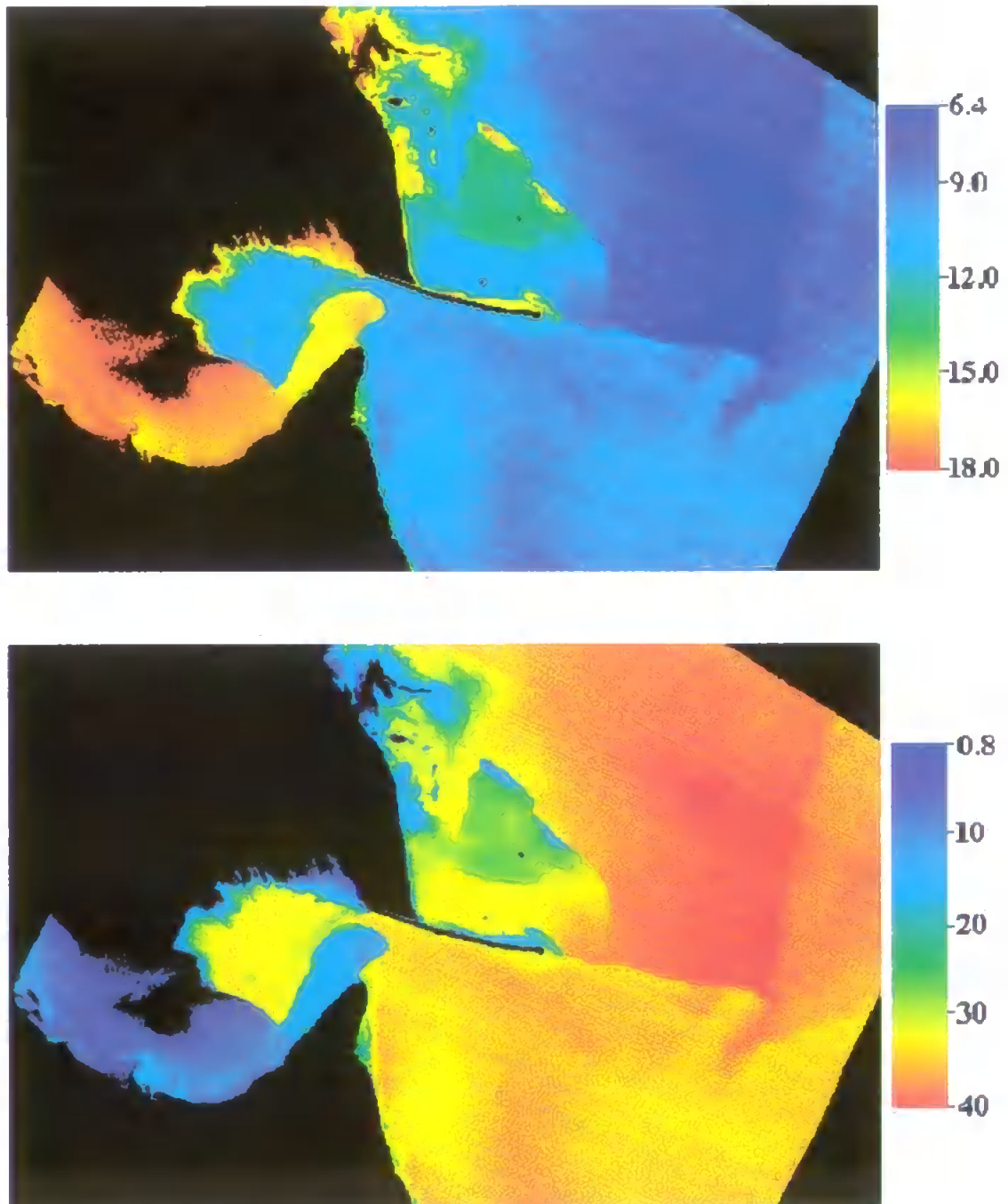


Figure 4.16 : Geometrically correct ATM images depicting a) temperature in °C (top) & b) salinity in psu (bottom) acquired at LW + 4h on 4 May 1995 over the Tweed Estuary

#### 4.2.4 Geometric correction

Airborne images can suffer from a number of geometric distortions due to the instability of the aircraft. With the addition of the CASI to the NERC aircraft, the NERC ARSF took the important step of designing an Integrated Data System which synchronised the acquisition of ATM, CASI, and Global Positioning System (GPS) data (fig 3.4).

An Ashtech 3DF unit was purchased and installed (fig. 3.4). This uses phase interferometry, over four antennae fitted in a rigid cross shape on the aircraft roof, to measure pitch, roll and true heading in addition to GPS position at one antenna (Mockridge *et al.*, 1997). There are serious limitations in the 3DF unit for operational remote sensing due to its low attitude acquisition rate of 2Hz. More importantly, its lock on the local satellite cluster, necessary for definition of the system in 3D space, has a tendency to be undermined when the aircraft executes steep turns. These two problems were prevalent in all the data acquired for this study and thus stimulated much initially unforeseen research and development into solutions for their rectification.

Included within the navigation data stream is a measure of the degree of accuracy maintained by the 3DF unit on the local satellite cluster for each of the aircraft's location points during survey. This quantity is termed the position dilution of precision, or pdop, and is a quality measure of the position fixed by several GPS satellite observations. If the satellites are scattered across the sky and well distributed in the zenith (vertical angle) the measure of the position of the aircraft will be good and the pdop will be low. Conversely, if the satellites are clustered together, the quantification of position will be poor and the pdop high. In the absence of the original data which detailed the exact satellite cluster characteristics, and would thence enable the recalculation of the 3D position of the aircraft directly, the pdop was used as a surrogate for the reliability of any particular set of navigation records. Assuming that the lowest pdop corresponded to navigation information which contained fewer errors, the entire flight campaign's navigation could be altered to fit to that particular section of the datastream. A series of programs which worked on this assumption were developed in C and IDL. The software corrects an erroneous datastream by comparing it, the number of GPS satellites used and their pdop with data acquired before and after that segment. If the pdop lies below a threshold, the data is assumed to be of sufficient quality. If it has a high pdop, the data segment is shifted

to comply with the overall trend of the good quality data surrounding it. The navigation datastream is reset to compensate for any errors contained within and the images processed using the newly rectified navigation datasets.

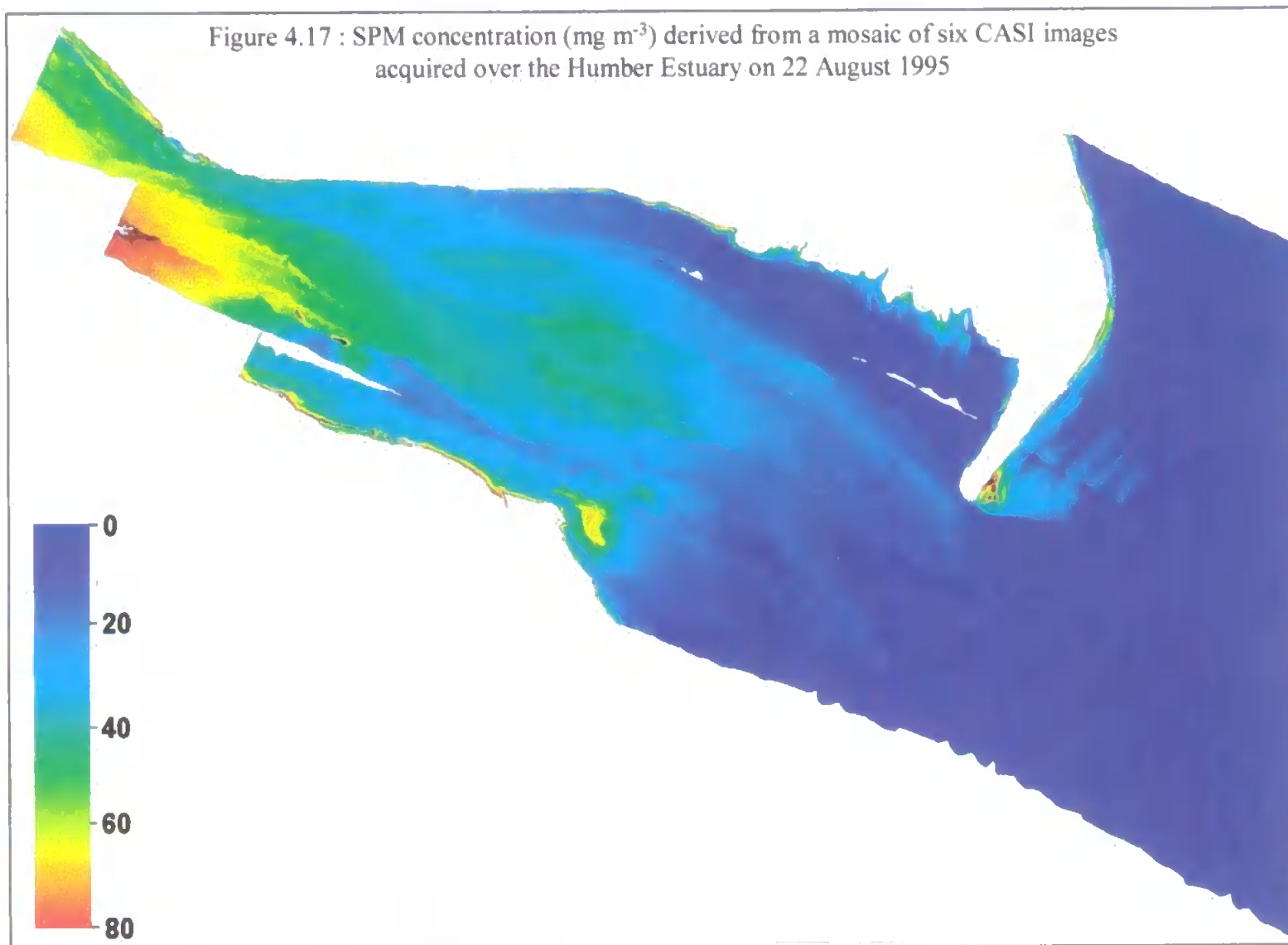
In addition to problems encountered with the navigation, many and varied discoveries were made concerning the imaged digital datastream itself. Depending on the quality of equipment operation and / or the command of the aircraft during survey, a variety of errors can creep into the imaged datastream. These included, for example, the misrepresentation of important information routinely recorded on the in-flight log sheets, misuse of the equipment and / or bad practice concerning data storage, backup and handling. The complexity and variety of possible factors affecting the quality of the data, and the sheer quantity of the remotely sensed data acquired both for LOIS and broadly within NERC, necessitated the development of a streamlined processing system which took the majority of the unwanted factors affecting the imaged datastreams into account. C-shells were scripted to handle the navigation correction software and to run it alongside the main NERC ARSF processing routines. In addition, the major errors affecting the imaged datastreams which resulted from a variety of external and internal (equipment) sources were identified through thorough familiarisation with the datasets. Their identification and correction were coded into the software and these are now routinely used to effectively and efficiently rectify current and historical data acquired using the NERC IDS.

Geometric correction using the corrected 3D vector data is applied to the image data through the *gcorr* program. *Gcorr* uses integrated attitude and position, datum shift, geoid-spheroid separation correction and projection parameters and integrates it with the scanner optic parameters to obtain pixel co-ordinates on a selected map projection (Mockridge *et al.*, 1997). Through nearest neighbour interpolation the image data is transformed into fully corrected rectilinear versions (e.g. figs. 4.16 & 4.17). The results are tested through comparison with Ordnance Survey landline and locally digitised linework where possible.

The overall accuracy of the geometric correction is at best within 3 - 4 pixels for all 1995 data acquired using the Integrated Data System. When comparing the images with sea-surface derived measurements it was not necessary to have greater geometric accuracy.

The geometric information contained within the image datastream was used to identify the ship or mooring on the image and then the area relating to the required target waters defined by eye. Using knowledge of the orientation of the flightline and of the time of day, it was possible to chose the relevant section of the image that would correspond to any measurements being taken from the water's surface at the same time. In the case of optical profiles this was the side of the ship facing into the sun and in the case of the *flux curtain* the section of water directly in front of the mooring, which itself always faces into the flow. The group of relevant pixels were interrogated and an area of between 10 and 30 pixels averaged to derive mean and standard deviation values for comparison with the surface-derived measurements. This ensured both spatial and temporal coincidence was maintained between the images and any measurements acquired at the sea-surface.

Within the CASI and ATM datastreams errors have been minimised wherever assumptions have had to be made and / or where software has limited progress. Errors may have been introduced into the datastreams due to an inadequate atmospheric correction (resulting from software limitations) although the use of a Rayleigh correction alone is considered adequate where further algorithm development relies on band ratios, as does the SPM algorithm developed and employed here. The thermal calibration of the ATM's thermal-infrared channels relies on the use of an assumed constant emissivity value for a particular water body. This assumption may be a source of error although the effects of this are minimised through the use of sea-based measurements to fine tune the sea-surface temperature images. Due to a concerted error minimisation effort, the calibrated and corrected CASI and ATM images are thus considered to be of a sufficient quality for use in the analyses proposed for this study.



## 5 Optics and Airborne Remote Sensing in the Humber Estuary

The calibrated and processed data acquired from the air and from the sea in and around the Humber Estuary are assessed and analysed in this chapter. The optical properties of the waters generate valuable information concerning their nature and content. When used in conjunction with hydrodynamically modelled data, a truly multi-dimensional view of the Humber's estuarine dynamics is revealed.

### 5.1 Classification of water types

A water classification based on Jerlov's (1976) empirical water classification technique outlined in section 2.4 was adopted for the Humber Estuary.  $K_d(\lambda)$  values were calculated for the datasets acquired in the Humber Estuary and offshore along the coastal stretch to the north (results in Appendix C). This was achieved through the application of equation 2-11 and the linear regression of  $\ln(E_d(\lambda, 0^-))$  against depth. In the absence of a 475 nm waveband as used by Jerlov (1976) (fig. 2.3), the  $K_d(\lambda)$  values for each wavelength were compared with, and regressed against, their associated  $K_d(490)$  values. The resulting regression relationships all sustained  $R^2$  values of over 0.95 and are graphically depicted in figure 5.1; to aid clarity the points themselves are not depicted. The relationships provide a more detailed insight into coastal water classification than Jerlov's (1976) original study (fig. 2.3) which mainly focused on waters of type **I**, **IA**, **IB**, **II** and **III** and less on the five more distinct coastal water classes of types **1**, **3**, **5**, **7** and **9**.

A similarity between the oceanic type **III** and coastal type **1** waters between 555 nm and 700 nm was exemplified by Jerlov (1976) in the transmittance curves measured for his study (fig. 5.2). He showed that there is a convergence of the transmittance curves for types **III** and **1** at wavelengths over 555 nm (fig. 5.2). This factor would make the boundary between oceanic type **III** and coastal type **1** less distinct in wavelengths above 555 nm. The trends shown in the profiled data acquired in the Humber Estuary and in the clearer North Sea waters (fig. 5.1a) follow those expected from Jerlov's (1976) predictions for wavelengths of 490 nm and below (table 2.1, fig. 2.3). However, at wavelengths over 555 nm (670 nm and 700 nm) an entirely different trend emerges (fig 5.1b). This is likely

to be due to the extreme SPM laden conditions in which the large majority of the profiles were acquired. The revelation of fig. 5.2 may help to explain the emergence of a change in trend at 510 nm and 555 nm located at the type 1 boundary (fig. 5.1b). The type 1 boundary could indicate the cross over point from oceanic to coastal type as the transmittance characteristics in coastal waters below 555 nm are dramatically different to those found above 555 nm (fig. 5.2).

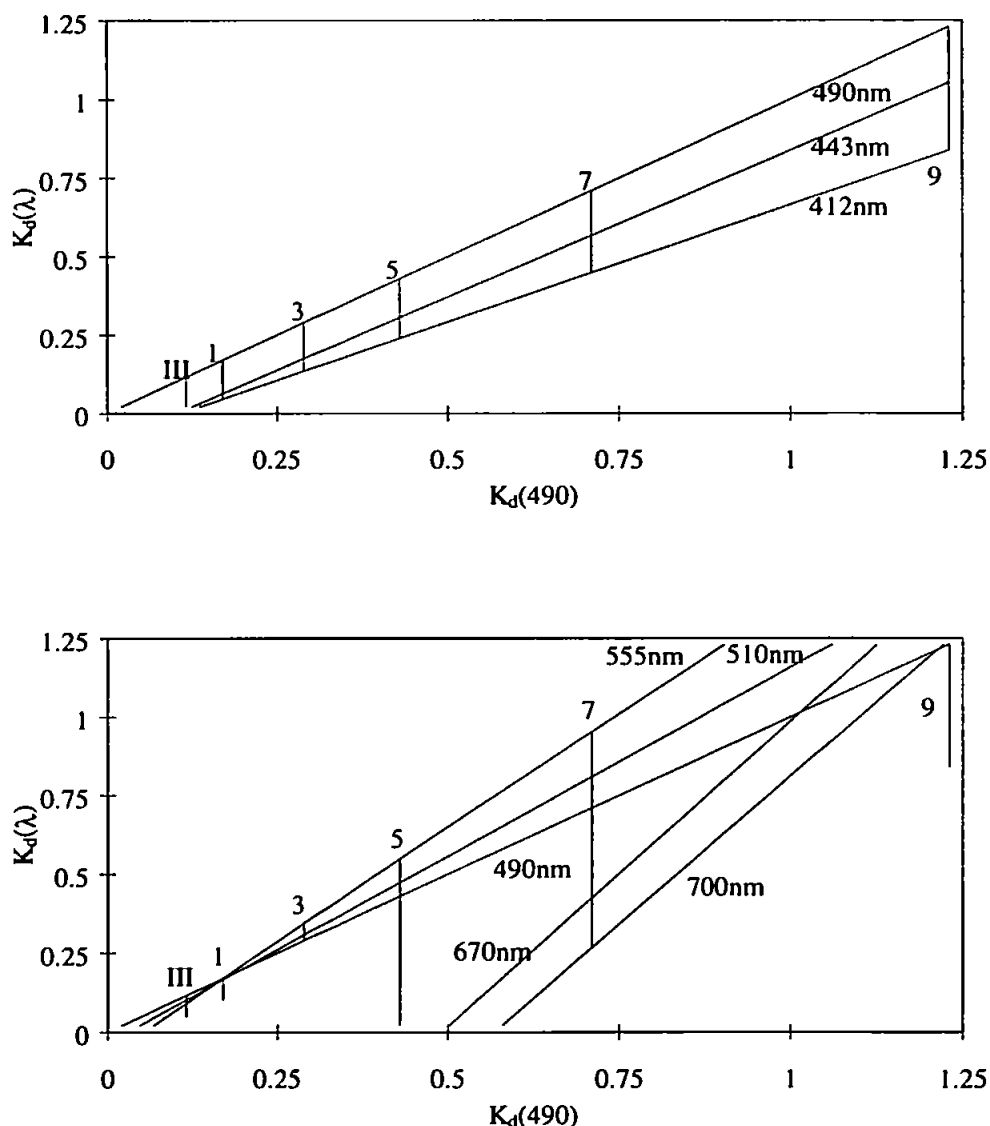


Figure 5.1a (top) & b (bottom) :  $K_d(\lambda)$  ( $\text{m}^{-1}$ ) and its relation to  $K_d(490)$  for the water masses of the Humber Estuary and the North Sea. Also detailed are the boundary limits for Jerlov's (1976) oceanic water type III and coastal water types 1, 3, 5, 7 and 9.



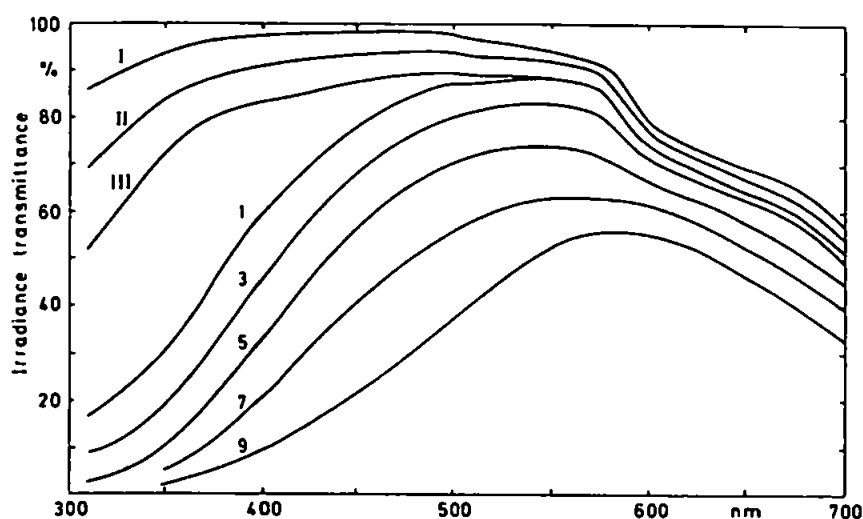


Figure 5.2 : Transmittance per metre of downward irradiance in the surface layer for optical water types - oceanic water types I, II, III and coastal water types 1, 3, 5, 7, 9 (Jerlov, 1976)

The profiles acquired for this study were classified according to the thresholds detailed in table 2.1. This was done by comparing the  $K_d(\lambda)$  values from table 2.1 to those derived for all the profiles (Appendix C). The wavelengths were matched to the ones detailed in table 2.1 as closely as possible although some interpolation was necessary (table 5.1). Type 1 waters were taken as the cross over point from oceanic to coastal type waters and an indication of the change from Morel & Prieur's (1977) case I to II waters.

Profile	Jerlov (1976)	Morel & Prieur (1977)	Maximum $z_{90}$ (m)
A, B	1	I / II	6.6
D, S	3	II	5.4
C, P, Q, R, T	5	II	3.6
I, J, O	7	II	1.8
E, F, G, H, K, L, M, N	9	II	1.5

Table 5.1 : Classification of water "types" according to Jerlov (1976) and "cases" according to Morel & Prieur (1977) for each profile. The maximum depth from which 90% of the original optical signal reached the surface,  $z_{90}$ , is also shown.

As a further check to verify the results of the water classifications  $z_{90}$  was calculated from equation 2-15 for all the profiles (results in Appendix C and maximum depth  $z_{90}$  values

calculated for each water type detailed in table 5.1). This provides a further insight into the nature of the waters by delineating the depth at which 90% of the light penetrates through the water column. The maximum  $z_{90}$  values for the different water types clearly highlight the progression of water classes from the clearer type 1 waters at the case I / II boundary whose  $z_{90}$  values reach 6.6 m, to the more turbid case II and type 9 where the maximum  $z_{90}$  found was only 1.5 m (table 5.1).

## 5.2 Diffuse attenuation and $K_d(490)$

An empirical relationship between  $K_d(490)$  and CZCS observations was discovered by Austin & Petzold (1981). Their algorithm employs the ratio of water-leaving radiance at 443 nm and 550 nm. It was devised using measurements acquired in waters where the majority of material was biogenic and contained a maximum chlorophyll concentration of  $1.5 \text{ mg m}^{-3}$ . In the open sea, the 520 nm to 550 nm ratio would be more relevant (Mayo *et al.*, 1993). The Austin & Petzold (1981)  $K_d(490)$  relationship is defined as:

$$K_d(490) = 0.022 + 0.088 \left( \frac{L_w(443)}{L_w(550)} \right)^{-1.491} \quad (5-1)$$

The results from the Austin & Petzold (1981) study were limited due to the restricted sensor capability of the CZCS and the atmospheric correction used. As a consequence, the results are suitable only for waters which have a  $K_d(490)$  of less than  $0.5 \text{ m}^{-1}$  (Stumpf & Pennock, 1991) and a predominance of absorbing material, namely case I waters.

Mueller & Trees (1996) devised a  $K_d(490)$  algorithm for SeaWiFS based on that developed by Austin & Petzold (1981) for the CZCS. They assessed the results from 242 profiled measurements obtained from a series of cruises which took place over different stretches of the world's oceans (fig. 5.3). Due to the characteristics of SeaWiFS, it was necessary to substitute the 550 nm waveband, which forms the basis of the Austin & Petzold (1981) routine, with 555 nm. Regression analysis for 42 of their profiles yielded a result with an  $R^2$  of 0.9 and defined:

$$K_d(490) = 0.022 + 0.100 \left( \frac{L_{WN}(443)}{L_{WN}(555)} \right)^{-1.300} \quad (5-2)$$

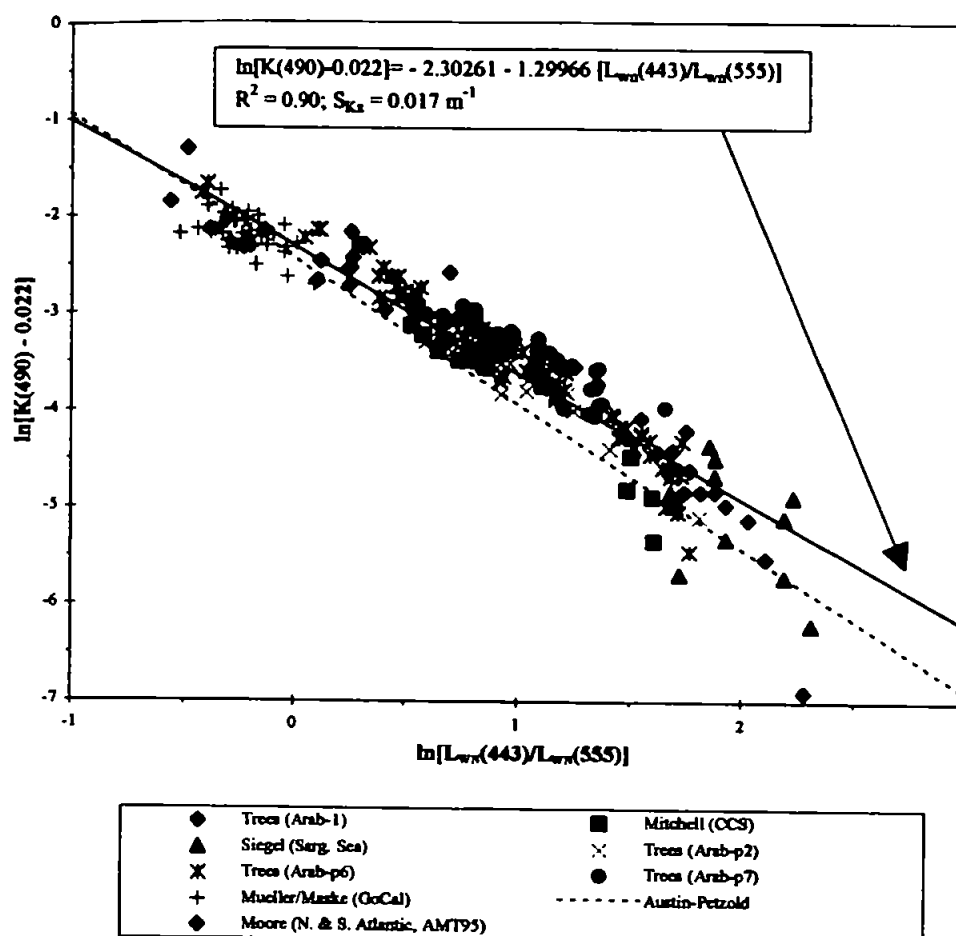


Figure 5.3 : SeaWiFS  $K_d(490)$  values acquired from a variety of oceanic cruises compared with calculated values as derived from equation 5-2 (Mueller & Trees, 1996)

Both Austin & Petzold (1981) and Mueller & Trees (1996) based their analyses on samples acquired predominantly in case *I* waters. The literature lacks an algorithm that handles case *II* waters. Turbid estuaries have  $K_d(490)$  values which range from  $0.5 \text{ m}^{-1}$  to approximately  $5 \text{ m}^{-1}$  and hence optical depths ranging from 2 m to 0.2 m. Their optical characteristics are primarily dependent upon the presence of SPM which has a strong backscatter component. This can be represented as:

$$K_d = K_s n_s + K_x \quad (5-3)$$

Stumpf & Pennock (1991)

where  $K_s$  is the specific diffuse attenuation coefficient for SPM,

$n_s$  is SPM concentration, and

$K_x$  is the diffuse attenuation coefficient for other constituents (water, chlorophyll, etc.).

To define a routine for  $K_d(490)$  derivation in case II waters, the Austin & Petzold (1981) theory was applied to the results from the twenty profiles (detailed in Appendix C) acquired during this study and mainly in case II waters (table 5.1).  $L_{WN}(443)$  and  $L_{WN}(555)$  were derived from the profiled measurements according to equation 2-21 and using values for  $F_0(\lambda)$  determined by Gregg *et al.* 1993. The ratio  $\frac{L_{WN}(443)}{L_{WN}(555)}$  was then compared to the  $K_d(490)$  profiled results (fig. 5.4). The regression analysis yielded an  $R^2$  of 0.797 and defined:

$$K_d(490) = 0.022 + 0.061 \left( \frac{L_{WN}(443)}{L_{WN}(555)} \right)^{-2.526} \quad (5-4)$$

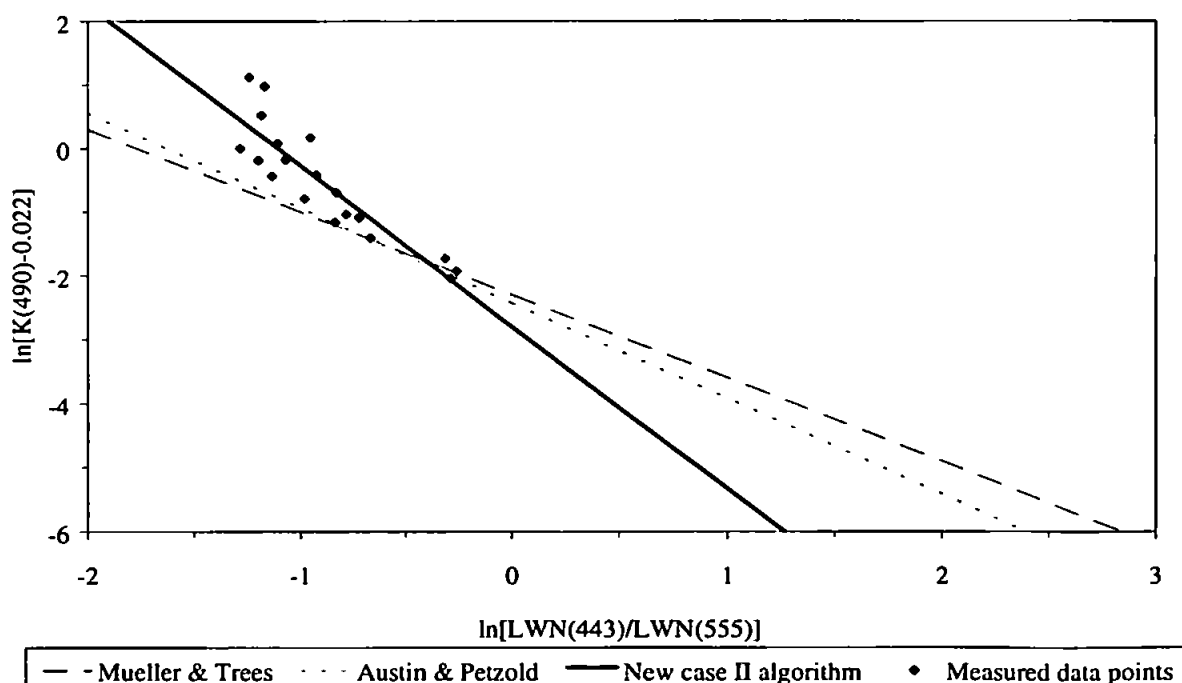


Figure 5.4 :  $K_d(490)$  algorithms as devised by Austin & Petzold (1981) and Mueller & Trees (1986). Their relation to the newly quantified case II algorithm and the measured  $K_d(490)$  results are shown.

The three equations (equations 5-1, 5-2 and 5-4) were used to derive  $K_d(490)$  from the twenty profiles (detailed in Appendix C) acquired during this study. Multiple regression analyses were performed using these results to relate them to SPM, chlorophyll and salinity measurements acquired simultaneously. Table 5.2 details the standardised coefficients for each variable in the multiple regression. This quantity allows the comparison of the relative influence individual variables have on the  $K_d(490)$  values by converting the original values to a standard deviate. The multiple regression equation takes the form:

$$\frac{K_d(490) - \overline{K_d(490)}}{\sigma_{K_d(490)}} = a \frac{X_s - \overline{X_s}}{\sigma_{X_s}} + b \frac{X_{ch} - \overline{X_{ch}}}{\sigma_{X_{ch}}} + c \frac{X_{sal} - \overline{X_{sal}}}{\sigma_{X_{sal}}} + d \quad (5-5)$$

where:  $s$ ,  $ch$  &  $sal$  represent SPM, chlorophyll and salinity respectively and  $a$ ,  $b$ ,  $c$  &  $d$  are the standardised coefficients.

The regressions yielded an  $R^2$  of 0.819 for the Austin & Petzold (1981) routine (equation 5-1), of 0.810 for the Mueller & Trees (1996) equation (equation 5-2) and of 0.880 for the newly derived case II algorithm (equation 5-4).

	Austin & Petzold	Mueller & Trees	New case II algorithm
SPM	0.273	0.283	0.200
Chlorophyll	0.783	0.771	0.855
Salinity	-0.023	-0.023	-0.11
$R^2$	0.819	0.810	0.880

Table 5.2 : Standardised coefficients and the coefficient of determination from the multiple regression of results from three  $K_d(490)$  algorithms and in-water constituents for twenty datasets

The results shown in table 5.2 support the newly quantified case II version of the Austin & Petzold (1981) routine (equation 5-4) and imply that the Mueller & Trees (1996) version (equation 5-2) does not describe case II waters as well. The ratio of  $K_d(490)$  to  $\frac{L_{wn}(443)}{L_{wn}(555)}$  increases exponentially as one moves from case I through to case II waters. The routine developed for  $K_d(490)$  by Mueller & Trees (1996) (equation 5-2), using samples acquired over case I waters only, thus becomes invalid for use in case II waters where  $K_d(490)$  values increase exponentially away from their idealised regression line (fig. 5.4).

### 5.3 SPM concentration from CASI images

CASI data were acquired over the Humber Estuary to provide sequential time series of data throughout significant fractions of the tide for the purposes of investigating sediment distributions for modelling and for the estimation of sediment fluxes. This was achieved by repeatedly flying transects across the mouth of the Humber Estuary along transaxial 1 and encompassing the *flux curtain* (fig. 3.9). These data were then calibrated and processed to derive the SPM concentrations (see section 4.2) that were evolving over these time scales. Imaged time series which spanned a variety of tidal fractions were acquired on five dates during 1995 (table 3.4). The SPM concentrations derived from the image data were interrogated to investigate the distribution of SPM across the mouth of the estuary during the times of data acquisition. This information was further used in the estimation of fluxes into and out of the estuary during the different tidal fractions.

#### 5.3.1 Two-dimensional Fourier Transforms of image data

A preliminary investigation was undertaken to ascertain the spatial frequency distribution of SPM across the images and so determine the axis along which the SPM features varied most. Two-dimensional Fourier transforms of image data provide a measure of the wavelength of SPM features and also indicate the axis along which SPM flux may be estimated; the SPM features found in the Humber Estuary generally take on the form of tongues extending into and out from the estuary mouth and would thus be represented as features perpendicular to the axis of maximum variation across the image.

The Fourier transform of an image gives an indication of its spatial frequency distribution by transforming it from “real” space ( $x, y$ ) to frequency space ( $\omega_x, \omega_y$ ). An image whose digital number (DN) values vary across it slowly will support low spatial frequencies and thus low values of  $\omega$  (fig. 5.5). Conversely, an image containing frequent sharp changes in DN values will have high spatial frequency components and high values of  $\omega$  (fig. 5.5). Thus, a profile across an image which has many “patches” of SPM will have a broader Fourier spectrum than one comprising more uniform concentration patterns.

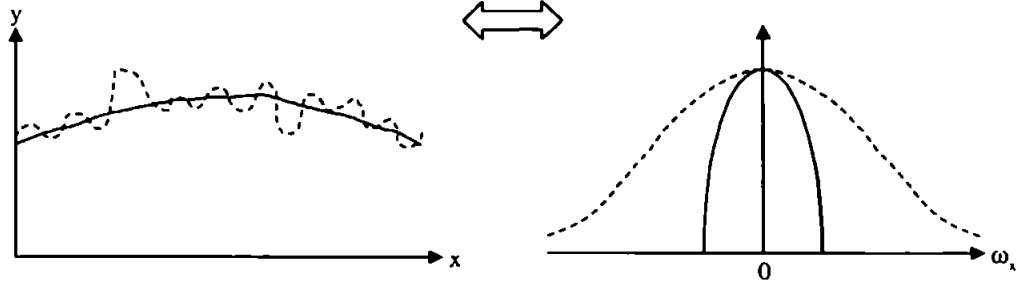


Figure 5.5 : Data transformation from “real space” (left) to Fourier space (right). The solid line depicts information taken from an image across which the DN values vary slowly (left). In this case the Fourier spectrum is narrow (right). Where DN values vary rapidly across a scene, as exemplified by the dashed line (left), the Fourier spectrum is much broader (right).

The complex function  $d(X,Y)$  defines a two-dimensional image ( $d$ ) of size  $N_X \times N_Y$  where  $0 \leq X \leq N_X - 1$  and  $0 \leq Y \leq N_Y - 1$ . The discrete Fourier transform defined over the same two-dimensional grid,  $D(\omega_x, \omega_y)$ , can be expressed mathematically as:

$$D(\omega_x, \omega_y) = \sum_{X=0}^{N_X-1} \sum_{Y=0}^{N_Y-1} d(X,Y) e^{\frac{-i2\pi X\omega_x}{N_X}} e^{\frac{-i2\pi Y\omega_y}{N_Y}} \quad (5-6)$$

If the sampling distance in the space domain is  $\Delta x$  then the highest spatial frequency found in the Fourier domain is  $\frac{1}{2\Delta x}$ , the Nyquist frequency ( $N_y$ ).

$D(\omega_x, \omega_y)$  contains information on the amplitude of the spectrum and the phase. The amplitude,  $|D(\omega_x, \omega_y)|$ , is commonly displayed as a grey scale image in which the value of the transform is represented as the corresponding intensity in the  $(\omega_x, \omega_y)$  plane (e.g. fig. 5.6). The high frequency components appear near the edges and the low frequency components near the centre (e.g. fig. 5.6).

An example SPM image was chosen from each of the five dates when CASI data was acquired (table 3.4). The images were Fourier transformed and their amplitude,  $|D(\omega_x, \omega_y)|$ , which highlights the size of any SPM patches, displayed as a grey scale

image (fig. 5.6). The results from each image depict the axis along which there is the maximum variation in SPM distribution and clustering. This is represented as a concentration of white patches or bands (fig. 5.6), i.e. high amplitude information. In all cases this lay along an axis which, although slightly varying from image to image, traversed the estuary in a roughly NNW - SSE direction. The solid lines in figure 5.6 depict the actual line across the estuary mouth chosen as the target transect used for further analysis of the image scenes. This transect deviates slightly from the ideal due to the fact that the image groups vary slightly in their spatial coverage but it was chosen to be as close to the ideal axis as possible. The transect was used to depict the SPM distributions and hence ascertain the nature of flux ebb and flow across the estuary mouth for each CASI image acquired.

### **5.3.2 SPM concentration distributions**

Figures 5.7 - 5.11 detail the twenty-seven SPM images derived from CASI data. The corresponding SPM concentrations determined from the transects across the estuary (shown as solid lines on the SPM images) are displayed alongside. On each transect, the location of the Bull light float can be identified as the  $0 \text{ kg m}^{-3}$  SPM feature at approximately 1400 m from Spurn Head.



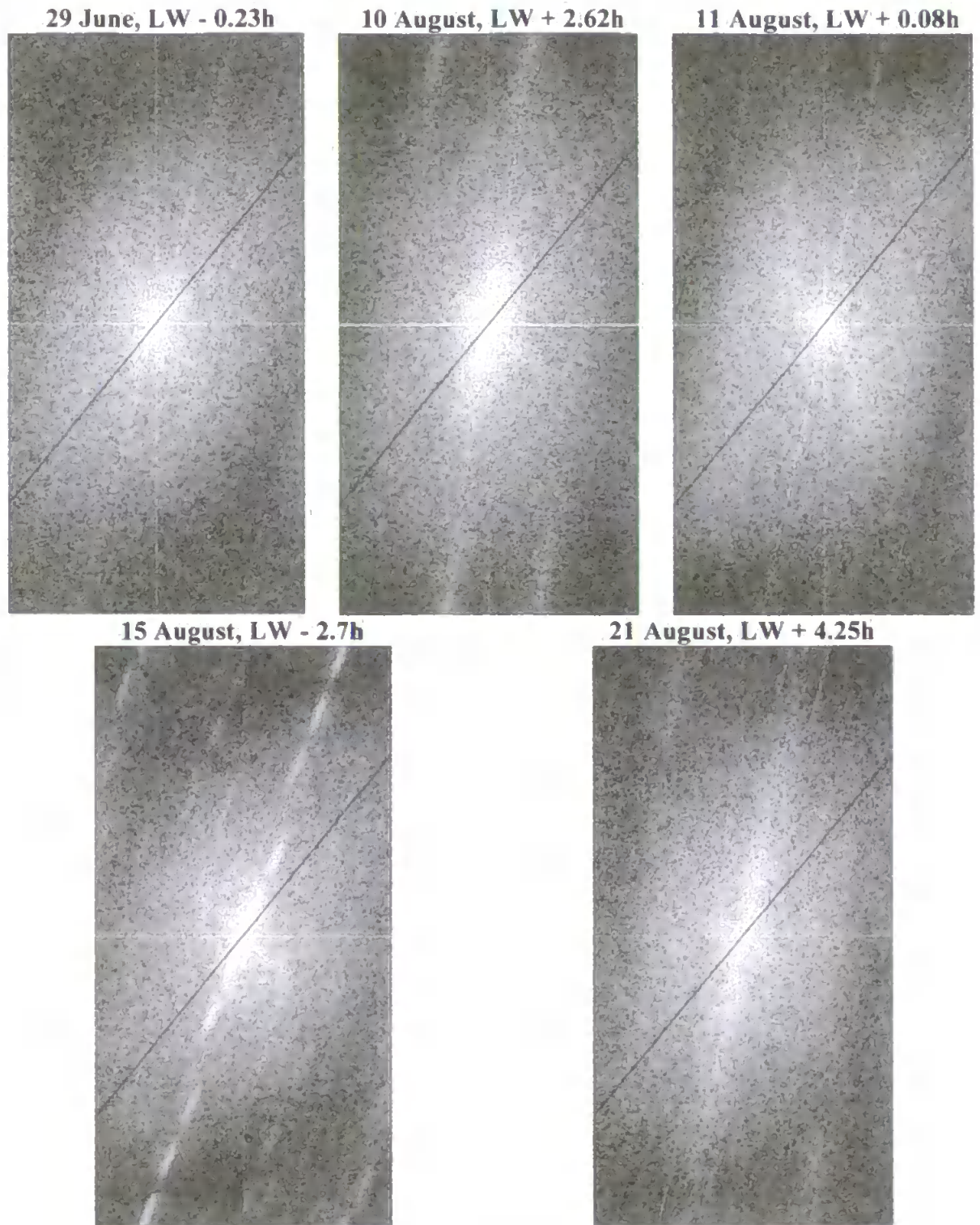


Figure 5.6 :  $|D(\omega_x, \omega_y)|$  values for 1024 x 2048 subsets of example SPM images from each of the five days of survey. The central axes define  $\omega_x$  and  $\omega_y$  and the solid lines depict the actual transect across the estuary mouth chosen for further analysis; the plots are orientated with north at the top.

Figure 5.7 : SPM concentrations ( $\text{kg m}^{-3}$ ) derived from CASI images (left) acquired on 29 June 1995 during spring tide conditions. SPM concentrations ( $\text{kg m}^{-3}$ ) procured from a transect taken across the Humber mouth in accordance with the solid lines shown on the images (left) are detailed to the right. The x-axis corresponds to distance from Spurn Head with zero representing Spurn Head itself and 6825 m Tetney Haven.

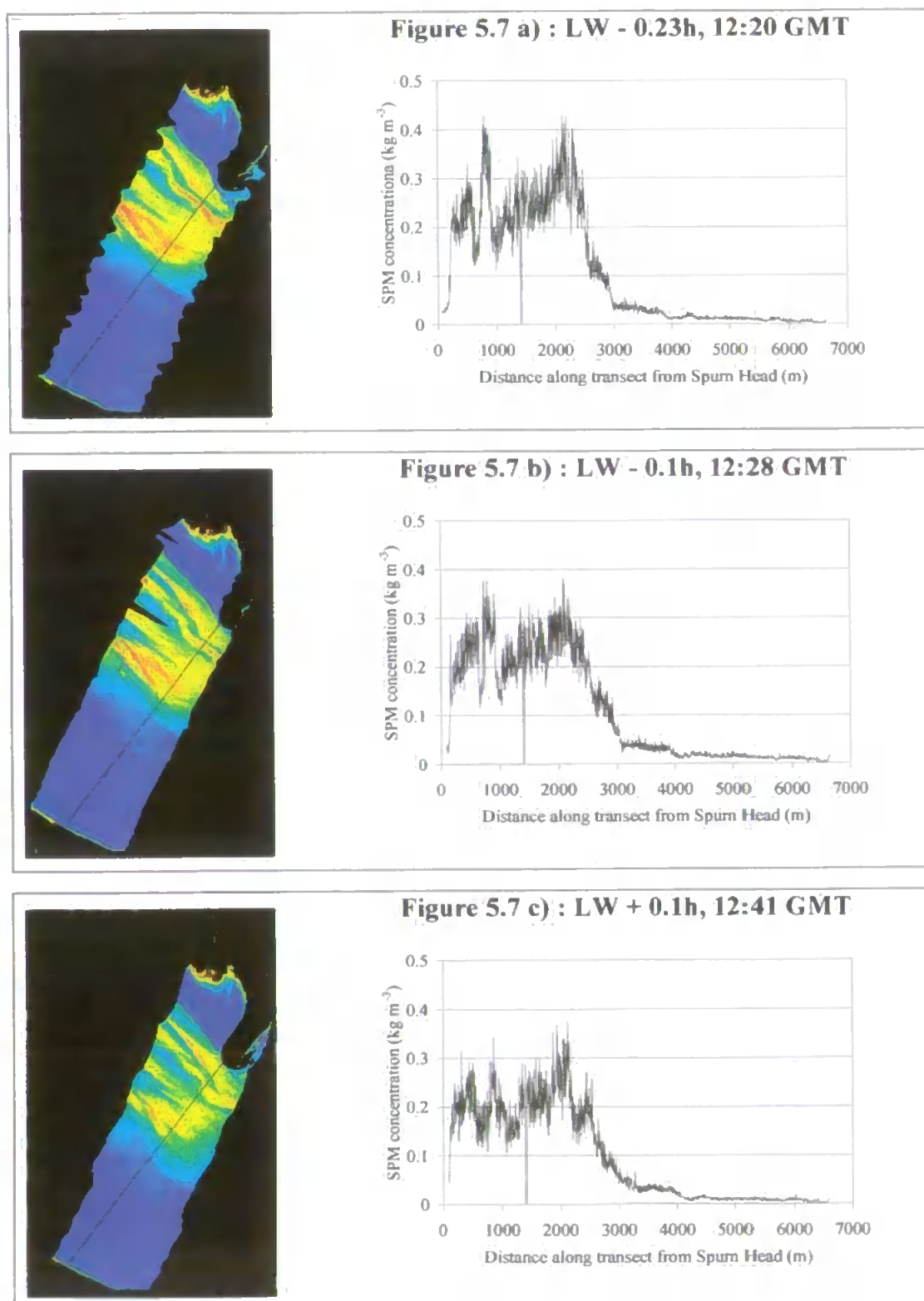
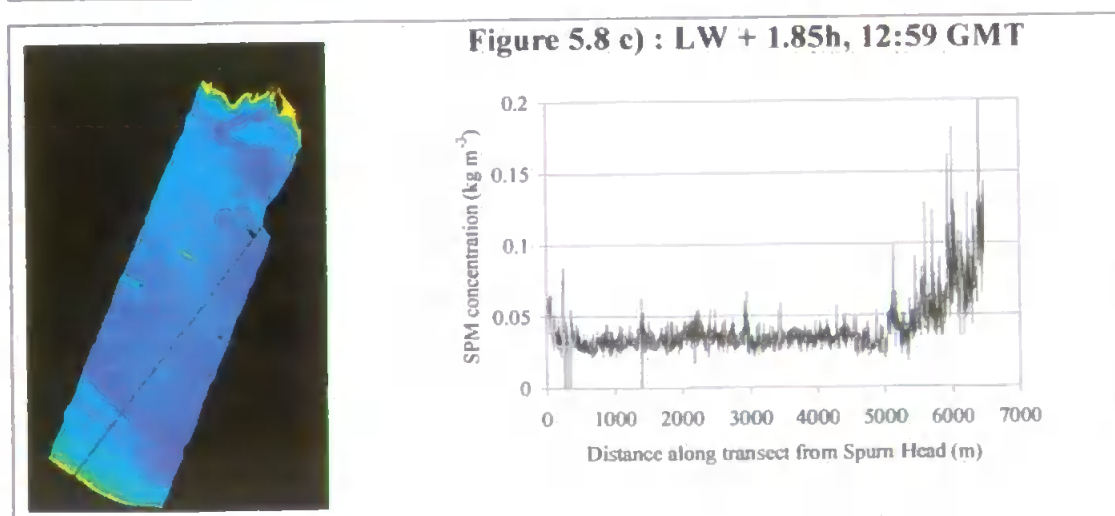
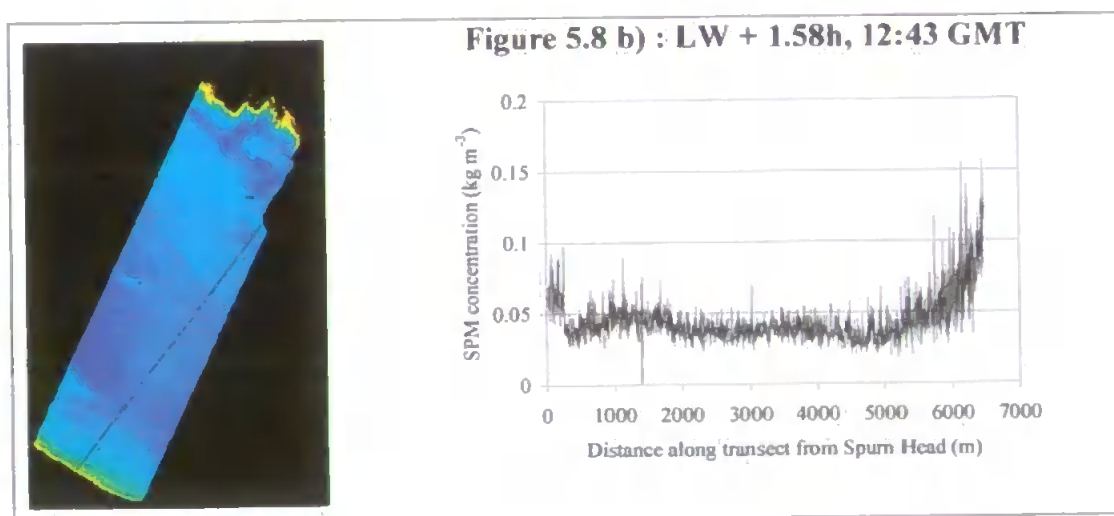
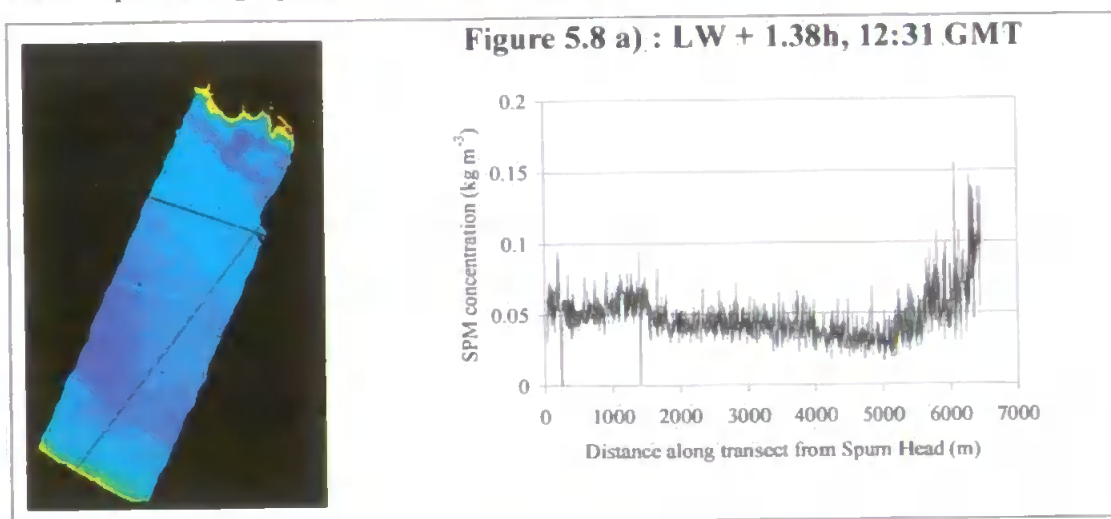
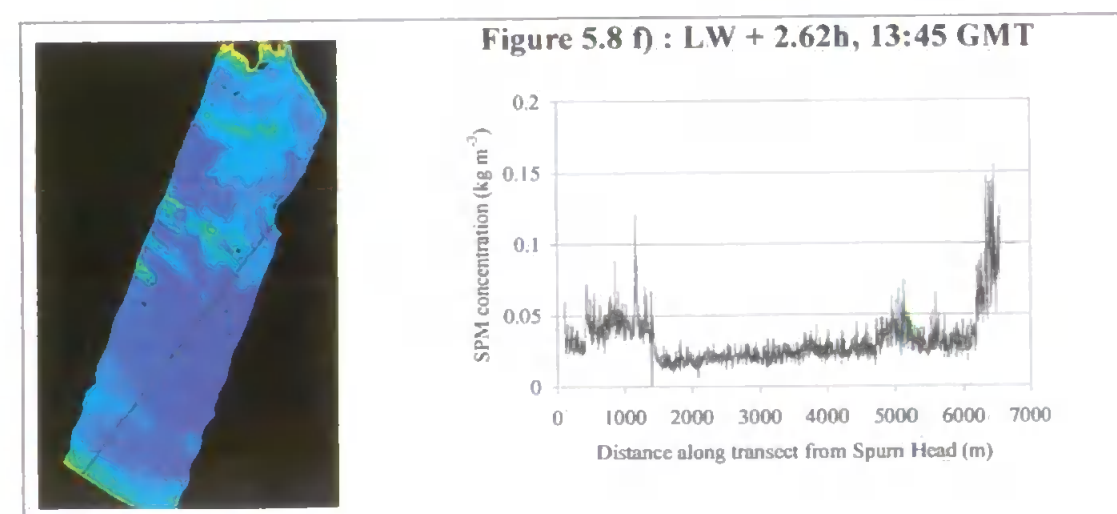
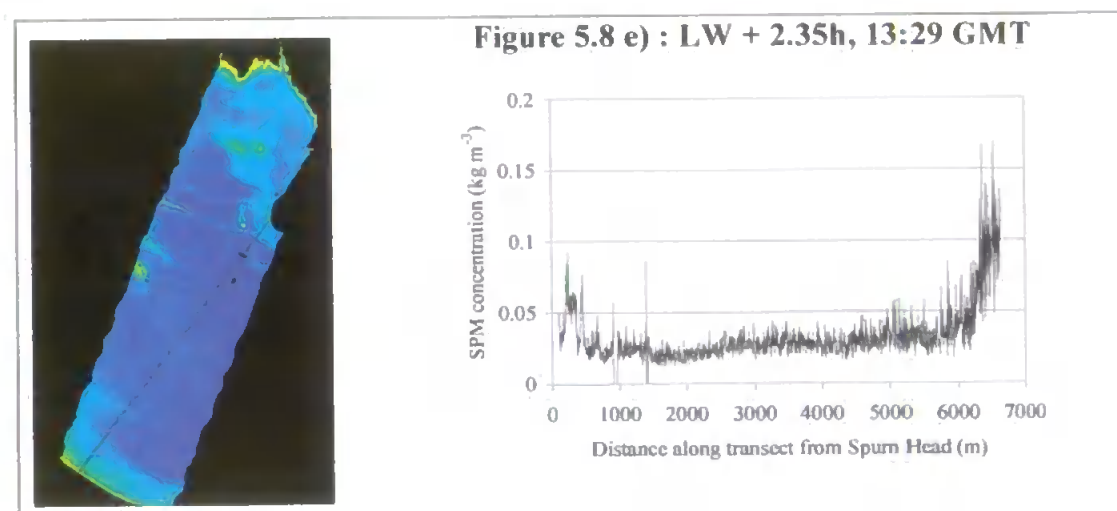
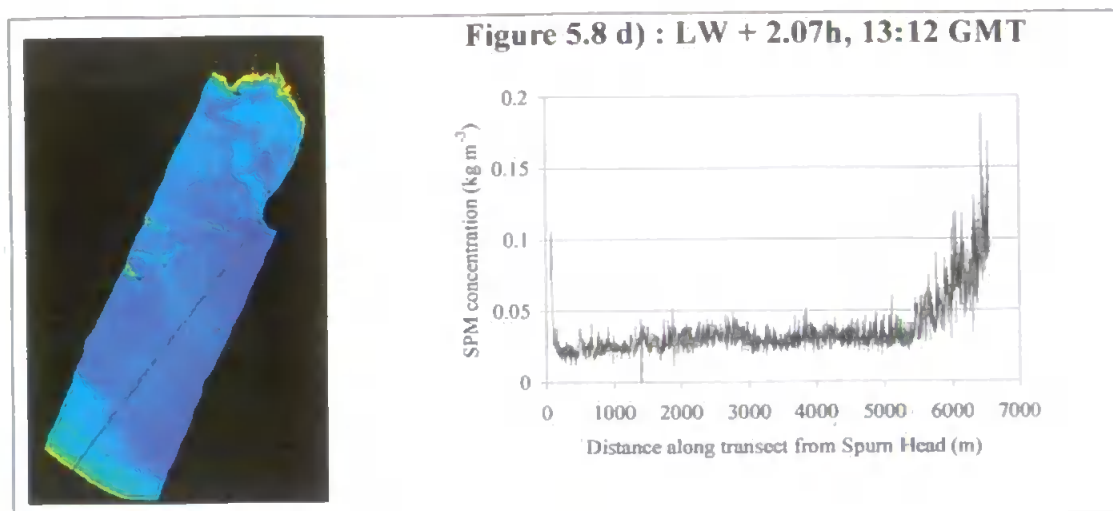
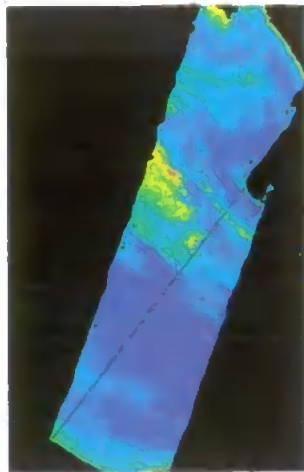


Figure 5.8 : SPM concentrations ( $\text{kg m}^{-3}$ ) derived from CASI images (left) acquired on 10 August 1995 one day before springs. SPM concentrations ( $\text{kg m}^{-3}$ ) procured from a transect taken across the Humber mouth in accordance with the solid lines shown on the images (left) are detailed to the right. The x-axis corresponds to distance from Spurn Head with zero representing Spurn Head itself and 6825 m Tetney Haven.









**Figure 5.8 g) : LW + 2.83h, 13:58 GMT**

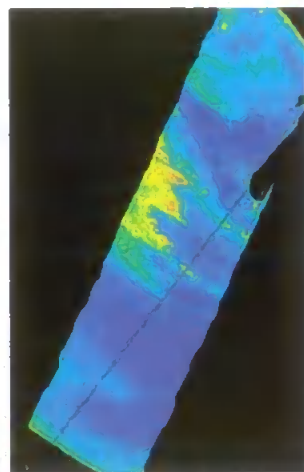
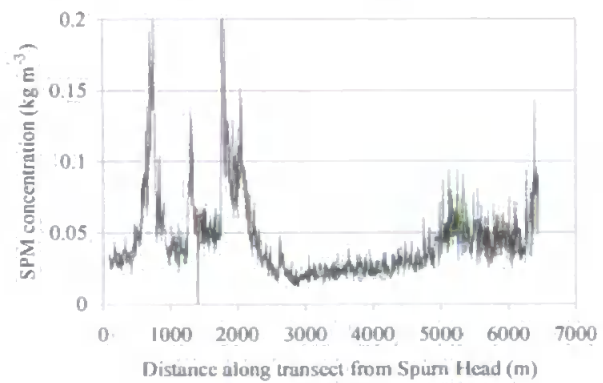


**Figure 5.8 h) : LW + 3.08h, 14:13 GMT**

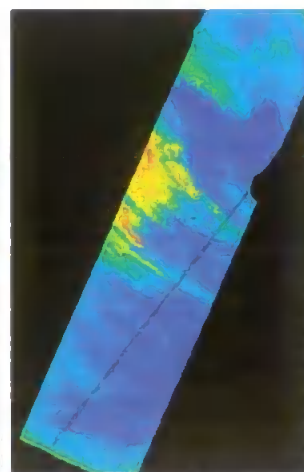
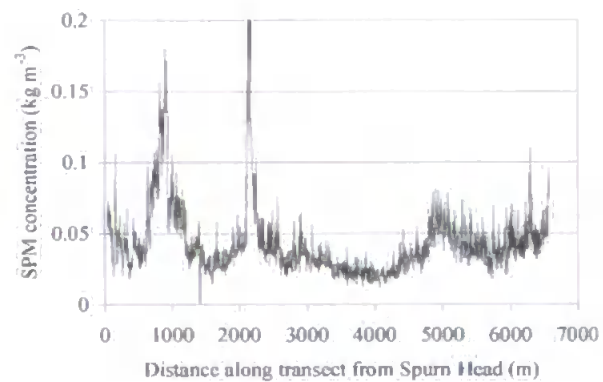


**Figure 5.8 i) : LW + 3.33h, 14:28 GMT**

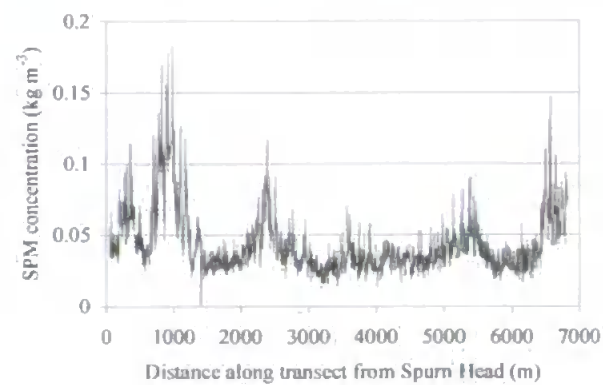


Figure 5.9 : SPM concentrations ( $\text{kg m}^{-3}$ ) derived from CASI images (left) acquired on 11 August 1995 during spring tidal conditions. SPM concentrations ( $\text{kg m}^{-3}$ ) procured from a transect taken across the Humber mouth in accordance with the solid lines shown on the images (left) are detailed to the right. The x-axis corresponds to distance from Spurn Head with zero representing Spurn Head itself and 6825 m Tetney Haven.

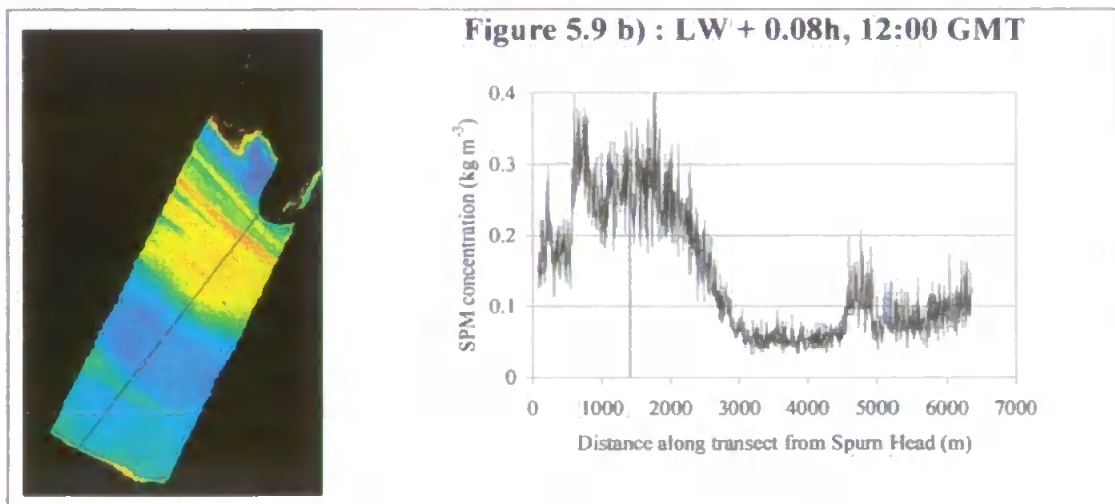
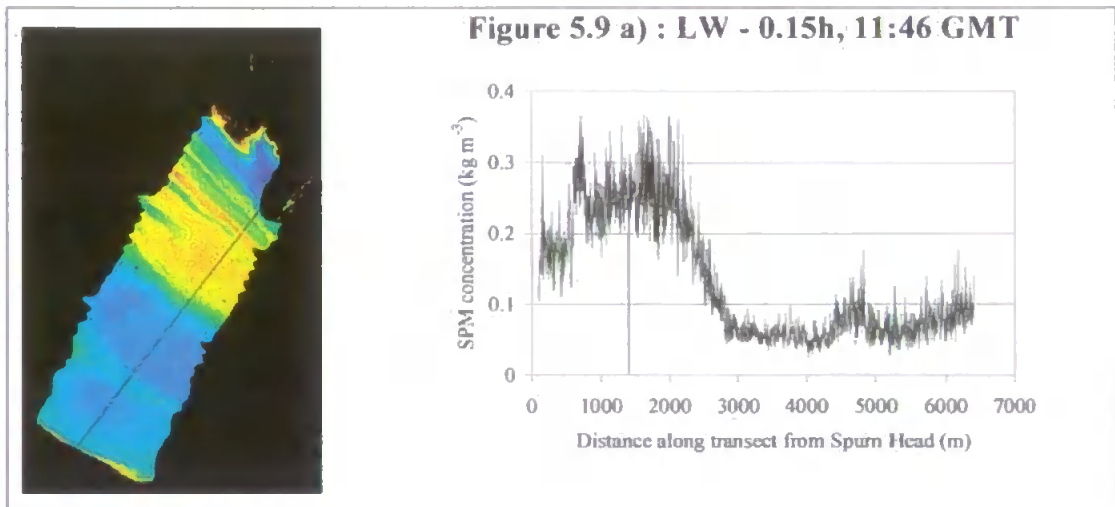
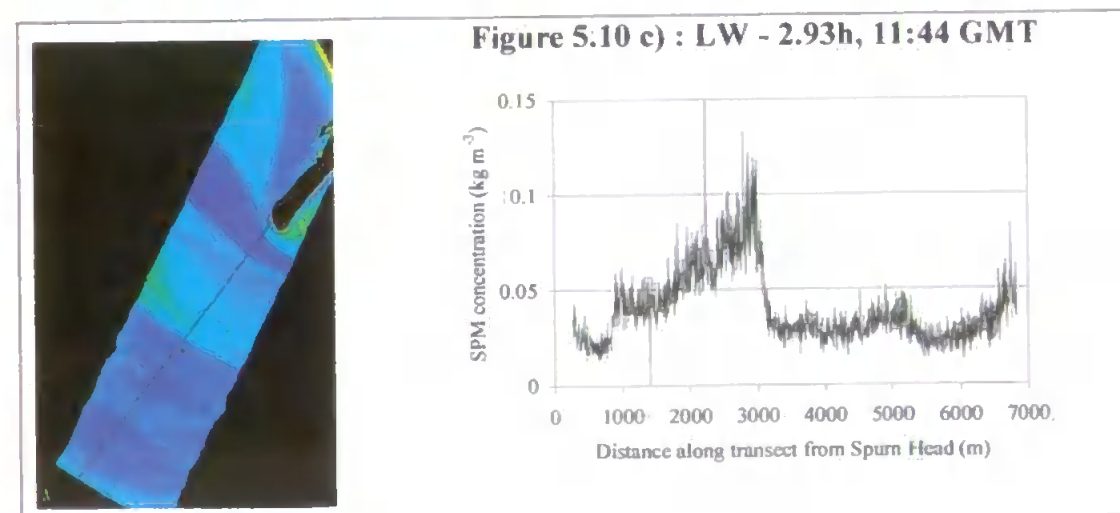
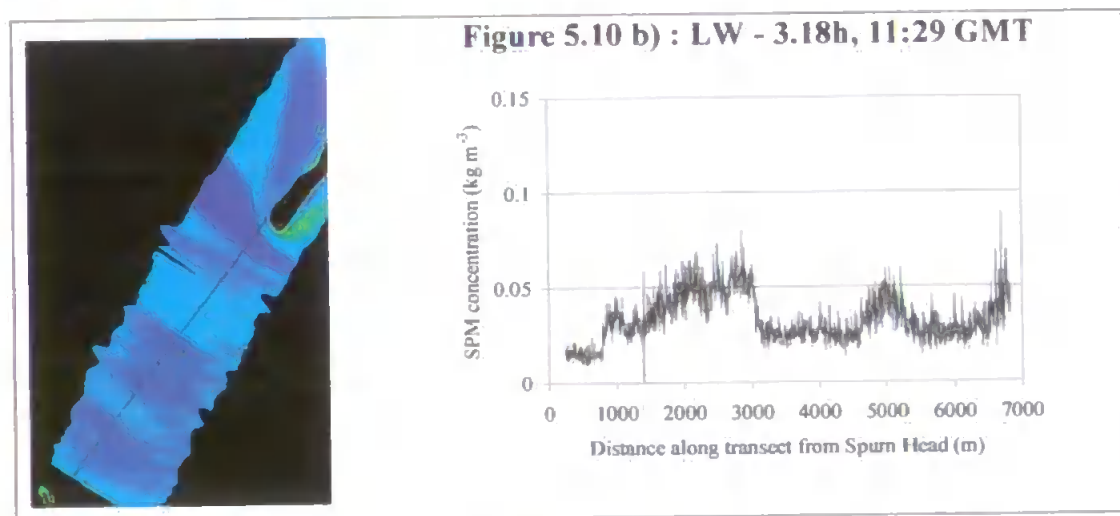
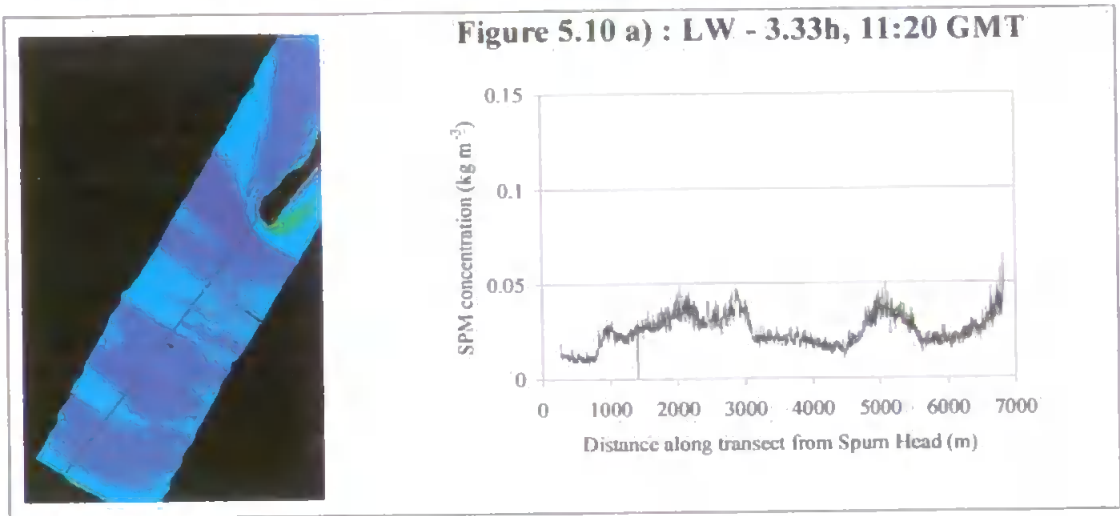


Figure 5.10 : SPM concentrations ( $\text{kg m}^{-3}$ ) derived from CASI images (left) acquired on 15 August 1995 four days after springs. SPM concentrations ( $\text{kg m}^{-3}$ ) procured from a transect taken across the Humber mouth in accordance with the solid lines shown on the images (left) are detailed to the right. The x-axis corresponds to distance from Spurn Head with zero representing Spurn Head itself and 6825 m Tetney Haven.



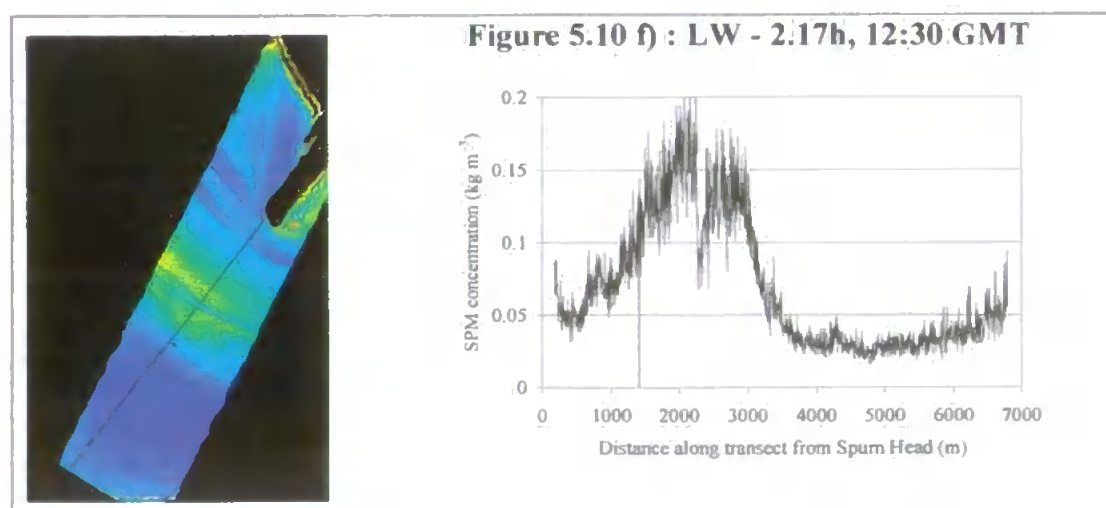
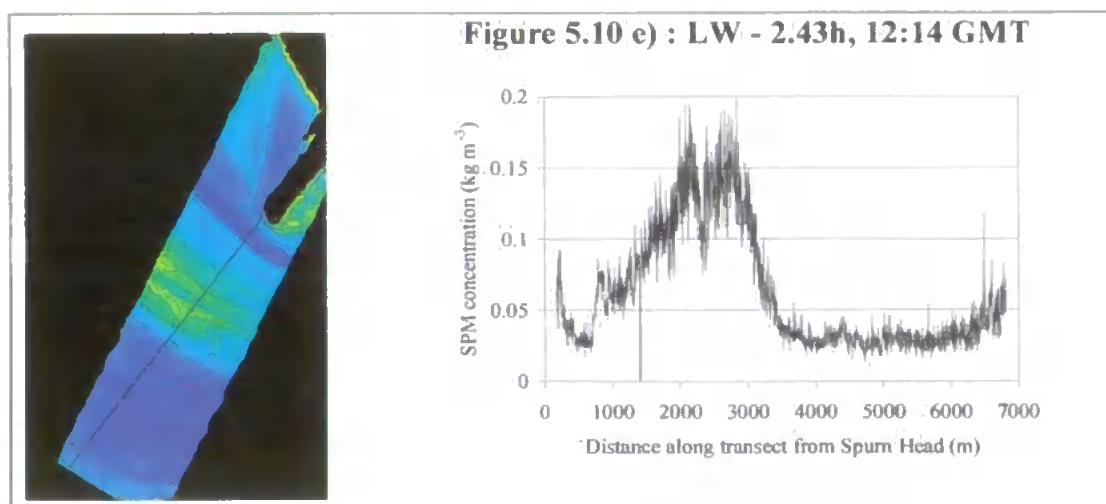
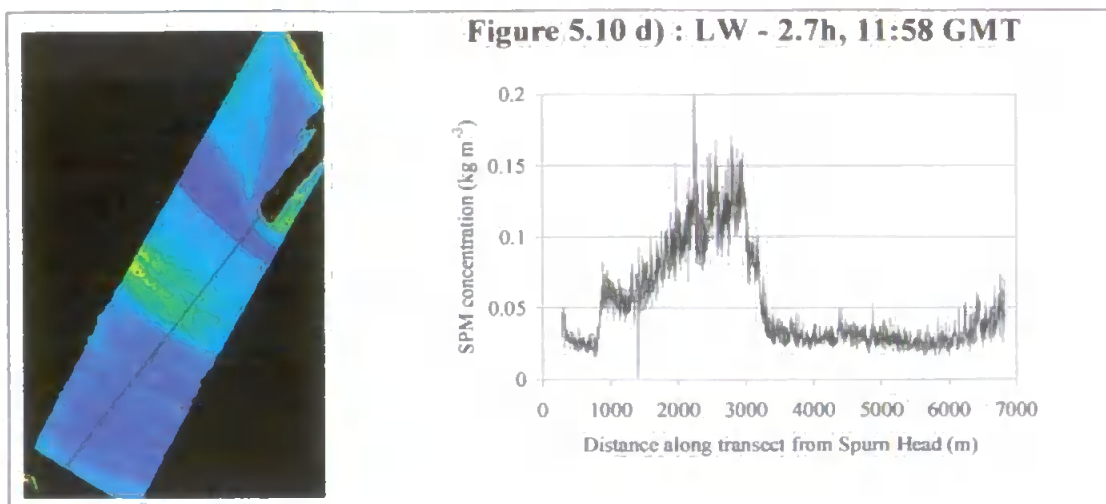
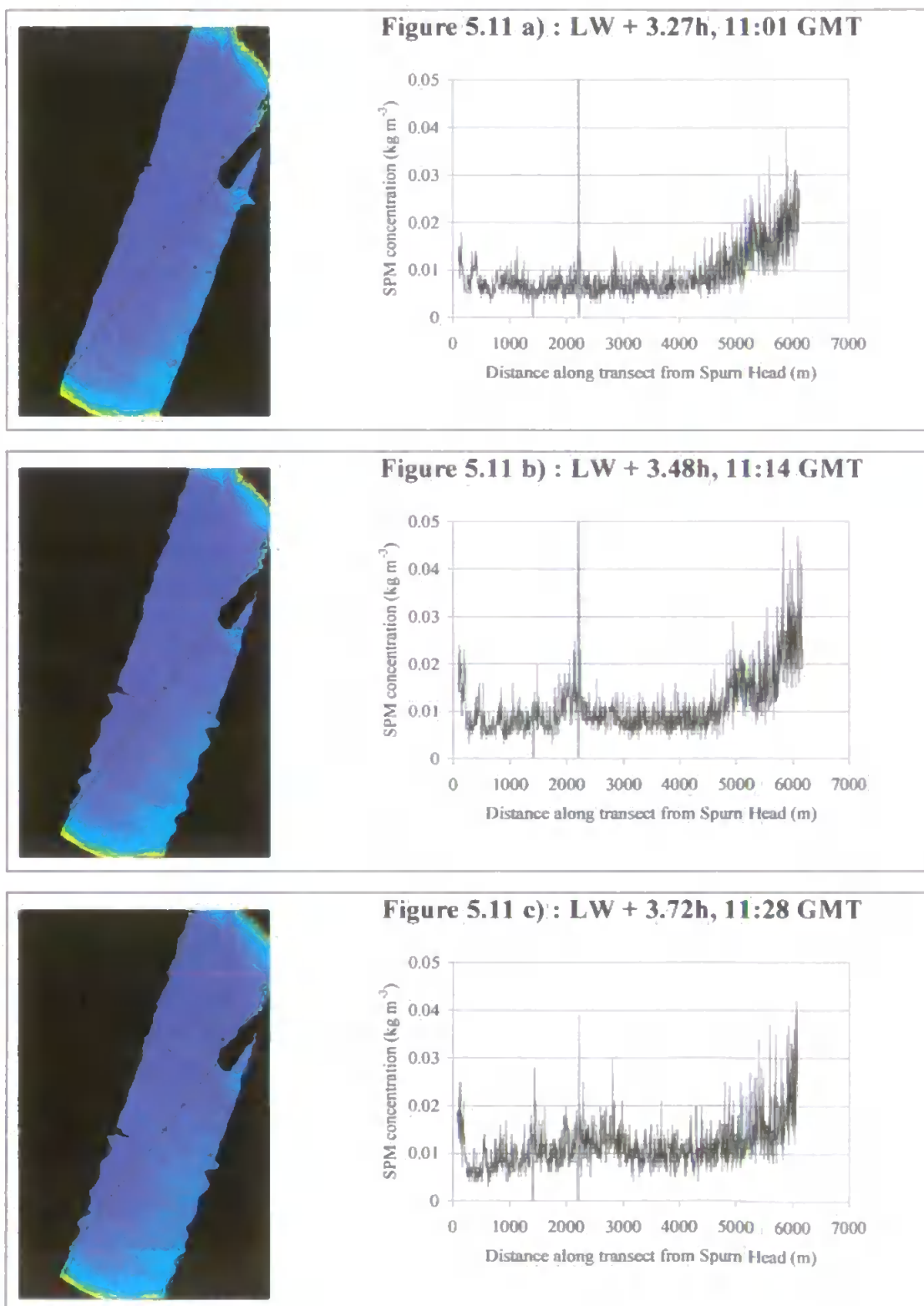
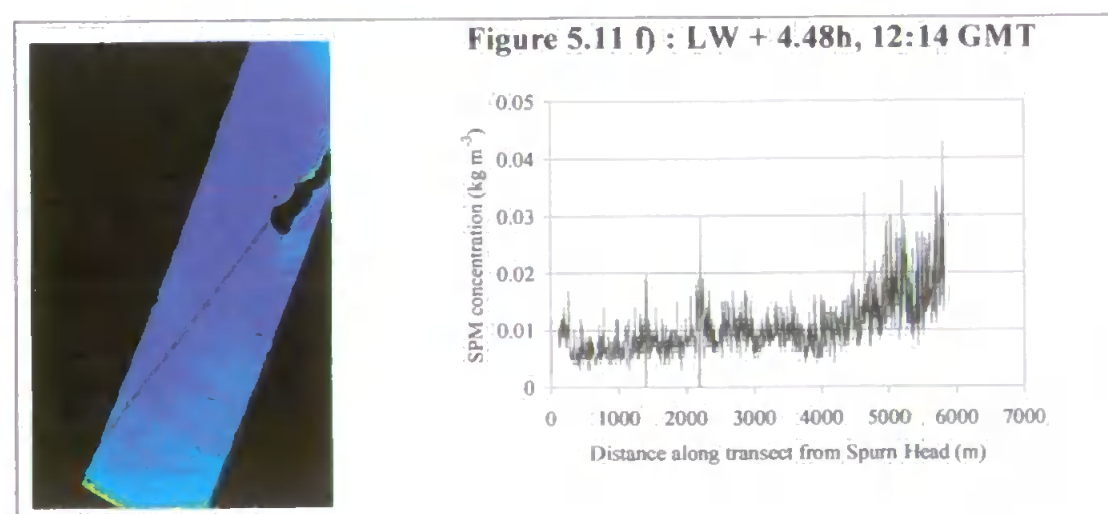
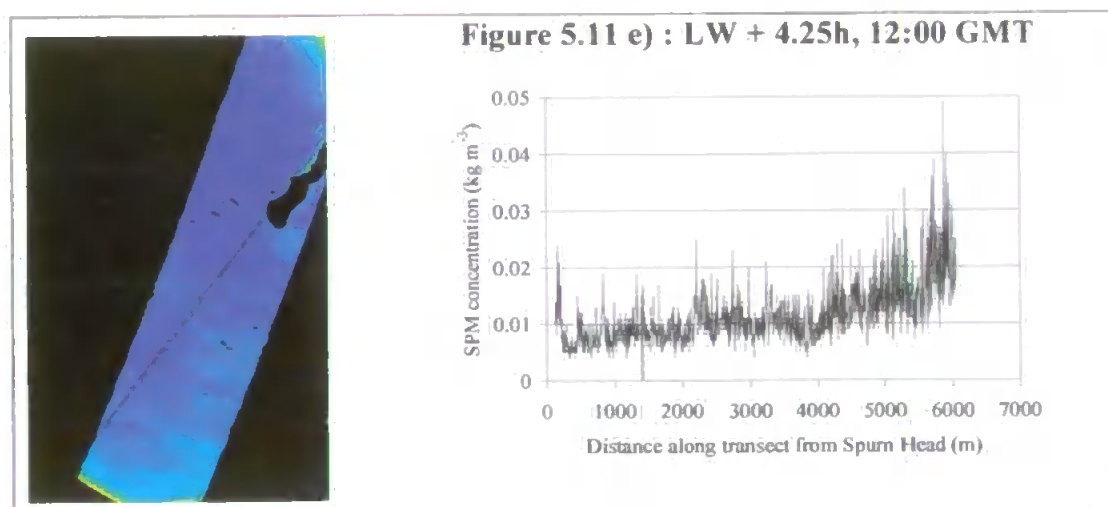
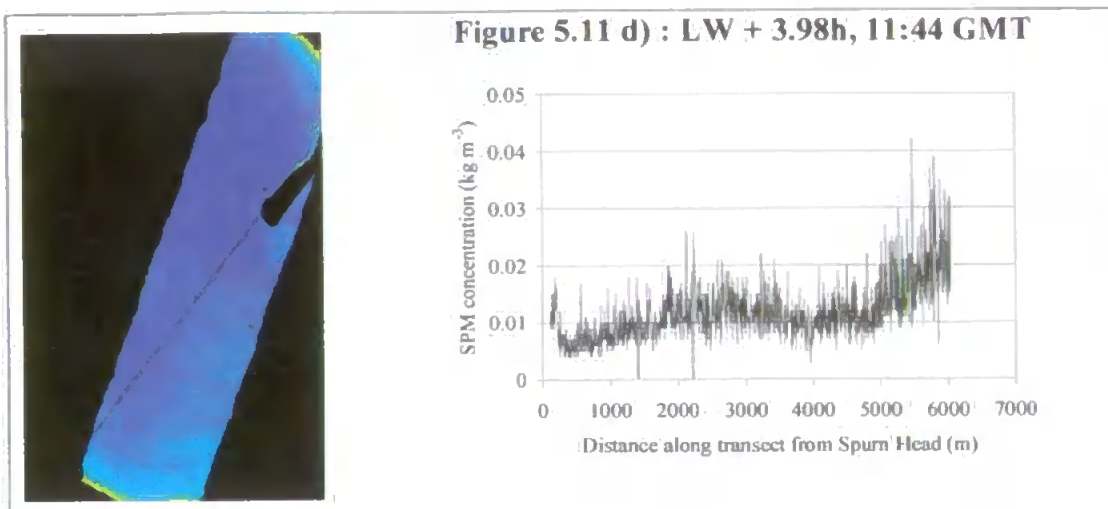
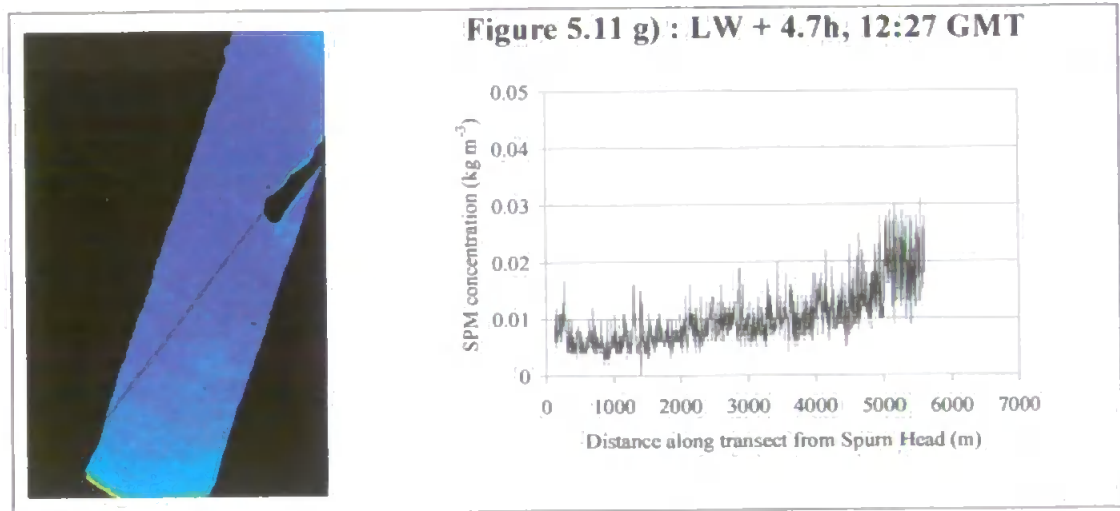




Figure 5.11 : SPM concentrations ( $\text{kg m}^{-3}$ ) derived from CASI images (left) acquired on 21 August 1995 during neap tide conditions. SPM concentrations ( $\text{kg m}^{-3}$ ) procured from a transect taken across the Humber mouth in accordance with the solid lines shown on the images (left) are detailed to the right. The x-axis corresponds to distance from Spurn Head with zero representing Spurn Head itself and 6825 m Tetney Haven.







The asymmetric nature of the concentration field across the Humber is clear from the cross-sectional transects and is especially apparent in figures 5.7, 5.9 and 5.10. Higher SPM concentrations were evident in the northern channels, and lower concentrations in the south, in the preceding few hours before low water (fig. 5.10) and also at and around low water itself (fig. 5.7 and 5.9). This mirrors the bathymetry relating to the cross-sectional transects (fig. 5.12). The northern channels are the deeper and it is here that the higher concentrations are found in the few hours before and at low water.

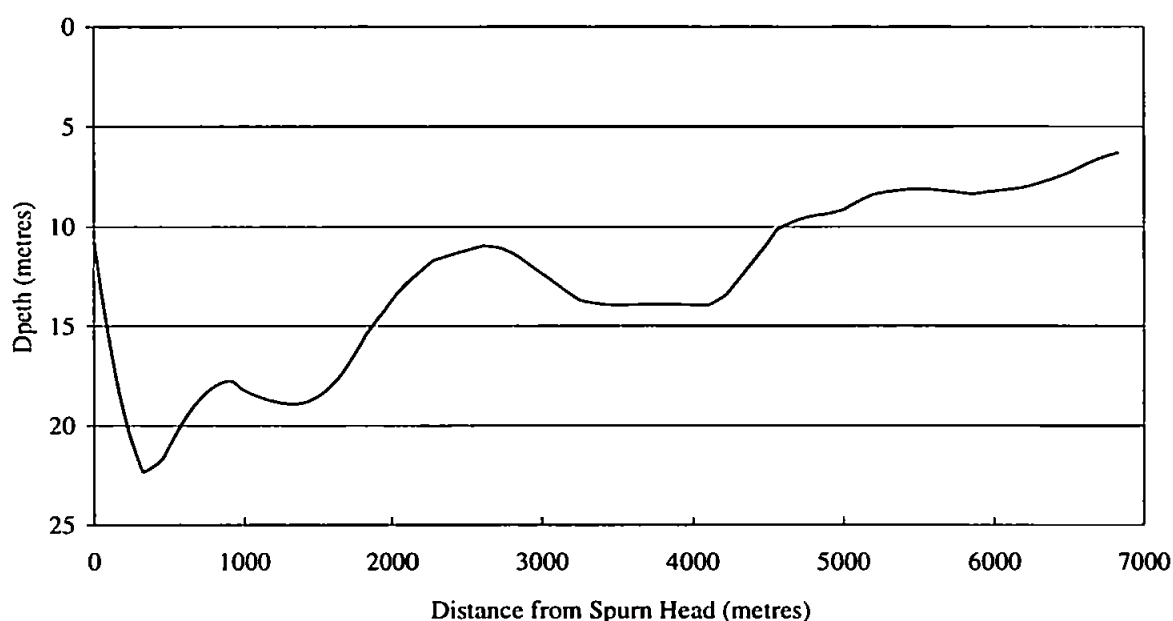


Figure 5.12 : Bathymetry across the Humber mouth derived from hydrographic charts and corresponding to the transects shown in figs. 5.7 - 5.11

SPM in the uppermost layers of the estuarine waters of the Humber are mainly fine grained. Median particle sizes range from 70  $\mu\text{m}$  to 110  $\mu\text{m}$  in the top few metres of the water column and probably comprise flocs of silt and clay and very fine sand (Uncles, R.J., *pers. comm.*). During the flood tide, fine particulate matter is resuspended as flow velocities increase. Sharp increases in SPM concentrations at various points across the transects can be particularly seen in fig. 5.8 from LW + 2.62h onwards. The patterns of resuspension are “streaky” at this stage of the flood tide and are probably influenced by the seabed distribution of sediment and by bedforms.

The places across the transects where concentrations drop to  $0 \text{ kg m}^{-3}$  indicate passage of the transect over a ship or mooring (N.B. the  $0 \text{ kg m}^{-3}$  at 1400 m always represents the Bull light float). These features are commonly preceded or followed by a sharp peak in SPM concentration due to the influence of the ship or mooring on the sediment dynamics in its locality. Figure 5.11 shows such features where in all but two images the transect passes over a ship (the  $0 \text{ kg m}^{-3}$  feature at 2200 m) and is immediately followed by a sharp peak in SPM concentration.

The stirring up of large quantities of SPM in the wake of a ship can also be distinguished. Visual inspection of the images identifies ships and their direction of travel and these can then be related to the transect plots. An example of this is found in fig. 5.8h at LW + 3.08h where a sharp peak that immediately followed a ship's passage is depicted as a feature at 2125 m. Concentrations here reach in excess of  $0.24 \text{ kg m}^{-3}$  (i.e. over twice the local background level) as water is stirred up from deeper in the water column by the ship's passage. This exemplifies the stratified nature of these waters and identifies the complex problem of modelling their sediment dynamics.

### **5.3.3 One-dimensional Fourier transforms of SPM concentration data**

The SPM concentration distribution across the Humber mouth is extremely patchy (figs. 5.7 - 5.11). The results highlighted in figure 5.6 show that SPM elongates into and out of the estuary across a transect spanning the mouth of the estuary. These fingers or jets of SPM have been nicknamed Snarks, after Lewis Carroll (Hadlington, 1995). The distribution of SPM concentration "patches" across the images were assessed by transforming the transect data into frequency space by the use of one-dimensional Fast Fourier Transforms (FFTs). The FFT is a numerical technique which enables the Fourier transform of a  $2^n$  (or  $2^n \times 2^n$ ) data series to be calculated efficiently by a computer. The FFT of each transect data series was accomplished through the use of signal processing tools within the Matlab PC software package. Matlab uses a fast Radix-2 FFT (see Krauss, *et al.*, 1994 for more details).

To increase the confidence level within the overall FFT estimate, the power spectrum estimate of a data sequence can be useful. This increases the number of Fourier transform estimates derived from the data series. Within Matlab this procedure is accomplished by

dividing the data into groups of  $m$  points ready to be FFTed. To ensure that the end points of each group is zero, and so reduce leakage into other frequencies, the data series is further windowed into groups of  $m/2$  points which overlap the original  $m$  points. Each windowed section is then FFTed and  $m/2$  Fourier estimates established which lie between zero and the Nyquist frequency ( $N_y$ ).

The 27 data series detailing SPM concentration along the Humber mouth transect were resampled to reduce / increase the number of points each dataset comprised so that they all contained 2048 ( $2^{11}$ ) data points. The data series were windowed into groups of 256 points with a further windowed overlap of 128 points. These groups of data points were FFTed and 128 Fourier estimates for each dataset attained. From these results the most frequently occurring SPM patch size in each dataset was sought. This was accomplished through knowledge that the frequency of the  $n$ th component is calculated by  $f = \frac{N_y}{n}$  and the period (or wavelength of patch) by  $p = \frac{1}{f}$ . The most frequently occurring SPM concentration patch size was related to the averaged surface velocity as derived from an hydrodynamic model (fig. 5.13). The surface velocities were calculated as values relating to that flow perpendicular to the Humber mouth transect which represents the predominant movement of water into and out of the estuary (this derivation is explained fully in section 5.4.1).

The relationship between the most frequently occurring SPM concentration patch size across the transect and the averaged surface velocity perpendicular to the transect was investigated further by attempting to fit a trendline to the data points depicted in fig. 5.13. The relationship the entire dataset has with surface velocity is non linear and the closest fit was found to be a polynomial one with the highest power of 5 for the independent variable and with an  $R^2$  of 0.44 (fig. 5.13). Although the relationship is poor there is obviously some dependence of patch size on surface velocity and hence tidal state. The images were acquired under different tidal conditions (i.e. at and between spring and neap tides) and so the relationship between patch size and tidal state will naturally not be a perfect one for this dataset.

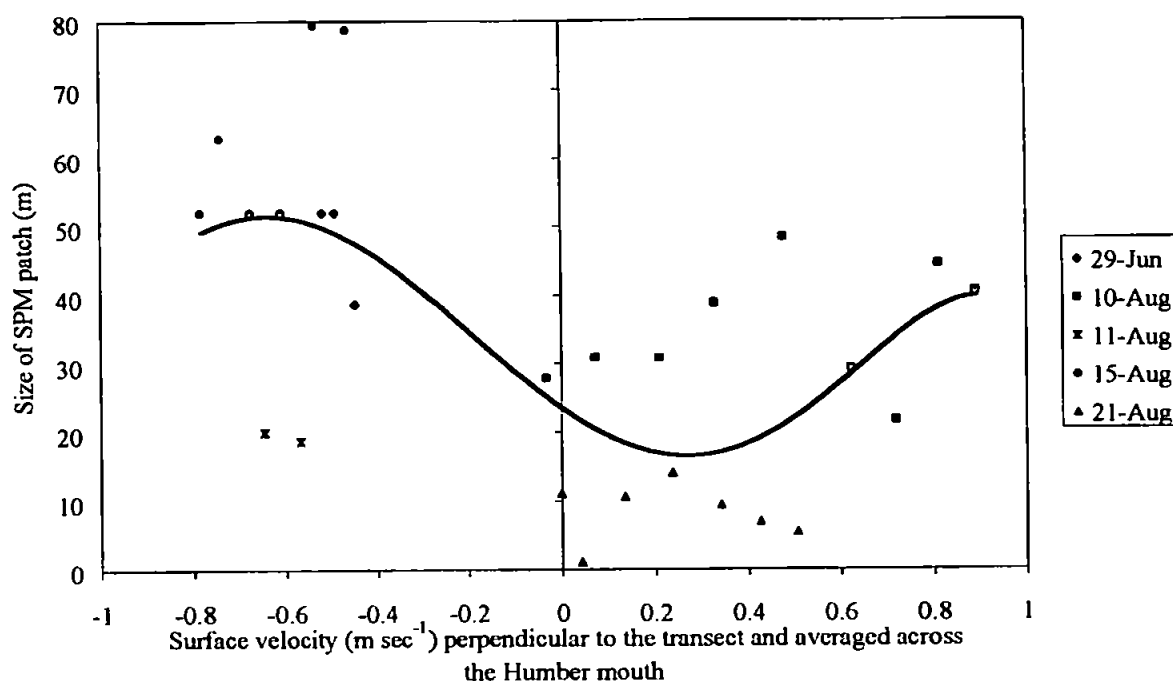


Figure 5.13 : Most frequently occurring SPM concentration patch size across each image related to the averaged surface velocity ( $\text{m sec}^{-1}$ ) into the estuary. The solid line represents a polynomial trendline fit to the data with the highest power of 5 for the independent variable. Data acquired during spring tidal conditions are represented in red, one day after springs in pink, four days after springs in green, and during neaps in blue.

## 5.4 SPM flux

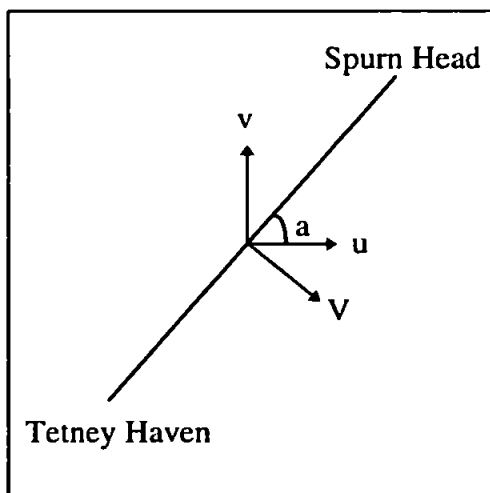
The accurate estimation of flux is important for the effective management of estuaries and the coastal zone from both environmental and socio-economic perspectives (Jay *et al.* 1997). The impact of anthropogenic influences on estuarine environments, the prediction of long-term change and the mechanism behind this change can only be achieved through flux estimation and assessment. SPM flux estimation is particularly important in the Humber Estuary due to the extremely mobile nature of the vast quantities of sediments contained within its waters. High SPM concentrations are supported by large flow velocities.

Previous studies have been largely limited by the calculation of flux at a single point only due to the limited spatial coverage of most surface-based monitoring exercises. Lane *et al.* (1997) identify that 'accurate flux calculations require consistently high spatial and temporal resolution across the cross section'. The use of remote sensing provides the

temporally instantaneous spatial resolution, but direct velocity measurements are normally sparse. Assessment of SPM fluxes can be made through the incorporation of hydrodynamic models, which estimate flow velocities and direction. This is an important application for operational coastal remote sensing as it reduces the need for costly and time-consuming surface-based monitoring.

#### 5.4.1 Calculation of SPM flux

The calculation of SPM flux needs to take into account the hydrodynamics of flow in three dimensions. The Depth Integrated Velocities And Solute Transport (DIVAST) hydrological model (Falconer and Owens, 1990) was used to model depth-averaged flows in the Humber Estuary. The DIVAST model outputs north and east velocity components for the estuary in coarse 1 km grid cells. This information was resampled for the transect across the mouth of the estuary to achieve velocities for each 2.5 m pixel. Depth-averaged velocity vectors perpendicular to the profile across the Humber mouth were then determined (fig. 5.14).



$$V(\text{seawards}) = u \sin a - v \cos a$$

$u$  &  $v$  are the east & north velocity components respectively,

$V$  is the depth-averaged velocity perpendicular to the transect across the Humber mouth, and  $a$  is the angle describing the transect.

Figure 5.14 : The derivation of depth-averaged velocity vectors perpendicular to the transect across the Humber mouth

The product of the resultant depth-averaged velocities into the estuary and image-derived SPM concentrations provide an estimate of surface SPM flux for each point along the profile. Total SPM flux was then estimated for each point by integrating these results with depth as derived from hydrographic charts (fig. 5.12). Tidal heights at the times of data acquisition were ascertained from Admiralty tide tables to calculate the area of water per



unit of cross-sectional distance present at each point across the transect. The published tidal heights are relative to chart datum and these were converted to heights relative to ordnance datum through the knowledge that chart datum at Spurn Head is 3.9 m above ordnance datum. Total SPM flux, assuming a uniform concentration with depth, was then calculated as the product of surface SPM concentration, depth averaged velocity and bathymetry ( $\pm$  tidal height relative to ordnance datum). Figure 5.15 - 5.19 show SPM fluxes in  $\text{kg m}^{-1} \text{s}^{-1}$  calculated for each transect (i.e. corresponding to figs. 5.7 - 5.11 respectively).

Figure 5.15 : SPM fluxes ( $\text{kg m}^{-1} \text{s}^{-1}$ ) into the Humber Estuary along each transect as derived from CASI images acquired on 29 June 1995. Positive values indicate flux into the estuary and negative out into the North Sea.

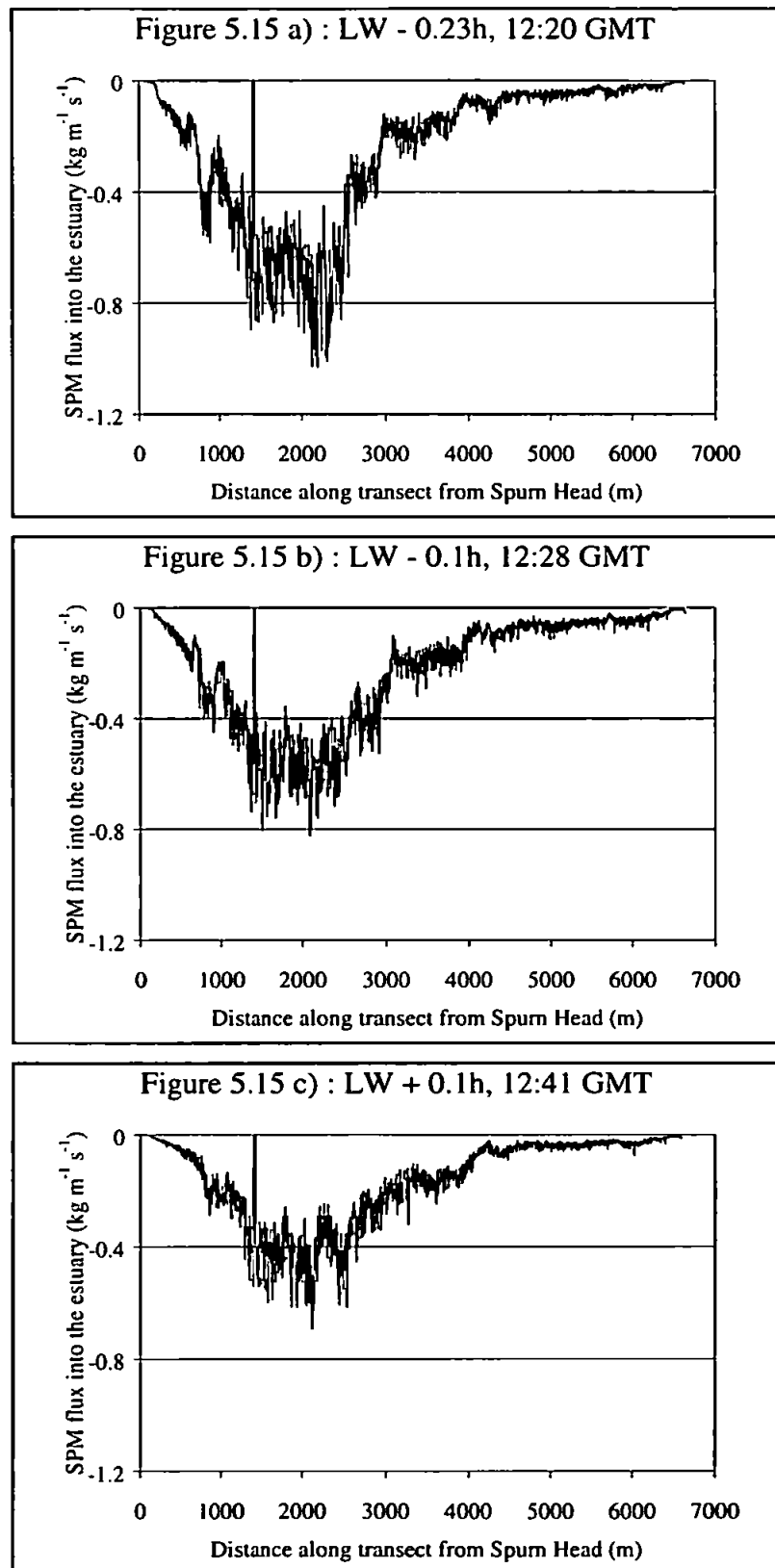


Figure 5.16 : SPM fluxes ( $\text{kg m}^{-1} \text{s}^{-1}$ ) into the Humber Estuary along each transect as derived from CASI images acquired on 10 August 1995. Positive values indicate flux into the estuary and negative out into the North Sea.

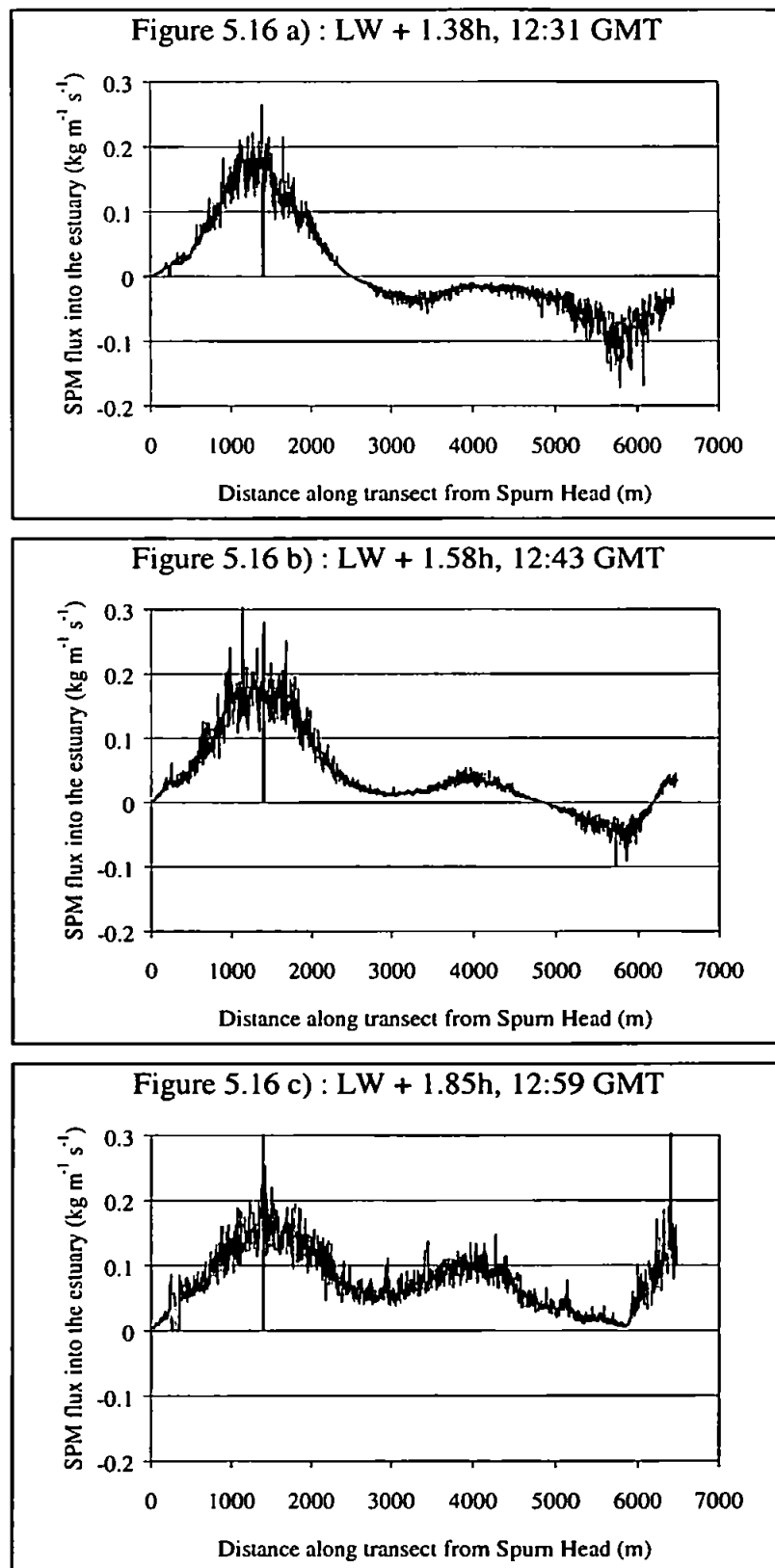


Figure 5.16 d) : LW + 2.07h, 13:12 GMT

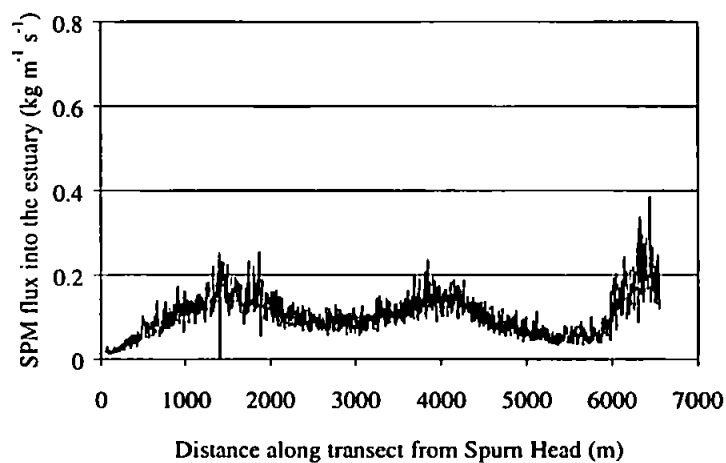


Figure 5.16 e) : LW + 2.35h, 13:29 GMT

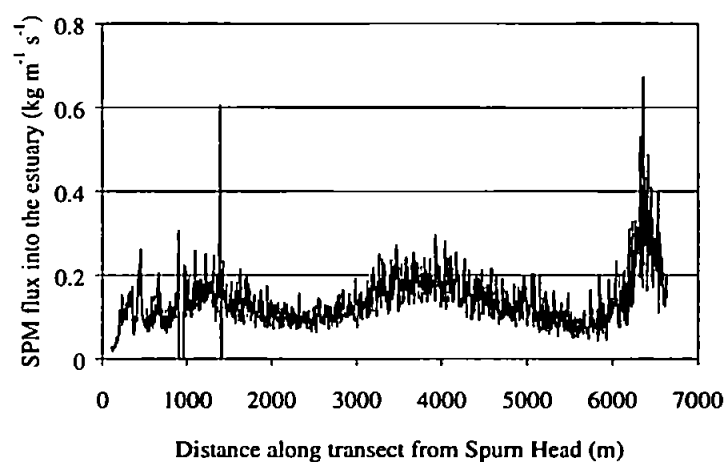


Figure 5.16 f) : LW + 2.62h, 13:45 GMT

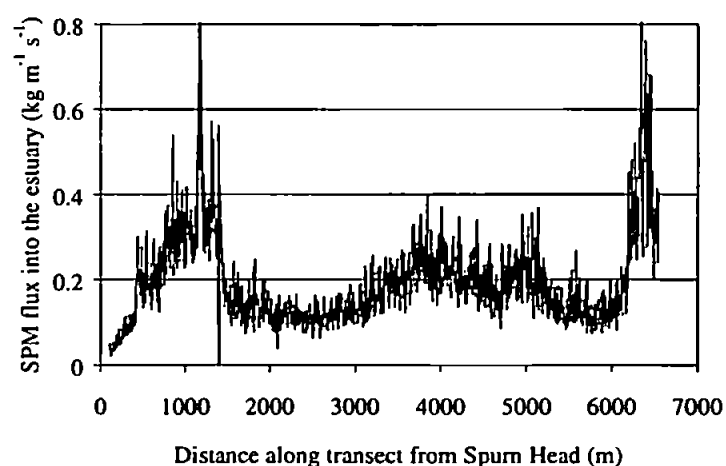


Figure 5.16 g) : LW + 2.83h, 13:58 GMT

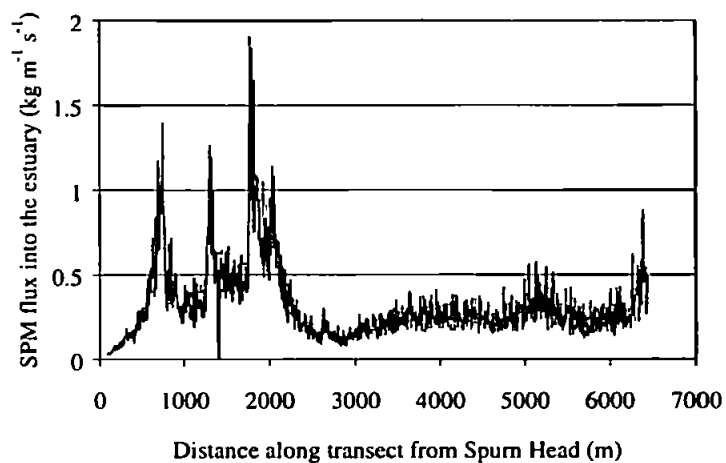


Figure 5.16 h) : LW + 3.08h, 14:13 GMT

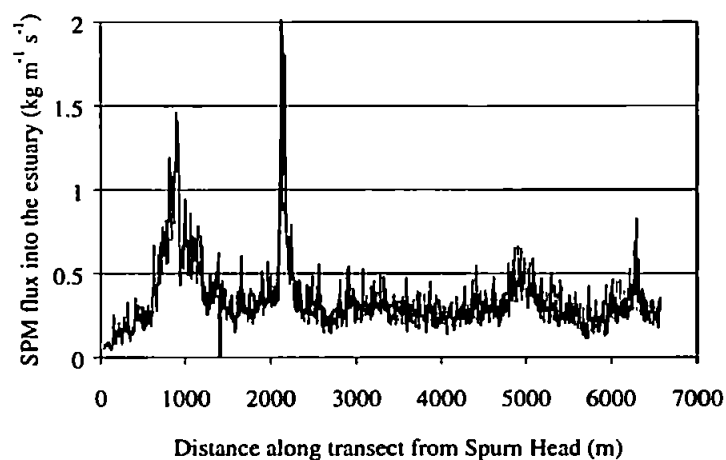


Figure 5.16 i) : LW + 3.33h, 14:28 GMT

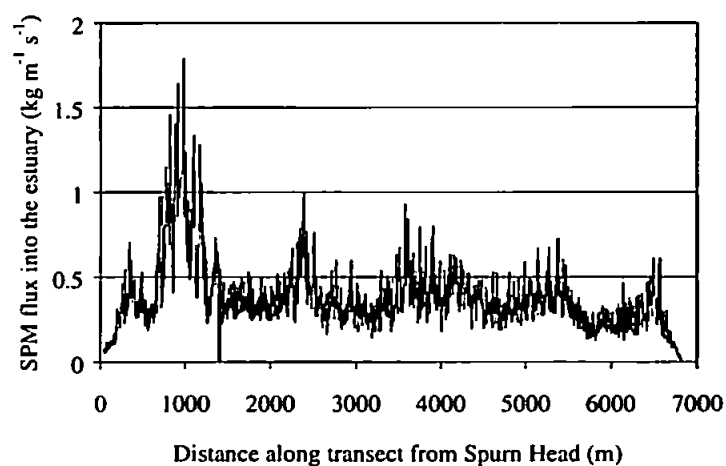


Figure 5.17 : SPM fluxes ( $\text{kg m}^{-1} \text{s}^{-1}$ ) into the Humber Estuary along each transect as derived from CASI images acquired on 11 August 1995. Positive values indicate flux into the estuary and negative out into the North Sea.

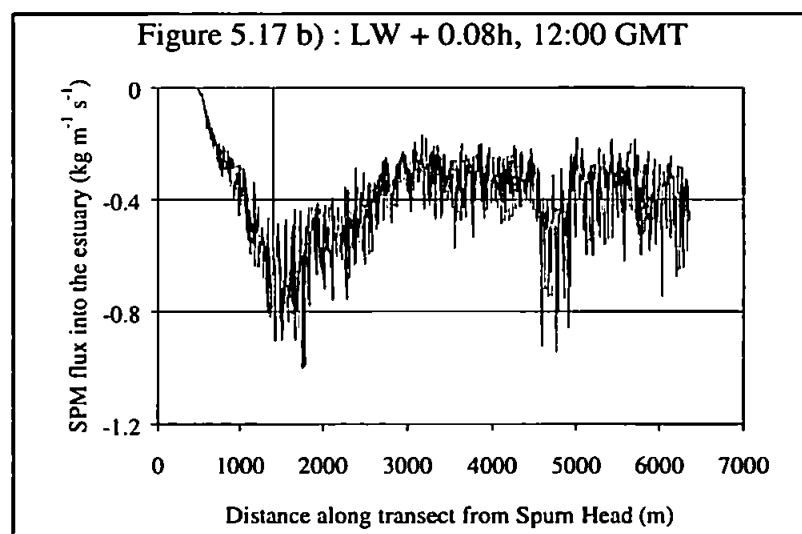
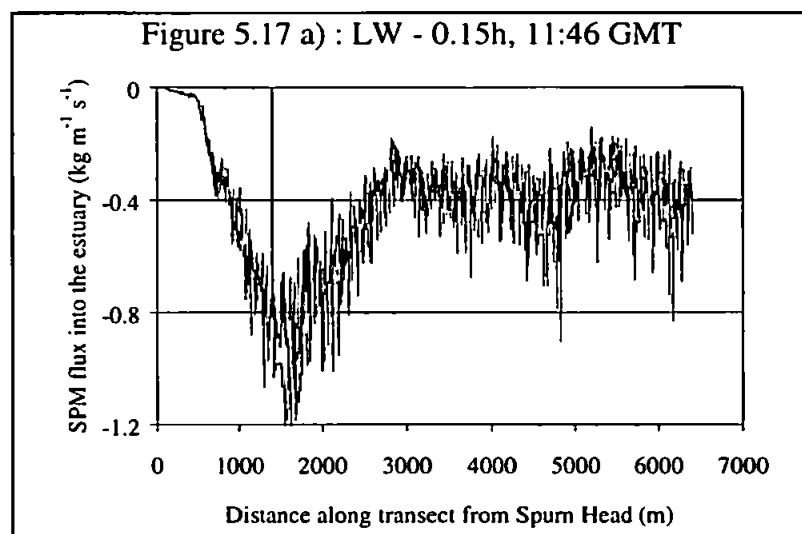


Figure 5.18 : SPM fluxes ( $\text{kg m}^{-1} \text{s}^{-1}$ ) into the Humber Estuary along each transect as derived from CASI images acquired on 15 August 1995. Positive values indicate flux into the estuary and negative out into the North Sea.

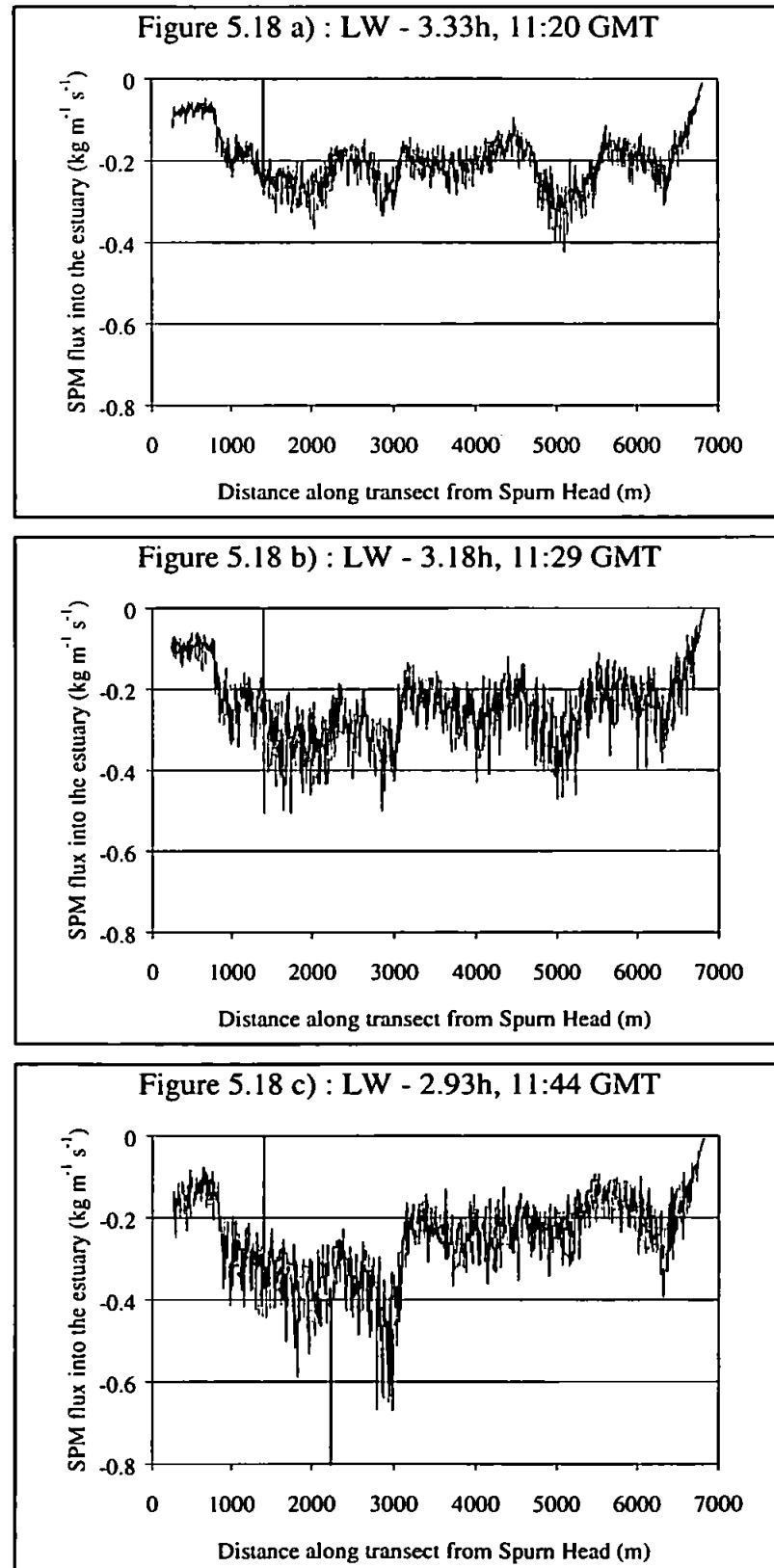


Figure 5.18 d) : LW - 2.7h, 11:58 GMT

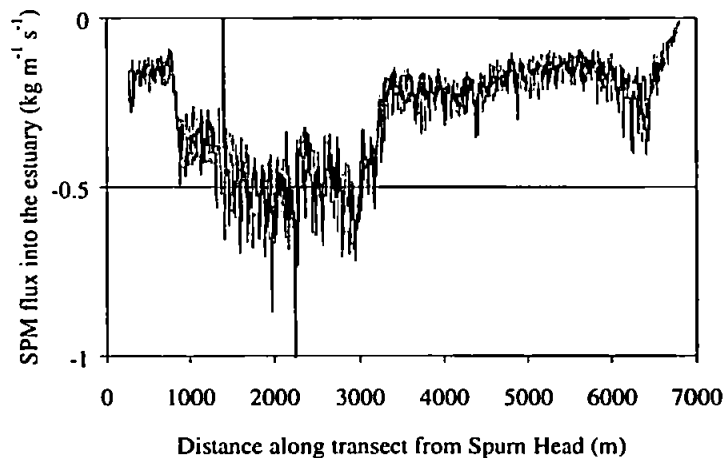


Figure 5.18 e) : LW - 2.43h, 12:14 GMT

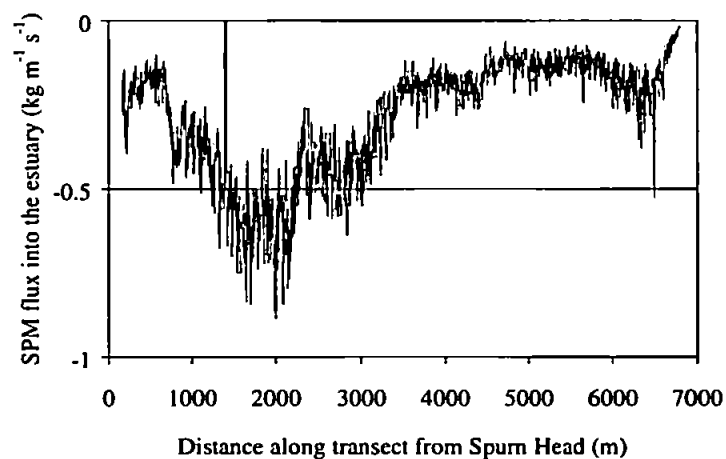


Figure 5.18 f) : LW - 2.17h, 12:30 GMT

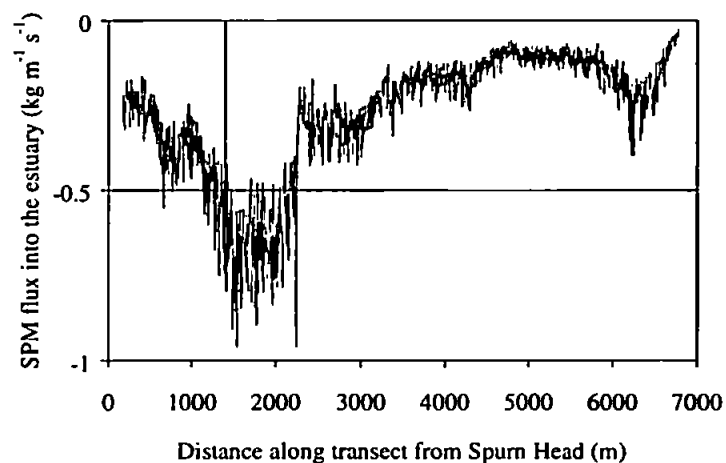




Figure 5.19 : SPM fluxes ( $\text{kg m}^{-1} \text{s}^{-1}$ ) into the Humber Estuary along each transect as derived from CASI images acquired on 21 August 1995. Positive values indicate flux into the estuary and negative out into the North Sea.

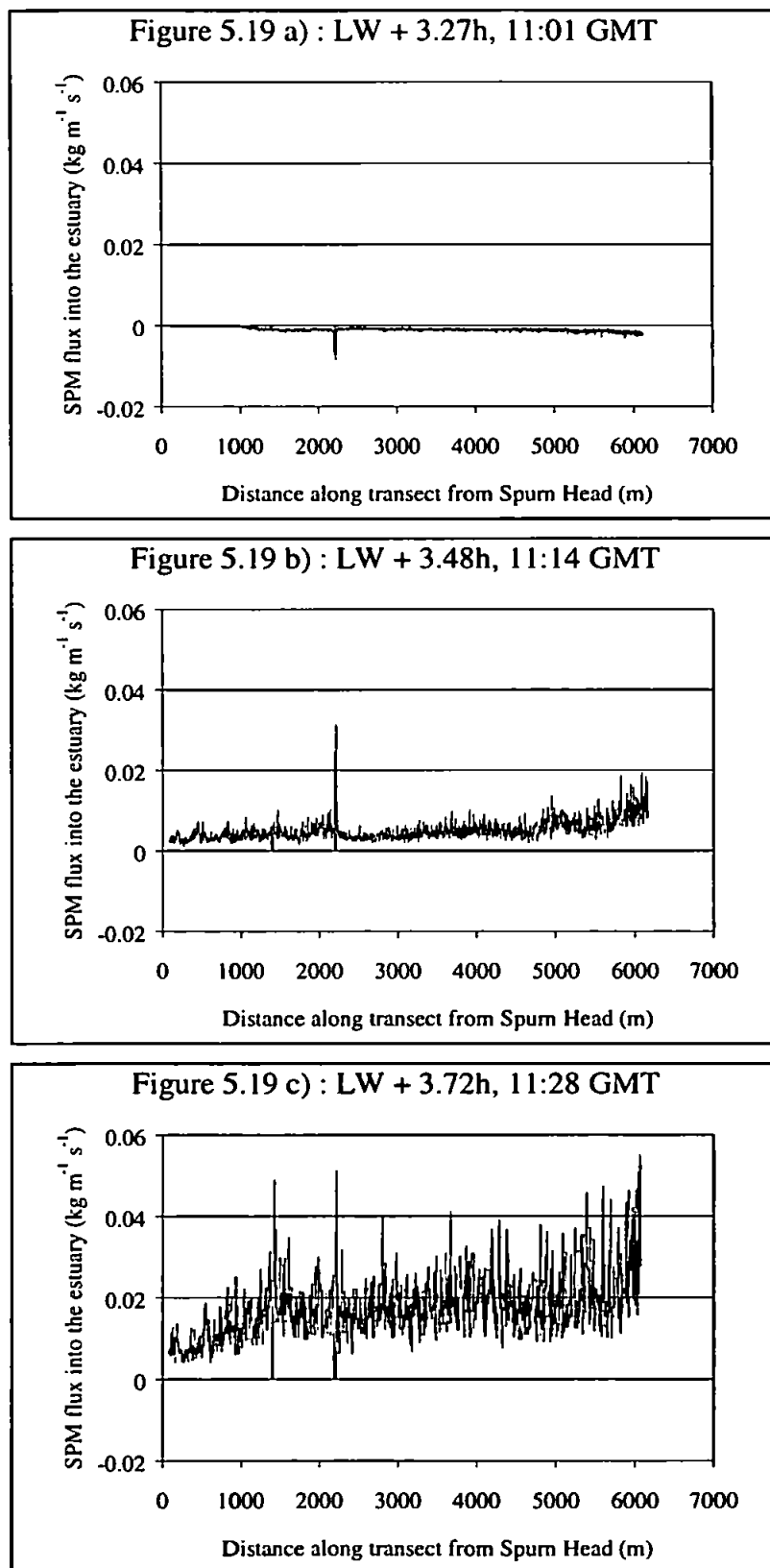


Figure 5.19 d) : LW + 3.98h, 11:44 GMT

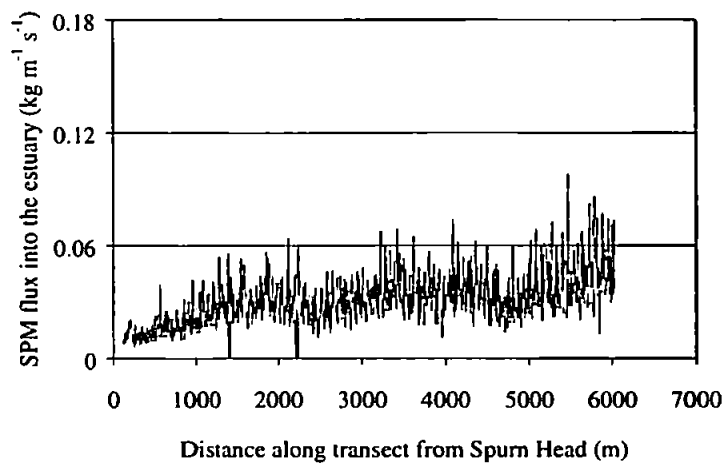


Figure 5.19 e) : LW + 4.25h, 12:00 GMT

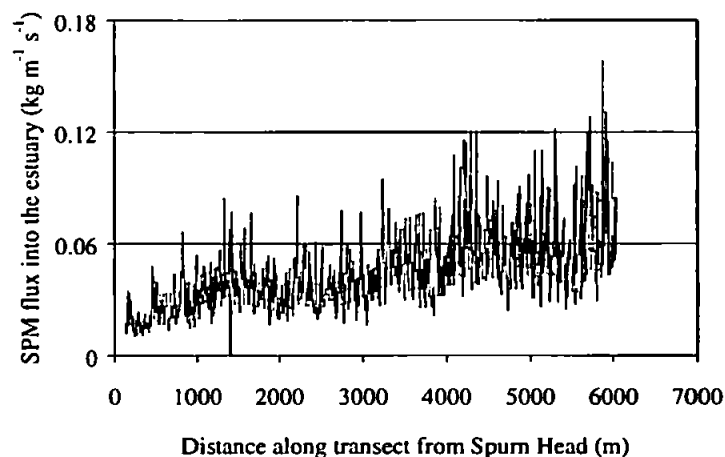
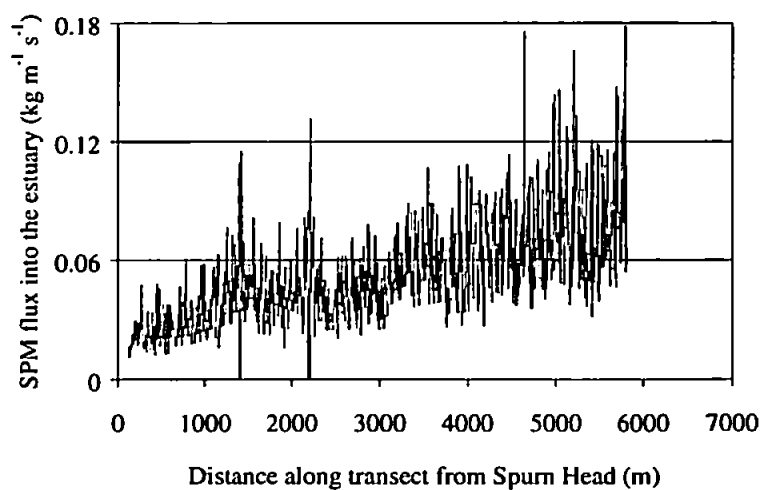
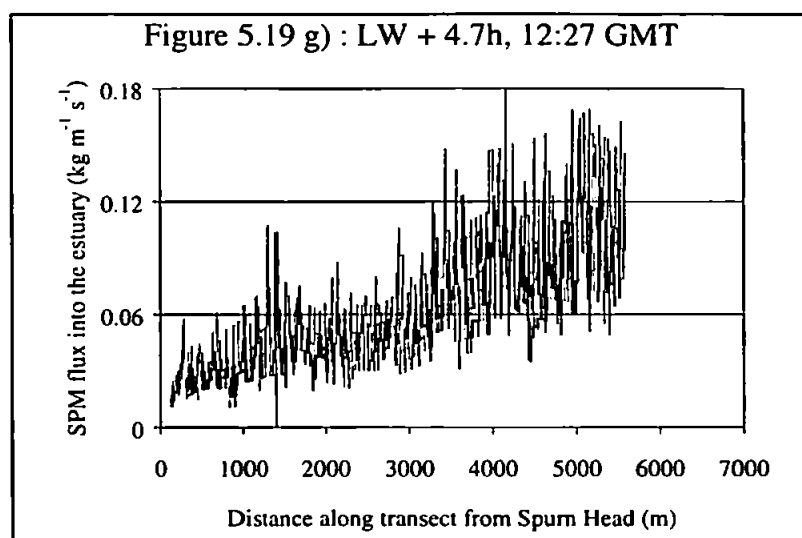


Figure 5.19 f) : LW + 4.48h, 12:14 GMT





### 5.4.2 Possible errors in SPM flux calculation

Field measurements acquired in the region of the Humber mouth have shown that SPM concentrations are highly stratified vertically down through the water column and increase with depth. Figure 5.20a shows a depth profile of SPM concentrations taken approximately 600 m to the west of Spurn Head (Uncles, R.J., *pers. comm.*). This increase with depth corresponds inversely to the Van-Veen profile (fig. 5.20b) where water velocities are shown to characteristically decrease towards the bed as SPM concentrations increase. SPM depth profiles will also vary with sediment and bedform type and slope and with current speed. The Rouse equation (e.g. Dyer, 1986) was fitted to the measured SPM depth profile. The equation describes concentration variation with depth as:

$$\frac{C_z}{C_a} = \left( \frac{a}{z} \right)^B \quad (5-7)$$

where  $C_z$  and  $C_a$  are SPM concentration at a height  $z$  and at a reference height  $a$  respectively, and

$$B = \frac{w_s}{\beta \kappa u_*}$$

where  $\beta$  is the ratio of the eddy diffusion coefficient for the sediment to that for the fluid (assumed to be 1; Dyer, 1986),

$\kappa$  is von Karman's constant (taken to be 0.4; Dyer, 1986),

$w_s$  is the settling velocity, and

$u_*$  is the friction velocity.

Surface velocities were averaged across the Humber mouth for each data series. These averaged values show the range of velocities experienced over the different stages of the tide (fig. 5.21). Velocity minima are reached shortly after LW + 1h during spring tides but, under neap conditions, this is achieved about two hours later at LW + 3h. Averaged surface velocities ranged from 0 to 0.9 m s<sup>-1</sup> with velocities reaching over 1 m s<sup>-1</sup> in some cases, particularly in the northern channels of the estuary. These large velocities coincided with the resuspension of sediment in these deeper channels. Using this information it was possible to justify the assumption that, in the case of the Humber Estuary,  $\frac{w_s}{u_*}$  (in equation

5-7) will be small due to the dominance of fine silts and clays in a fast flowing

environment. An initial estimate of 0.1 for  $\frac{w_s}{u_*}$  was taken and then iteratively changed to fit the Rouse equation (equation 5-7) to the measured SPM profile (fig. 5.20a).

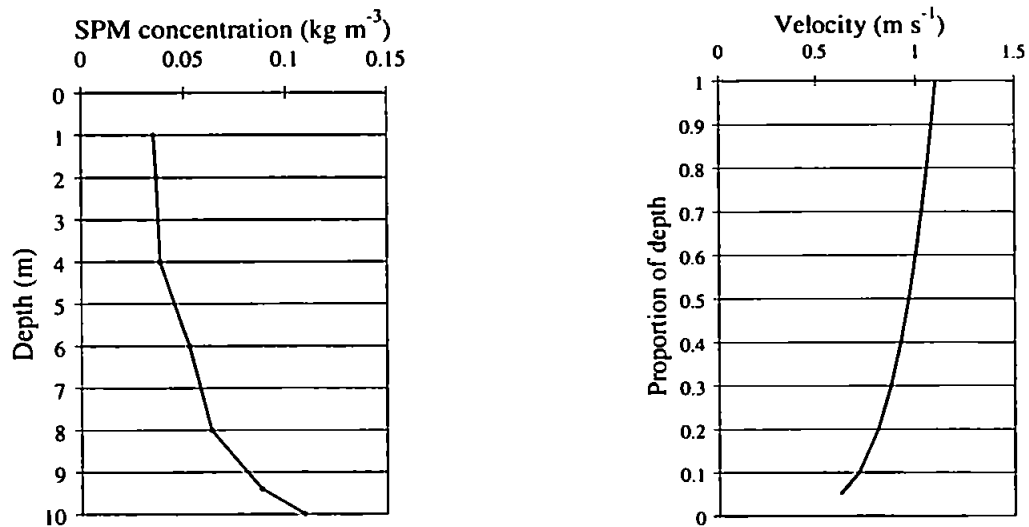


Figure 5.20a (left) : A typical depth profile of SPM concentrations acquired approximately 600 m to the west of Spurn Head at Hawke (Uncles, R.J., *pers. comm.*)

Figure 5.20b (right) : Van-Veen profile showing the variation of water velocity with depth (e.g. Uncles and Jordan, 1994)

A final value of 0.5 was derived for  $B$  in equation 5-7. Using this value in equation 5-7, the measured SPM concentrations (fig. 5.20a) were integrated with depth and a total concentration for the entire profile of 0.471 kg m<sup>-3</sup> derived. If the surface SPM concentration value taken from fig. 5.20a is assumed to be a constant with depth, and  $B$  again taken as 0.5 in the Rouse equation, a total concentration of 0.315 kg m<sup>-3</sup> is obtained. Thus in this example, the assumption of uniform SPM concentration with depth provides an estimate that is in error by 33%. However, in the absence of reliable models that describe SPM concentrations down through the water column during the measurement period and over the study site, a uniform concentration with depth has been assumed here. The limitations of this assumption must be recognised and the possible errors in the calculation of fluxes appreciated.

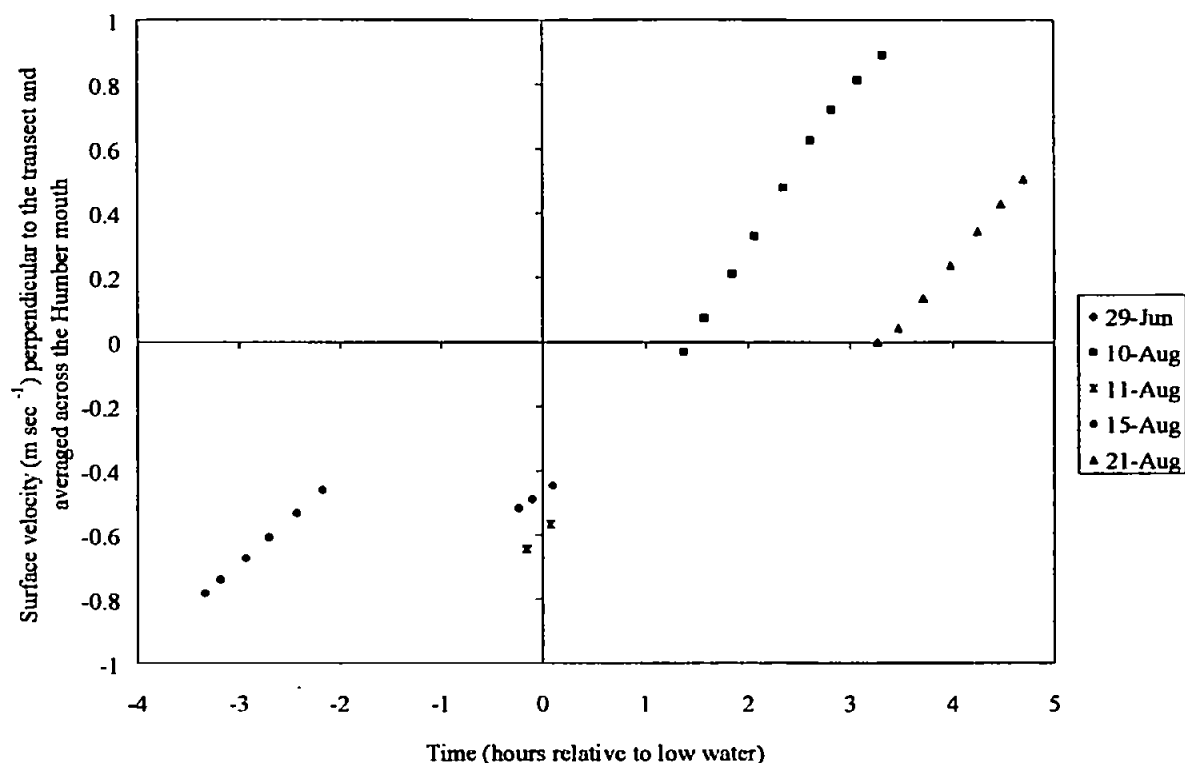


Figure 5.21 : Surface velocities ( $\text{m sec}^{-1}$ ), derived from the DIVAST model, averaged across the Humber mouth transect for each of the 27 datasets. Data acquired during spring tidal conditions are represented in red, one day after springs in pink, four days after springs in green, and during neaps in blue.

### 5.4.3 SPM fluxes in the Humber Estuary

The SPM fluxes into and out of the estuary were estimated by calculating the area under the transect curves (i.e. figs. 5.15 - 5.19). This enabled the comparison of the flux estimates at the different tidal states (fig. 5.22).

By integrating throughout the observed time sequences, an estimate of SPM flux for each section of the tide can be estimated (fig. 5.23). Although the survey dates did not cover the range of dates and times which would extend the study across the full tidal cycle and over all spring and neap tidal conditions (table 3.4), it is still possible to appreciate the nature of SPM flux in the Humber Estuary.

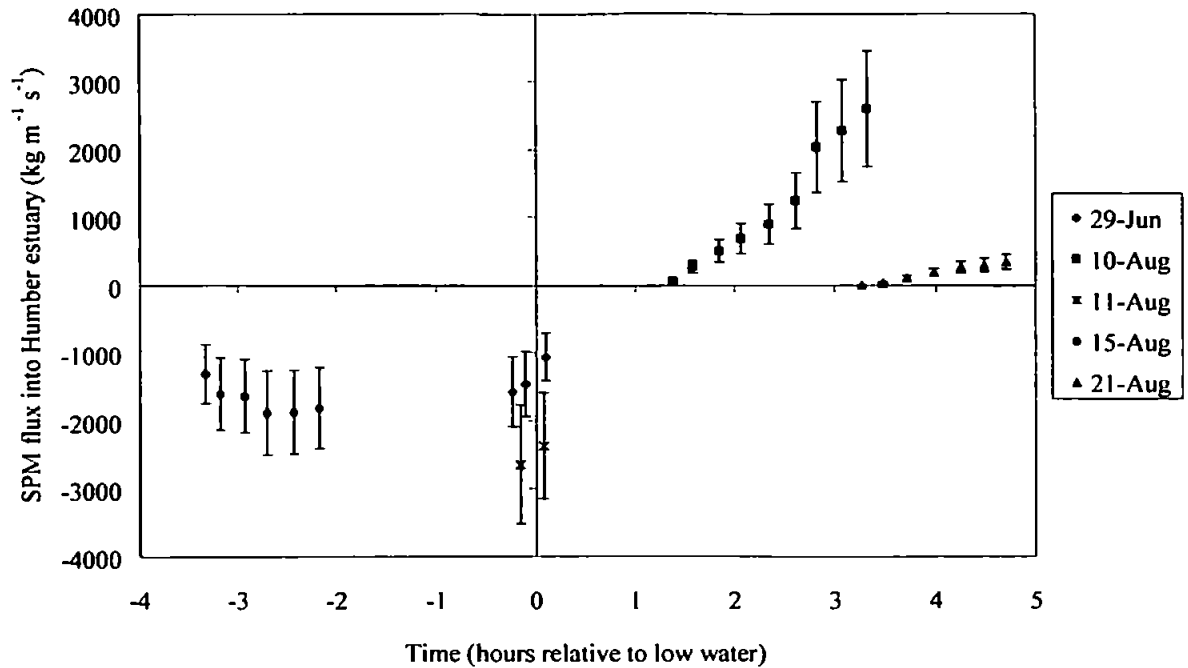


Figure 5.22 : Total SPM flux into the estuary ( $\text{kg m}^{-1} \text{s}^{-1}$ ) for each dataset covering the five days of survey. Data acquired during spring tidal conditions are represented in red, one day after springs in pink, four days after springs in green, and during neaps in blue. The error bars represent the  $\pm 33\%$  uncertainty in the flux calculations.

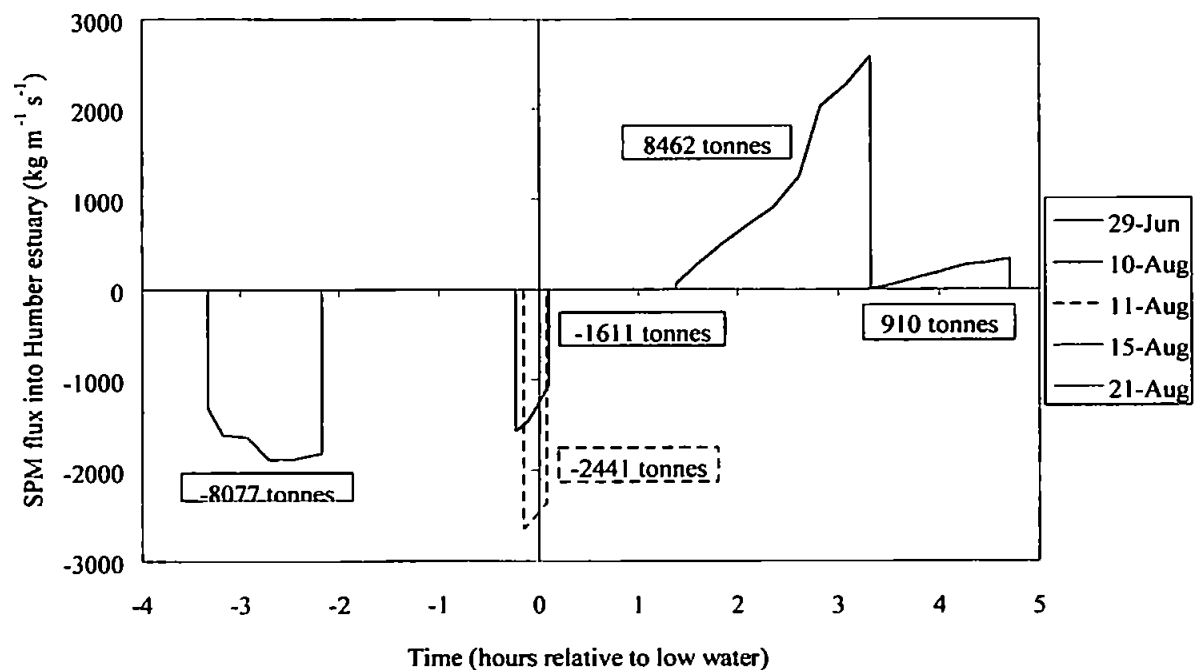


Figure 5.23 : Total SPM flux into the estuary ( $\text{kg m}^{-1} \text{s}^{-1}$ ) for each dataset covering the five days of survey. The total flux integrated for each survey has been calculated as the area under the curve and is specified in the related text boxes.

## 6 Discussion

Remote sensing has a useful and important role to play in coastal and estuarine studies. An aircraft is a more flexible platform than a satellite upon which to mount remote sensing instrumentation. The response time to good weather is quicker from the air and the data turnaround is also much faster. The instrumentation can be directed over whichever target may be necessary at any time within the aircraft's constraints. This flexibility is not readily available from space and the aircraft's synoptic coverage not obtainable from surface-based monitoring.

The CASI has been shown to be an extremely useful tool in the monitoring and quantification of the coastal and estuarine environment. In particular its use in conjunction with continuous surface-based measurements at a few key locations, from, for example, buoys, has proven to be both effective and enlightening. The programmable bandwidths available to the operator mean that the instrument can be customised for different environments to highlight certain features in response to the hypotheses underlying the campaign. The NERC ARSF routines ensure that the data are adequately and easily radiometrically calibrated. The atmospheric correction routines employed within the COAST software did not fully atmospherically correct the image data as required. Comparisons with measured water-leaving radiance identified the shortcomings within the software. Rayleigh corrected images were also output from COAST and the algorithms used in their determination deemed correct through comparison with coincidently measured datasets. The Rayleigh corrected images were used in the further processing stages. However, this may not always be justified as the target area is located close to heavy industry. An excess of particulates within the atmosphere could increase the effects of aerosol scattering to such a degree that the Rayleigh correction of image data might not be sufficient and a full atmospheric correction would be imperative.

The SPM ratio algorithm has been shown to perform well with the data acquired during this study ( $R^2$  of 0.952; section 4.2.3.1). However, there were no independent datasets available with which to execute a thorough comparative analysis. The use of the SPM algorithm with other similar datasets over this stretch of the estuary must be viewed with



some caution as conditions over and within the water must be similar. Such algorithms are not fully portable in space as the characteristics within the water can radically change from place to place, as can the general atmospheric environment through which the light passes from the water's surface to reach the sensor. If, for example, the levels of chlorophyll reach a state whereby they effect the results output from the SPM ratio algorithm, they would need to be accounted for and quantified separately within the algorithm. The algorithm was portable over the datasets used here and has been proven to give good results when compared to data acquired from the water's surface ( $R^2$  of 0.952, section 4.2.3.1).

The ATM has been shown here and in other studies (e.g. Callison *et al.*, 1987) to be useful when investigating sea-surface temperature (section 4.2.3.2). The emissivity of the water's surface is the unknown which must be assumed. The assumption of a constant emissivity was made and the sea-surface temperatures resulting from this matched the measured results well. In the case of the Tweed estuary where measurements were taken from a vessel located within the estuary, it was possible to apply the measured temperature / salinity relationship to the image data. The salinity images allow further insight into the estuary's characteristics and dynamics. However, this procedure would be difficult to replicate elsewhere and / or for a different survey period without supplemental sea-truth measurements.

## 6.1 Water classification and $K_d(490)$

Water classification is important for the characterisation of the optical properties of the target aquatic medium. Jerlov's (1976) water classifications work well for wavelengths less than 555 nm (section 5.1). For 670 nm and 700 nm the trend lines differ from Jerlov's ideal (fig. 5.1b). This is probably due to the extreme SPM laden nature of the waters in and around the Humber Estuary. The classification can be refined by using the  $z_{90}$  measure (equation 2-15) which delineates the maximum depth to which most (90%) of the light penetrates. Morel & Prieur's (1977) coarser classification is insufficient for detailed work within coastal and estuarine waters but does provide a general demarcation of the coastal and oceanic water margins.

An algorithm for  $K_d(490)$  based on Austin & Petzold (1981)'s theory developed in case *I* waters is missing from the literature for the case *II* scenario. The Mueller & Trees (1996) algorithm (equation 5-2) also describes case *I* but not case *II* waters.  $K_d(490)$  values have been shown to increase exponentially away from their linear regression line and a new algorithm has been devised to describe the conditions in turbid case *II* waters (equation 5-4) that hitherto have not been addressed. The new algorithm has been developed for use where SPM concentrations lie between 0.44 and 34.06 mg m<sup>-3</sup> and chlorophyll concentrations between 0.46 and 12.05 µg m<sup>-3</sup>. As conditions become even more sediment laden, a further algorithm may be required to describe these more extreme situations.

## 6.2 Possible errors in the data processing

Many of the image processing stages involve the unavoidable inclusion of errors within the procedures employed. These were limited to a minimum where possible by maintaining rigorous equipment calibration procedures although errors will still be present within the data streams. These may vary from a minimum error of 1% in the calibration of the PML-Satlantic to over 10% in the radiometric calibration of the ATM. Surface-based data acquisition was executed in accordance with NASA's SeaWiFS protocols (Mueller & Austin, 1995) to minimise any contamination from external sources and errors in the datastream. From the air, a set of guidelines were followed prior to, during and after airborne data acquisition. Once the image data had been procured, it was compared at each stage of the processing chain to the results obtained from the in-water optical measurements and to discrete samples acquired from the sea surface. The algorithms devised for SPM (in the Humber), temperature and salinity (in the Tweed) were compared to sea-based measurements. The Tweed data comprised measurements taken from a small vessel and the Humber from the Bull Light Float. These both only constitute a single test site within an image which relate to a few pixels only. Care was taken to identify the relevant section of the image and a group of pixels was then interrogated to derive the mean and standard deviation values for that particular target. This ensured that no anomalies were picked up and reduced the effects of any noise within the data streams. However, errors within the data may still be present and were found to range from 1% - 15% depending on how uniform the target waters were. Relating the relationship between the images and those measurements acquired from the sea surface to the much larger

image picture inevitably introduces additional unquantifiable errors. This is, however, unavoidable due to the commonly experienced lack of available surface-based test sites to relate to the remotely sensed image which itself covers a large expanse of water. Ultimately this highlights the unique nature of remotely sensed imaging which provides fully spatial information not available through surface monitoring.

The waters of the Humber Estuary are known to be highly stratified at times and the example of SPM concentration with depth (fig. 5.20a) highlights the possible error in using uniform concentration with depth in SPM flux estimations. Using the Rouse equation (equation 5-7) the error has been estimated to be possibly as much as 33% (section 5.4.2). The DIVAST model used to derive current velocities, and hence estimate fluxes, across the estuary for the surveyed times must also be queried. The model is relatively coarse and, to achieve a unique set of values corresponding to each imaged data point across the estuary, interpolation was necessary. This does not therefore account for any small scale variations in velocity structure induced from small scale bathymetric features and could cause the flux estimates to be in error. A finer resolution three-dimensional model of the Humber Estuary would be a better information source and, with the subsequent development of such models within the extended LOIS framework, any future analysis of this nature should not be hampered by such issues.

Although the possible errors in the flux quantities calculated here could be as much as 33%, the data clearly shows the tidal patterns and the order of magnitude of SPM fluxes that pass into and out of the Humber Estuary (figs. 5.22 and 5.23). This is something that has hitherto not been quantified on the spatial and temporal scales seen here. One such example of the information available is the magnitude of the difference between the SPM fluxes experienced at neaps to those under spring conditions. Very low flux estimates were found during the neap tide in comparison to the spring. The difference in the lag time between low water and the take-off of the flood into the estuary is also apparent with an approximate two hour difference between spring (flood begins approximately 1.5 hours after low water) and neap (flood begins at approximately 3.5 hours after low water) conditions.

### 6.3 Verification of the flux estimates

To test the reliability of the SPM flux calculations, related flux estimates were sought in the literature. Annual flux quantities and budgets were readily available such as those detailed in McCave (1987). However, it would not be justified to extrapolate the flux estimates from this study to an annual estimate of SPM flux as the data was acquired over a relatively sparse array of tidal states. The impossibility of achieving an annual flux estimate is exemplified by the results from 29 June and 11 August. Both surveys covered a period at and around low water during spring tides. These two similar tidal conditions generated flux estimates which differed approximately 1.5 fold across the surveyed time frame. The dates are almost two months apart and this result may exemplify the seasonal nature of SPM fluxes into and out from the estuary and that fluxes probably increase as summer progresses into autumn. The spring and neap cycles are also very important in that fluxes estimated during a spring tide will be inherently dissimilar to those acquired at the same stage of the tide but during neap conditions. Weather, e.g. heavy rainfall, high winds, storms along the Holderness coast, etc., must also play a factor in the actual quantity of flux moving across the Humber mouth although its actual role cannot be assessed for this study due to a lack of information. One would thus need a complete annual coverage of image data to achieve a truly accurate annual flux estimate.

Hardisty & Rouse (1996) detail preliminary work into flux monitoring across the Humber Estuary undertaken within LOIS. Their figures quantify SPM fluxes into the estuary averaged for spring and neap floods and ebbs. This is itself a questionable action given the finding laid out in the previous paragraph detailing the dramatically different results found for two similar low water spring tidal conditions. Hardisty & Rouse (1996) calculated that during springs the average flux on the flood is  $165 \times 10^3$  tonnes and on the ebb is  $77 \times 10^3$  tonnes. During neaps they calculated the flux on the flood to be  $162 \times 10^3$  tonnes and on the ebb  $94 \times 10^3$  tonnes. They also quote an averaged flood and ebb figure of  $120 \times 10^3$  tonnes calculated by Pethick (1994) which ties in well with their results. A comparative result of  $100 \times 10^3$  tonnes per flood tide was published in the Independent newspaper (Hadlington, 1995). The figures vary slightly and all are averaged across the entire flood or ebb tide, in the case of Pethick (1994) across both. The quantities calculated here (fig. 5.23) do not span the entire section of either flood or ebb tides. It is impossible, therefore, to compare the results directly.

Due to the lack of other flux data acquired from either conventional sea-surface measurements or from better models of the estuary, it was not possible to conclusively verify the flux quantities depicted in figures 5.22 and 5.23. An attempt was made to compare the data to some of Hardisty & Rouse (1996)'s results by comparing the ratio of their flux estimates for the spring and ebb floods ( $165 \times 10^3$  tonnes :  $162 \times 10^3$  tonnes respectively or 1.02:1) to that derived from the smaller sections of the spring flood and ebb covered for this study. The total flux of  $8.462 \times 10^3$  tonnes calculated for 10 August covered a 1.98 hour section of the spring flood tide from LW + 1.38h to LW + 3.33h. The total flux of  $8.077 \times 10^3$  tonnes calculated for 15 August covered a 1.16 hour section of the ebb tide four days after springs and spanning the time period LW - 3.33h to LW - 2.17h. The 10 August data was recalculated to span the same period relative to low water as the 15 August data, i.e. LW + 2.17h to LW + 3.33h. This resulted in a new quantity of  $7.737 \times 10^3$  tonnes. The comparative ratio to Hardisty & Rouse (1996)'s flood to ebb 1.02:1 was thus defined for the small section of the tide here as 1:1.04 ( $7.737 \times 10^3$  tonnes :  $8.077 \times 10^3$  tonnes). The dissimilarity of the results is explained by the difference in the state of the spring to neap cycle under survey for this study. The 10 August survey targeted a spring tide just beginning to flood in earnest while the 15 August highlighted a tide 4 days after springs and well into the ebb (figs. 5.22 and 5.23).

Comparison with Hardisty & Rouse's (1996) estimates does not verify the flux estimates calculated here. However, the results they quote are based upon calculations derived from point measurements and are thus not really valid for extrapolation across the entire mouth of the estuary. The flux estimates presented in this thesis take information derived from digital image data whose strength lies in the definition of spatial variability within the surface waters of the estuary. This gives the much broader picture which was not available to Hardisty & Rouse (1996) and questions the reliability of their results.

During the life span of LOIS a detailed flux monitoring framework was set up across the Humber mouth by the University of Hull, the *flux curtain*. Throughout 1995 (the main focus for this study) the equipment was installed and tested. The data generated did thus not comprise a complete dataset for the practical comparison of the SPM flux results derived for this study. Unfortunately, it is only since 1995 that the *flux curtain* has begun to generate a unique and comprehensive array of flux data and, even though the data is

representative of single points across the estuary only, the *flux curtain* would be an ideal source for subsequent validation of any studies of this nature undertaken in the future.

#### 6.4 SPM concentration and flux distributions across the Humber mouth

Suspended Particulate Matter moves into and out of the Humber Estuary in patches which are probably formed as a result of bathymetric influence and / or the resuspension of sediments particularly at higher water velocities (examples may be found extensively throughout the image sequences depicted in figs. 5.7 - 5.11). In order to exemplify the “patchiness” of the SPM concentration field across the Humber Estuary, Fourier transforms on one-dimensional transects derived from SPM images were performed (section 5.3.3). From analysis of the transect data which spanned the Humber mouth, it was possible to determine the most frequently occurring size of SPM patch within each dataset (fig. 5.13). Generally, the most frequently occurring patch size found for each image decreased with a reduction in surface velocity; patch sizes reached a minimum between 0.2 and 0.3 m sec<sup>-1</sup>. This relationship was found to be best described by a polynomial fit (highest power of 5) but yielded an R<sup>2</sup> of only 0.44 possibly due to the sparse temporal coverage of the images. Thus, this relationship alone could not be suggested as a useful indicator of total SPM concentration or flux into or out of the estuary. According to J. Hardisty (quoted in Hadlington, 1995), rough calculations have shown that up to 50% of the SPM moving into or out of the estuary do so in patches, or Snarks, which he specifies as having a width of approximately 100 m. From visual scrutiny of the images (figs. 5.7 - 5.11) it is possible to ascertain that there are different sizes of patches across the estuary and that their width is not a constant.

To test the importance of patches in SPM transport in the Humber Estuary, the relationships between patch size and the SPM concentration, SPM flux, water depth, and surface velocity perpendicular to the transect, within each patch were assessed. The patches across the transect profile were identified by first passing a moving average filter (covering ten points either side of the target value) over the datastream to smooth out any high frequency information which can be assumed to be within-patch variation or noise. The patches were then identified by finding the troughs within the datastream which separated out one patch from another. Patches were delineated as sections of data lying between two troughs and at a minimum separation distance of 20 m (e.g. fig. 6.1). The

results will differ from those generated by Fourier analysis which would identify some of the larger scale features, spanning two or more smaller patches, and would eliminate much of the higher frequency noise. The involvement of noise in the datastream has been minimised by smoothing (averaging) the data first. No information on the larger scale features (within which two or more smaller patches lie) will be included. As the hypothesis under test is that the smaller scale SPM patches (quoted as approximately 100 m wide in Hadlington, 1995) are considered important for sediment transport, this method of patch determination was considered satisfactory. For each patch the within-patch total SPM concentration and total SPM flux was determined by calculating the area under the curve for the two parameters (e.g. fig. 6.1). Averaged surface velocity and averaged water depth for each patch were also calculated.

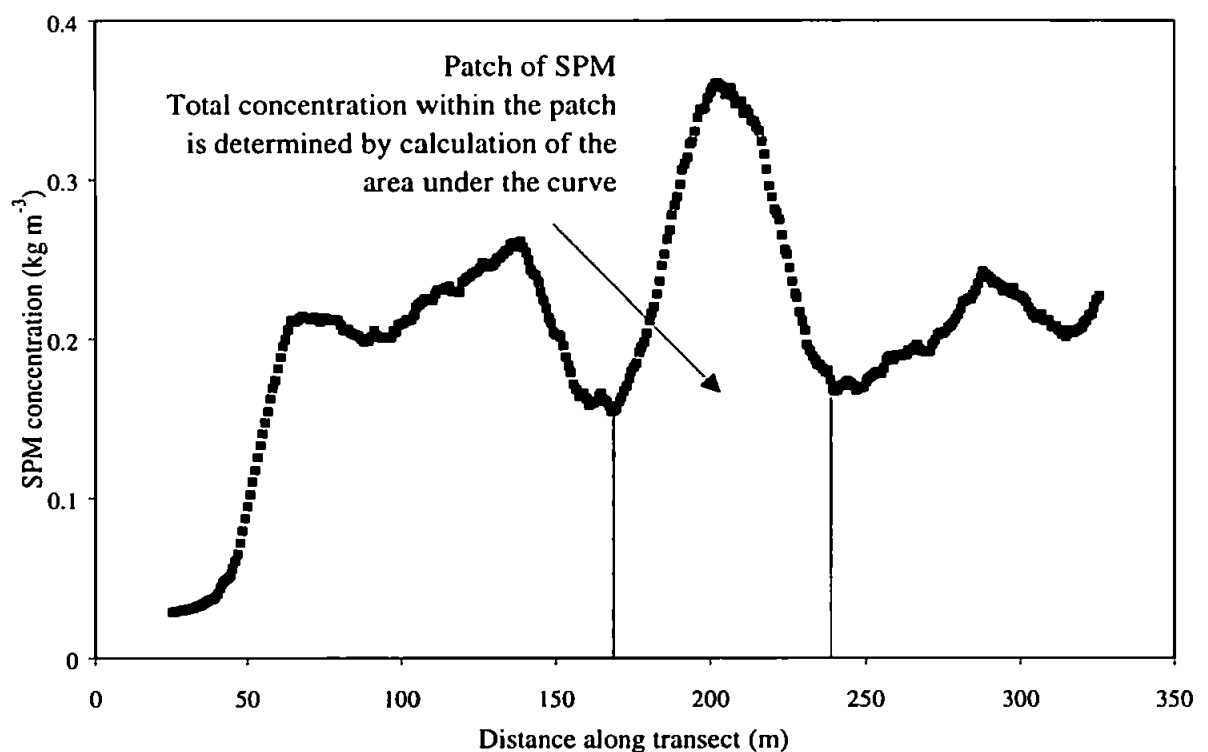


Figure 6.1 : An example of patch delineation using the transect data acquired across the Humber mouth from CASI images (figs. 5.7 - 5.11). The data has been smoothed with an averaging filter and the patch is defined as a section between two troughs in the concentration distribution. Total SPM concentration and flux within the patch is calculated as the area under the curve; averaged depth and velocity as mean values across the patch.

To test Hardisty's claim that 50% of the total SPM is transported across the mouth in patches of roughly 100 m, the total flux contained within patch sizes less than 50 m, between 50 m and 100 m and over 100 m were determined for each transect dataset (fig. 6.2 and table 6.1). Considering the patch sizes from all of the transect datasets it was found that most of the SPM flux moving into or out of the estuary does so in patches spanning less than 50 m (a mean from all datasets of 86% of the total). This is further supported by the Fourier transform results (fig. 5.13). On average 11% of the flux is transported in 50 - 100 m patches, and 3% is carried within patches over 100 m wide (fig. 6.1 & table 6.1). This data suggests that the smaller patches (< 50 m in width) play the dominant role in SPM transport and it is these that could provide a useful insight into the determination of SPM concentration and transport from remote sensing.

Percentage total flux transported	Patch sizes		
	< 50 m	50 - 100 m	> 100 m
mean (%)	86	11	3
maximum (%)	97	21	19
minimum (%)	64	3	0

Table 6.1 : The mean, maximum and minimum percentages of the total flux transported across the Humber mouth transect in the different patch sizes of < 50 m, 50 - 100 m and > 100 m considering all 27 image datasets



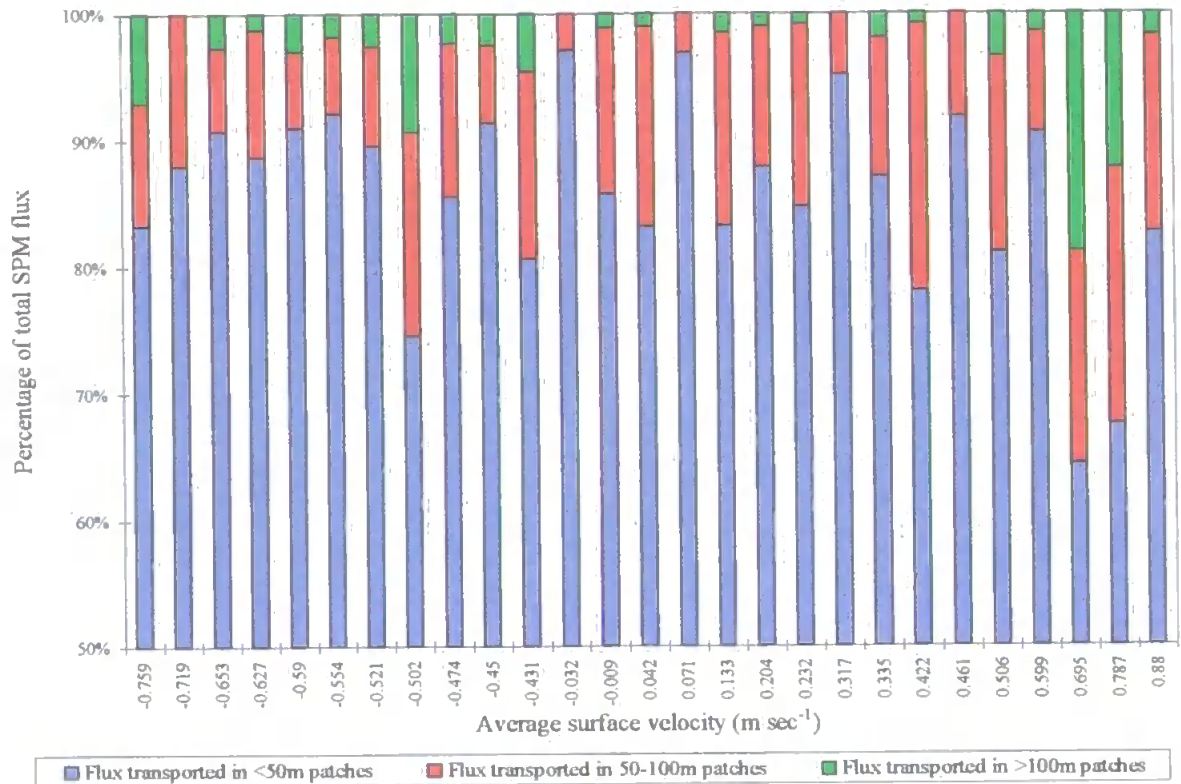


Figure 6.2 : The percentage of total SPM flux moving into or out of the Humber Estuary contained within patch sizes < 50 m, 50 m - 100 m and > 100 m for each image transect. The results are related to averaged surface velocities into the estuary. The first 50% of SPM flux is not shown as in all cases this is transported in patches less than 50 m wide.

It was considered that the actual size of patch may play a key role in the transport of SPM across the Humber mouth and that it may be possible to relate the size of patch directly to SPM concentration and / or flux. If indeed the relationships are significant it could be possible to use the size of patch as a surrogate for SPM concentration and / or flux across the Humber mouth. In such a case, one would need only a radiometrically (preferably atmospherically) correct image to determine the spatial distribution of patches across the estuary as SPM concentration across the image could be inferred from patch size rather than derived using image processing techniques. This would remove many processing stages, and so reduce time and effort. The results could be used as a key input into hydrodynamic models of the region necessary for environmental monitoring and coastal zone management. Modelling eliminates costly fieldwork and data acquisition both in time and resources. Data such as that generated here is necessary to first define the model and then to test its results. This is an area where remote sensing can assist by generating

data with the synoptic coverage necessary, together with an invaluable temporal element through sequential repeat coverage of a particular target site.

Pearson's correlation coefficient matrices were determined for each data series to evaluate the relative influence of each parameter on another and on the size of the patch they are contained within (results in Appendix E). Matrices were also derived for the log relationships of all the parameters and groups of data points (Appendix E).

Patch size and within-patch total SPM concentration maintain a significant relationship (taken here to be a relationship yielding a correlation coefficient of 0.7 or more) across all datasets except those acquired on 29 June and one dataset each from the 11 and 15 August surveys (Appendix E & fig. 6.3). The data series acquired at LW + 0.08h on 11 August exhibits a relationship with a correlation coefficient of 0.69 and this was assumed to be close enough to the (arbitrarily) chosen threshold of 0.7 to retain its significance for the purposes of future analysis. Thus it is hypothesised that it would be possible to use patch size directly to determine within-patch total SPM concentration for all days of survey except where average surface velocities lie between 0 and  $-0.5 \text{ m sec}^{-1}$  (fig. 6.3).

In an attempt to find a significant relationship between patch size and within-patch total SPM concentration for those surface velocities lying between 0 and  $-0.5 \text{ m sec}^{-1}$ , the Pearson's correlation coefficients defining the relationships between the logged parameters were consulted. For data acquired on 10, 15 and 21 August, i.e. all data except those acquired during spring conditions, an improvement in significance to that of their linear equivalent was found (Appendix E & fig. 6.4). It was thus hypothesised that the patch size / SPM concentration relationship (fig. 6.3) could be employed for data acquired during spring tidal conditions such as those experienced on 11 August (but not on 29 June) and the  $\ln(\text{patch size}) / \ln(\text{SPM concentration})$  relationship (fig. 6.4) for data acquired during tidal conditions other than these (10, 15 and 21 August). The conditions experienced on 29 June posed a more complex problem given that there is no direct significant linear nor logarithmic relationship between patch size and within-patch total SPM concentration. Other more indirect approaches were thus investigated.

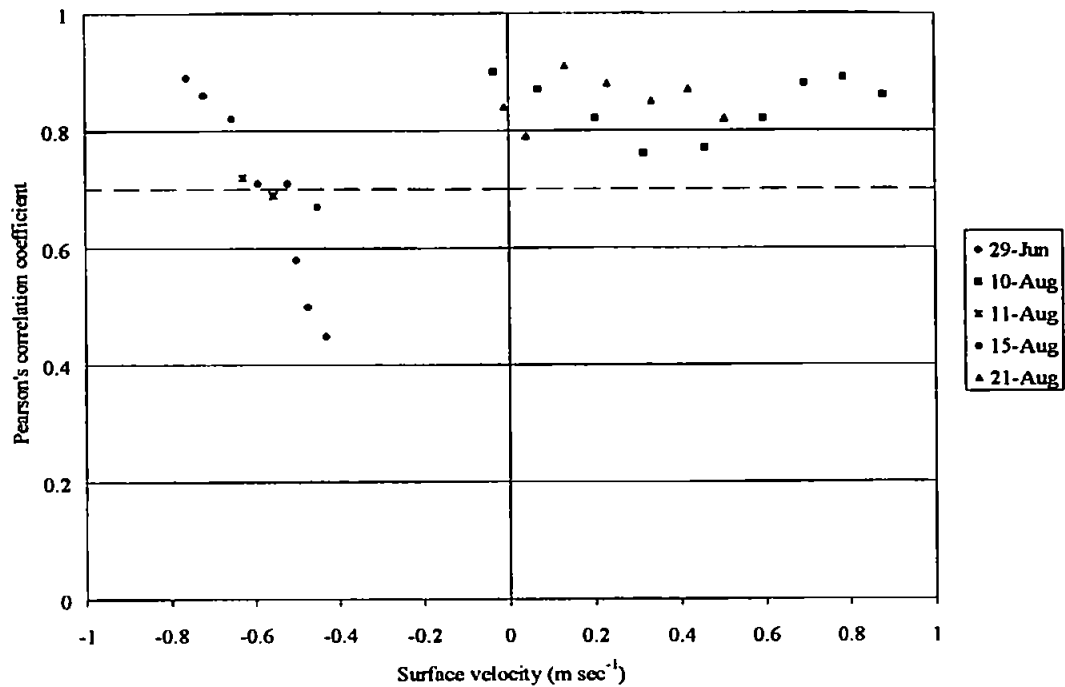


Figure 6.3 : Pearson's correlation coefficients describing the relationship between patch size and within-patch total SPM concentration. The coefficients for each dataset are plotted against the averaged surface velocity into the estuary for the survey.

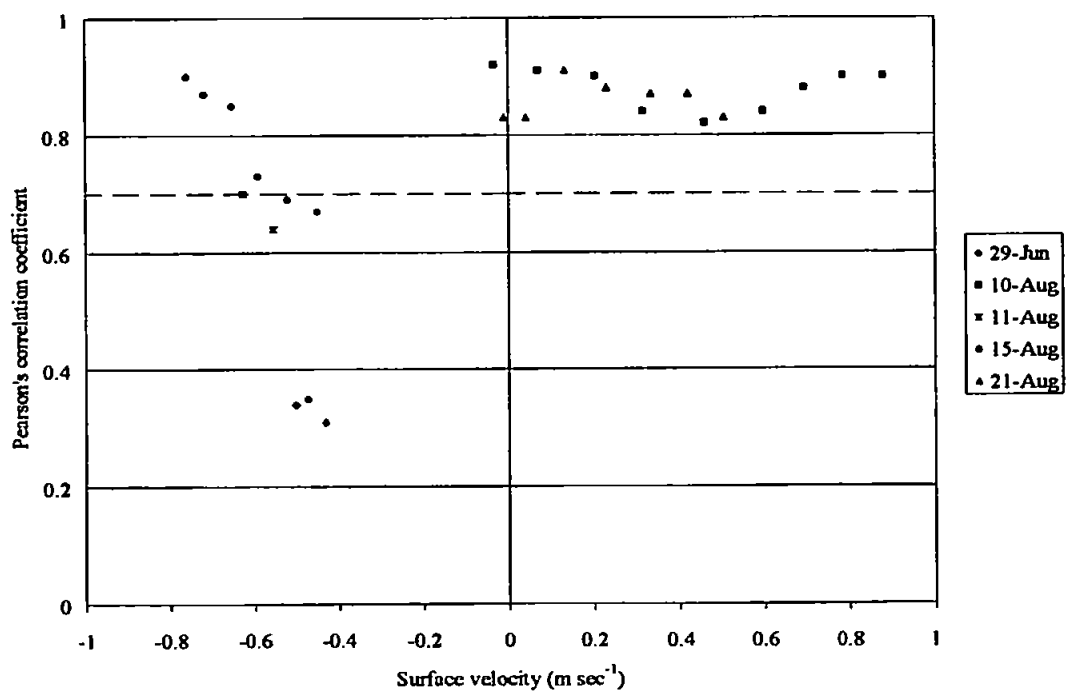


Figure 6.4 : Pearson's correlation coefficients describing the relationship between  $\ln(\text{patch size})$  and  $\ln(\text{within-patch total SPM concentration})$ . The coefficients for each dataset are plotted against the averaged surface velocity into the estuary for the survey.

The relationship between within-patch averaged surface velocity and  $\ln(\text{within-patch averaged water depth})$  maintains a significant relationship for 29 June (Appendix E & fig. 6.5). A further significant relationship is evident for 29 June between within-patch averaged surface velocity and  $\ln(\text{within-patch total SPM concentration})$  (Appendix E & fig. 6.6). Thus it may be possible to derive within-patch total SPM concentration for conditions such as those experienced on 29 June indirectly from within-patch averaged water depth (assumed to be a known quantity alongside patch size) through the determination and use of within-patch averaged surface velocity. It is thus hypothesised that one can derive within-patch total SPM concentration from patch size either directly or indirectly for other similarly assessed datasets acquired during the tidal conditions discussed in this study (table 6.2). Obviously there are large gaps in the temporal coverage of this particular study and it is suggested that the use of one relationship over another would be more clearly defined with the addition of more data. The use of the relationships summarised in table 6.2, however, do exemplify the possible practical use of such analysis in the Humber Estuary and the consequential vast reduction in traditional surface-based monitoring time and cost.

Date	Tidal state	Times relative to low water	Significant relationships to derive within-patch SPM concentration
29 June	springs	-0.23h to +0.1h	$\ln(z) \rightarrow v$ $v \rightarrow \ln(s)$
10 August	1 day before springs	+1.38h to +3.33h	$\ln(x) \rightarrow \ln(s)$
11 August	springs	-0.15h to +0.08h	$x \rightarrow s$
15 August	4 days after springs	-3.33h to -2.17h	$\ln(x) \rightarrow \ln(s)$
21 August	neaps	+3.27h to +4.7h	$\ln(x) \rightarrow \ln(s)$

Table 6.2 : Summary of the significant relationships suggested for use in the derivation of within-patch total SPM concentration from the known quantities of patch size and within-patch averaged water depth.  $x$  = patch size,  $s$  = within-patch total SPM concentration,  $v$  = within-patch averaged surface velocity, and  $z$  = within-patch averaged water depth.

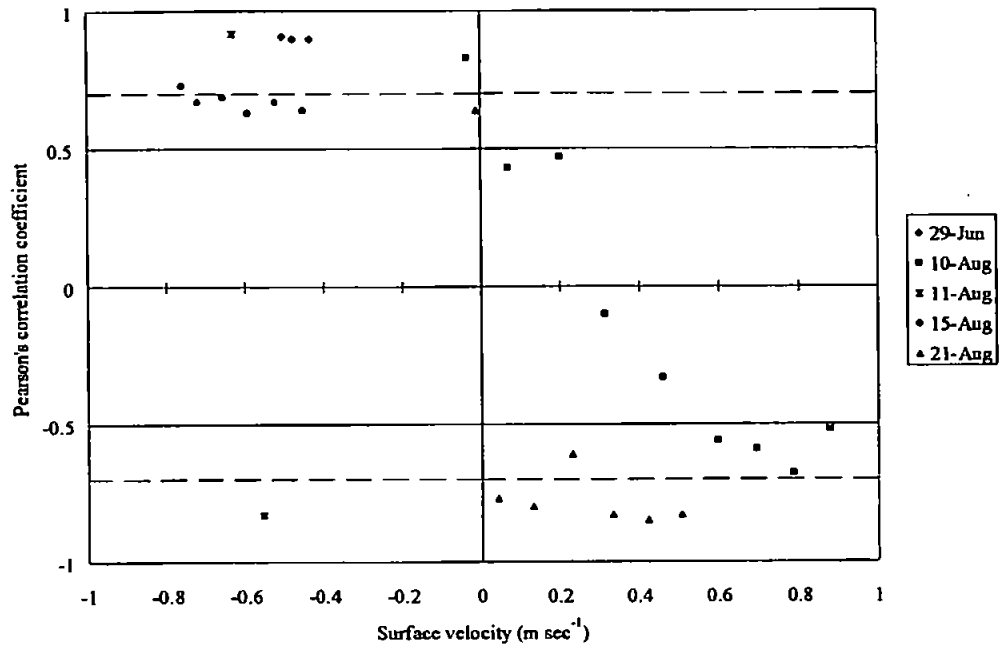


Figure 6.5 : Pearson's correlation coefficients describing the relationship between within-patch averaged velocity and  $\ln(\text{within-patch averaged water depth})$ . The coefficients for each dataset are plotted against the averaged surface velocity into the estuary for the survey.

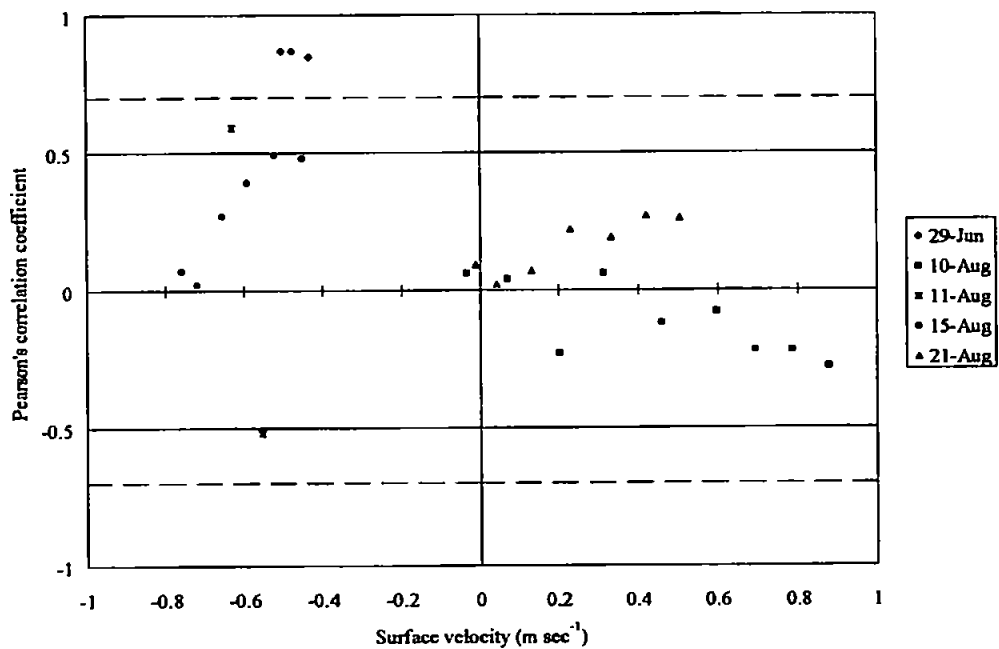


Figure 6.6 : Pearson's correlation coefficients describing the relationship between within-patch averaged velocity and  $\ln(\text{within-patch total SPM concentration})$ . The coefficients for each dataset are plotted against the averaged surface velocity into the estuary for the survey.

A similar analysis was followed to ascertain the possible use of patch size to determine within-patch total SPM flux directly or indirectly from patch size. The relationship between these two parameters is not uniformly significant (Appendix E & fig. 6.7) and the derivation of within-patch total SPM flux can probably only be assessed from patch size directly under the conditions experienced on 11 August. The relationship between within-patch total SPM concentration and total flux was thus interrogated as a possible indirect avenue through which flux may be derived (Appendix E & fig. 6.8). Significant relationships emerged for the data acquired on 29 June, 10 August (latter section of the survey only), 15 August and 21 August (fig. 6.8). For these conditions it could thus be possible to use these relationships to derive within-patch total SPM flux from the previously determined concentration results. The first three datasets acquired on 10 August yielded insignificant relationships (figs. 6.7 & 6.8) and it appeared impossible to suggest a useful methodology to use in the derivation of within-patch total SPM flux. It is again suggested that the analysis would benefit from the addition of more data to fill in the temporal gaps. More concrete suggestions for the application of these types of analytical reasoning could then be made. A summary of the suggested methodologies as derived from this study's datasets is detailed in table 6.3.

Date	Tidal state	Times relative to low water	Significant relationships to derive within-patch SPM flux
29 June	springs	-0.23h to +0.1h	$s \rightarrow f$
10 August	1 day before springs	+1.38h to +3.33h	$s \rightarrow f$ (LW + 2.07h and later only)
11 August	springs	-0.15h to +0.08h	$x \rightarrow f$
15 August	4 days after springs	-3.33h to -2.17h	$s \rightarrow f$
21 August	neaps	+3.27h to +4.7h	$s \rightarrow f$

Table 6.3 : Summary of the significant relationships suggested for use in the derivation of within-patch total SPM flux from the known quantities of patch size and within-patch total SPM concentration.  $x$  = patch size,  $s$  = within-patch total SPM concentration, and  $f$  = within-patch total SPM flux.

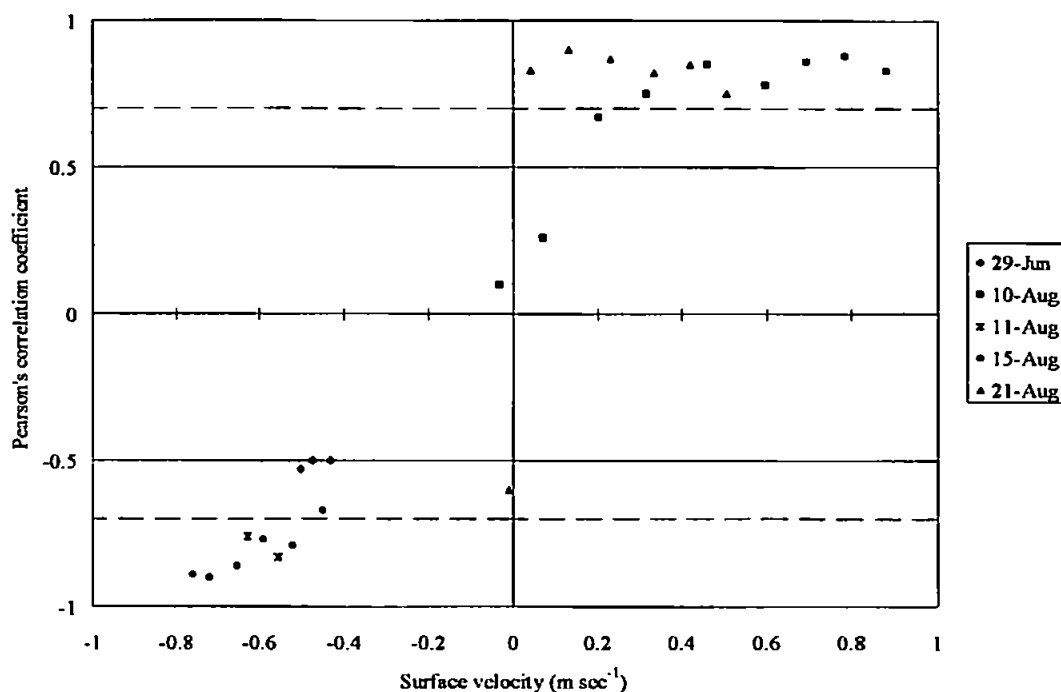


Figure 6.7 : Pearson's correlation coefficients describing the relationship between patch size and within-patch total SPM flux. The coefficients for each dataset are plotted against the averaged surface velocity into the estuary for the survey.

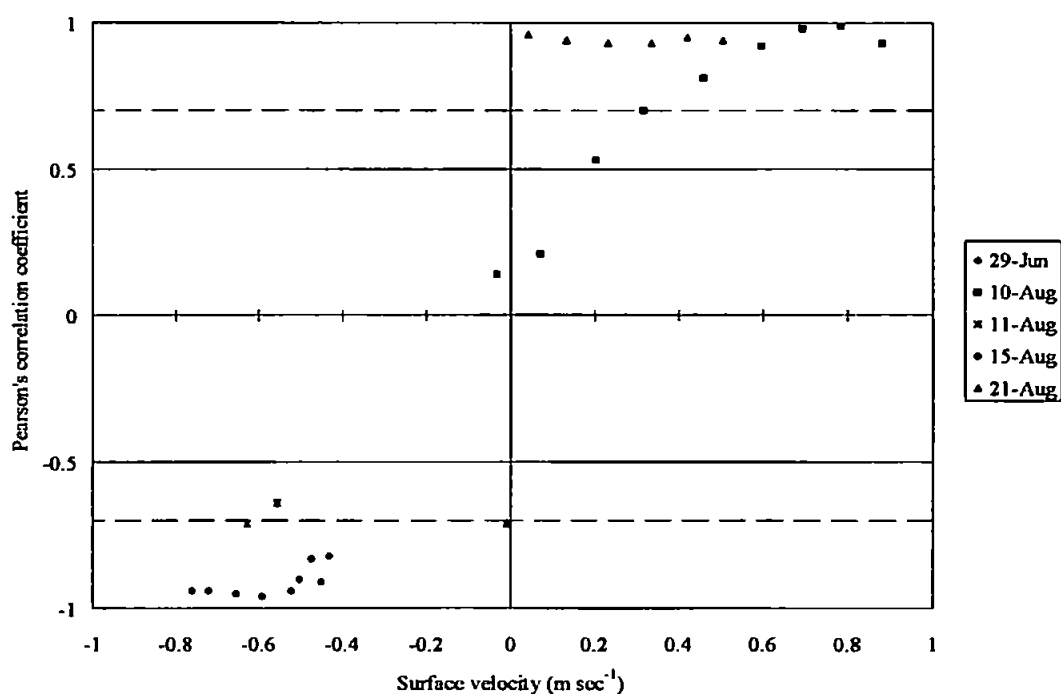


Figure 6.8 : Pearson's correlation coefficients describing the relationship between within-patch total SPM concentration and within-patch total SPM flux. The coefficients for each dataset are plotted against the averaged surface velocity into the estuary for the survey.

It is interesting to note that the only dataset from which within-patch total SPM concentration and total SPM flux can be derived directly from patch size is that acquired on 11 August (low water springs). However, the surveyed datasets on this date comprised only two images and thus may not be truly representative of these conditions. The results from the 29 June survey suggest a more indirect way of deriving SPM concentration through the definition of within-patch averaged surface velocity. Again this dataset comprised only three points but this factor together with the results from 11 August may point to the fact that at or around low water and / or under spring tidal conditions the relationships between the parameters determining within-patch total SPM concentration are less distinct. Likewise, the data acquired on 10 August did not conform to the majority rule that within-patch total SPM concentration and total SPM flux are linearly related. The data series begins to conform as the tide progresses into the flood but for the first three image data transects (LW + 1.38h to LW + 1.85h) the relationships were not significant. This may be explained by the effects of particle settling when water velocities are low and decelerating. In general, the best relationships are found where velocities are increasing and high. In the absence of any evidence to suggest any clear change from the significant use of one relationship over another in the derivation of either within-patch total SPM concentration or total SPM flux, the results are summarised as exemplifying two generally significant relationships:

- $\ln(\text{patch size})$  and  $\ln(\text{within-patch total SPM concentration})$ , and
- within-patch total SPM concentration and within-patch total SPM flux.

Although the two previously summarised results apply to the majority of the data acquired, there still remains a degree of uncertainty in using the relationships for data acquired under conditions similar to those datasets which did not conform to one or both of them (e.g. conditions similar to those experienced on 29 June, 10 and 11 August). What is required is an algorithm which continuously delivers the required quantities from all datasets with a high significance. An approach which incorporated all known quantities (patch size and within-patch averaged water depth), and not just a single entity, was thus adopted. Algorithms for the derivation of within-patch total SPM concentration and total SPM flux were developed through multi-regression analyses. Equations 6-1 and 6-2 were thus defined.



$$\ln(s) = \frac{\ln(h) + a \cdot h + b \ln(x) + c}{d} \quad 6-1$$

where:  $s$  = within-patch total SPM concentration ( $\text{kg m}^{-3}$ ),

$f$  = within-patch total SPM flux ( $\text{kg m}^{-2} \text{s}^{-1}$ ),

$x$  = patch size (m),

$h$  = within-patch averaged water depth (m), and

$a$ ,  $b$ ,  $c$  &  $d$  are constants derived from multi-regression analysis (table 6.4).

Date	Time (hours relative to LW)	average surface velocity ( $\text{m sec}^{-1}$ )	a	b	c	d	R <sup>2</sup>
29 June	-0.23	-0.502	0.087	-0.034	1.474	0.028	0.971
	-0.1	-0.474	0.086	-0.033	1.469	0.033	0.971
	0.1	-0.431	0.084	-0.038	1.511	0.031	0.971
10 August	1.38	-0.032	0.092	0.147	0.868	-0.148	0.979
	1.58	0.071	0.086	0.133	0.973	-0.13	0.981
	1.85	0.204	0.079	0.145	0.998	-0.147	0.984
	2.07	0.317	0.075	0.126	1.088	-0.131	0.98
	2.35	0.461	0.078	0.112	1.098	-0.108	0.987
	2.62	0.599	0.078	0.085	1.199	-0.088	0.989
	2.83	0.695	0.077	0.071	1.278	-0.065	0.986
	3.08	0.787	0.076	0.058	1.335	-0.056	0.985
	3.33	0.88	0.076	0.064	1.321	-0.062	0.981
11 August	-0.15	-0.627	0.107	0.036	1.066	-0.035	0.965
	0.08	-0.554	0.107	0.028	1.1	-0.038	0.963
15 August	-3.33	-0.759	0.074	-0.035	1.693	0.034	0.981
	-3.18	-0.719	0.076	-0.052	1.71	0.052	0.98
	-2.93	-0.653	0.077	-0.041	1.644	0.04	0.979
	-2.7	-0.59	0.079	-0.029	1.576	0.033	0.979
	-2.43	-0.521	0.082	-0.039	1.554	0.032	0.976
	-2.17	-0.45	0.082	-0.028	1.523	0.03	0.977
21 August	3.27	-0.009	0.066	0.102	1.188	-0.101	0.994
	3.48	0.042	0.067	0.076	1.308	-0.081	0.989
	3.72	0.133	0.068	0.054	1.412	-0.053	0.984
	3.98	0.232	0.091	-0.309	2.693	0.301	0.931
	4.25	0.335	0.063	0.087	1.336	-0.082	0.987
	4.48	0.422	0.058	0.132	1.208	-0.12	0.991
	4.7	0.506	0.058	0.097	1.363	-0.095	0.989

Table 6.4 : The coefficients a, b, c and d corresponding to equation 6-1, their R<sup>2</sup> values and the averaged surface velocity during survey.

$$f = \frac{h + a \ln(h) + b \ln(x) + c}{d} \quad 6-2$$

where:  $f$  = within-patch total SPM flux ( $\text{kg m}^{-2} \text{s}^{-1}$ ),

$x$  = patch size (m),

$h$  = within-patch averaged water depth (m), and

$a$ ,  $b$ ,  $c$  &  $d$  are constants derived from multi-regression analysis (table 6.5).

Date	Time (hours relative to LW)	average surface velocity ( $\text{m sec}^{-1}$ )	a	b	c	d	R <sup>2</sup>
29 June	-0.23	-0.502	10.482	0.289	-13.985	0.033	0.97
	-0.1	-0.474	10.616	0.321	-14.214	0.07	0.971
	0.1	-0.431	10.688	0.325	-14.528	0.069	0.971
10 August	1.38	-0.032	10.641	0.016	-13.853	0.054	0.971
	1.58	0.071	11.211	-0.069	-14.965	-0.005	0.974
	1.85	0.204	11.331	0.058	-15.631	-0.027	0.974
	2.07	0.317	11.608	0.155	-16.517	-0.047	0.972
	2.35	0.461	11.597	-0.273	-15.658	0.097	0.977
	2.62	0.599	12.315	-0.174	-17.754	0.061	0.979
	2.83	0.695	12.492	0.02	-18.572	0.003	0.978
	3.08	0.787	12.767	0.067	-19.336	-0.002	0.981
	3.33	0.88	13.014	0.089	-19.998	-0.002	0.977
	3.33	0.88	13.014	0.089	-19.998	-0.002	0.977
11 August	-0.15	-0.627	9.382	0.332	-11.348	0.043	0.966
	0.08	-0.554	9.24	0.393	-11.295	0.042	0.962
15 August	-3.33	-0.759	13.409	0.487	-21.773	0.096	0.983
	-3.18	-0.719	13.123	0.767	-21.418	0.154	0.982
	-2.93	-0.653	12.772	0.46	-19.953	0.088	0.98
	-2.7	-0.59	12.368	0.241	-18.478	0.047	0.978
	-2.43	-0.521	11.768	0.291	-17.175	0.036	0.973
	-2.17	-0.45	11.751	0.066	-16.586	0.014	0.975
	-2.17	-0.45	11.751	0.066	-16.586	0.014	0.975
21 August	3.27	-0.009	13.033	0.187	-20.364	6.292	0.984
	3.48	0.042	13.676	-0.133	-21.462	2.286	0.983
	3.72	0.133	13.87	0.182	-22.424	-0.482	0.983
	3.98	0.232	11.33	1.917	-19.204	-2.527	0.911
	4.25	0.335	14.297	0.001	-23.121	-0.082	0.984
	4.48	0.422	14.598	-0.11	-23.568	-0.064	0.986
	4.7	0.506	14.784	-0.005	-24.531	-0.02	0.983

Table 6.5 : The coefficients a, b, c and d corresponding to equation 6-2, their R<sup>2</sup> values and the averaged surface velocity during survey.

In all cases the  $R^2$  value is high for both the definition of within-patch total SPM concentration and of total SPM flux from equations 6-1 and 6-2 respectively (table 6.4 & fig. 6.9 and table 6.5 & fig. 6.10 respectively). In all but one case the  $R^2$  value is above 0.95 which represent very significant results. The one case where the  $R^2$  value lies below 0.95 represents the dataset acquired at LW + 3.98h on 21 August. This dataset was not included in further analyses.

It was hypothesised that if the distribution of the a, b, c and d coefficients for the two equations 6-1 and 6-2 were significantly related to averaged surface velocity for the survey (i.e. tidal state and condition) it may be possible to predict their specific quantities for use with any similarly surveyed data not included here. Relating to equation 6-1, figures 6.11, 6.12, 6.13 and 6.14 depict the variation in the a, b, c and d coefficients respectively according to averaged surface velocity for the survey. c and d both have a reasonably significant relationship with averaged surface velocity with  $R^2$  values over 0.75, a and b however do not. The coefficients relating to equation 6-2 are depicted in a similar fashion with a, b, c and d represented in figures 6.15, 6.16, 6.17 and 6.18 respectively. In this case only the b coefficient has a reasonably significant relationship with averaged surface velocity ( $R^2$  of 0.73) and d may actually be a near-zero constant.

It was evaluated that the surveyed data included in this study do not provide sufficient information to use in the derivation of a predictive model which defines all the unknowns (a, b, c & d) necessary in the resolution of equations 6-1 and 6-2 for any similarly surveyed dataset. The underlying ethos that equations 6-1 and 6-2 present do however pave the way for the development of such a model. The inclusion of many more similar datasets now readily available from the LOIS archive could allow this to become a reality.

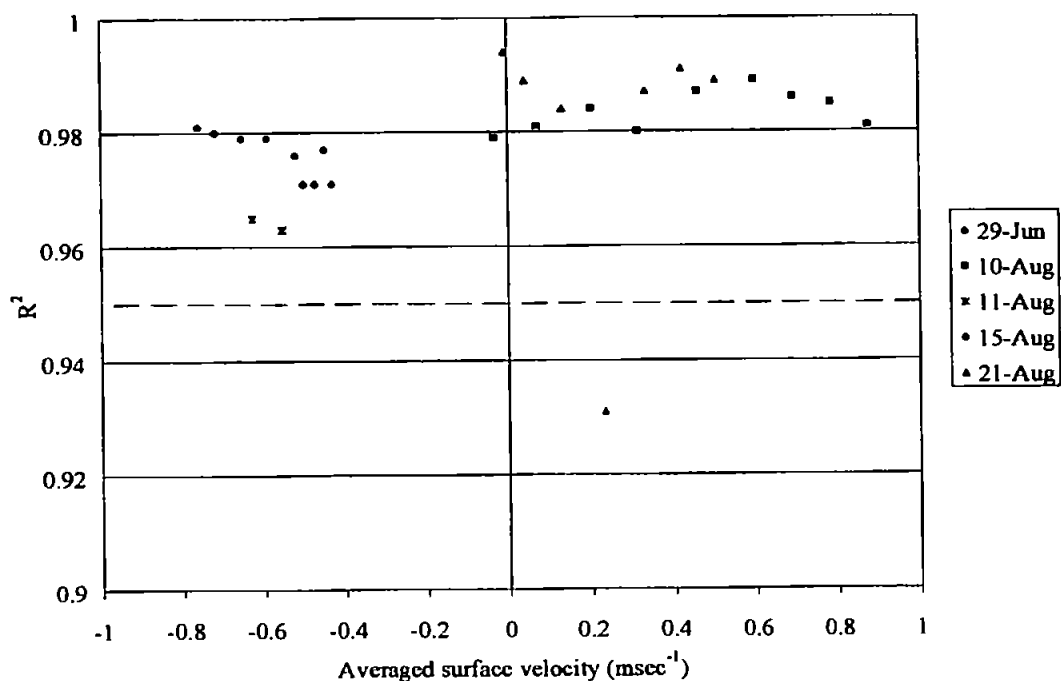


Figure 6.9 :  $R^2$  values describing the goodness of fit of equation 6-1 (to derive within-patch total SPM concentration) to the 27 surveyed datasets. The dotted line represents the threshold where  $R^2$  is 0.95.

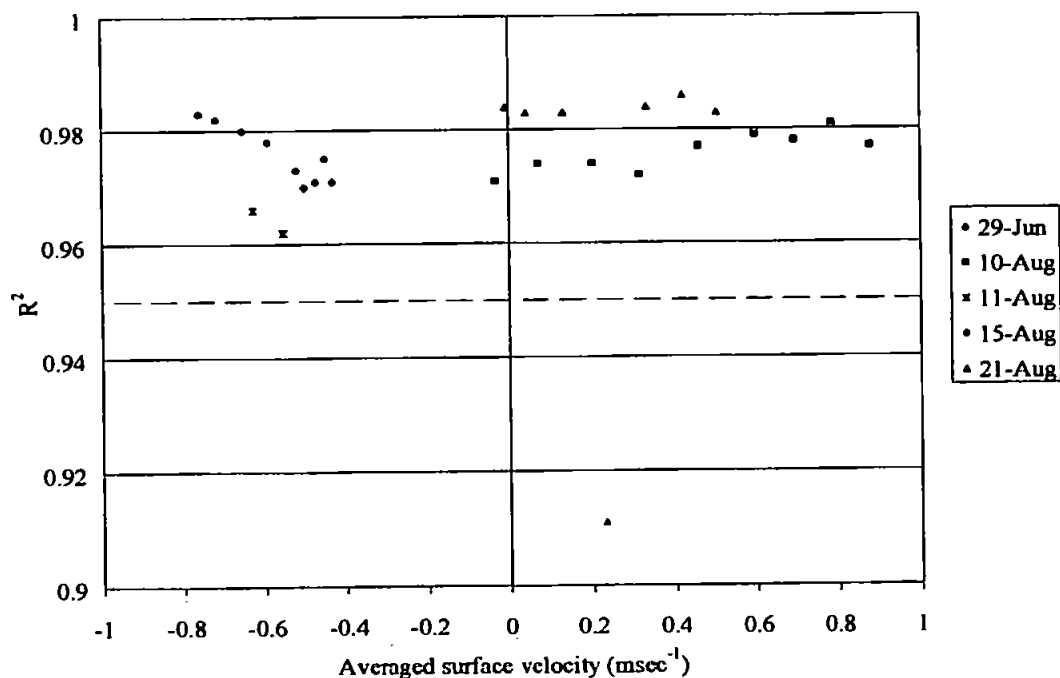


Figure 6.10 :  $R^2$  values describing the goodness of fit of equation 6-2 (to derive within-patch total SPM flux) to the 27 surveyed datasets. The dotted line represents the threshold where  $R^2$  is 0.95.

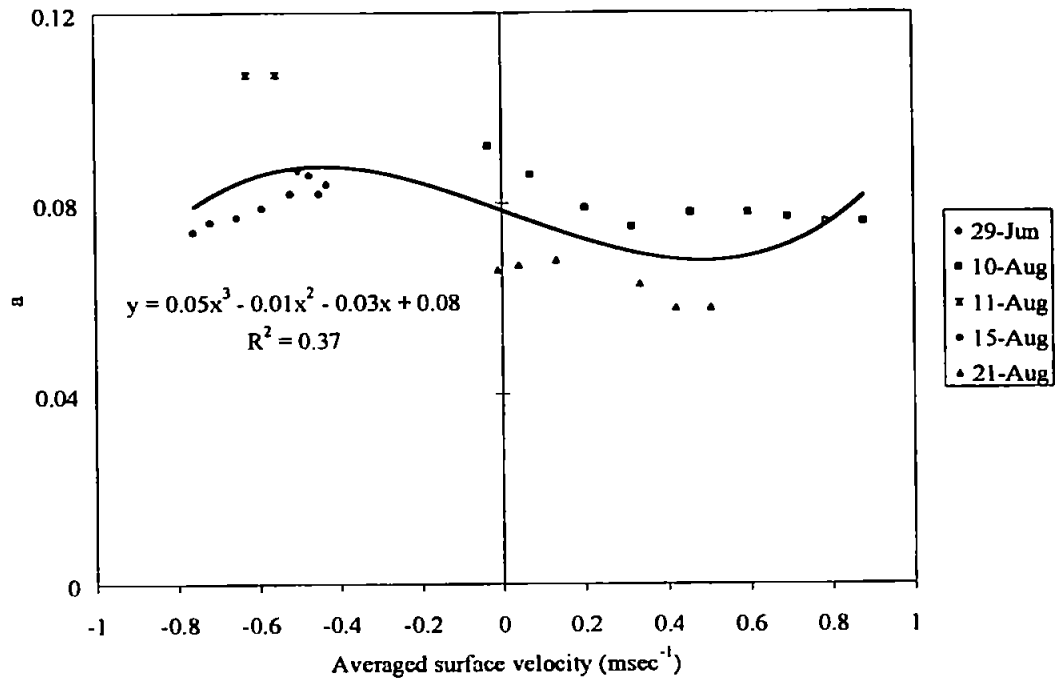


Figure 6.11 : The coefficient a from equation 6-1 for 26 of the datasets. The trendline describes the distribution of the coefficient in relation to the averaged surface velocity for the survey.

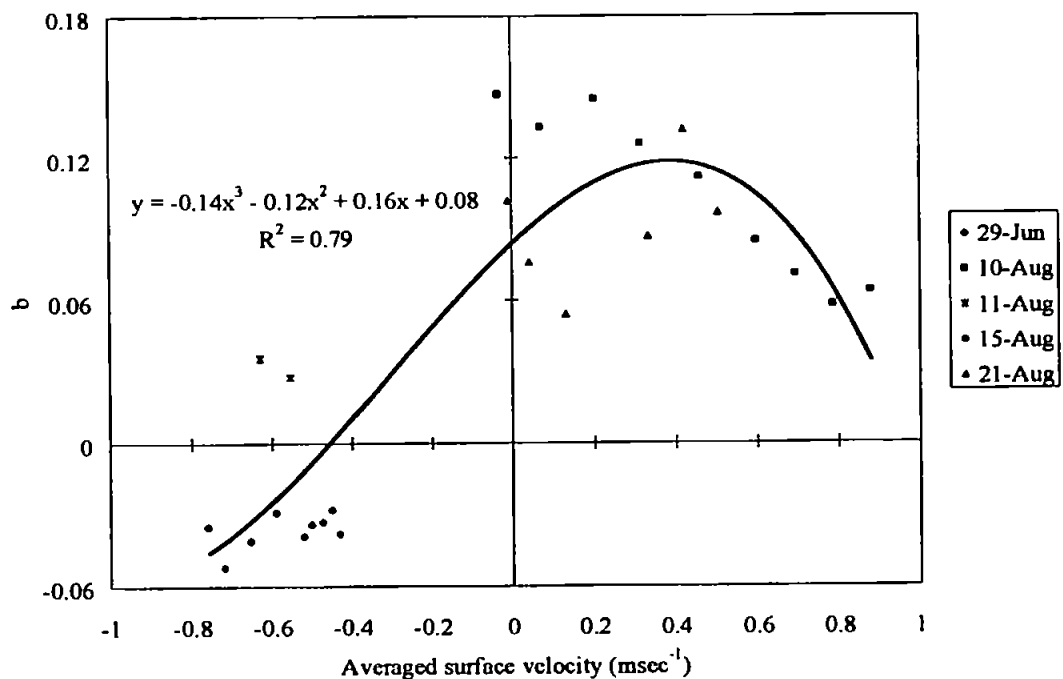


Figure 6.12 : The coefficient b from equation 6-1 for 26 of the datasets. The trendline describes the distribution of the coefficient in relation to the averaged surface velocity for the survey.

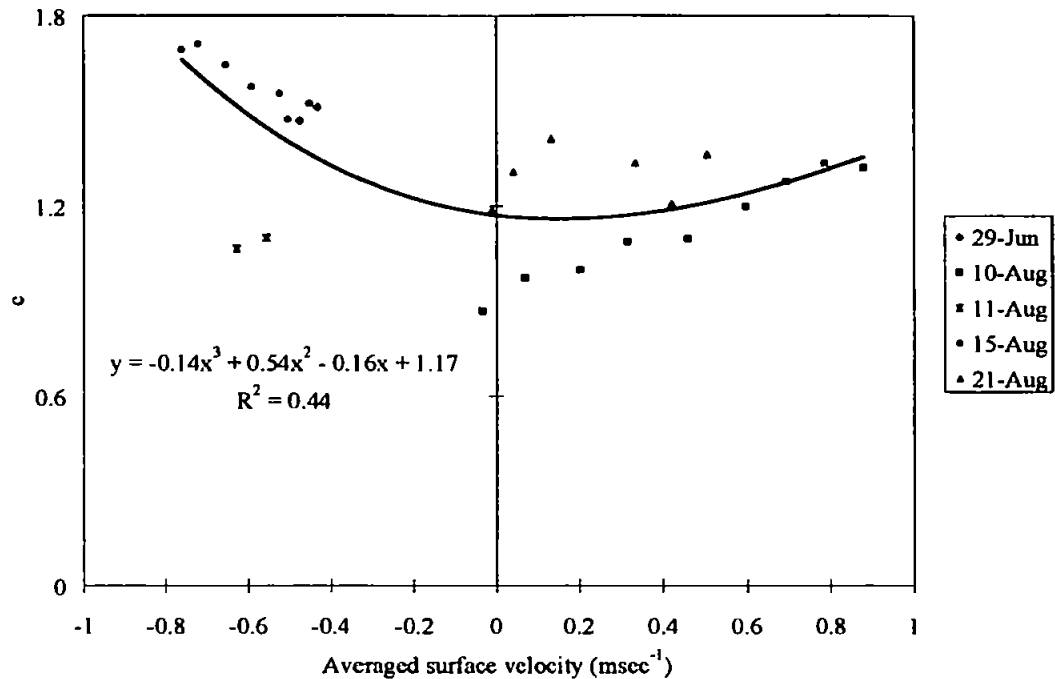


Figure 6.13 : The coefficient c from equation 6-1 for 26 of the datasets. The trendline describes the distribution of the coefficient in relation to the averaged surface velocity for the survey.

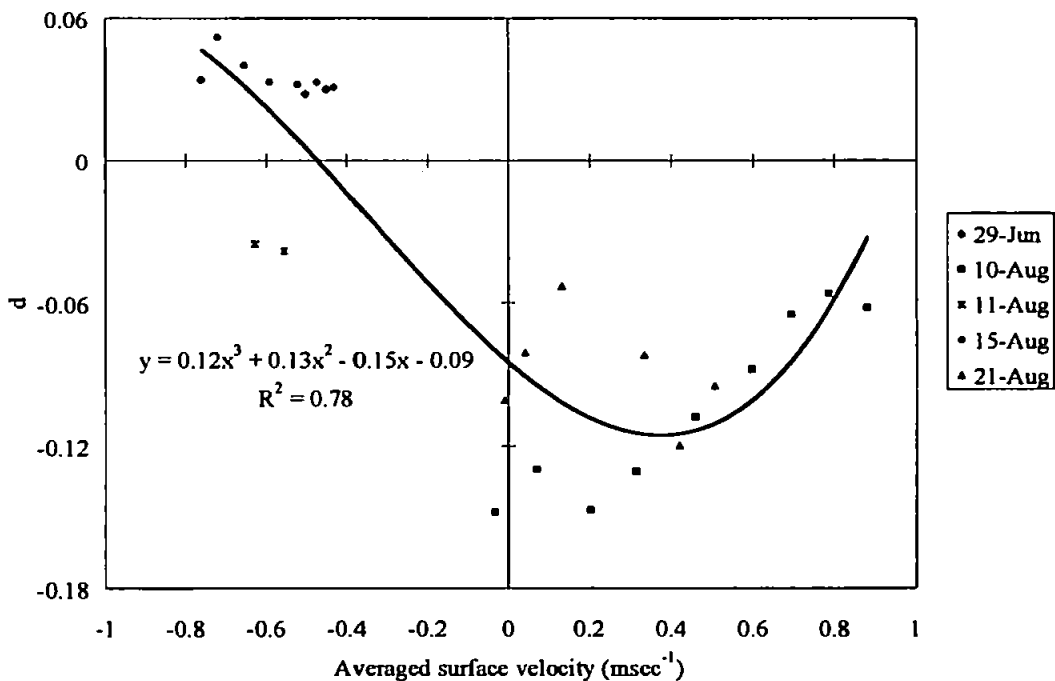


Figure 6.14 : The coefficient d from equation 6-1 for 26 of the datasets. The trendline describes the distribution of the coefficient in relation to the averaged surface velocity for the survey.

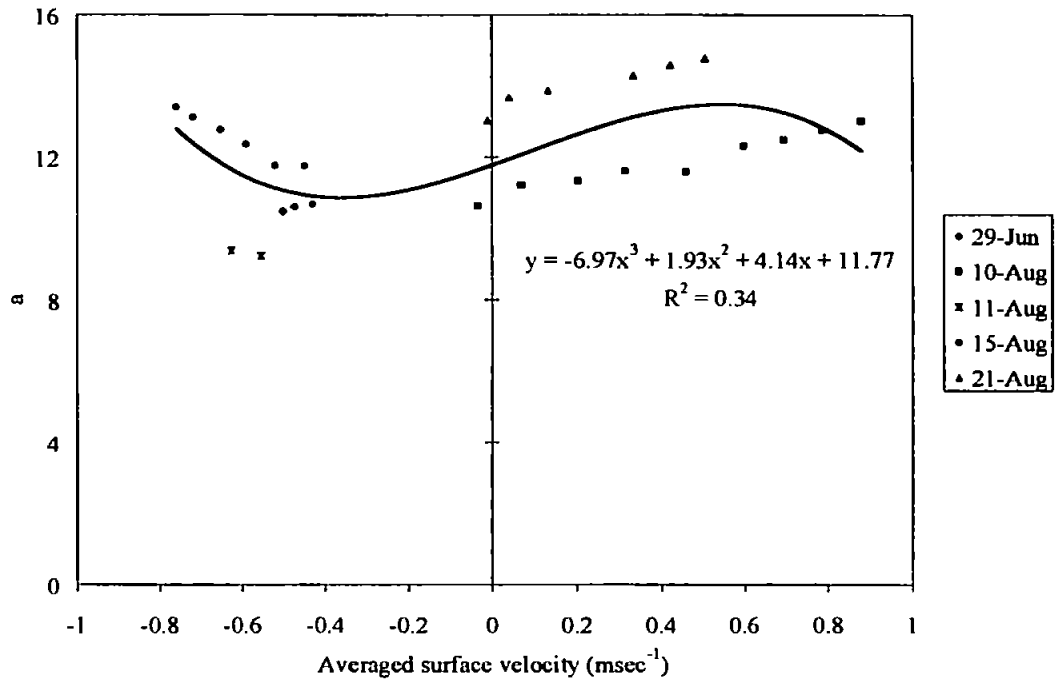


Figure 6.15 : The coefficient a from equation 6-2 for 26 of the datasets. The trendline describes the distribution of the coefficient in relation to the averaged surface velocity for the survey.

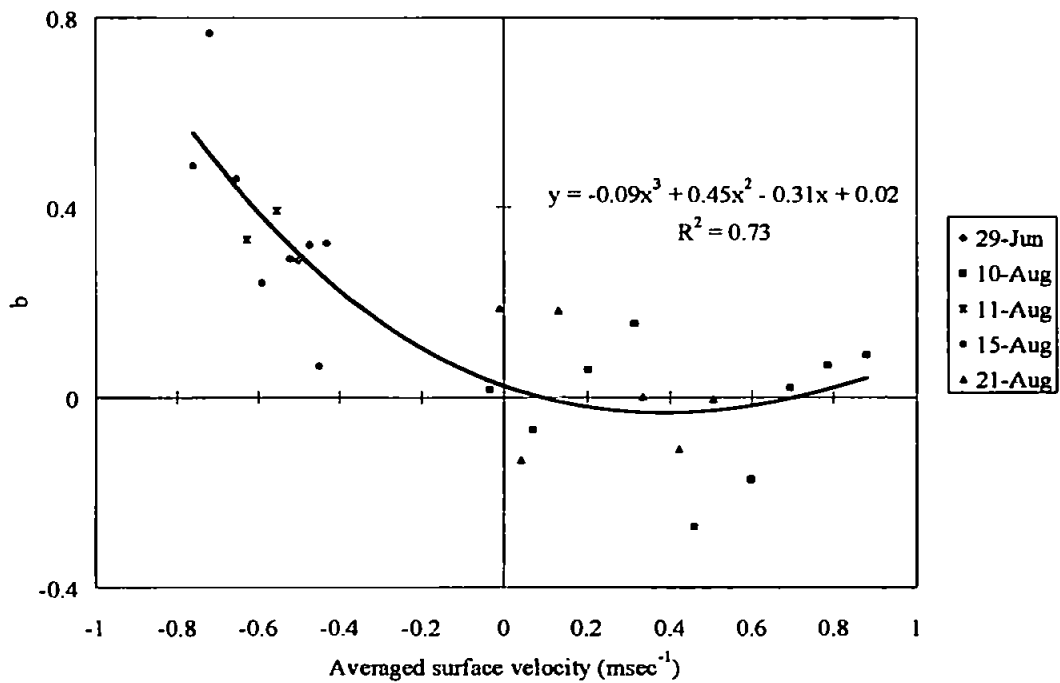


Figure 6.16 : The coefficient b from equation 6-2 for 26 of the datasets. The trendline describes the distribution of the coefficient in relation to the averaged surface velocity for the survey.

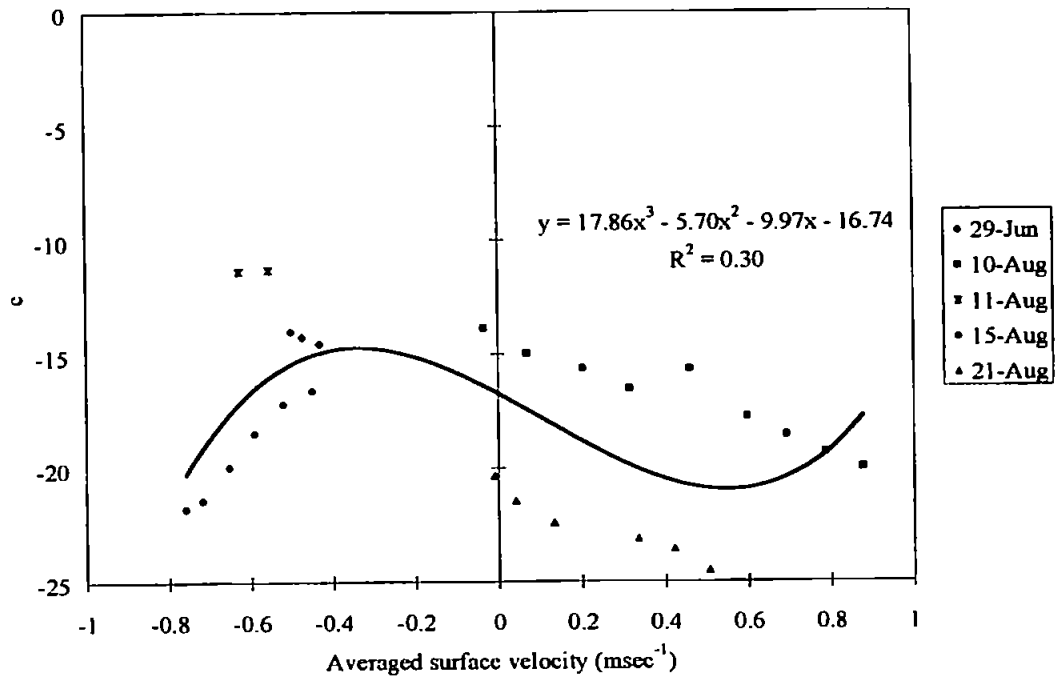


Figure 6.17 : The coefficient c from equation 6-2 for 26 of the datasets. The trendline describes the distribution of the coefficient in relation to the averaged surface velocity for the survey.

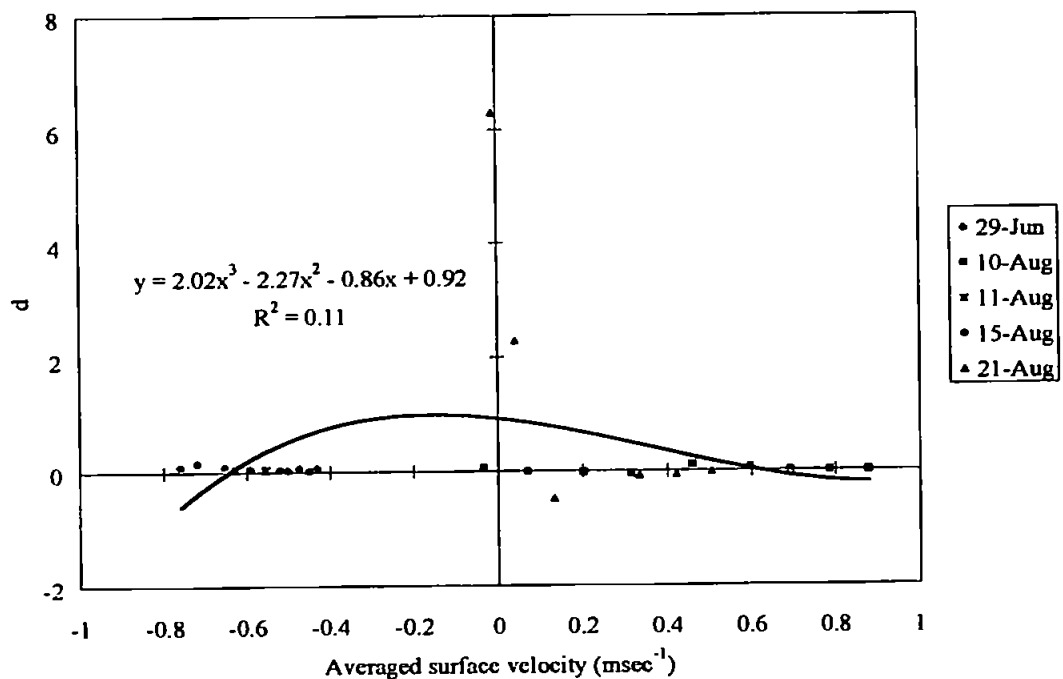


Figure 6.18 : The coefficient d from equation 6-2 for 26 of the datasets. The trendline describes the distribution of the coefficient in relation to the averaged surface velocity for the survey.



## **7 Summary and Recommendations for Future Work**

The use of airborne remote sensing in the coastal zone has been addressed through the development and validation of practical image processing and data analysis techniques for use in the Humber and Tweed Estuaries. The achievements of the original aims of study (section 1.1) are addressed in this section and recommendations for future work made.

### **7.1 The achievements of the original aims of study**

The achievements of this study are related to the original aims set out in section 1.1 as follows:

- 1. To explore the practical use of airborne remote sensing in the coastal zone for the quantification of suspended particulate matter (SPM) concentration, SPM flux, sea-surface temperature and salinity*

Airborne remote sensing has proved to be a useful and worthy technology for use in the coastal zone and in particular for estuarine studies. An aircraft's flexibility is its main advantage over the use of satellite monitoring. The acquisition of truly synoptic image sequences provides an unique and invaluable insight into estuarine dynamics. It has, however, been impossible, during the lifetime of this study, to generate image data spanning an entire tidal cycle and covering all spring and neap conditions. This was mainly caused by unfavourable weather conditions during proposed surveys. The utilisation of a variety of images acquired over the Tweed and Humber Estuaries has been demonstrated in this study. The ATM has been shown to be a useful tool from which sea-surface temperature can be determined and salinity derived (section 4.2.3.2 & Appendix F : Uncles, *et al.*, 1999). In the Humber Estuary the CASI has been employed and tested for use in SPM concentration derivation and SPM flux estimation (section 4.2.3.1 & chapter 5). This type of information has been defined in greater detail than is presently exemplified in the literature due to the finer spatial resolution and the wider two-dimensional coverage area furnished by the use of airborne remote sensing. Such information represents essential and hitherto unseen evidence of estuarine and coastal dynamics and would provide a key input into hydrodynamic models of the region important for effective estuarine and coastal zone management.

2. *To develop a protocol for the sea-truthing of remotely sensed airborne data acquired using the Compact Airborne Spectrographic Imager (CASI) and the Airborne Thematic Mapper (ATM) and to generate a comprehensive dataset as part of the core Land-Ocean Interaction Study (LOIS) field programme*

The author took part in numerous cruises spanning the Humber Estuary and the North Sea. The protocols for sea-based data acquisition and the coordination of the aircraft with the ship were developed throughout 1994 and were put into active operation during 1995 (section 3.3). Comprehensive sea-based in-water optical profile data acquisition protocols were devised based on those already laid down by the SeaWiFS committee (Mueller & Austin, 1995). A reliable communication link between ship and aircraft was maintained and sampling from the sea and from the air was undertaken in concert. All airborne data acquired in the vicinity of the ships could thus be validated through comparison with the results which the in-water optical profiles yielded.

3. *To assess the optical characteristics of the waters surveyed and to develop a  $K_d(490)$  algorithm for use in the coastal zone*

In-water optical profiles were employed to assess the surveyed waters of the Humber Estuary and North Sea. Water classifications extending from Jerlov's (1976) and Morel & Prieur's (1977) theories were used to define the coastal and estuarine conditions monitored during this study (section 5.1). This information provides the researcher with an overall view of the nature and content of the waters under study. For a more detailed analysis of the optical characteristics of the case II waters of the Humber Estuary and its environs, a  $K_d(490)$  algorithm, which takes as its basis the theory put forward by Austin & Petzold (1981), was developed for use in coastal waters (section 5.2).

4. *To utilise and enhance the processing routines used to correct the CASI and ATM*

Each image processing stage was assessed and validated through comparison with in-water optical profiled data (chapter 4). The main focus of the enhancement of the processing routines used to correct NERC CASI and ATM data comprised the development of automated correction procedures for erroneous location and attitude data contained within the datastream (section 4.2.4). This information is necessary for the geometric correction of NERC image data and it was found that much of the information originally present

within the datastream was of insufficient quality. Much effort thus went into the development of routines to allow the rectification of erroneous data points. These routines are now used for all NERC CASI and ATM data acquired using the IDS.

*5. To test atmospheric correction routines developed for use with the CASI*

The atmospheric correction routines contained within the COAST software were tested through comparison with in-water optical profile data acquired coincident with CASI images (section 4.2.2). The fully atmospherically corrected results did not compare well with those measured. It is suggested that the Rayleigh scattering correction is effective but that the full atmospheric correction, which comprises a Rayleigh and an aerosol correction, does not perform well for the datasets acquired for this study.

*6. To develop and substantiate algorithms to quantify SPM concentration in the Humber Estuary using CASI data and sea-surface temperature and salinity in the Tweed Estuary using ATM data*

An algorithm for the derivation of SPM concentration from CASI data acquired in the Humber Estuary was devised and tested (section 4.2.3.1). An automated routine for the determination of sea-surface temperature from thermal-infrared ATM data was enhanced for use in the Tweed Estuary and an algorithm to derive salinity determined (section 4.2.3.2). These algorithms were used successfully within this study to investigate the nature and content of the estuarine waters of the Humber and Tweed. The detailed definition of SPM concentrations and sea-surface temperature and salinity that airborne remote sensing provides for particular sections of the tidal cycle is an important addition to the information available to estuarine and coastal zone managers.

*7. To develop a methodology for the estimation of SPM flux in the Humber Estuary through the incorporation of SPM concentration information derived from CASI images and hydrodynamically modelled flows*

Two-dimensional Fourier Transforms of the SPM concentration images were employed to assess the transect line along which the maximum variation of SPM concentrations and so movement of flux lay (section 5.3.1). A transect was taken from each image which lay close to this ideal and encompassed as much image data as possible, the images having slightly different spatial coverages. The transect data were then used, in conjunction with

information derived from an hydrodynamic model and hydrographic charts, to estimate SPM fluxes into and out of the Humber mouth (section 5.4). Present methodologies are coarse-grained and employ point measurements for their definition. The use of remotely sensed images provides a spatially coherent representation of SPM distribution and movement and suggests a more practical alternative to flux calculation. The use of a variety of images acquired at different tidal states and under different tidal conditions enabled an insight into the nature of sediment movement during this study. One-dimensional Fourier Transforms of the transect datasets yielded information pertaining to the fact that SPM moves in patches which elongate into and out of the mouth on the flood and ebb (section 5.3.3). The importance of the patches was determined by attempting to derive a crude model through which it would be possible to predict SPM concentration and flux within the patches from the patch size alone (section 6.4). Algorithms to enable this were set up and generated results with an  $R^2$  of over 0.9 for each image when using constants within the algorithm specific to an individual dataset (equations 6-1 and 6-2). It was impossible to devise a model to monitor the variations in the algorithms' constants for all potential surveys as the data available for this study covered a relatively sparse array of tidal states and conditions. However, with the addition of more data to test the methodology further, the use of airborne remote sensing and spatial analysis techniques to estimate SPM concentration and flux could be a better approach for estuarine and coastal zone managers to adopt over traditional point monitoring.

## **7.2 Recommendations for future work**

Comparisons with conventionally monitored and derived estimates of SPM flux for the survey period were not possible. The end of the Land-Ocean Interaction Study sees the amalgamation of all the data acquired under its umbrella. The vast archive of CASI and ATM image data acquired for LOIS is now more readily available and its quality is assured. If a complete tidal cycle of CASI images exists (or near-complete as an aircraft is limited by the need to refuel) it would be possible to gain flux estimates across the complete tidal range. It may be possible to incorporate data acquired under differing spring and neap conditions by scaling each according to their tidal state. This was not possible here due to the diversity of the surveyed conditions. The availability of more airborne and surface-based data acquired under the LOIS banner would also allow the beginning of work towards an annual flux estimate. It would also enable the

comprehensive validation of the SPM flux derivation techniques demonstrated in this study with actual measurements. In addition, the high resolution hydrodynamic models of the North Sea and Humber Estuary, which are still being developed within an extended LOIS framework, will provide a potential source for data validation.

Within LOIS a vast amount of airborne data was acquired and has now been processed. The natural extension of this work would be to delve into the archive of airborne data to unearth CASI images acquired over the Humber mouth. The larger picture of the nature of SPM and its movement which this study has started to highlight could then be built up. In particular, the contribution of datasets from all types and states of the tide would enable the worker to demonstrate the nature of the estuary throughout the tidal cycle and also during spring and neap conditions.

Future work could address the question of SPM concentration and SPM flux estimation in the Humber Estuary directly from patch size and within-patch water depth, two readily accessible quantities from airborne images and hydrographic charts / digital elevation models respectively. The inclusion of more data should conclusively ascertain the relevance of patch size to SPM flux and thus enable the derivation of a model to predict SPM concentration and SPM flux directly from patch size and within-patch water depth. This would reduce the necessity for expensive and time consuming fieldwork and would provide an essential data source for hydrodynamic modellers who require this sort of information to develop and validate their models.

The success of this type of study provides a unique and novel insight into the flux exchange between the land and sea. The value of remote sensing when adopting an integrated coastal zone management approach is becoming more widely recognised as techniques improve. The usefulness, flexibility and transportability of the multi-dimensional approach reported here is one such important use and a unique information source for the coastal zone manager.

## References

- Aas, E. & Korsbø, B., 1997, *Self-shading effect by radiance meters on upward radiance observed in coastal waters*, Limnology & Oceanography, **42(5)**, 968-974
- Allan, T.D., 1983, *Oceanography from space*, in Cracknell, A.P. (ed.), Remote Sensing Applications in Marine Science and Technology, Dordrecht, Holland : Reidel, 1-6
- Anger, C. D., Babey, S.K. & Adamson, R.J., 1990, *A New Approach to Imaging Spectroscopy*, In Imaging Spectroscopy of the Terrestrial Environment, Vane, G. (ed.), Proc. SPIE 1298, 72-86
- Arnett, R., 1991, *Estuarine Pollution : A case study of the Humber*, Geography, 67-69
- Austin, R.W & Petzold, T.J., 1981, *The determination of the diffuse attenuation coefficient of sea water using the Coastal Zone Color Scanner*, In Gower, J.F.R. (ed.), Oceanography from space, Plenum Press, 239-256
- Bartolucci, L.A., Robinson, B.F. & Silva, L.F., 1977, *Field measurements of the spectral response of natural waters*, Photogrammetric Engineering & Remote Sensing, **43**, 595-598
- Bhargava, D.S., & Mariam, D.W., 1991, *Light penetration depth, turbidity and reflectance related relationships and models*, ISPRS Journal of Photogrammetry & Remote Sensing, **46**, 217-230
- Bhargava, D.S., & Mariam, D.W., 1990, *Spectral reflectance relationships to turbidity generated by different clay materials*, Photogrammetric Engineering and Remote Sensing, **56(2)**, 225-229
- Bottrell, H. & Matthews, A., 1994 *Functional specification of the atmospheric correction and suspended particulate matter concentration models for use in the COAST project*, in Peck, T.M., Compilation of the deliverables for milestone 3 of the COAST project, 3T986D005/1.0
- Bricaud, A. & Morel, A., 1987, *Atmospheric corrections and interpretation of marine radiances in CZCS imagery : Use of a reflectance model*, Oceanologica Acta, **7**, 33-50
- Bukata, R.P., Jerome, J.H., Kondratyev, K.Y. & Poznyakov, D.V., 1995, Optical properties and remote sensing of inland and coastal waters, CRC Press, Boca Raton, Florida, 362pp

- Callison, R.D., Blake, P. & Anderson, J.M., 1987, *The quantitative use of Airborne Thematic Mapper thermal infrared data*, International Journal of Remote Sensing, **8**(1), 113-126
- Cracknell, A.P. & Hayes, L.W.B., 1991, Introduction to Remote Sensing, Taylor & Francis, London, 293pp
- Curran, P.J., Hansom, J.D., Plummer, S.E & Pedley, M.I., 1987, *Multispectral remote sensing of nearshore suspended sediments: A pilot study*, International Journal of Remote Sensing, **8**(1), 103-112
- Curran, P.J. & Novo, E.M.M., 1988, *The relationship between suspended sediment concentration and remotely sensed spectral radiance : A review*, Journal of Coastal Research, **4**(3), 351-368
- Dekker, A.G., Malthus, T.J & Seyhan, E., 1991, *Quantitative modeling of inland water quality for high-resolution MSS systems*, IEEE Transactions on Geoscience & Remote Sensing, **29**(1), 89-95
- Doerffer, R., Fischer, J., Stössel, M., Brockmann, C. & Grassl, H., 1989, *Analysis of Thematic Mapper data for studying the suspended matter distribution in the coast are of the German Bight (North Sea)*, Remote Sensing of the Environment, **28**, 61-73
- Dyer, K.R., 1986, Coastal and estuarine sediment dynamics, John Wiley & Sons, UK, 342pp
- Falconer, R.A. & Owens, P.H., 1990, *Numerical Modeling of Suspended Sediment Fluxes in Estuarine Waters*, Estuarine, Coastal and Shelf Science, **31**, 745-762
- Ferrier, G., 1995, *A field study of the variability in the suspended sediment concentration-reflectance relationship*, International Journal of Remote Sensing, **16**(14), 2713-2720
- Gordon, H.R., Brown, O.B., Evans, R.H., Brown, J.W., Smith, R.C., Baker, K.S. & Clark, D.K., 1988, *A semianalytic radiance model of ocean color*, Journal of Geophysical Research, **93**(D9), 10909-10924
- Gordon, H.R., Brown, O.B. & Jacobs, M.M., 1975, *Computed relationships between the inherent and apparent optical properties of a flat homogenous ocean*, Applied Optics, **14**, 417-427
- Gordon, H.R. & McCluney, W.R., 1975, *Estimation of the depth of sunlight penetration in the sea for remote sensing*, Applied Optics, **14**(2), 413-416

- Gordon, H.R. & Morel, A.Y., 1983, *Remote assessment of ocean color for interpretation of satellite visible imagery*, Lecture Notes on Coastal and Estuarine Studies, Springer-Verlag, New York, Berlin, Heidelberg, Tokyo, 19-28
- Gordon, H.R. & Wang, M., 1994, *Retrieval of water-leaving radiance and aerosol optical thickness over the oceans with SeaWiFS: a preliminary algorithm*, Applied Optics, **33**(3), 443-452
- Gregg, W.W., Chen, F.C., Mezaache, A.L., Chen, J.D. & Whiting, J.A., 1993, *The simulated SeaWiFS data set, Version 1*, NASA Technical memorandum 104566, vol. 9, Hooker, S.B., Firestone, E.R. & Indest, A.W. (eds.), NASA Goddard Space Flight Center, Maryland, USA, 17pp
- Hadlington, S., 1995, *Muddy secrets of the Humber*, The Independent, 27 June 1995, Section 2, 14
- Han, L., 1997, *Spectral Reflectance with varying suspended sediment concentrations in clear and algae-laden waters*, Photogrammetric Engineering & Remote Sensing, **63**(6), 701-705
- Han, L. & Rundquist, D.C., 1994, *The response of both surface reflectance and underwater light field to various levels of suspended sediments: preliminary results*, Photogrammetric Engineering & Remote Sensing, **60**(12), 1463-1471
- Hardisty, J., 1996, <http://www.hull.ac.uk/HumberNet>
- Hardisty, J., Huntley, D.A., Metcalfe, S.E., Marsden, T.K. & Rouse, H.L., 1995, *Modelling and in situ measurement of sediment flux in the lower Humber with particular reference to freshwater controls, tidal and storm forcing*, In LOIS RACS(C) Second Annual Workshop, 27-29 September, Bristol, UK, LOIS publication No. 54, 8-4
- Hardisty, J. & Rouse, H.L., 1996, *The Humber Observatory : Monitoring, modelling and management for the coastal environment*, Journal of Coastal Research, **12**(3), 683-690
- Jay, D.A., Geyer, W.R., Uncles, R.J., Vallino, J., Largier, J. & Boynton, W.R., 1997, *A Review of Recent Developments in Estuarine Scalar Flux Estimation*, Estuaries, **20**, 262-280
- Jerlov, N.G., 1976, Marine Optics, Elsevier Scientific Publishing Company, Amsterdam, The Netherlands, 231pp



- Kirk, J.T.O., 1994, *The relationship between the inherent and apparent optical properties of surface waters and its dependence on the shape of the volume scattering function*, In Spinrad, R.W., Carder, A.L. & Perry, M.J. (eds.), Ocean Optics, Oxford University Press, 40-58
- Kirk, J.T.O., 1983, Light and photosynthesis in aquatic systems, Cambridge University Press
- Krauss, T.P., Shure, L. & Little, J.N., 1994, Signal processing toolbox : User's guide, The Math Works, Inc., Mass., USA
- Lane, A., Prandle, D., Harrison, A.J., Jones, P.D. & Jarvis, C.J., 1997, *Measuring Fluxes in Tidal Estuaries: Sensitivity to Instrumentation and Associated Data Analyses*, Estuarine, Coastal and Shelf Science, **45**, 433-451
- McCave, I.N., 1987, *Fine sediment sources and sinks around the East Anglian coast (UK)*, Journal of the Geological Society, London, **144**, 149-152
- Mayo, M., Karnieli, A., Gitelson, A. & Ben-Avraham, Z., 1993, *Determination of suspended sediment concentrations from CZCS data*, Photogrammetric Engineering & Remote Sensing, **59(8)**, 1265-1269
- Mockridge, W., Leach, M. & Wilson, A.K., 1997, *Integrating a Daedalus 1268 ATM, attitude GPS and AHRS to achieve scan rate geometric correction*, Third International Airborne Remote Sensing Conference and Exhibition, 7-10 July 1997, Copenhagen, Denmark, **1**, 158-165
- Moore, G.F., Aiken, J., & Lavender, S.J., 1999, *The atmospheric correction of water colour and the quantitative retrieval of suspended particulate matter in case II waters: application to MERIS*, International Journal of Remote Sensing, **20(9)**, 1713-1733
- Morel, A., 1974, *Optical properties of pure sea water*, In, Jerlov, N.G. & Nielsen, S.E., (eds.), Optical aspects of oceanography, Academic Press, London
- Morel, A. & Prieur, L., 1977, *Analysis of variations in ocean color*, Limnology & Oceanography, **22(4)**, 709-722
- Mueller, J.L. & Austin, R.W., 1995, *Ocean optics protocols for SeaWiFS validation, Revision 1*, NASA Technical Memorandum 104566, vol. **25**, Hooker, S.B., Firestone, E.R. & Acker, J.G. (eds.), NASA, Goddard Space Flight Center, Maryland, USA, 67pp
- Mueller, J.L. & Austin, R.W., 1992, *Ocean optics protocols for SeaWiFS validation*, NASA Technical Memorandum 104566, vol. **5**, Hooker S.B. & Firestone E.R. (eds.), NASA, Goddard Space Flight Center, Maryland, USA, 43pp

- Mueller, J.L. & Trees, C.C., 1996, *Revised SeaWiFS pre-launch algorithm for the diffuse attenuation coefficient  $K(490)$* , CHORS technical memorandum 006-96, San Diego State University, USA
- Munday, J.C. & Alföldi, T.T., 1979, *Landsat test of diffuse reflectance models for aquatic suspended solids measurement*, Remote Sensing of the Environment, **8**, 169-183
- Nanu, L. & Robertson, C., 1993, *The effect of suspended sediment depth distribution on coastal water spectral reflectance : Theoretical simulation*, International Journal of Remote Sensing, **14**(2), 225-239
- National Rivers Authority, 1993, The quality of the Humber Estuary 1980-1990, Stanley Hunt Print Ltd., UK
- Natural Environment Research Council, 1992, Land-Ocean Interaction Study. Science plan for a community research project, NERC, UK
- Novo, E.M.M., Hansom, J.D. & Curran, P.J., 1989, *The effect of viewing geometry and wavelength on the relationship between reflectance and suspended sediment concentration*, International Journal of Remote Sensing, **10**(8), 1357-1372
- Pethick, J.S., 1994, *Humber Estuary: Coastal processes and conservation*, unpubl. Report to English Nature by the Institute of Estuarine and Coastal Studies, The University of Hull, 56pp
- Pethick, J.S., 1988, *The physical characteristics of the Humber*, In Jones, N.V. (ed.), A dynamic estuary : Man, nature and the Humber, Hull University Press, 31-45
- Robinson, M-C. & Morris, K.P., 1997, *The Validation of Atmospheric Correction Algorithms for the CASI in the Coastal Zone*, Proceedings of the Third International Airborne Remote Sensing Conference and Exhibition, 7-10 July 1997, Copenhagen, Denmark, ERIM, Michigan, vol. 2, II-455-II-462
- Ritchie, J.C., Schiebe, F.R. & Cooper, C.M., 1983, *Spectral measurements of surface suspended matter in an oxbow lake in the lower Mississippi valley*, Journal of Freshwater Ecology, **2**(2), 175-181
- Ritchie, J.C., Schiebe, F. & McHenry, J.R., 1976, *Remote Sensing of suspended sediments in surface waters*, Photogrammetric Engineering Remote Sensing, **42**(12), 1539 - 1545
- Stumpf, R.P. & Pennock, J.R., 1991, *Remote estimation of the diffuse attenuation coefficient in a moderately turbid estuary*, Remote Sensing of the Environment, **38**, 183-191

- Stumpf, R.P & Pennock, J.R., 1989, *Calibration of a general optical equation for remote sensing of suspended sediments in a moderately turbid estuary*, Journal of Geophysical Research, **94(C10)**, 14363-14371
- Tassan, S., 1997, *A numerical model for the detection of sediment concentration in stratified river plumes using Thematic Mapper data*, International Journal of Remote Sensing, **18(12)**, 2699-2705
- Tassan, S., 1993, *An improved in-water algorithm for the determination of chlorophyll and suspended sediment concentration from Thematic Mapper data in coastal waters*, International Journal of Remote Sensing, **14(6)**, 1221-1229
- Tassan, S. & Sturm, B., 1986, *An algorithm for the retrieval of sediment content in turbid coastal waters from CZCS data*, International Journal of Remote Sensing, **7(5)**, 643-655
- Turner, R.K., Lorenzoni, I., Beaumont, N., Bateman, I.J., Langford, I.H. & McDonald, A.L., 1998, *Coastal management for sustainable development : Analysing environmental and socio-economic changes on the UK coast*, The Geographical Journal, **164(3)**, 269-281
- Uncles, R.J., *personal communication*, Centre for Coastal and Marine Sciences, Plymouth Marine Laboratory, Prospect Place, West Hoe, Plymouth PL1 3DH
- Uncles, R.J. & Jordan, M.B., 1994, *Measurements of Tidal Currents and Estimated Energy Fluxes in the Bristol Channel*, In, Beven, K.J., (ed.), Mixing and Transport in the Environment, John Wiley & Sons., 221-245
- Uncles, R.J. & Stephens, J.A., 1997, *Dynamics of turbidity in the Tweed Estuary*, Estuarine, Coastal & Shelf Science, **45**, 745-758
- Uncles, R.J. & Stephens, J.A., 1996, *Salt intrusion in the Tweed Estuary*, Estuarine, Coastal & Shelf Science, **43**, 271-294
- Uncles, R.J., Stephens, J.A. & Plummer, D.H., 1997a, *Sediment characteristics and transport in the Humber-Ouse Estuary*, Land-Ocean Interaction Study Second annual meeting, 18 - 20 March 1997, Hull, LOIS publication No. 323, NERC, UK
- Uncles, R.J., Stephens, J.A. & Murphy, R.J., 1997b, *Aircraft and sea-truth observations of a small-scale estuarine intrusion front*, Journal of Marine Systems, **12**, 199-219
- Viollier, M. & Sturm, B., 1984, *CZCS data analysis in turbid coastal water*, Journal of Geophysical Research, **89(D4)**, 4977-4985

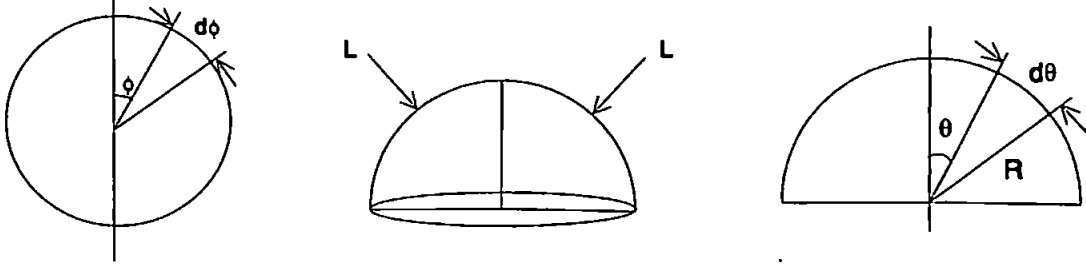
- Wilson, A.K., *personal communication*, Section for Earth Observation, Institute of Terrestrial Ecology, Monks Wood, Abbots Ripton, Huntingdon, Cambridgeshire PE17 2LS, UK
- Wilson, A.K., 1995, NERC Scientific Services Airborne Remote Sensing handbook, NERC, UK
- Wilson, A.K., 1988, *Calibration of ATM Thermal Data*, Proceedings of the 1986 NERC Airborne workshop, IH Wallingford, 24 February 1998, NERC, 219 - 231
- Wilson, A.K., Mockridge, W. & Robinson, M-C., 1997, *Post-processing to achieve radiometric and geometric correction of ATM and CASI data*, Third International Airborne Remote Sensing Conference and Exhibition, 7-10 July 1997, Copenhagen, Denmark, 1, 447-454
- Xia, L., 1993, *A united model for quantitative remote sensing of suspended sediment concentration*, International Journal of Remote Sensing, 14(14), 2665-2676

## Appendix A : Acronyms

AHRS	Attitude and Heading Reference System
ARSF	Airborne Remote Sensing Facility
ATM	Airborne Thematic Mapper
CASI	Compact Airborne Spectrographic Imager
CCD	Charge Coupled Detector
CH	Challenger cruise identifier
COAST	Coastal Earth Observation Application for Sediment Transport
CTD	Conductivity, Temperature and Depth monitoring apparatus
CZCS	Coastal Zone Color Scanner
DIVAST	Depth Integrated Velocities And Solute Transport
DN	Digital Number
DOM	Dissolved Organic Matter
FFT	Fast Fourier Transform
<i>gcorr</i>	Geometric correction software
GFF	Glass fibre filter F
GIS	Geographic Information System
GPS	Global Positioning System
HDF	Hierarchical Data Format
IDS	Integrated Data System
ILS	Incident Light Sensor
LHS	Left-hand side
LOIS	Land-Ocean Interaction Study
LW	Low Water
MC	Vertical profiling stations related to transaxial flightlines across the Humber Estuary
MSS	Multi-Spectral Scanner
NASA	National Aeronautics and Space Administration
NERC	Natural Environment Research Council
NIR	Near-infrared
NRA	National Rivers Authority
PC	Personal Computer

<i>pdop</i>	position, dilution of precision
PML	Plymouth Marine Laboratory
RACS(C)	Rivers, Atmospheres, Estuaries and Coasts Study (Estuaries & Coasts)
RHS	Right-hand side
SeaWiFS	Sea Wide Field-of-view Sensor
SPM	Suspended Particulate Material
SV	Sea Vigil cruise identifier
SWIR	Shortwave-infrared
TIR	Thermal-infrared
TM	Landsat Thematic Mapper
VP	Vertical profile stations along the offshore track from the Humber mouth
3D	Three-dimensional

## Appendix B : Proof that $Q = \pi$ for a Lambertian reflector



where:  $L$  is the radiance (directional flux) hitting the surface of a sphere, whose radius is  $R$ , at an angle  $\theta$  with the vertical and  $\phi$  with the horizontal.

$$\frac{E}{L} = \int_0^{\frac{\pi}{2}} \int_0^{2\pi} \frac{R d\theta R \sin \theta d\phi \cos \phi}{R^2}$$

where:  $E$  is the irradiance (diffuse flux)

$$\frac{E}{L} = \int_0^{\frac{\pi}{2}} \sin \theta \cos \theta [2\pi] d\theta$$

$$\frac{E}{L} = 2\pi \int_0^{\frac{\pi}{2}} \frac{1}{2} \sin 2\theta d\theta = \pi \left[ -\frac{1}{2} \cos 2\theta \right]_0^{\frac{\pi}{2}}$$

$$\frac{E}{L} = \pi \left[ -\frac{1}{2} \cos \pi + \frac{1}{2} \cos 0 \right] = \pi \left[ \frac{1}{2} + \frac{1}{2} \right] = \pi$$

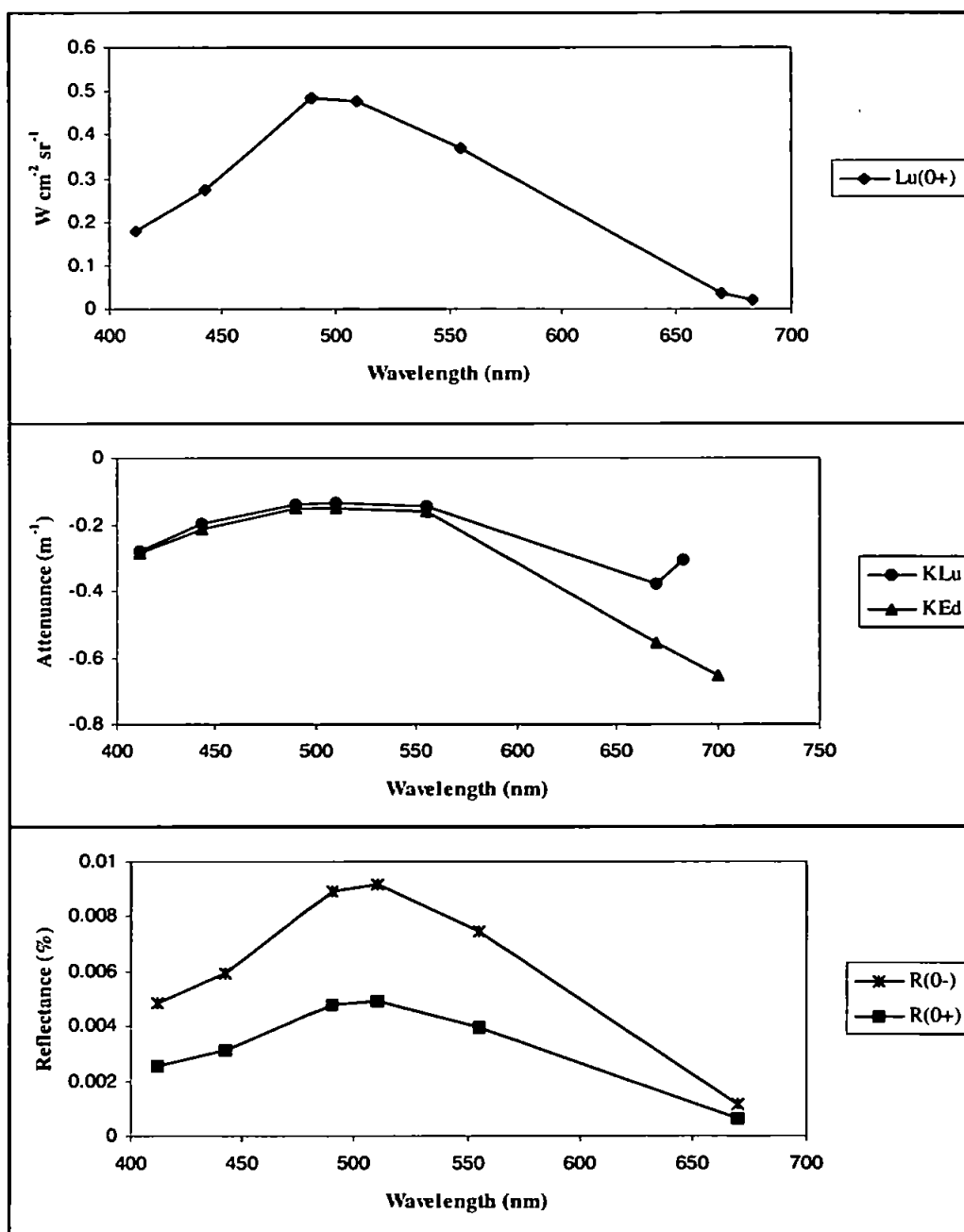
$$E = L\pi$$

$$Q = \frac{E}{L}$$

$Q = \pi$ for a perfectly absorbing Lambertian water surface
--

**Profile A : 6 April 1995 (CH118a), 10:23 - 11:14 GMT**SPM concentration =  $0.44 \text{ mg m}^{-3}$  Chlorophyll concentration =  $0.46 \text{ mg m}^{-3}$  Salinity = 34.36

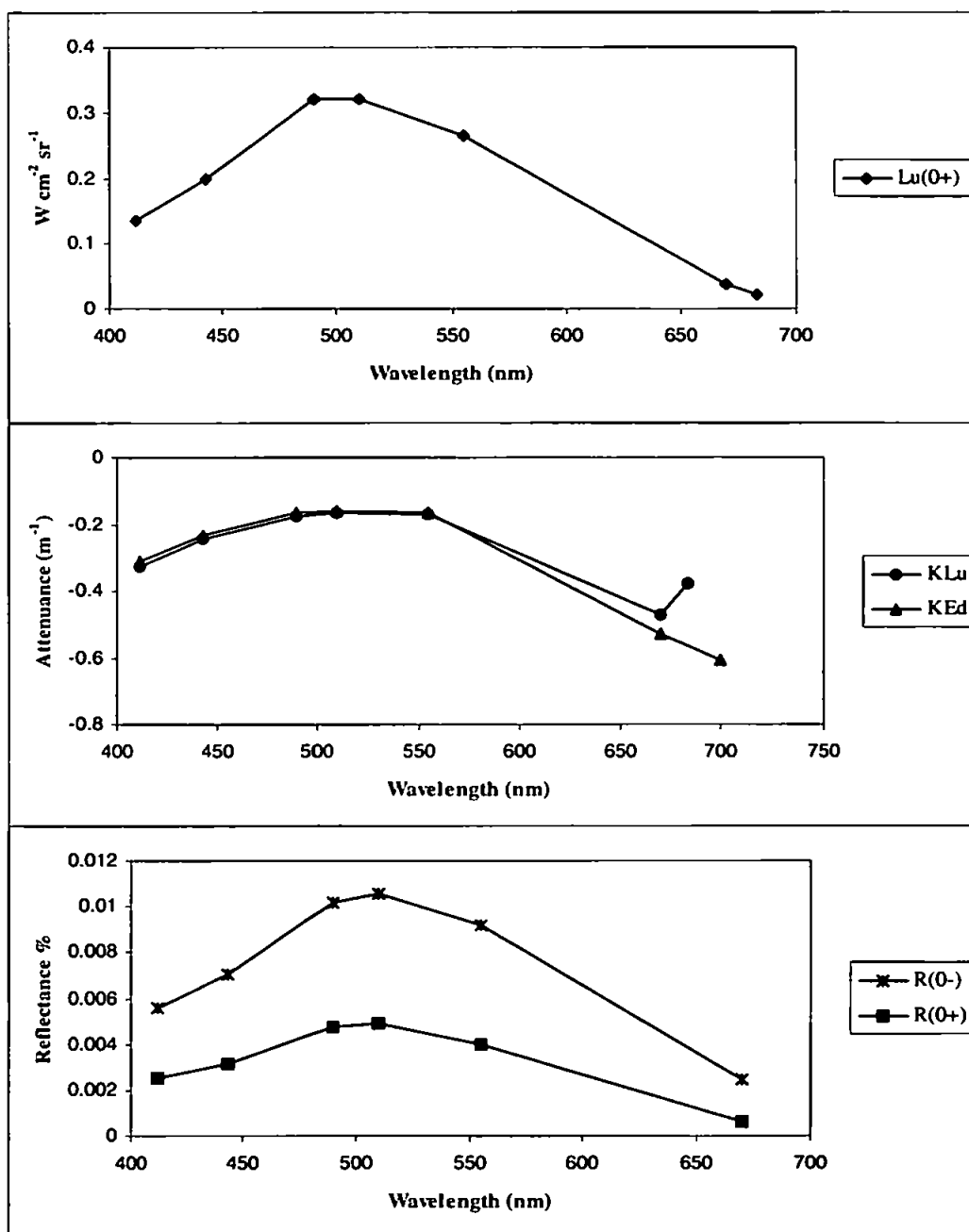
$\lambda$	$L_u(0^-)$	$L_u(0^+)$	$K_{Lu}$	$E_d(0^-)$	$K_{Ed}$	$R(0^-)$	$R(0^+)$	$z_{90}$
412	0.3304	0.1779	-0.2820	68.2336	-0.2840	0.0048	0.0026	-3.5211
443	0.5041	0.2724	-0.1989	84.6794	-0.2133	0.0060	0.0031	-4.6890
490	0.8933	0.4848	-0.1387	99.9569	-0.1515	0.0089	0.0048	-6.6006
510	0.8759	0.4760	-0.1349	95.3094	-0.1511	0.0092	0.0049	-6.6193
555	0.6803	0.3708	-0.1447	90.9808	-0.1611	0.0075	0.0040	-6.2056
670	0.0634	0.0347	-0.3804	54.3745	-0.5535	0.0012	0.0006	-1.8068
683	0.0362	0.0198	-0.3039					
700				33.8401	-0.6565			-1.5232





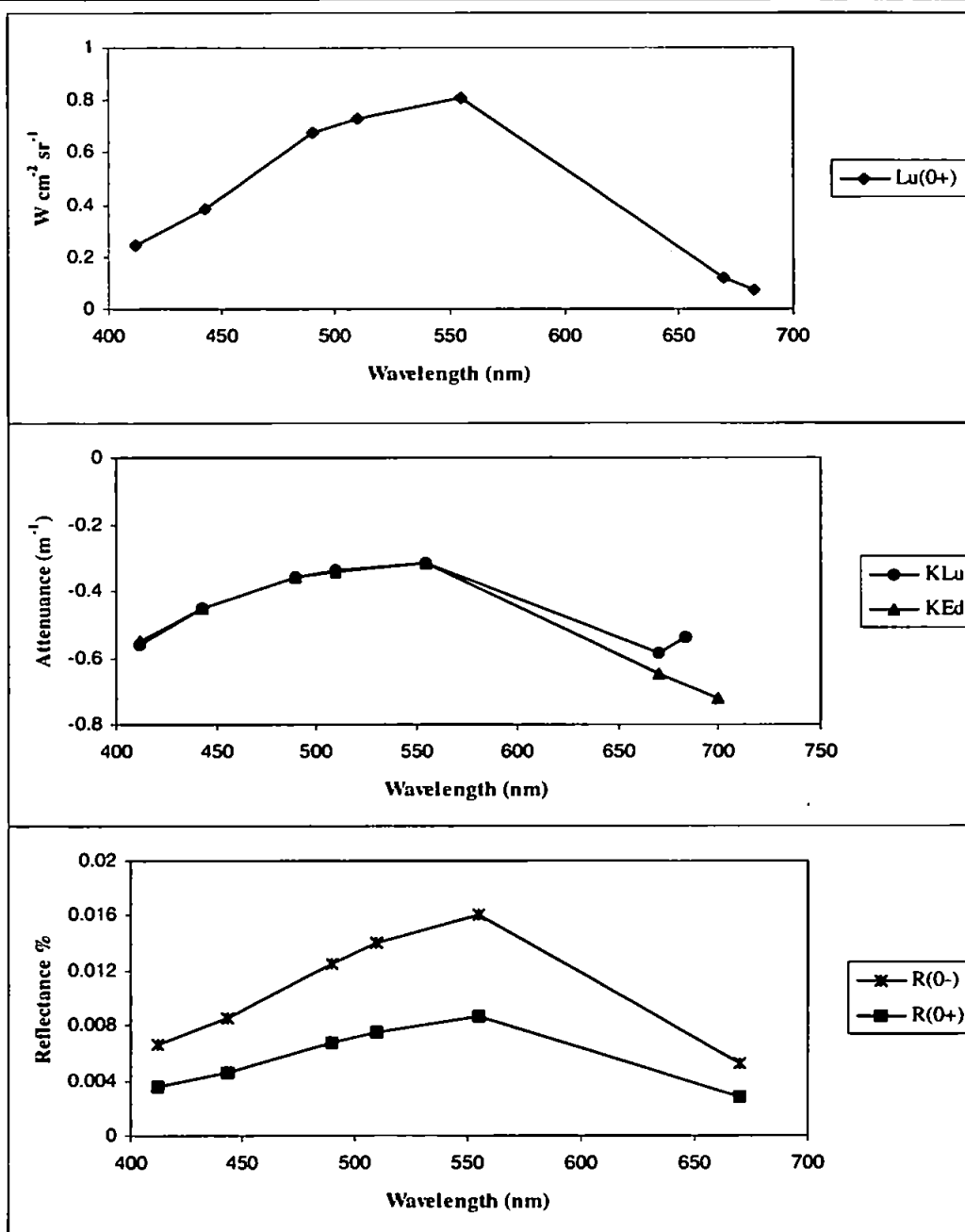
**Profile B : 10 April 1995 (CH118a), 10:35 - 10:46 GMT**SPM concentration =  $0.72 \text{ mg m}^{-3}$  Chlorophyll concentration =  $0.32 \text{ mg m}^{-3}$  Salinity = 34.20

$\lambda$	$L_u(0^-)$	$L_u(0^+)$	$K_{Lu}$	$E_d(0^-)$	$K_{Ed}$	$R(0^-)$	$R(0^+)$	$z_{90}$
412	0.2498	0.1345	-0.3285	44.6685	-0.3113	0.0056	0.0030	-3.2123
443	0.3696	0.1997	-0.2428	52.5556	-0.2359	0.0070	0.0037	-4.2398
490	0.5930	0.3218	-0.1748	58.4643	-0.1673	0.0101	0.0054	-5.9780
510	0.5885	0.3198	-0.1671	55.7243	-0.1632	0.0106	0.0056	-6.1274
555	0.4852	0.2644	-0.1729	52.9975	-0.1683	0.0092	0.0049	-5.9410
670	0.0699	0.0383	-0.4741	28.9190	-0.5285	0.0024	0.0013	-1.8922
683	0.0404	0.0221	-0.3794					
700				16.8099	-0.6065			-1.6488



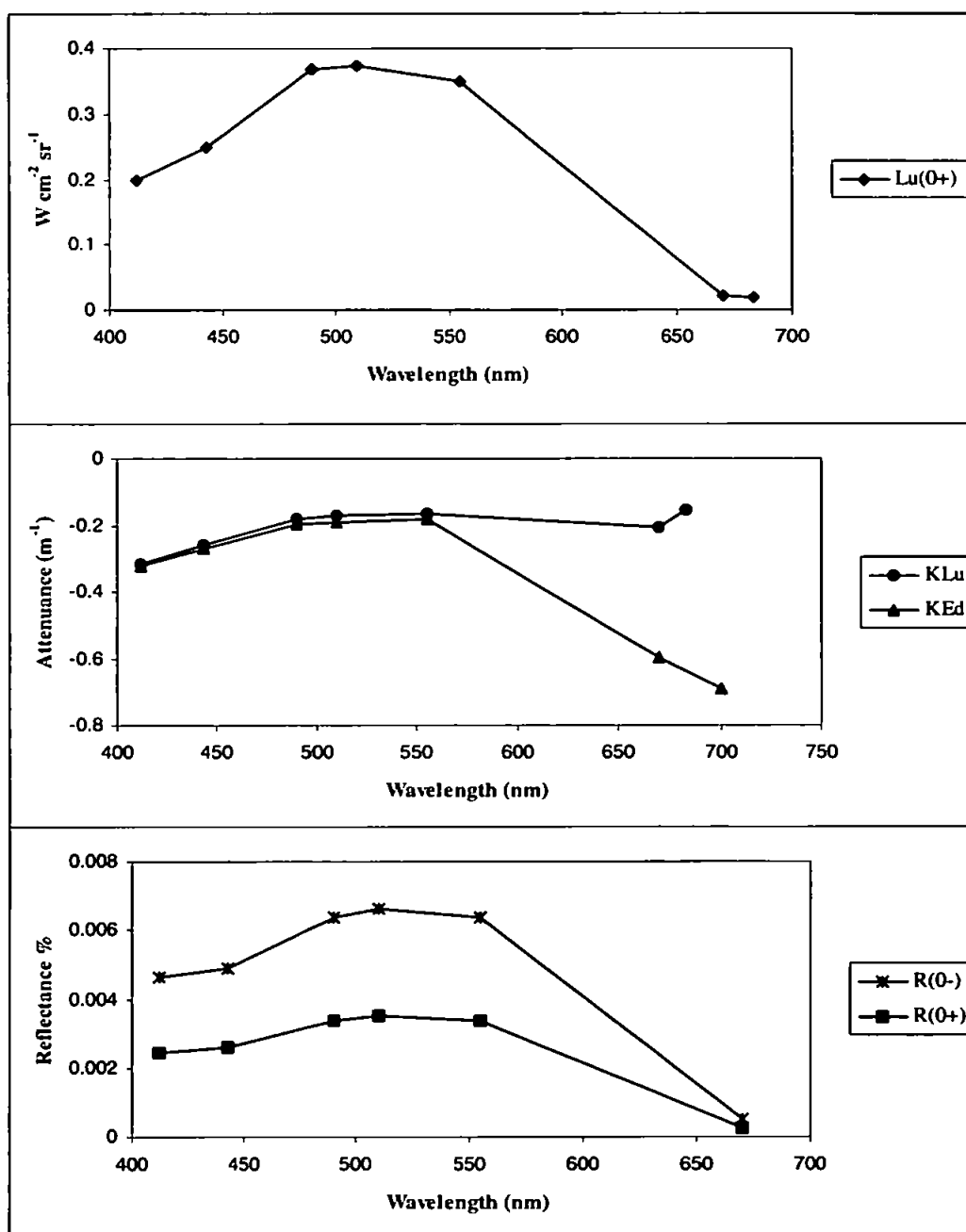
**Profile C : 12 April 1995 (CH118a), 09:35 - 10:22 GMT**SPM concentration =  $3.15 \text{ mg m}^{-3}$  Chlorophyll concentration =  $0.9 \text{ mg m}^{-3}$  Salinity = 34.22

$\lambda$	$L_u(0^-)$	$L_u(0^+)$	$K_{Lu}$	$E_d(0^-)$	$K_{Ed}$	$R(0^-)$	$R(0^+)$	$z_{90}$
412	0.4500	0.2422	-0.5624	67.375739	-0.55064	0.0067	0.0035	-1.8161
443	0.7111	0.3842	-0.4520	82.813989	-0.4531	0.0086	0.0046	-2.2070
490	1.2494	0.6780	-0.3581	99.621001	-0.35782	0.0125	0.0067	-2.7947
510	1.3395	0.7279	-0.3399	95.898659	-0.3419	0.0140	0.0075	-2.9248
555	1.4806	0.8069	-0.3164	92.146067	-0.31779	0.0161	0.0087	-3.1467
670	0.2191	0.1200	-0.5893	41.979693	-0.64915	0.0052	0.0028	-1.5405
683	0.1371	0.0751	-0.5414					
700				27.312569	-0.72062			-1.3877



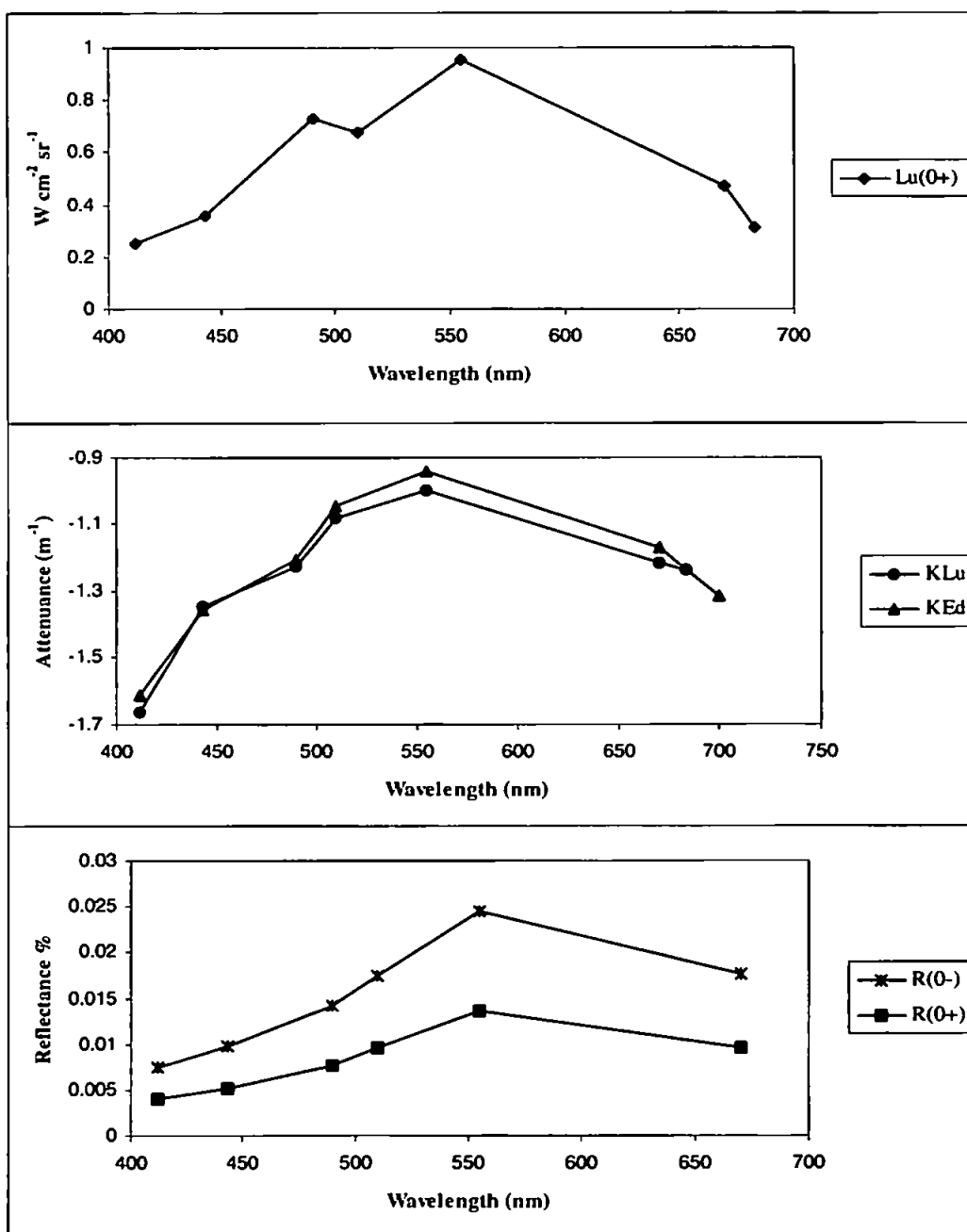
**Profile D : 21 April 1995 (CH118b), 09:51 - 10:27 GMT**SPM concentration =  $0.74 \text{ mg m}^{-3}$  Chlorophyll concentration =  $1.4 \text{ mg m}^{-3}$  Salinity = 34.54

$\lambda$	$L_u(0^-)$	$L_u(0^+)$	$K_{Lu}$	$E_d(0^-)$	$K_{Ed}$	$R(0^-)$	$R(0^+)$	$z_{90}$
412	0.3699	0.1991	-0.3157	79.8289	-0.3213	0.0046	0.0024	-3.1120
443	0.4620	0.2496	-0.2584	94.4374	-0.2703	0.0049	0.0026	-3.6990
490	0.6805	0.3693	-0.1830	106.8510	-0.1987	0.0064	0.0034	-5.0320
510	0.6868	0.3732	-0.1705	103.9822	-0.1903	0.0066	0.0035	-5.2557
555	0.6408	0.3493	-0.1643	100.7827	-0.1838	0.0064	0.0034	-5.4422
670	0.0372	0.0204	-0.2068	73.5021	-0.5973	0.0005	0.0003	-1.6743
683	0.0327	0.0179	-0.1552					
700				58.7422	-0.6887			-1.4519



**Profile E : 23 April 1995 (CH118b), 10:37 - 10:55 GMT**SPM concentration =  $12.84 \text{ mg m}^{-3}$  Chlorophyll concentration =  $0.79 \text{ mg m}^{-3}$  Salinity = 34.21

$\lambda$	$L_u(0^-)$	$L_u(0^+)$	$K_{Lu}$	$E_d(0^-)$	$K_{Ed}$	$R(0^-)$	$R(0^+)$	$z_{90}$
412	0.4621	0.2488	-1.6643	62.3907	-1.6118	0.0074	0.0039	-0.6204
443	0.6676	0.3607	-1.3472	68.7874	-1.3576	0.0097	0.0052	-0.7366
490	1.3439	0.7292	-1.2256	94.7526	-1.2049	0.0142	0.0076	-0.8299
510	1.2374	0.6724	-1.0831	70.8195	-1.0456	0.0175	0.0095	-0.9564
555	1.7474	0.9523	-1.0003	71.3406	-0.9404	0.0245	0.0135	-1.0634
670	0.8640	0.4733	-1.2177	49.1916	-1.1725	0.0176	0.0095	-0.8529
683	0.5639	0.3090	-1.2362					
700				52.4761	-1.3181			-0.7587

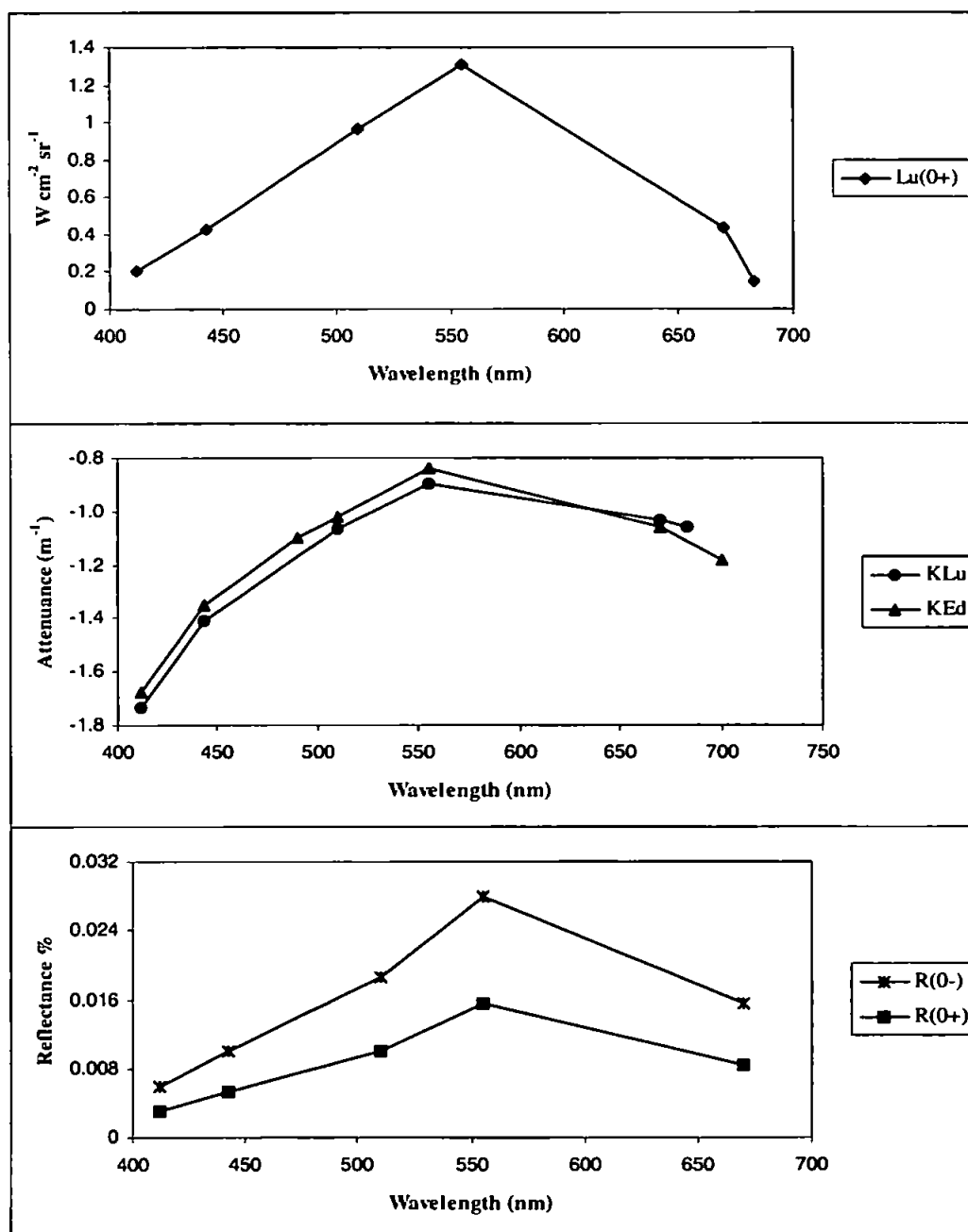


**Profile F : 19 July 1995 (SV23), 13:53 - 14:04 GMT**SPM concentration =  $10.07 \text{ mg m}^{-3}$ 

Chlorophyll concentration = N/A

Salinity = 32.19

$\lambda$	$L_u(0^-)$	$L_u(0^+)$	$K_{Lu}$	$E_d(0^-)$	$K_{Ed}$	$R(0^-)$	$R(0^+)$	$z_{90}$
412	0.3761	0.2025	-1.7367	63.2279	-1.6775	0.0059	0.0031	-0.5961
443	0.7826	0.4228	-1.4131	78.9438	-1.3530	0.0099	0.0053	-0.7391
490				95.5033	-1.1003			-0.9089
510	1.7821	0.9685	-1.0634	96.0423	-1.0208	0.0186	0.0101	-0.9796
555	2.3943	1.3049	-0.8988	85.6915	-0.8403	0.0279	0.0155	-1.1901
670	0.7991	0.4377	-1.0364	51.6177	-1.0629	0.0155	0.0084	-0.9408
683	0.2637	0.1445	-1.0601					
700				47.4715	-1.1846			-0.8442

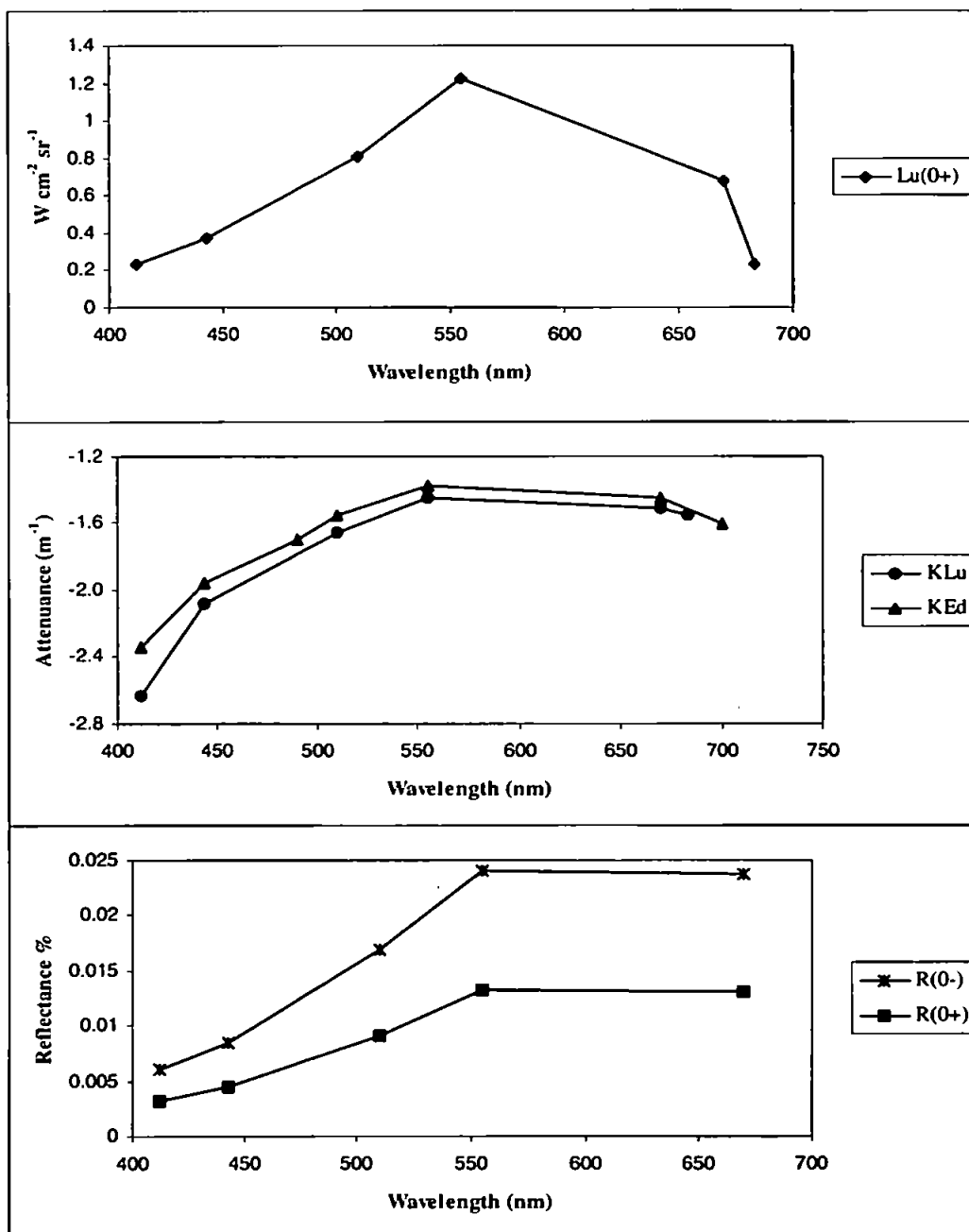


**Profile G : 19 July 1995 (SV23), 14:20 - 14:29 GMT**SPM concentration =  $16 \text{ mg m}^{-3}$ 

Chlorophyll concentration = N/A

Salinity = 32.62

$\lambda$	$L_u(0^-)$	$L_u(0^+)$	$K_{Lu}$	$E_d(0^-)$	$K_{Ed}$	$R(0^-)$	$R(0^+)$	$z_{90}$
412	0.4286	0.2307	-2.6313	70.9190	-2.3404	0.0060	0.0032	-0.4273
443	0.6797	0.3673	-2.0864	80.4574	-1.9567	0.0084	0.0045	-0.5110
490				96.3354	-1.7019			-0.5876
510	1.4875	0.8084	-1.6560	88.3022	-1.5489	0.0168	0.0091	-0.6456
555	2.2414	1.2216	-1.4489	92.9222	-1.3809	0.0241	0.0133	-0.7242
670	1.2347	0.6763	-1.5163	52.0504	-1.4535	0.0237	0.0130	-0.6880
683	0.4277	0.2344	-1.5569					
700				53.9858	-1.6020			-0.6242

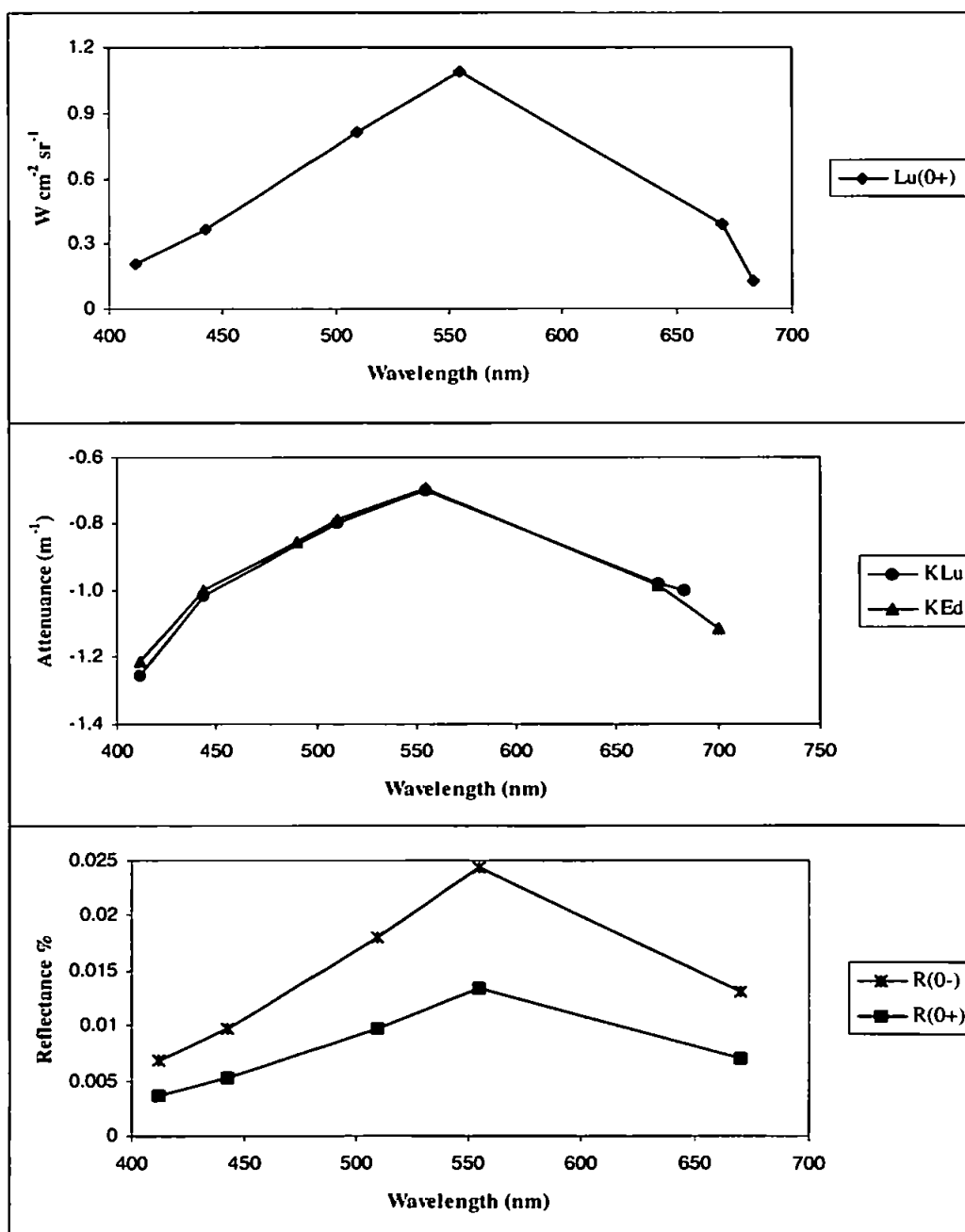


**Profile H : 19 July 1995 (SV23), 14:58 - 15:04 GMT**SPM concentration =  $9.39 \text{ mg m}^{-3}$ 

Chlorophyll concentration = N/A

Salinity = 33.10

$\lambda$	$L_u(0^-)$	$L_u(0^+)$	$K_{Lu}$	$E_d(0^-)$	$K_{Ed}$	$R(0^-)$	$R(0^+)$	$z_{90}$
412	0.3882	0.2090	-1.2553	57.1881	-1.2107	0.0068	0.0036	-0.8260
443	0.6764	0.3655	-1.0145	69.4047	-1.0000	0.0097	0.0052	-0.9999
490				88.0694	-0.8563			-1.1678
510	1.4908	0.8102	-0.7960	82.9363	-0.7850	0.0180	0.0098	-1.2740
555	1.9928	1.0861	-0.7003	81.7990	-0.6932	0.0244	0.0134	-1.4426
670	0.7170	0.3928	-0.9791	55.0872	-0.9861	0.0130	0.0070	-1.0141
683	0.2358	0.1292	-0.9999					
700				52.4029	-1.1121			-0.8992

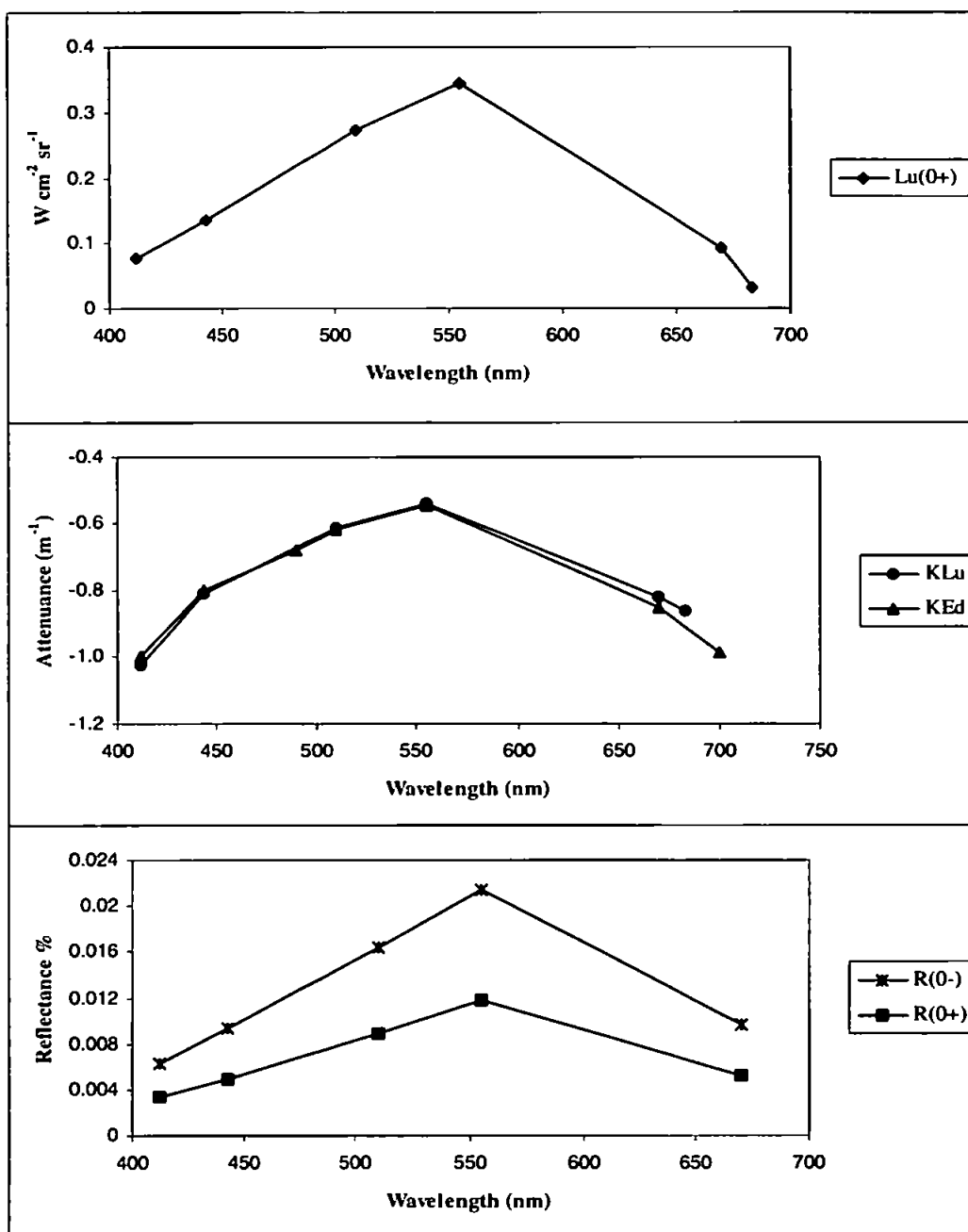


**Profile I : 19 July 1995 (SV23), 15:32 - 15:40 GMT**SPM concentration =  $8.09 \text{ mg m}^{-3}$ 

Chlorophyll concentration = N/A

Salinity = 33.20

$\lambda$	$L_u(0^-)$	$L_u(0^+)$	$K_{Lu}$	$E_d(0^-)$	$K_{Ed}$	$R(0^-)$	$R(0^+)$	$z_{90}$
412	0.1449	0.0780	-1.0222	23.2012	-0.9982	0.0062	0.0033	-1.0018
443	0.2493	0.1347	-0.8125	26.7724	-0.8012	0.0093	0.0050	-1.2481
490				32.8292	-0.6788			-1.4731
510	0.5013	0.2724	-0.6145	30.6802	-0.6187	0.0163	0.0088	-1.6164
555	0.6338	0.3454	-0.5399	29.6360	-0.5477	0.0214	0.0117	-1.8260
670	0.1688	0.0925	-0.8192	17.4615	-0.8530	0.0097	0.0052	-1.1723
683	0.0588	0.0322	-0.8635					
700				16.0029	-0.9872			-1.0130



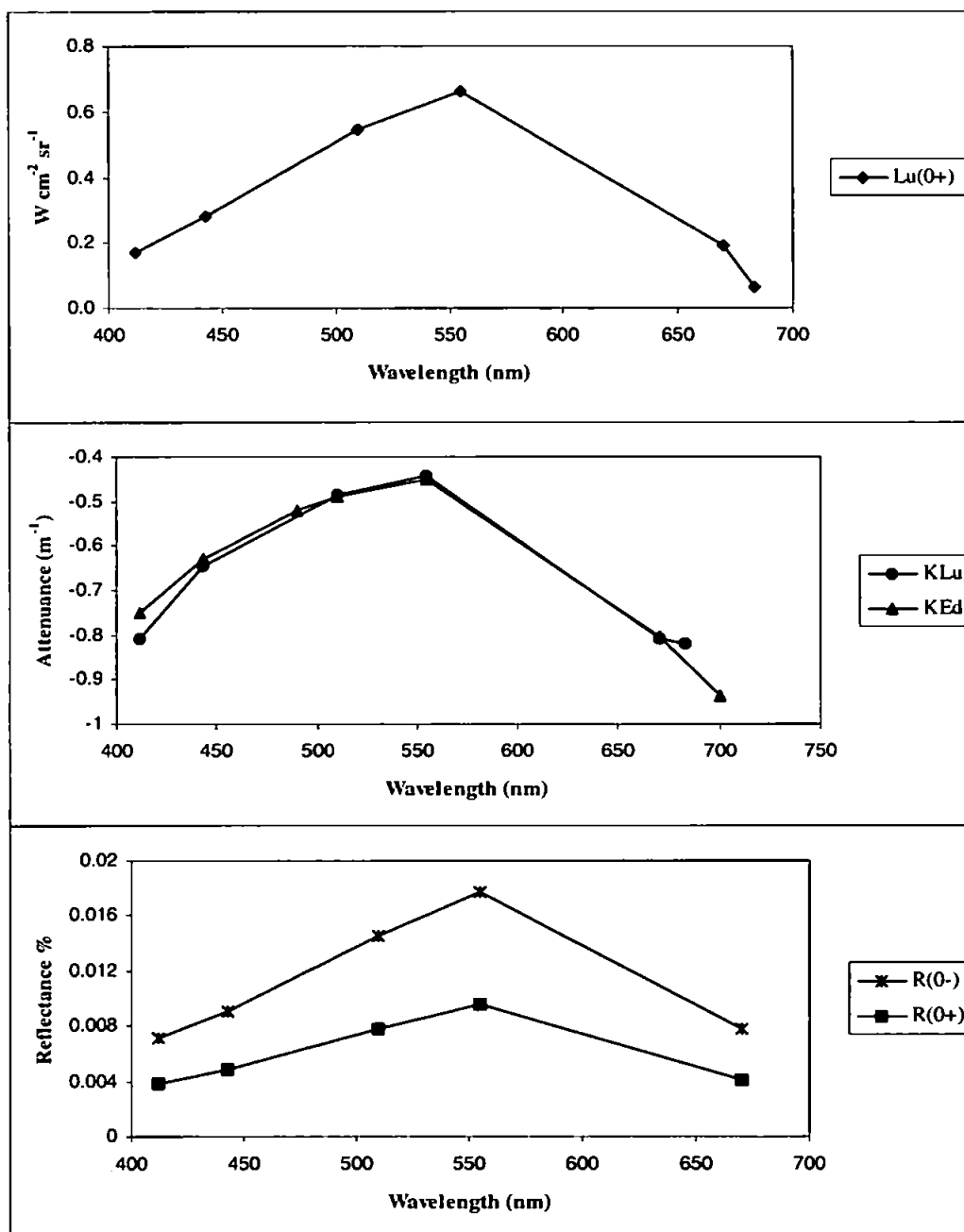


**Profile J : 19 July 1995 (SV23), 15:58 - 16:07 GMT**SPM concentration =  $5.63 \text{ mg m}^{-3}$ 

Chlorophyll concentration = N/A

Salinity = 33.34

$\lambda$	$L_u(0^-)$	$L_u(0^+)$	$K_{Lu}$	$E_d(0^-)$	$K_{Ed}$	$R(0^-)$	$R(0^+)$	$z_{90}$
412	0.3177	0.1711	-0.8103	44.3500	-0.7520	0.0072	0.0038	-1.3298
443	0.5227	0.2824	-0.6471	57.6360	-0.6280	0.0091	0.0048	-1.5924
490				71.5241	-0.5210			-1.9193
510	1.0056	0.5465	-0.4874	69.2977	-0.4912	0.0145	0.0078	-2.0360
555	1.2113	0.6601	-0.4417	68.3802	-0.4505	0.0177	0.0096	-2.2197
670	0.3464	0.1897	-0.8091	44.6463	-0.8045	0.0078	0.0041	-1.2430
683	0.1170	0.0641	-0.8220					
700				39.6339	-0.9381			-1.0660

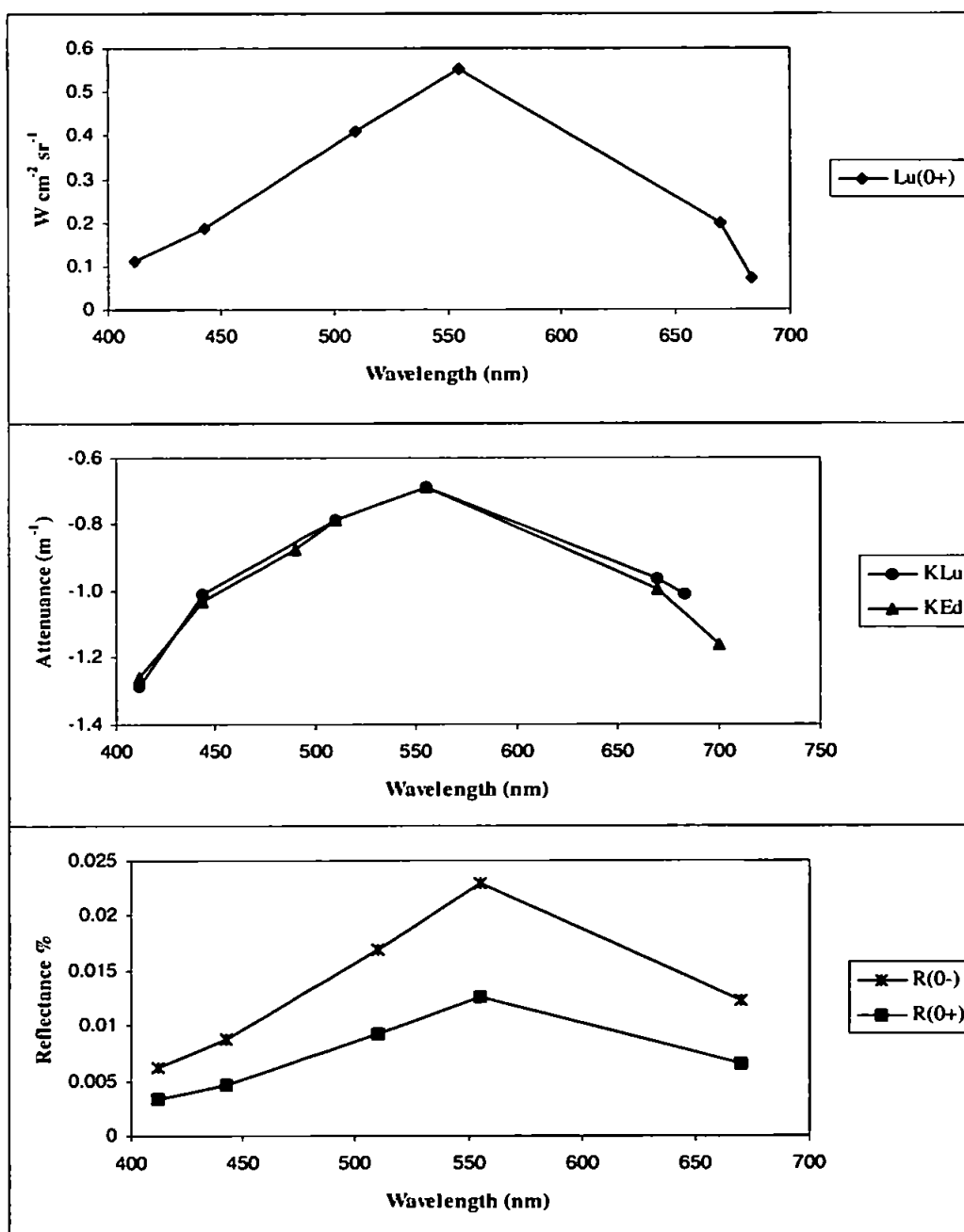


**Profile K : 19 July 1995 (SV23), 16:32 - 16:39 GMT**SPM concentration =  $8.59 \text{ mg m}^{-3}$ 

Chlorophyll concentration = N/A

Salinity = 32.92

$\lambda$	$L_u(0^-)$	$L_u(0^+)$	$K_{Lu}$	$E_d(0^-)$	$K_{Ed}$	$R(0^-)$	$R(0^+)$	$z_{90}$
412	0.2039	0.1098	-1.2867	32.9783	-1.2575	0.0062	0.0033	-0.7952
443	0.3453	0.1866	-1.0115	39.7853	-1.0332	0.0087	0.0046	-0.9679
490				49.0049	-0.8762			-1.1413
510	0.7503	0.4077	-0.7857	44.2539	-0.7846	0.0170	0.0092	-1.2745
555	1.0111	0.5511	-0.6860	44.0373	-0.6903	0.0230	0.0126	-1.4487
670	0.3615	0.1980	-0.9636	29.4974	-0.9955	0.0123	0.0066	-1.0045
683	0.1284	0.0703	-1.0119					
700				29.9954	-1.1593			-0.8626

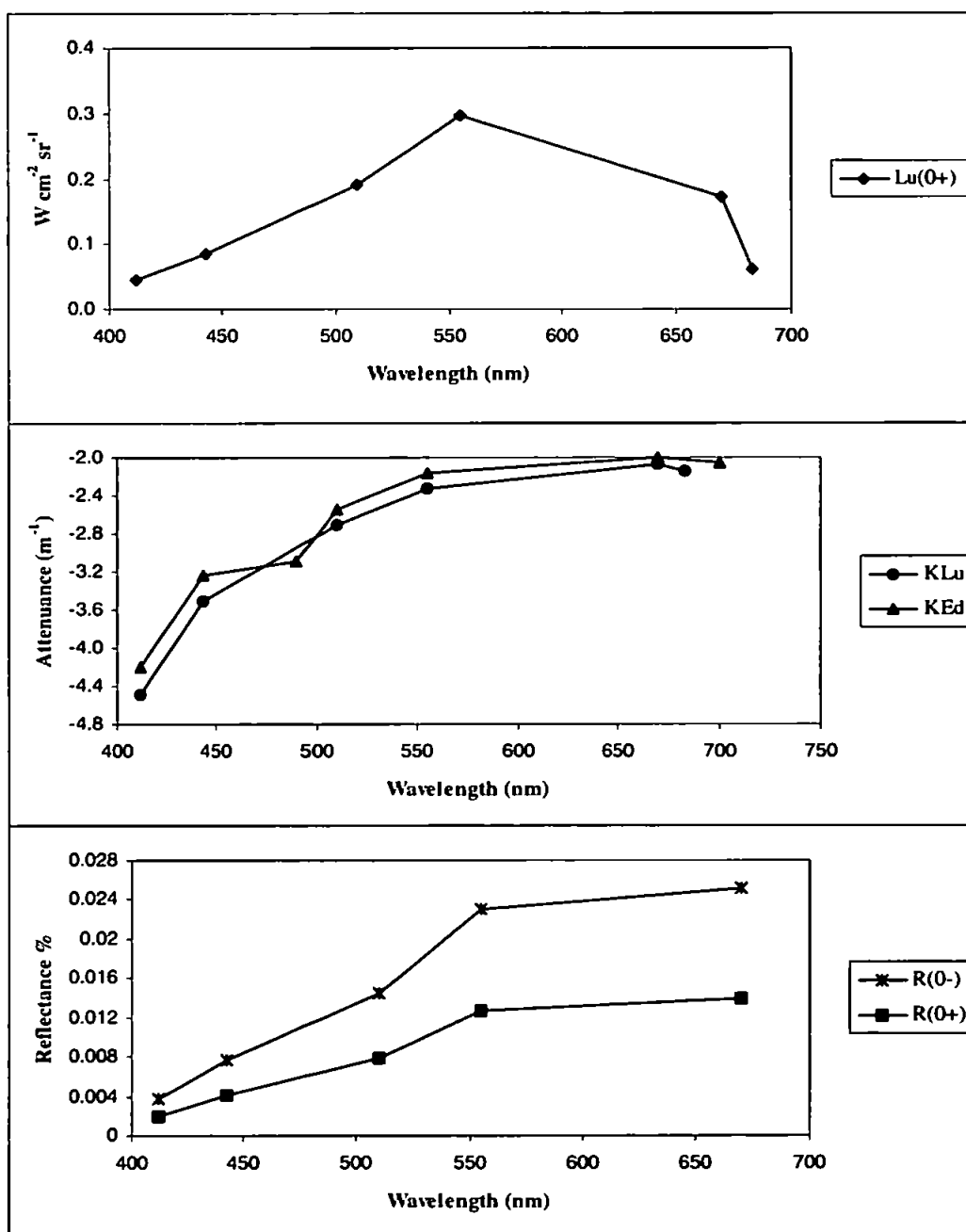


**Profile L : 19 July 1995 (SV23), 17:26 - 17:33 GMT**SPM concentration =  $27.48 \text{ mg m}^{-3}$ 

Chlorophyll concentration = N/A

Salinity = 31.18

$\lambda$	$L_u(0^-)$	$L_u(0^+)$	$K_{Lu}$	$E_d(0^-)$	$K_{Ed}$	$R(0^-)$	$R(0^+)$	$Z_{90}$
412	0.0817	0.0440	-4.4847	22.1698	-4.2055	0.0037	0.0019	-0.2378
443	0.1560	0.0843	-3.5088	20.3262	-3.2302	0.0077	0.0041	-0.3096
490				33.7185	-3.0847			-0.3242
510	0.3523	0.1915	-2.7063	24.3395	-2.5488	0.0145	0.0078	-0.3923
555	0.5446	0.2968	-2.3231	23.5890	-2.1707	0.0231	0.0127	-0.4607
670	0.3144	0.1722	-2.0649	12.4784	-1.9994	0.0252	0.0139	-0.5002
683	0.1133	0.0621	-2.1369					
700				11.2958	-2.0630			-0.4847

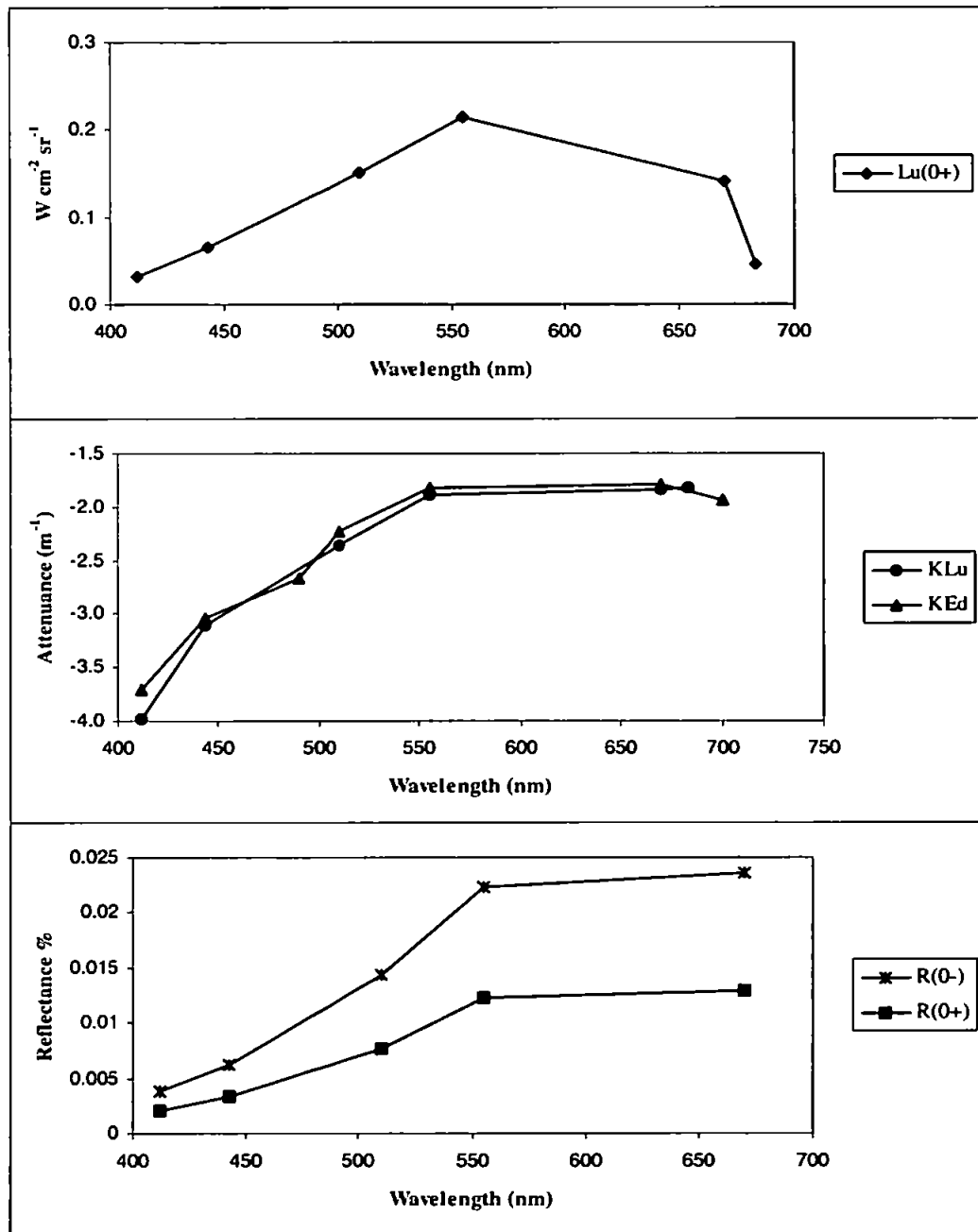


**Profile M : 19 July 1995 (SV23), 17:53 - 17:59 GMT**SPM concentration =  $23.11 \text{ mg m}^{-3}$ 

Chlorophyll concentration = N/A

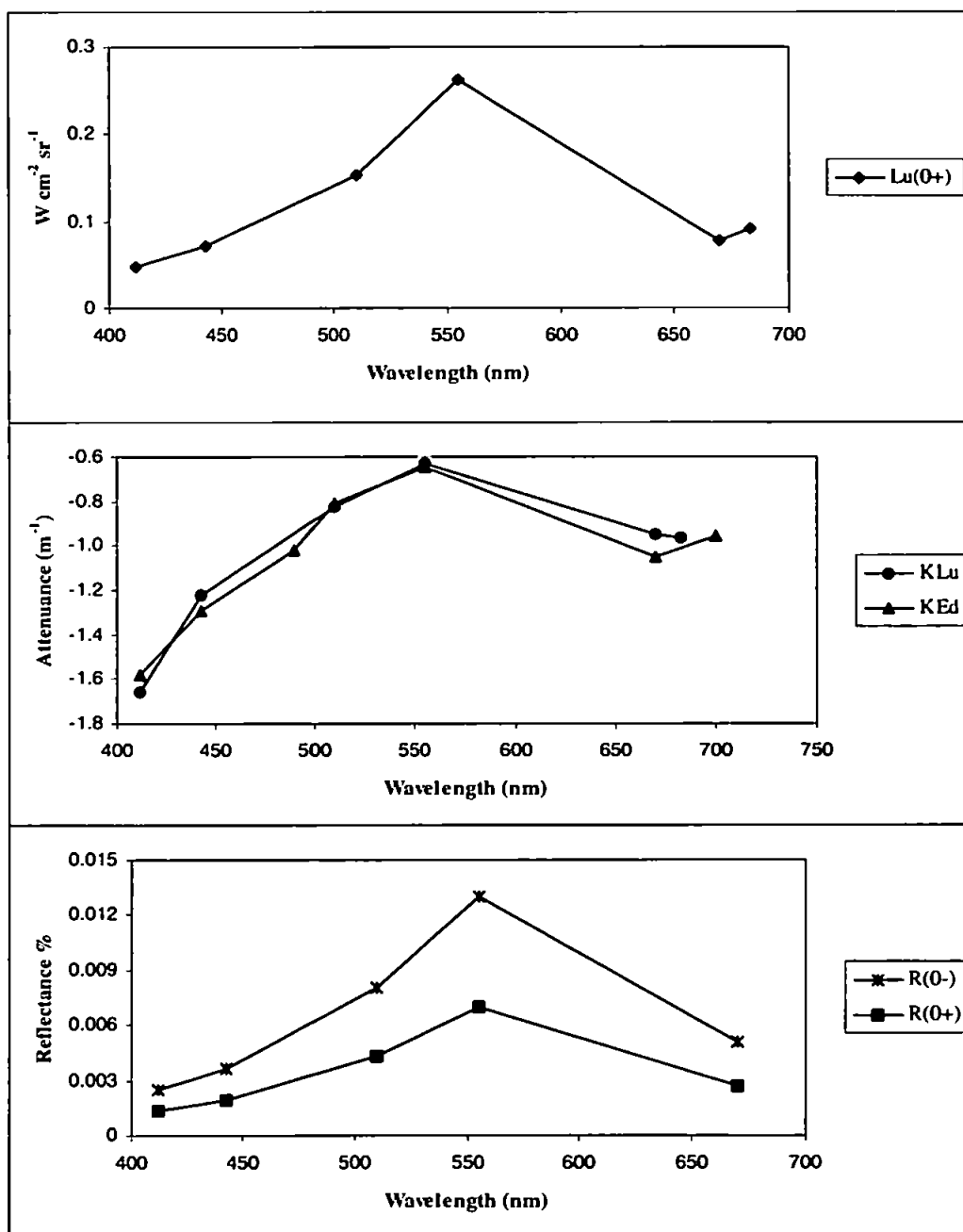
Salinity = 31.02

$\lambda$	$L_u(0^-)$	$L_u(0^+)$	$K_{Lu}$	$E_d(0^-)$	$K_{Ed}$	$R(0^-)$	$R(0^+)$	$z_{90}$
412	0.0608	0.0327	-3.9840	15.8140	-3.7034	0.0038	0.0020	-0.2700
443	0.1207	0.0652	-3.1140	19.2374	-3.0482	0.0063	0.0033	-0.3281
490				24.3798	-2.6728			-0.3741
510	0.2795	0.1519	-2.3586	19.5010	-2.2341	0.0143	0.0077	-0.4476
555	0.3927	0.2140	-1.8847	17.5629	-1.8171	0.0224	0.0123	-0.5503
670	0.2570	0.1408	-1.8373	10.9368	-1.7925	0.0235	0.0129	-0.5579
683	0.0847	0.0464	-1.8196					
700				10.6812	-1.9361			-0.5165



**Profile N : 23 August 1995 (SV24), 08:42 - 08:46 GMT**SPM concentration =  $19.44 \text{ mg m}^{-3}$  Chlorophyll concentration =  $12.05 \text{ mg m}^{-3}$  Salinity = 34.69

$\lambda$	$L_u(0^-)$	$L_u(0^+)$	$K_{Lu}$	$E_d(0^-)$	$K_{Ed}$	$R(0^-)$	$R(0^+)$	$z_{90}$
412	0.0876	0.0472	-1.6571	34.7276	-1.5808	0.0025	0.0013	-0.6326
443	0.1315	0.0710	-1.2209	36.5118	-1.2966	0.0036	0.0019	-0.7712
490				46.8792	-1.0199			-0.9805
510	0.2819	0.1532	-0.8243	35.0258	-0.8076	0.0080	0.0043	-1.2382
555	0.4796	0.2614	-0.6301	36.8218	-0.6448	0.0130	0.0070	-1.5508
670	0.1409	0.0772	-0.9487	27.9291	-1.0504	0.0050	0.0027	-0.9520
683	0.1683	0.0922	-0.9642					
700				22.8310	-0.9604			-1.0413

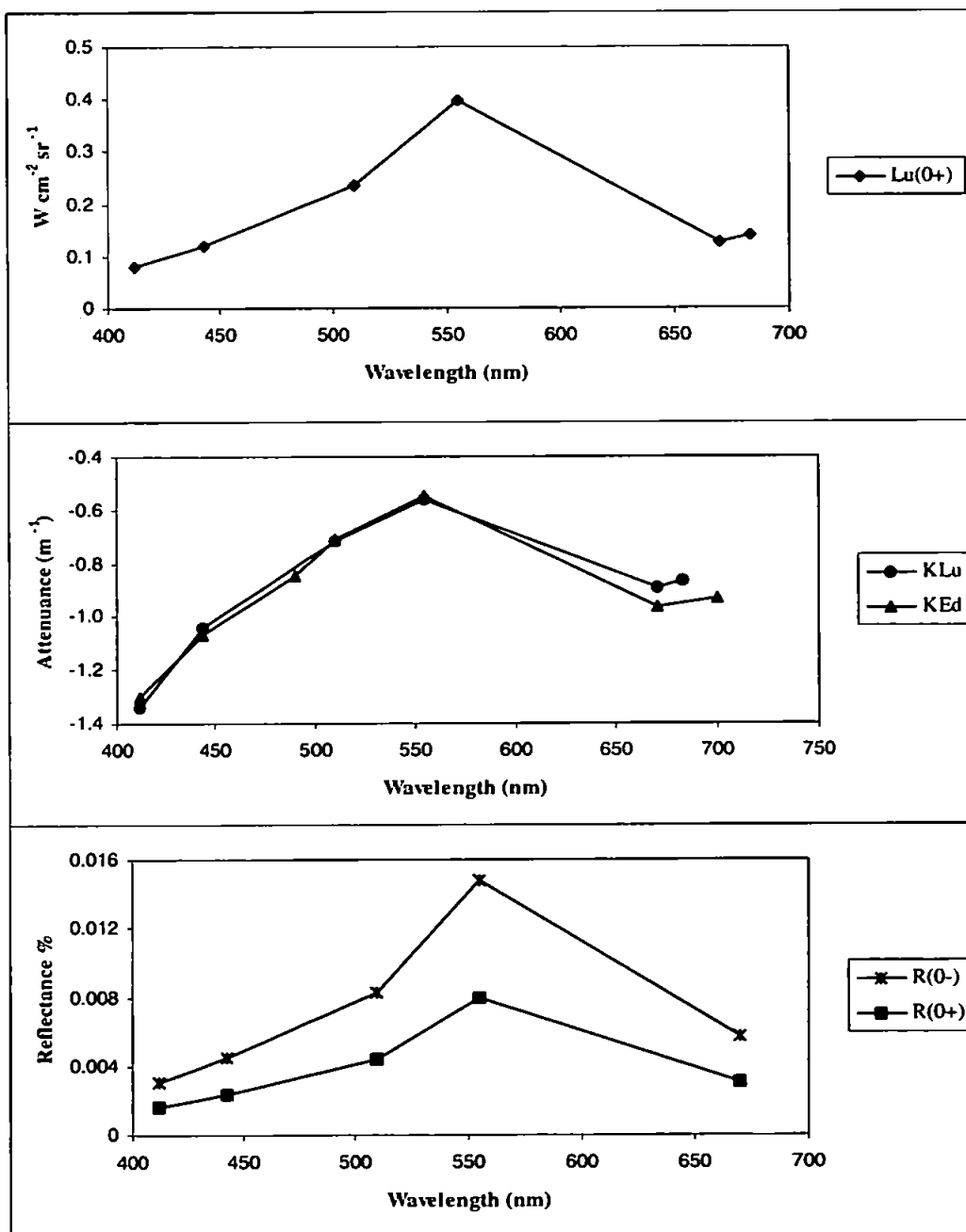


**Profile O : 23 August 1995 (SV24), 09:08 - 09:12 GMT**SPM concentration =  $19.08 \text{ mg m}^{-3}$ 

Chlorophyll concentration = N/A

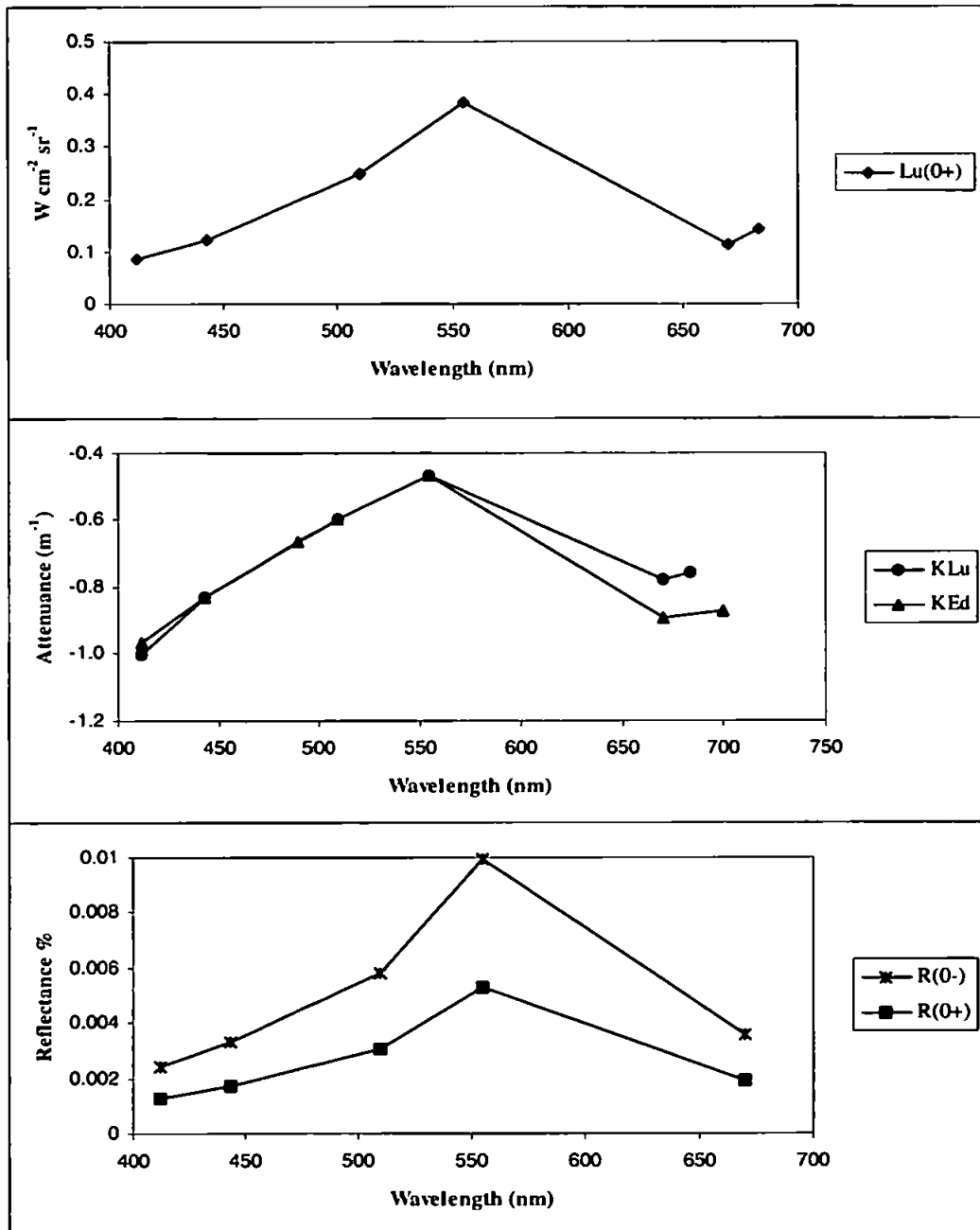
Salinity = 32.76

$\lambda$	$L_u(0^-)$	$L_u(0^+)$	$K_{Lu}$	$E_d(0^-)$	$K_{Ed}$	$R(0^-)$	$R(0^+)$	$z_{90}$
412	0.1483	0.0798	-1.3419	48.5262	-1.3054	0.0031	0.0016	-0.7661
443	0.2180	0.1178	-1.0442	48.5138	-1.0697	0.0045	0.0024	-0.9349
490				60.8384	-0.8476			-1.1798
510	0.4344	0.2361	-0.7186	52.5803	-0.7134	0.0083	0.0044	-1.4016
555	0.7288	0.3972	-0.5616	49.4203	-0.5518	0.0147	0.0079	-1.8122
670	0.2275	0.1246	-0.8906	39.7782	-0.9645	0.0057	0.0030	-1.0368
683	0.2542	0.1393	-0.8699					
700				34.4387	-0.9349			-1.0697



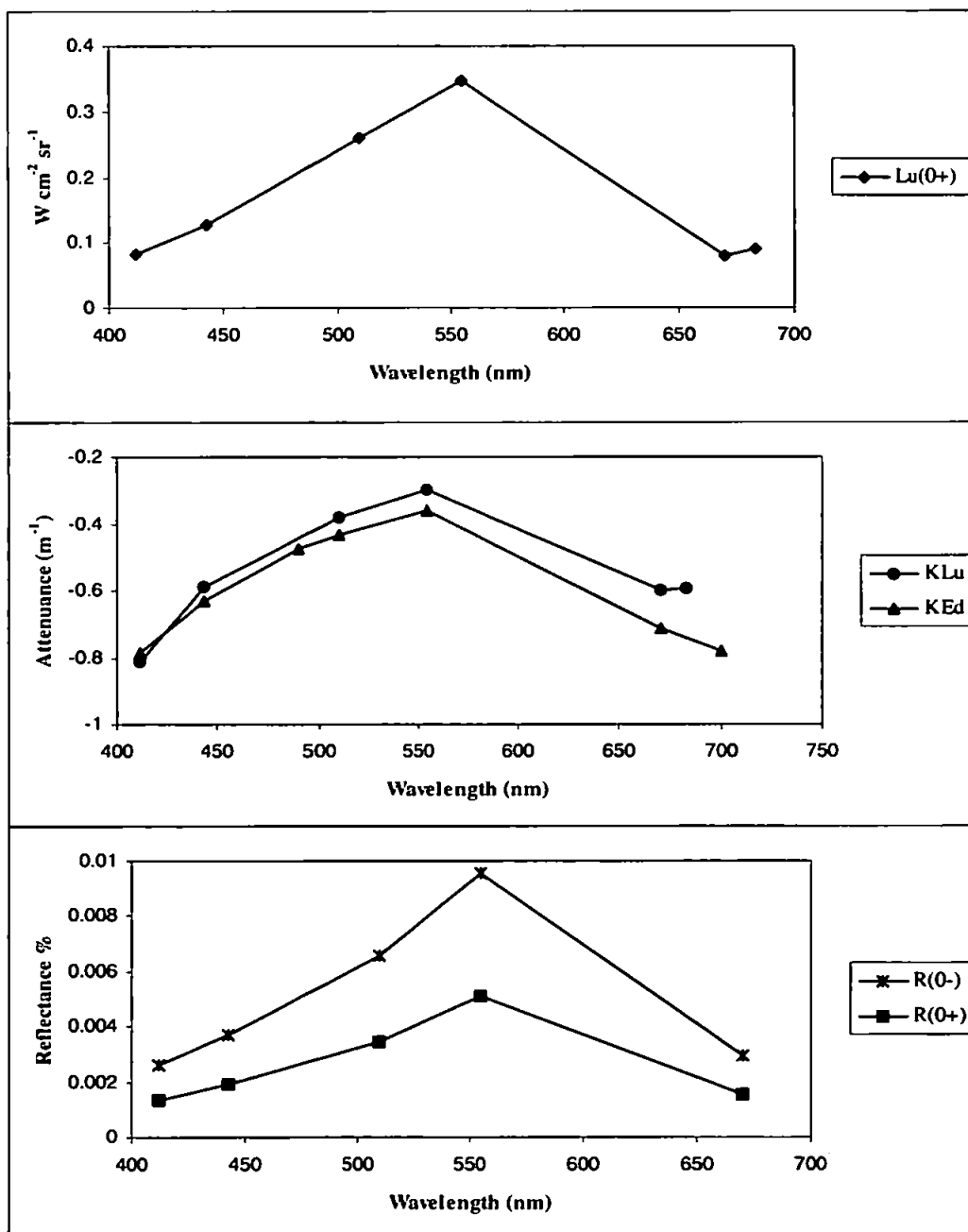
**Profile P : 23 August 1995 (SV24), 09:30 - 09:35 GMT**SPM concentration =  $11.24 \text{ mg m}^{-3}$  Chlorophyll concentration =  $10.04 \text{ mg m}^{-3}$  Salinity = 35.50

$\lambda$	$L_u(0^-)$	$L_u(0^+)$	$K_{Lu}$	$E_d(0^-)$	$K_{Ed}$	$R(0^-)$	$R(0^+)$	$z_{90}$
412	0.1623	0.0874	-1.0051	67.2109	-0.9685	0.0024	0.0013	-1.0326
443	0.2237	0.1209	-0.8320	67.8716	-0.8333	0.0033	0.0017	-1.2001
490				82.7399	-0.6663			-1.5009
510	0.4590	0.2494	-0.5985	78.9435	-0.5954	0.0058	0.0031	-1.6795
555	0.7022	0.3827	-0.4658	70.7872	-0.4700	0.0099	0.0053	-2.1276
670	0.2044	0.1119	-0.7810	56.9868	-0.8940	0.0036	0.0019	-1.1186
683	0.2606	0.1428	-0.7585					
700				49.1418	-0.8738			-1.1444



**Profile Q : 23 August 1995 (SV24), 09:59 - 10:03 GMT**SPM concentration =  $11.14 \text{ mg m}^{-3}$  Chlorophyll concentration =  $4.59 \text{ mg m}^{-3}$  Salinity = 35.04

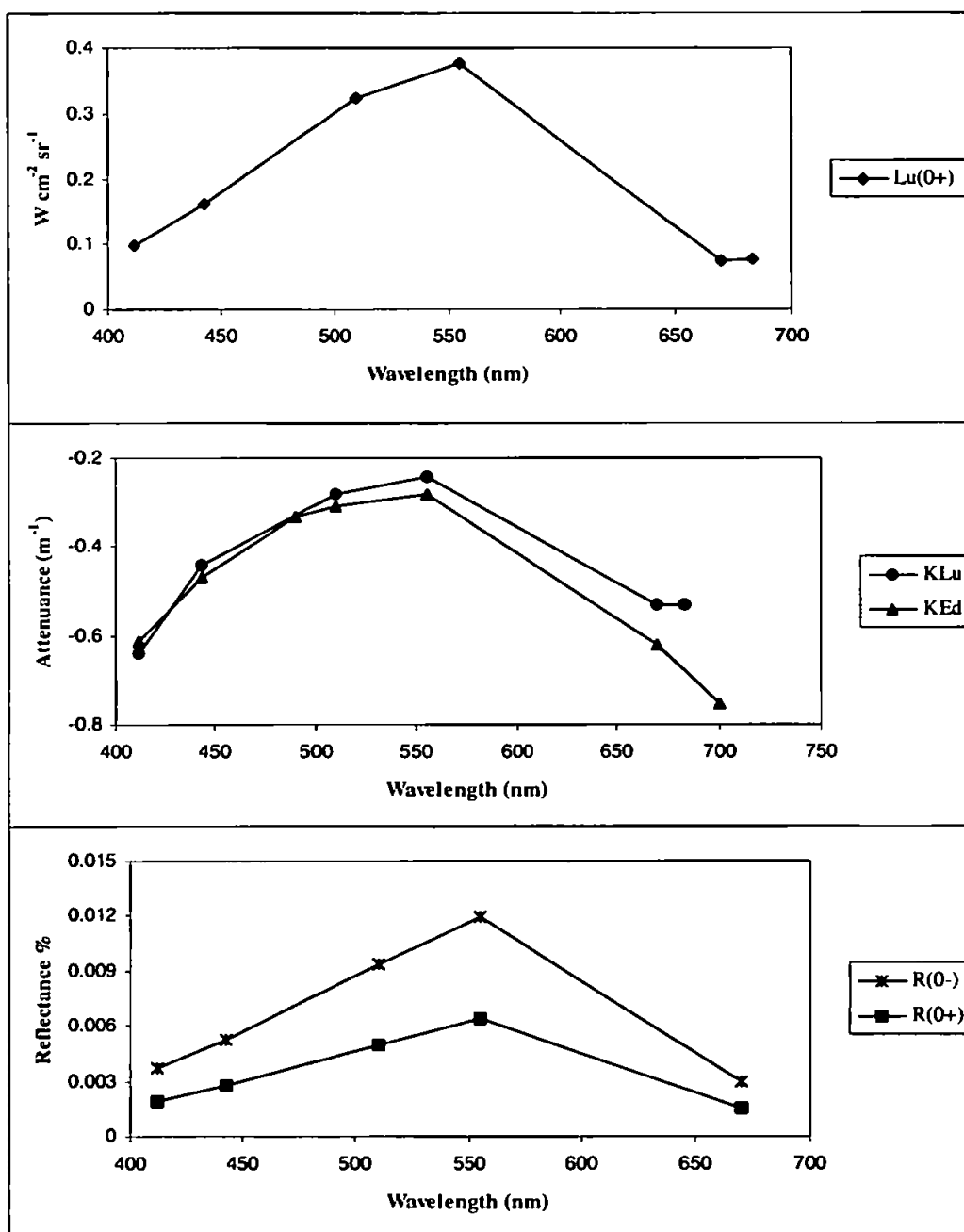
$\lambda$	$L_u(0^-)$	$L_u(0^+)$	$K_{Lu}$	$E_d(0^-)$	$K_{Ed}$	$R(0^-)$	$R(0^+)$	$z_{90}$
412	0.1514	0.0815	-0.8123	58.5357	-0.7872	0.0026	0.0014	-1.2703
443	0.2360	0.1275	-0.5884	63.8965	-0.6326	0.0037	0.0019	-1.5807
490				74.3206	-0.4734			-2.1123
510	0.4760	0.2587	-0.3827	72.9009	-0.4327	0.0065	0.0035	-2.3111
555	0.6353	0.3463	-0.3000	66.6229	-0.3619	0.0095	0.0051	-2.7632
670	0.1450	0.0794	-0.5995	49.4633	-0.7162	0.0029	0.0015	-1.3962
683	0.1652	0.0906	-0.5924					
700				38.6571	-0.7816			-1.2794





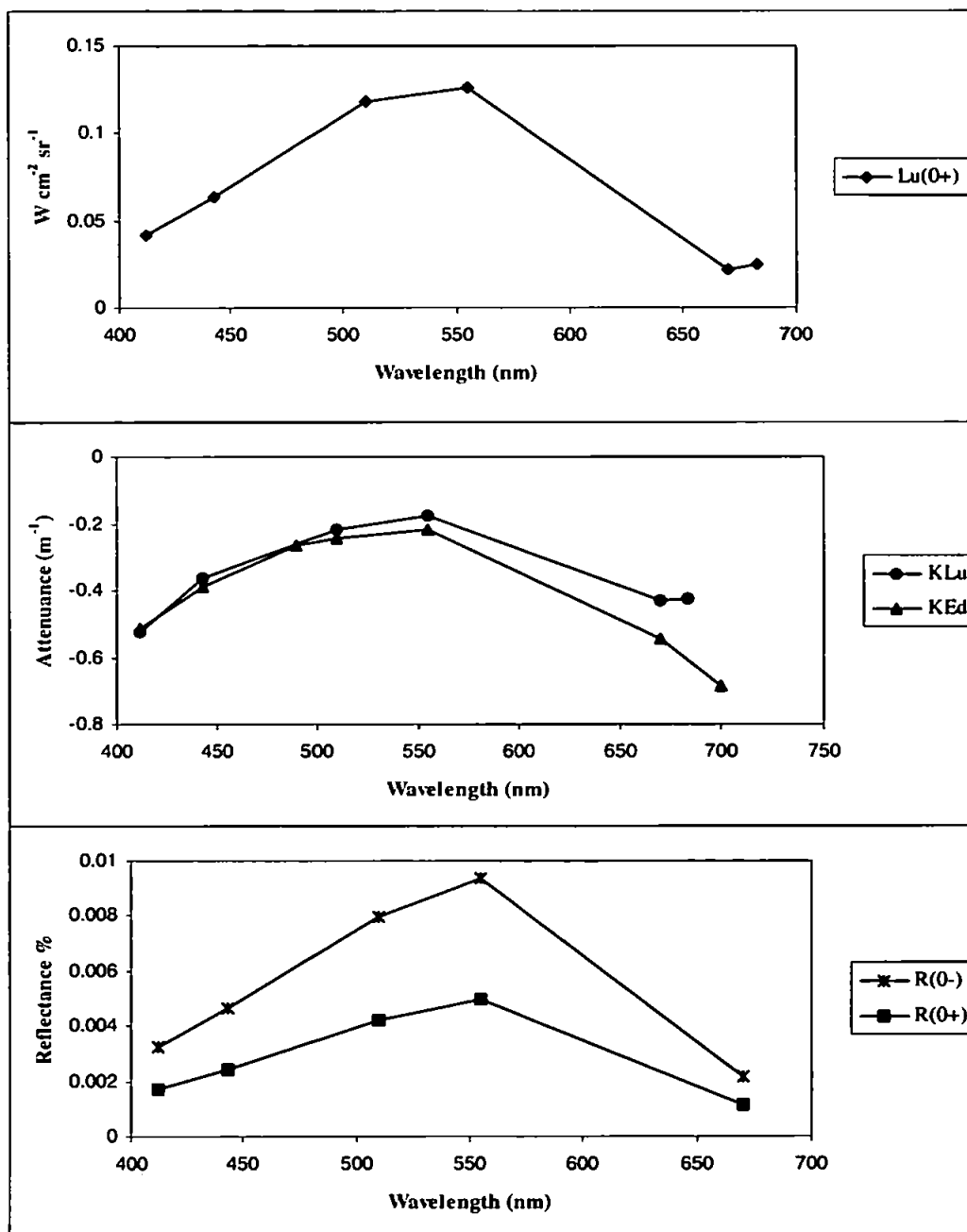
**Profile R : 23 August 1995 (SV24), 10:27 - 10:30 GMT**SPM concentration =  $7.9 \text{ mg m}^{-3}$  Chlorophyll concentration =  $1.13 \text{ mg m}^{-3}$  Salinity = 33.33

$\lambda$	$L_u(0^-)$	$L_u(0^+)$	$K_{Lu}$	$E_d(0^-)$	$K_{Ed}$	$R(0^-)$	$R(0^+)$	$z_{90}$
412	0.1842	0.0991	-0.6386	49.8520	-0.6120	0.0037	0.0019	-1.6340
443	0.2972	0.1606	-0.4403	56.1134	-0.4682	0.0053	0.0028	-2.1358
490				64.0305	-0.3339			-2.9951
510	0.5930	0.3222	-0.2805	63.4334	-0.3110	0.0093	0.0050	-3.2155
555	0.6926	0.3774	-0.2430	58.1279	-0.2801	0.0119	0.0064	-3.5708
670	0.1373	0.0752	-0.5329	46.2214	-0.6224	0.0030	0.0016	-1.6066
683	0.1379	0.0756	-0.5311					
700				37.1193	-0.7550			-1.3245



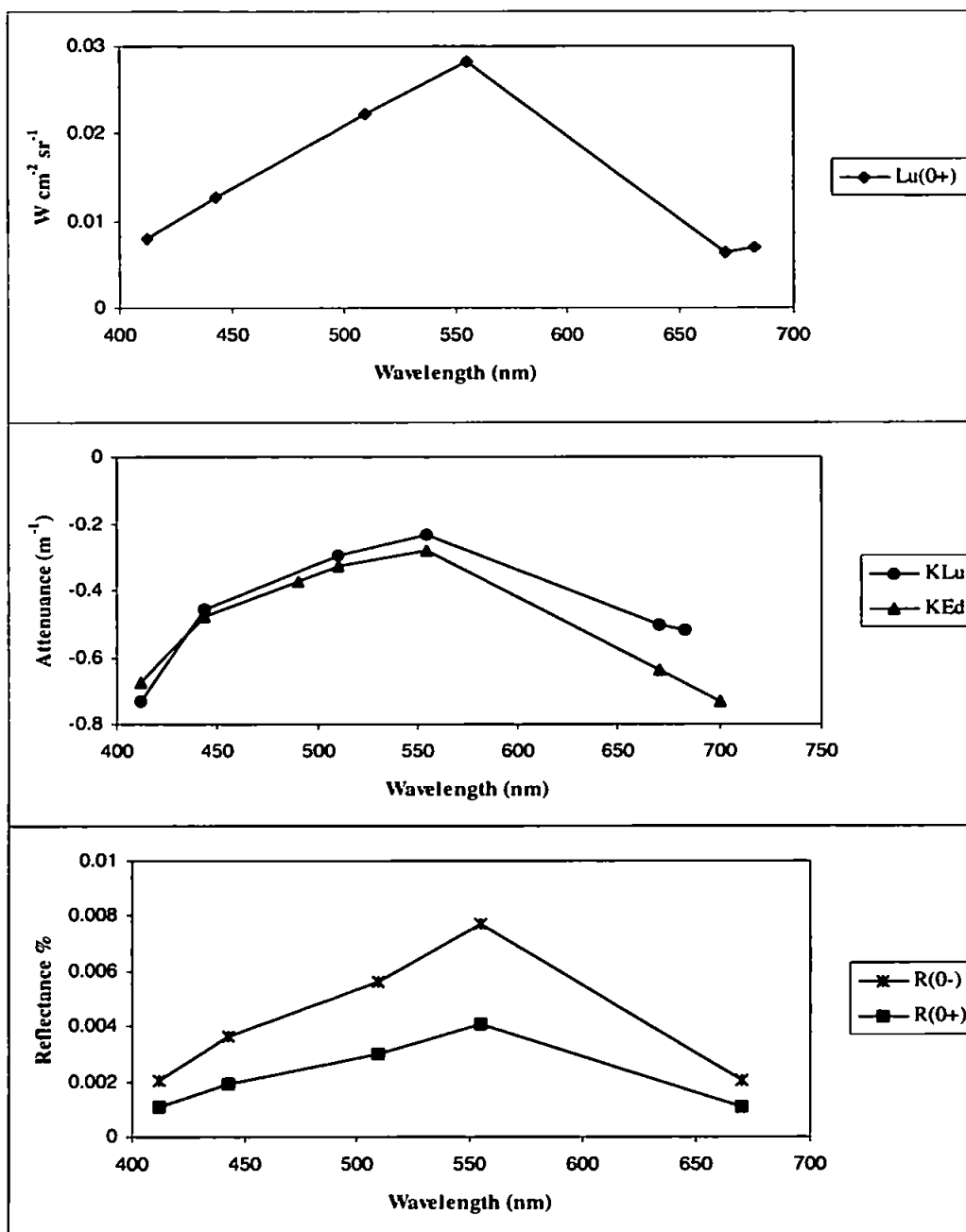
**Profile S : 23 August 1995 (SV24), 10:51 - 10:55 GMT**SPM concentration =  $7.9 \text{ mg m}^{-3}$  Chlorophyll concentration =  $1.18 \text{ mg m}^{-3}$  Salinity = 30.22

$\lambda$	$L_u(0^-)$	$L_u(0^+)$	$K_{Lu}$	$E_d(0^-)$	$K_{Ed}$	$R(0^-)$	$R(0^+)$	$z_{90}$
412	0.0772	0.0416	-0.5248	23.7865	-0.5147	0.0032	0.0017	-1.9427
443	0.1172	0.0633	-0.3655	25.2245	-0.3900	0.0046	0.0024	-2.5642
490				27.9860	-0.2670			-3.7460
510	0.2176	0.1183	-0.2156	27.3961	-0.2429	0.0079	0.0042	-4.1166
555	0.2316	0.1262	-0.1770	24.8029	-0.2176	0.0093	0.0050	-4.5966
670	0.0392	0.0215	-0.4335	18.0104	-0.5467	0.0022	0.0011	-1.8291
683	0.0459	0.0252	-0.4275					
700				15.2698	-0.6871			-1.4555



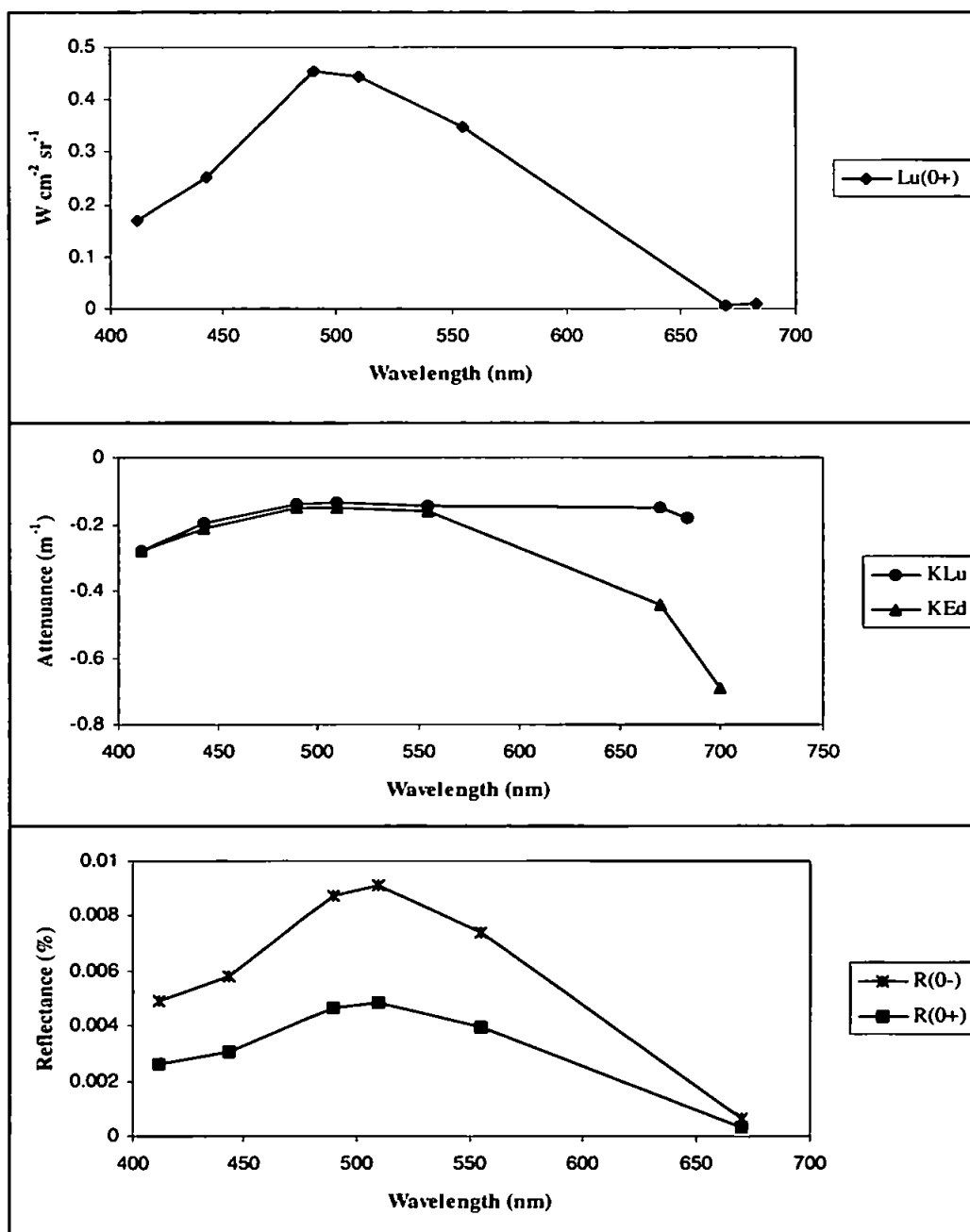
**Profile T : 23 August 1995 (SV24), 11:25 - 11:26 GMT**SPM concentration =  $34.06 \text{ mg m}^{-3}$  Chlorophyll concentration =  $1.49 \text{ mg m}^{-3}$  Salinity = 33.33

$\lambda$	$L_u(0^-)$	$L_u(0^+)$	$K_{Lu}$	$E_d(0^-)$	$K_{Ed}$	$R(0^-)$	$R(0^+)$	$z_{90}$
412	0.0147	0.0079	-0.7322	7.1818	-0.6736	0.0021	0.0011	-1.4845
443	0.0234	0.0127	-0.4570	6.4073	-0.4768	0.0037	0.0019	-2.0974
490				7.7966	-0.3757			-2.6617
510	0.0411	0.0223	-0.2941	7.3021	-0.3281	0.0056	0.0030	-3.0475
555	0.0519	0.0283	-0.2338	6.7143	-0.2817	0.0077	0.0041	-3.5502
670	0.0117	0.0064	-0.5060	5.7535	-0.6376	0.0020	0.0011	-1.5684
683	0.0128	0.0070	-0.5218					
700				4.2841	-0.7348			-1.3609



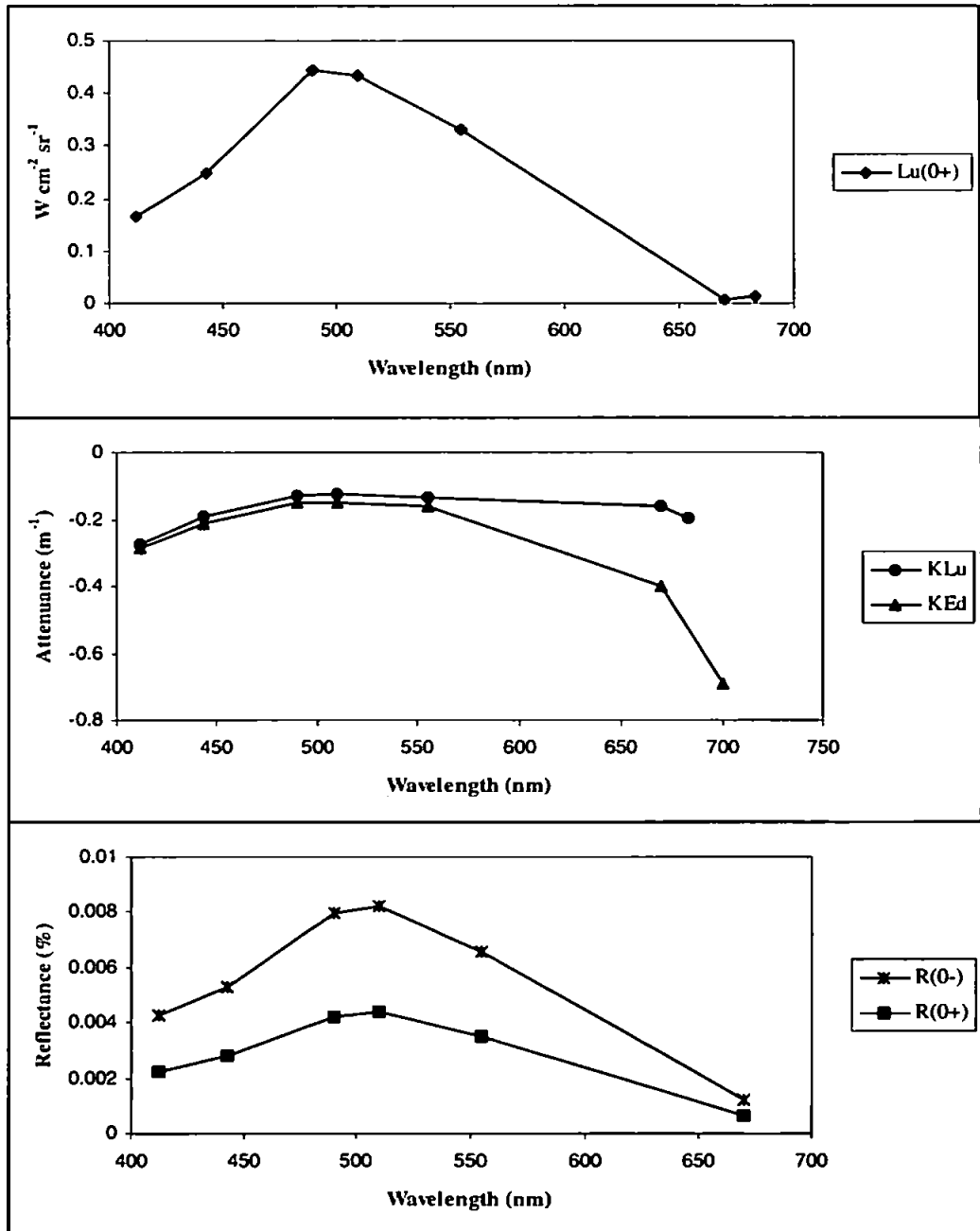
6 April 1995 (CH118a), 10:34 GMT

$\lambda$	$L_u(0^-)$	$L_u(0^+)$	$K_{Lu}$	$E_d(0^-)$	$K_{Ed}$	$R(0^-)$	$R(0^+)$	$z_{90}$
412	0.3163	0.1703	-0.2825	64.5204	-0.2824	0.0049	0.0026	-3.5415
443	0.4678	0.2528	-0.1980	80.4014	-0.2118	0.0058	0.0031	-4.7208
490	0.8332	0.4521	-0.1379	95.3661	-0.1506	0.0087	0.0046	-6.6408
510	0.8193	0.4453	-0.1342	90.2560	-0.1499	0.0091	0.0048	-6.6690
555	0.6368	0.3471	-0.1442	85.9731	-0.1601	0.0074	0.0039	-6.2457
670	0.0122	0.0067	-0.1518	19.2456	-0.4434	0.0006	0.0003	-2.2552
683	0.0195	0.0107	-0.1830					
700				43.7564	-0.6912			-1.4469



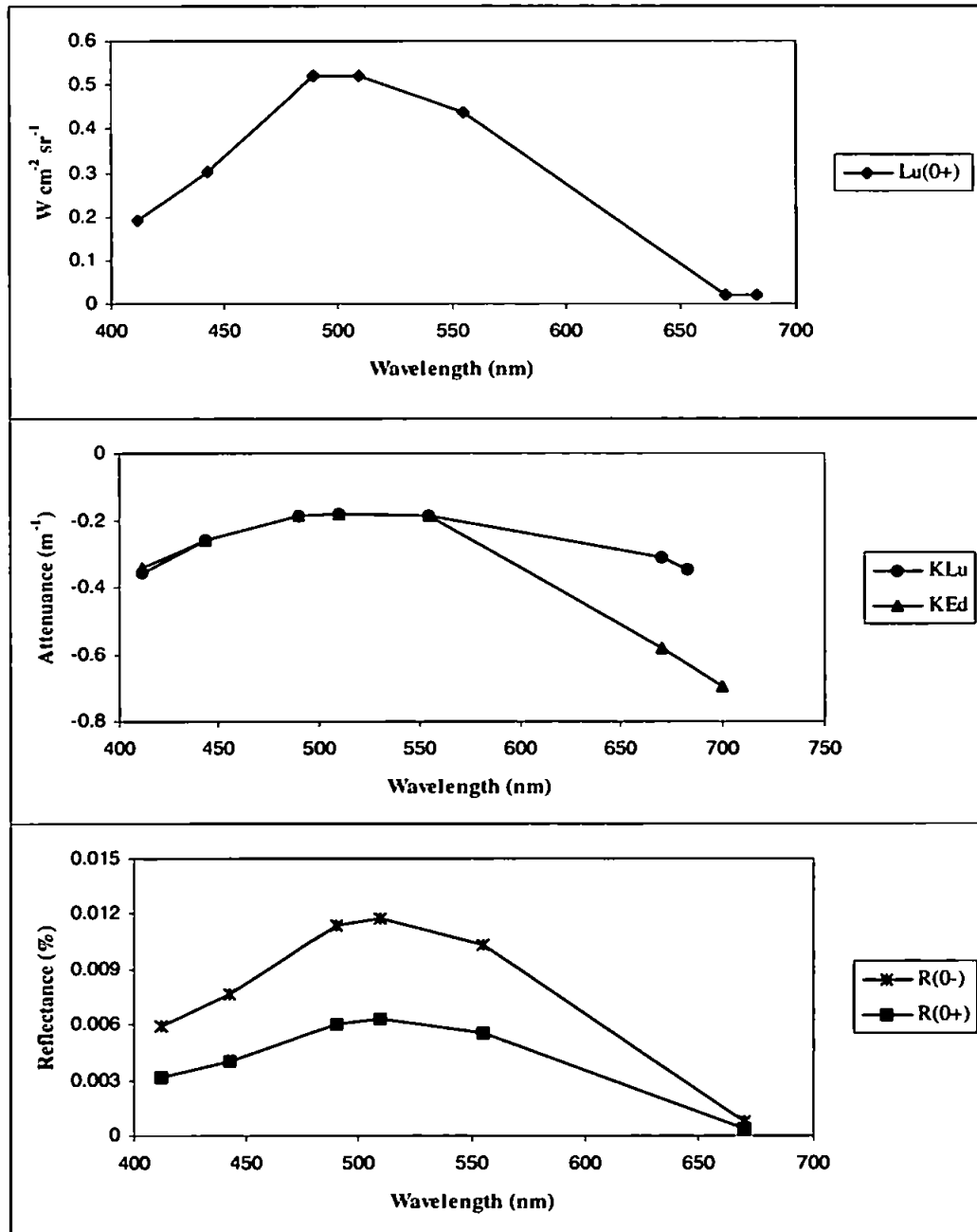
6 April 1995 (CH118a), 10:57 GMT

$\lambda$	$L_u(0^-)$	$L_u(0^+)$	$K_{Lu}$	$E_d(0^-)$	$K_{Ed}$	$R(0^-)$	$R(0^+)$	$z_{90}$
412	0.3045	0.1640	-0.2739	71.2502	-0.2843	0.0043	0.0023	-3.5176
443	0.4608	0.2490	-0.1903	87.1661	-0.2129	0.0053	0.0028	-4.6972
490	0.8155	0.4425	-0.1302	102.5748	-0.1510	0.0080	0.0042	-6.6223
510	0.7995	0.4345	-0.1265	97.2661	-0.1501	0.0082	0.0044	-6.6612
555	0.6073	0.3310	-0.1349	92.1349	-0.1596	0.0066	0.0035	-6.2642
670	0.0149	0.0081	-0.1619	12.5275	-0.4022	0.0012	0.0006	-2.4863
683	0.0247	0.0135	-0.1949					
700				43.7564	-0.6912			-1.4469



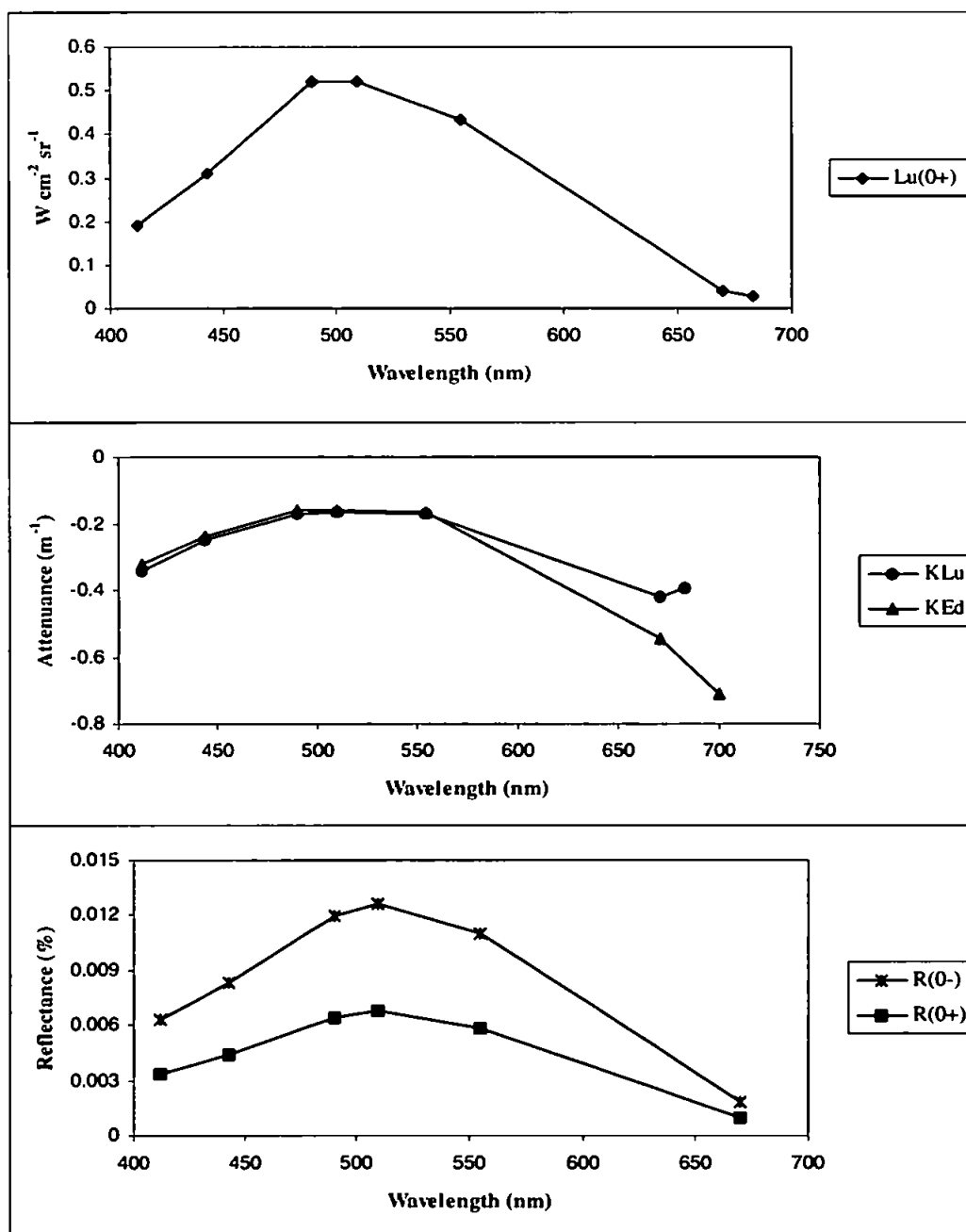
6 April 1995 (CH118a), 13:29 GMT

$\lambda$	$L_u(0^-)$	$L_u(0^+)$	$K_{Lu}$	$E_d(0^-)$	$K_{Ed}$	$R(0^-)$	$R(0^+)$	$z_{90}$
412	0.3554	0.1914	-0.3580	59.6592	-0.3428	0.0060	0.0031	-2.9175
443	0.5582	0.3016	-0.2602	72.9876	-0.2578	0.0076	0.0041	-3.8785
490	0.9622	0.5221	-0.1870	84.9019	-0.1855	0.0113	0.0061	-5.3897
510	0.9582	0.5207	-0.1802	81.6752	-0.1824	0.0117	0.0063	-5.4813
555	0.8040	0.4382	-0.1872	77.8228	-0.1885	0.0103	0.0055	-5.3056
670	0.0384	0.0210	-0.3106	47.7839	-0.5805	0.0008	0.0004	-1.7225
683	0.0370	0.0203	-0.3492					
700				31.5972	-0.6969			-1.4348



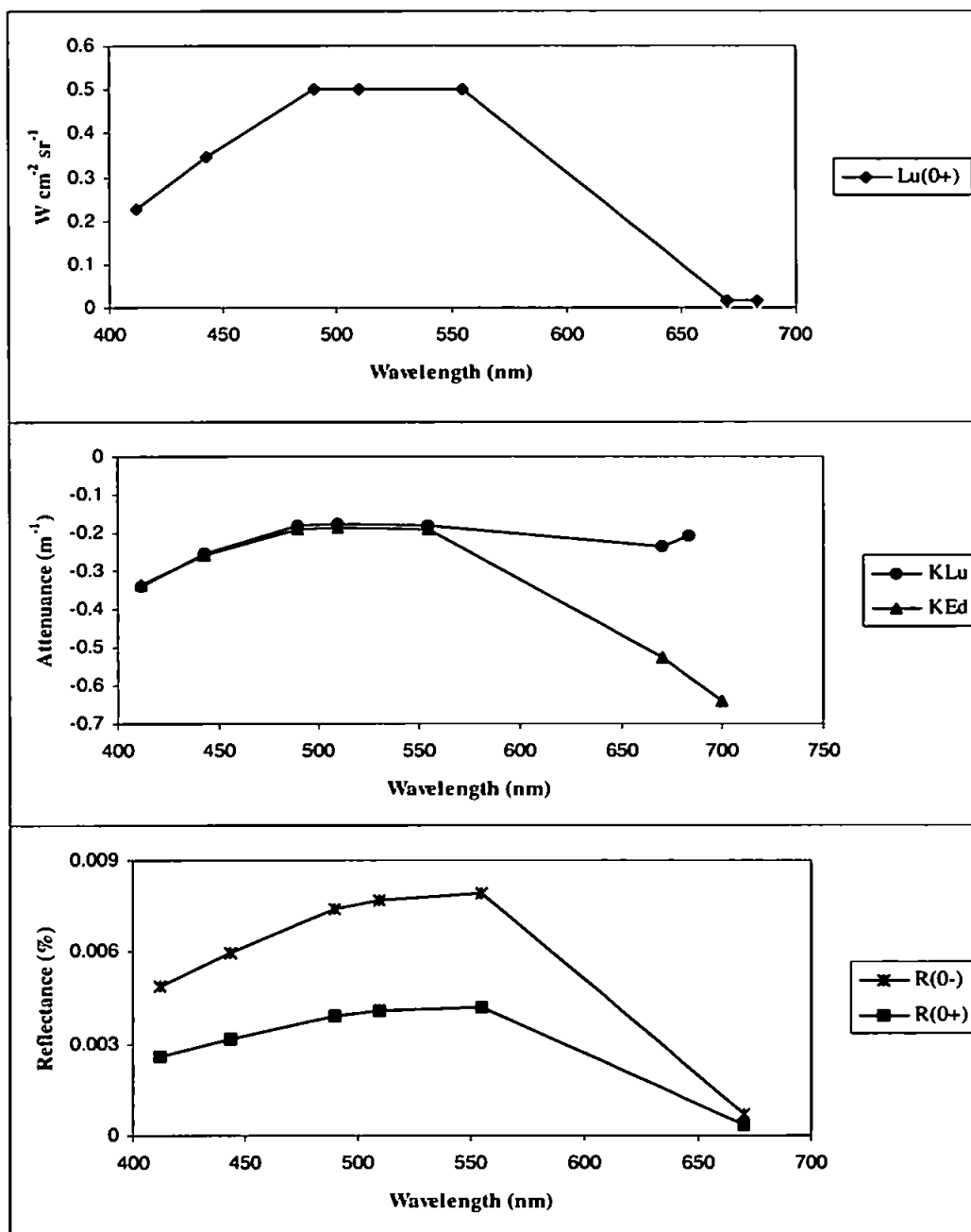
6 April 1995 (CH118a), 13:36 GMT

$\lambda$	$L_u(0^-)$	$L_u(0^+)$	$K_{Lu}$	$E_d(0^-)$	$K_{Ed}$	$R(0^-)$	$R(0^+)$	$Z_{90}$
412	0.3515	0.1892	-0.3451	55.6373	-0.3215	0.0063	0.0033	-3.1108
443	0.5737	0.3100	-0.2511	68.9749	-0.2373	0.0083	0.0044	-4.2138
490	0.9594	0.5206	-0.1711	80.0275	-0.1636	0.0120	0.0064	-6.1143
510	0.9567	0.5199	-0.1638	76.1111	-0.1585	0.0126	0.0067	-6.3088
555	0.7983	0.4351	-0.1691	72.7611	-0.1645	0.0110	0.0059	-6.0789
670	0.0738	0.0405	-0.4212	40.5181	-0.5431	0.0018	0.0010	-1.8411
683	0.0473	0.0259	-0.3922					
700				35.1648	-0.7099			-1.4086



10 April 1995 (CH118a), 10:41 GMT

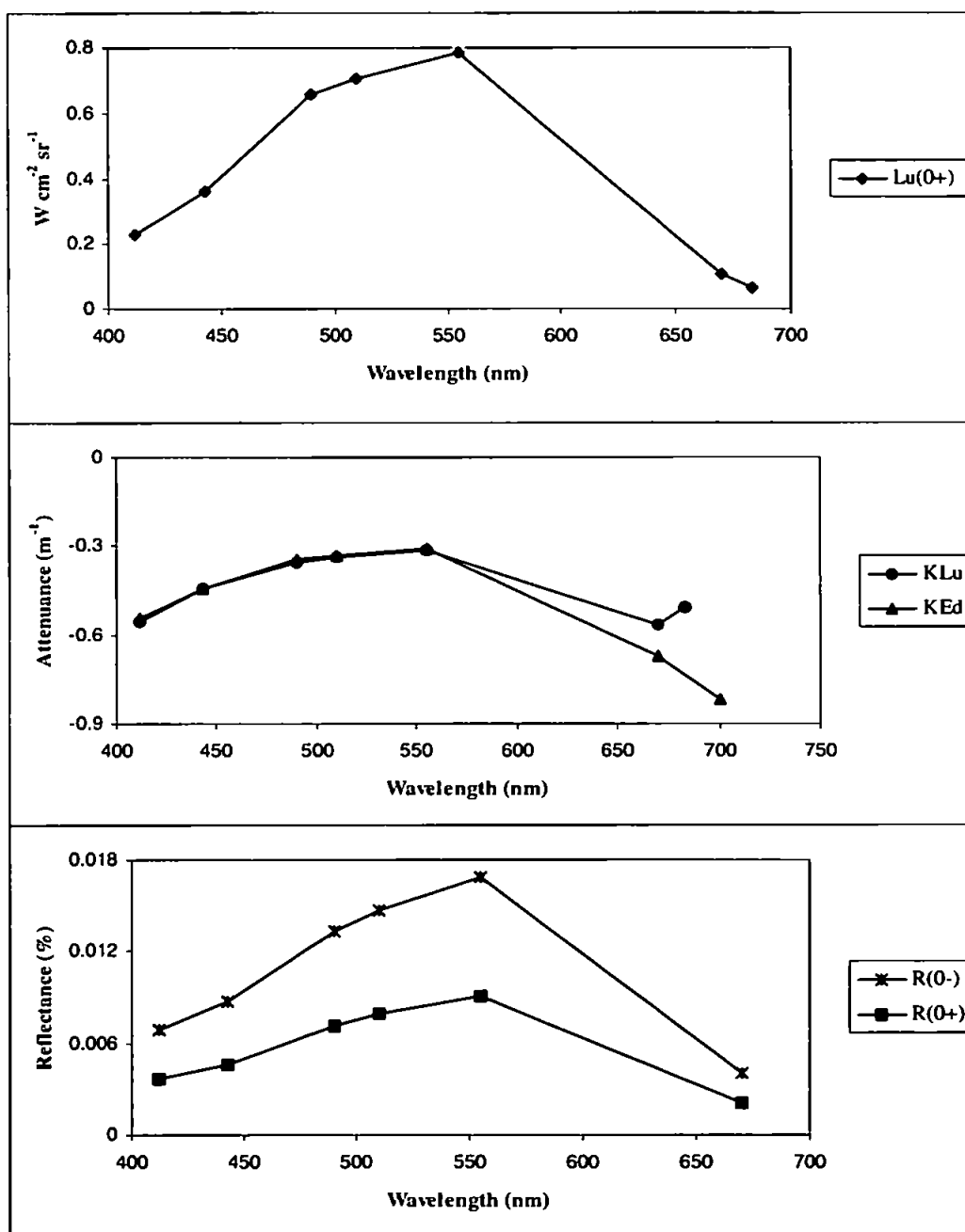
$\lambda$	$L_u(0^-)$	$L_u(0^+)$	$K_{Lu}$	$E_d(0^-)$	$K_{Ed}$	$R(0^-)$	$R(0^+)$	$z_{90}$
412	0.4244	0.2285	-0.3391	87.5517	-0.3344	0.0048	0.0026	-2.9900
443	0.6374	0.3444	-0.2524	107.2301	-0.2587	0.0059	0.0031	-3.8647
490	0.9253	0.5021	-0.1831	125.4862	-0.1894	0.0074	0.0039	-5.2802
510	0.9191	0.4995	-0.1760	119.8926	-0.1852	0.0077	0.0041	-5.3991
555	0.9216	0.5023	-0.1827	116.1553	-0.1908	0.0079	0.0042	-5.2401
670	0.0312	0.0171	-0.2358	47.3383	-0.5285	0.0007	0.0003	-1.8921
683	0.0287	0.0157	-0.2105					
700				32.6025	-0.6420			-1.5577





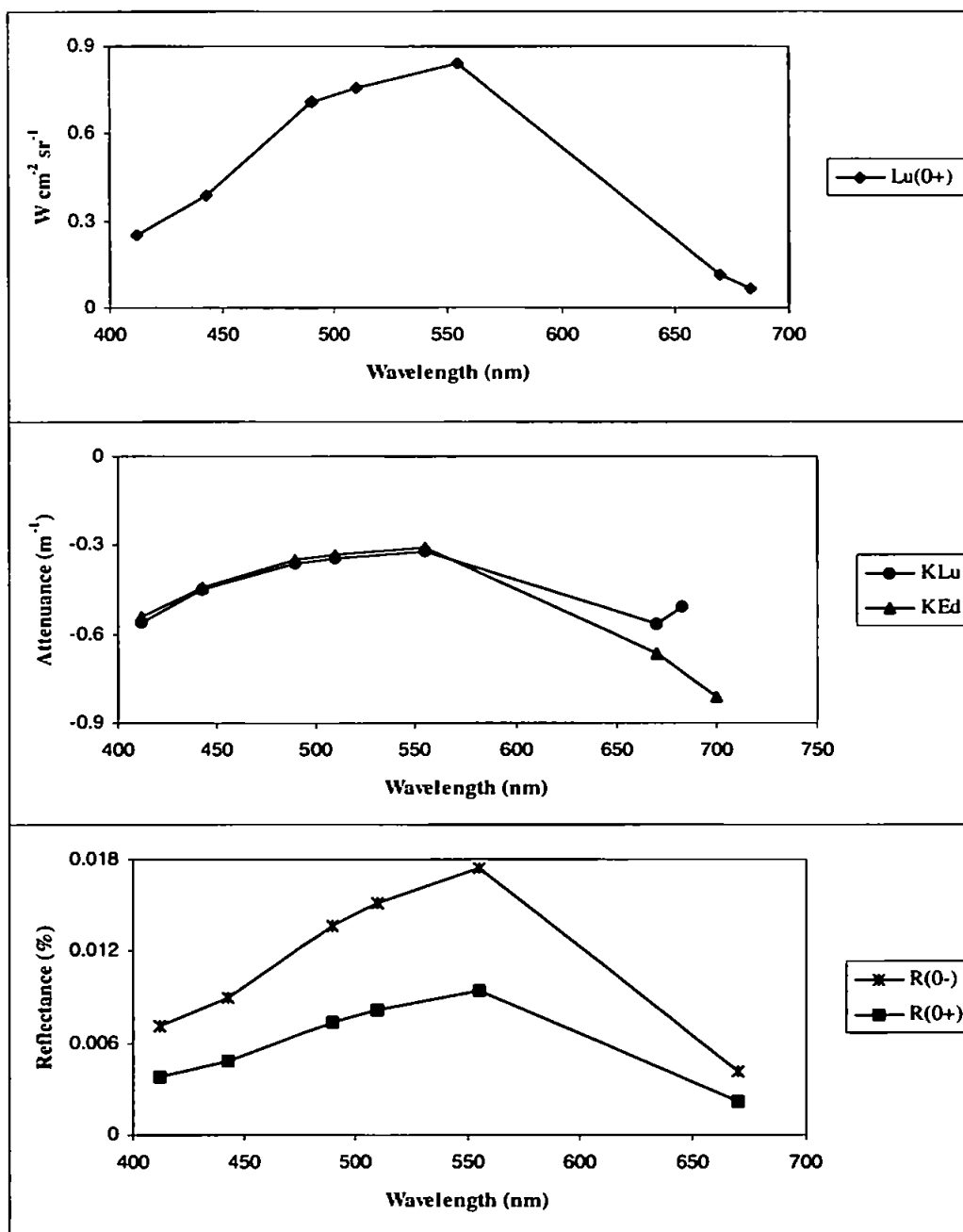
12 April 1995 (CH118a), 09:53 GMT

$\lambda$	$L_u(0^-)$	$L_u(0^+)$	$K_{Lu}$	$E_d(0^-)$	$K_{Ed}$	$R(0^-)$	$R(0^+)$	$z_{90}$
412	0.4280	0.2304	-0.5565	62.2590	-0.5408	0.0069	0.0036	-1.8491
443	0.6696	0.3618	-0.4454	76.7670	-0.4440	0.0087	0.0046	-2.2525
490	1.2089	0.6560	-0.3549	91.2019	-0.3473	0.0133	0.0071	-2.8794
510	1.2968	0.7047	-0.3368	88.2968	-0.3321	0.0147	0.0079	-3.0115
555	1.4379	0.7836	-0.3140	85.5126	-0.3091	0.0168	0.0091	-3.2353
670	0.1938	0.1062	-0.5677	48.7151	-0.6724	0.0040	0.0021	-1.4872
683	0.1145	0.0628	-0.5073					
700				47.7006	-0.8188			-1.2213



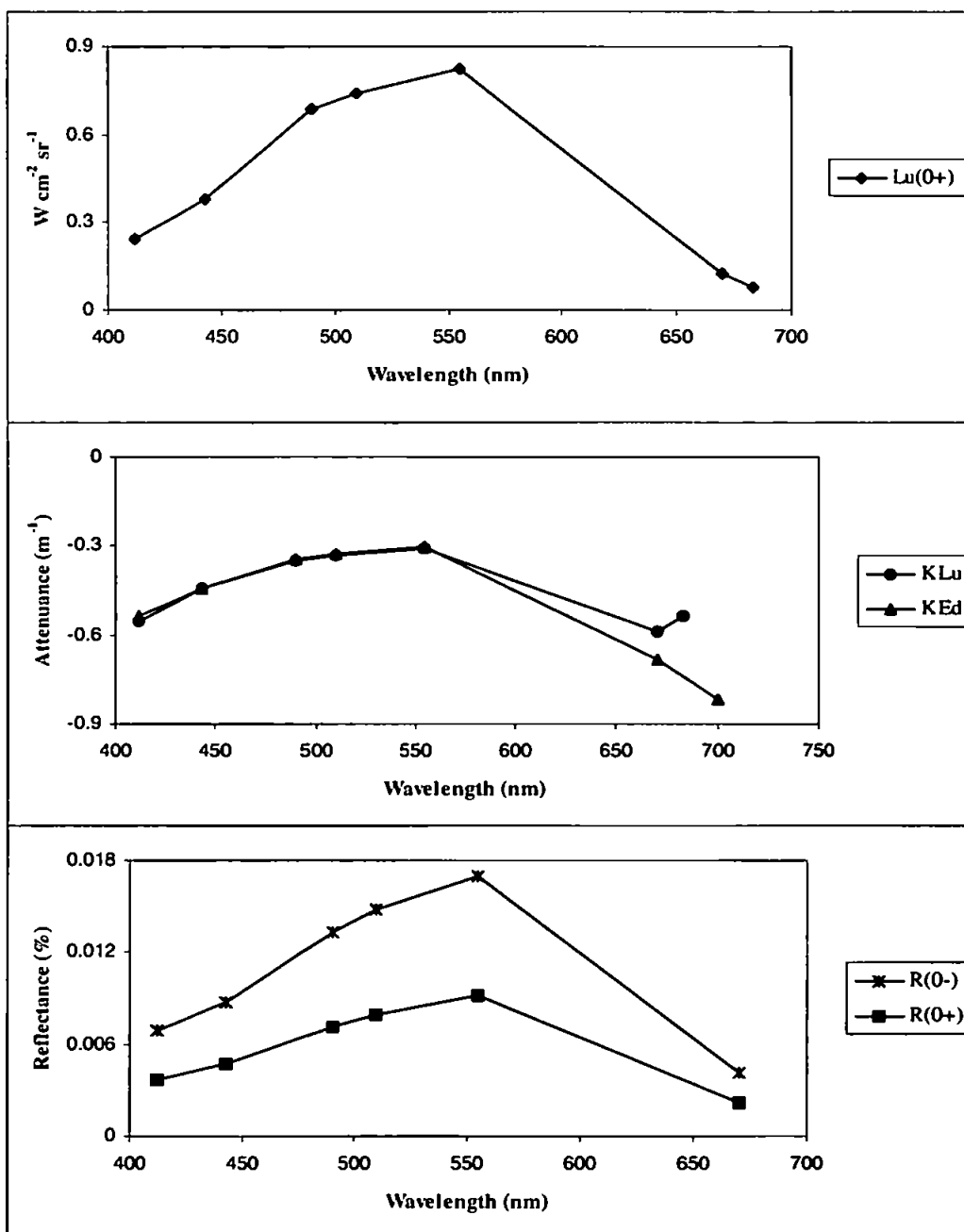
12 April 1995 (CH118a), 10:02 GMT

$\lambda$	$L_u(0^-)$	$L_u(0^+)$	$K_{Lu}$	$E_d(0^-)$	$K_{Ed}$	$R(0^-)$	$R(0^+)$	$z_{90}$
412	0.4634	0.2495	-0.5638	65.6692	-0.5447	0.0071	0.0037	-1.8359
443	0.7208	0.3895	-0.4513	80.4109	-0.4467	0.0090	0.0048	-2.2389
490	1.3017	0.7063	-0.3611	95.1497	-0.3496	0.0137	0.0074	-2.8608
510	1.3946	0.7579	-0.3429	92.0282	-0.3342	0.0152	0.0082	-2.9925
555	1.5456	0.8424	-0.3199	88.8770	-0.3107	0.0174	0.0094	-3.2181
670	0.2024	0.1109	-0.5677	48.9612	-0.6675	0.0041	0.0022	-1.4981
683	0.1211	0.0664	-0.5089					
700				46.7720	-0.8098			-1.2349



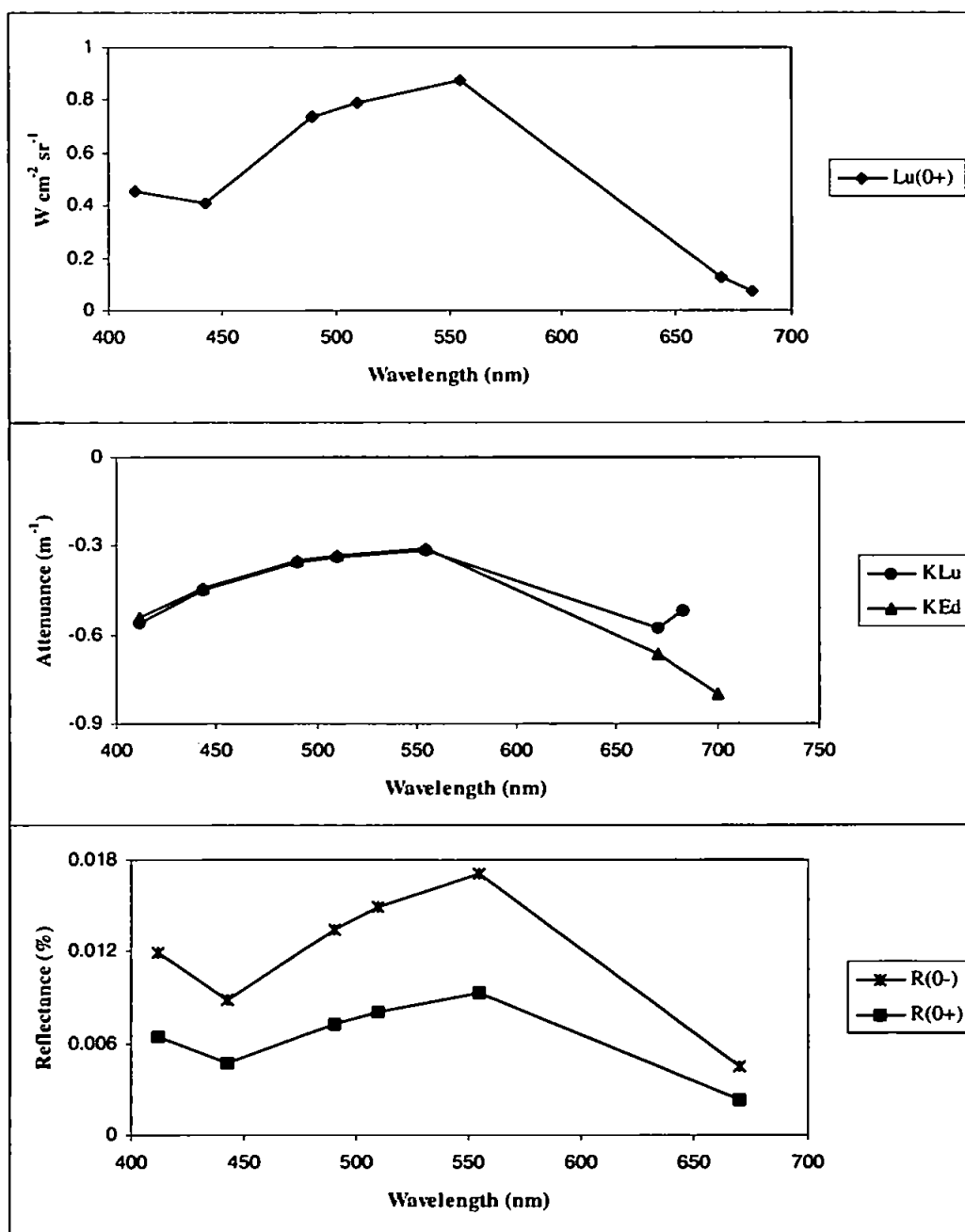
12 April 1995 (CH118a), 10:11 GMT

$\lambda$	$L_u(0^-)$	$L_u(0^+)$	$K_{Lu}$	$E_d(0^-)$	$K_{Ed}$	$R(0^-)$	$R(0^+)$	$Z_{90}$
412	0.4472	0.2408	-0.5548	65.5006	-0.5400	0.0068	0.0036	-1.8520
443	0.7049	0.3809	-0.4446	80.4839	-0.4426	0.0088	0.0047	-2.2592
490	1.2662	0.6871	-0.3536	95.0809	-0.3454	0.0133	0.0072	-2.8953
510	1.3588	0.7384	-0.3354	91.9615	-0.3301	0.0148	0.0080	-3.0298
555	1.5087	0.8222	-0.3120	88.9786	-0.3068	0.0170	0.0092	-3.2600
670	0.2259	0.1238	-0.5877	54.1032	-0.6830	0.0042	0.0022	-1.4641
683	0.1412	0.0774	-0.5386					
700				50.1662	-0.8167			-1.2245



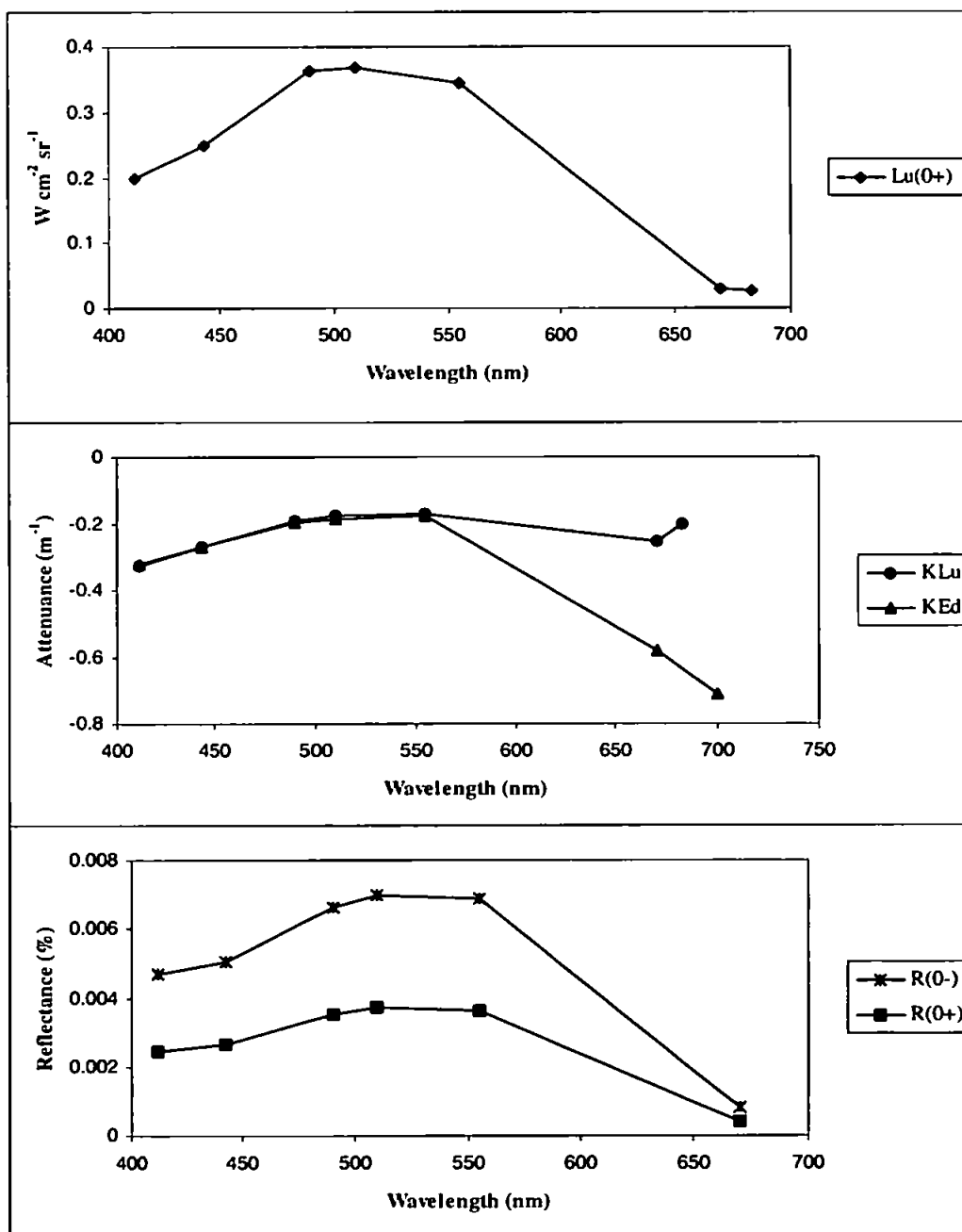
12 April 1995 (CH118a), 10:20 GMT

$\lambda$	$L_u(0^-)$	$L_u(0^+)$	$K_{Lu}$	$E_d(0^-)$	$K_{Ed}$	$R(0^-)$	$R(0^+)$	$z_{90}$
412	0.8380	0.4511	-0.5628	70.4219	-0.5454	0.0119	0.0064	-1.8336
443	0.7562	0.4086	-0.4497	85.8741	-0.4468	0.0088	0.0047	-2.2383
490	1.3579	0.7369	-0.3586	101.1361	-0.3493	0.0134	0.0072	-2.8632
510	1.4505	0.7883	-0.3400	97.4733	-0.3335	0.0149	0.0080	-2.9981
555	1.6063	0.8754	-0.3165	93.8718	-0.3099	0.0171	0.0093	-3.2270
670	0.2259	0.1237	-0.5784	51.0155	-0.6639	0.0044	0.0023	-1.5062
683	0.1340	0.0734	-0.5197					
700				48.6574	-0.8035			-1.2446



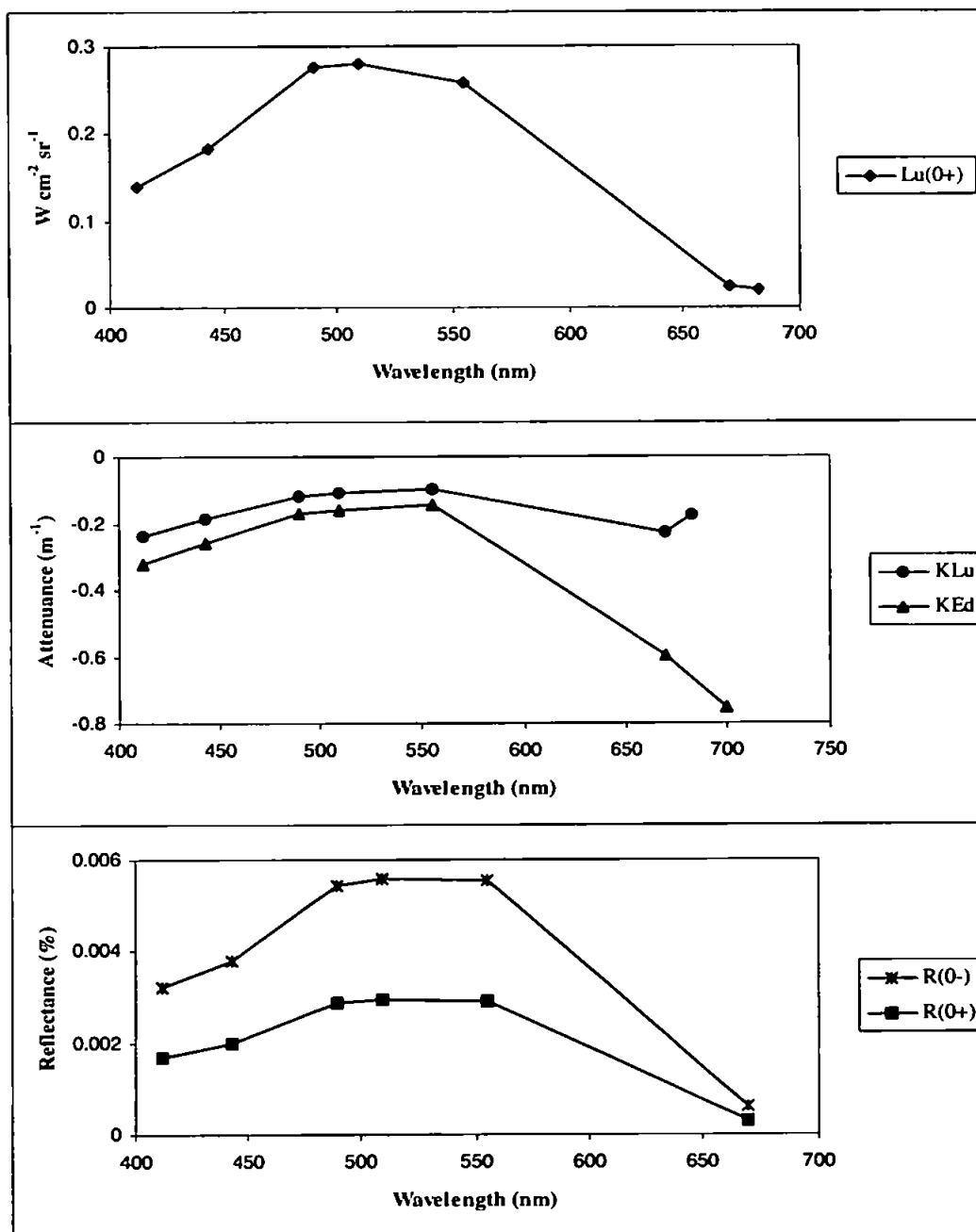
21 April 1995 (CH118b), 09:55 GMT

$\lambda$	$L_u(0^-)$	$L_u(0^+)$	$K_{Lu}$	$E_d(0^-)$	$K_{Ed}$	$R(0^-)$	$R(0^+)$	$z_{90}$
412	0.3709	0.1997	-0.3284	79.1320	-0.3217	0.0047	0.0025	-3.1089
443	0.4604	0.2488	-0.2686	91.5960	-0.2695	0.0050	0.0027	-3.7108
490	0.6687	0.3629	-0.1898	101.0426	-0.1953	0.0066	0.0035	-5.1204
510	0.6769	0.3679	-0.1770	96.6894	-0.1851	0.0070	0.0037	-5.4039
555	0.6322	0.3445	-0.1716	91.9961	-0.1767	0.0069	0.0036	-5.6608
670	0.0554	0.0304	-0.2561	67.8612	-0.5802	0.0008	0.0004	-1.7234
683	0.0488	0.0268	-0.2002					
700				70.0779	-0.7092			-1.4100



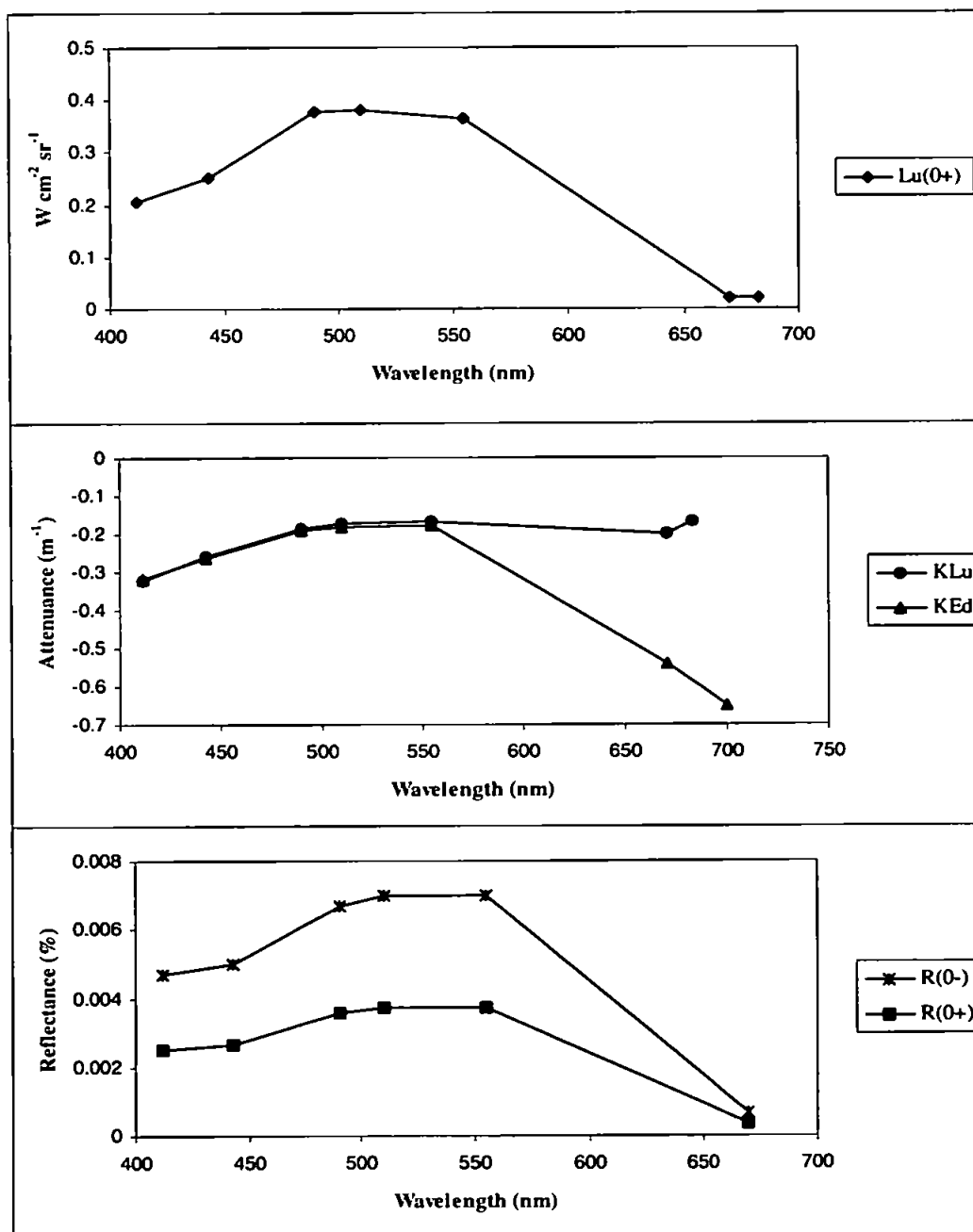
21 April 1995 (CH118b), 10:14 GMT

$\lambda$	$L_u(0^-)$	$L_u(0^+)$	$K_{Lu}$	$E_d(0^-)$	$K_{Ed}$	$R(0^-)$	$R(0^+)$	$z_{90}$
412	0.2572	0.1385	-0.2375	79.7746	-0.3234	0.0032	0.0017	-3.0924
443	0.3367	0.1819	-0.1895	89.2365	-0.2580	0.0038	0.0020	-3.8763
490	0.5099	0.2767	-0.1201	93.6794	-0.1691	0.0054	0.0029	-5.9144
510	0.5150	0.2799	-0.1086	92.1183	-0.1614	0.0056	0.0030	-6.1976
555	0.4746	0.2586	-0.1003	85.7493	-0.1454	0.0055	0.0029	-6.8799
670	0.0424	0.0232	-0.2302	68.5569	-0.5998	0.0006	0.0003	-1.6672
683	0.0361	0.0198	-0.1786					
700				75.1872	-0.7548			-1.3248



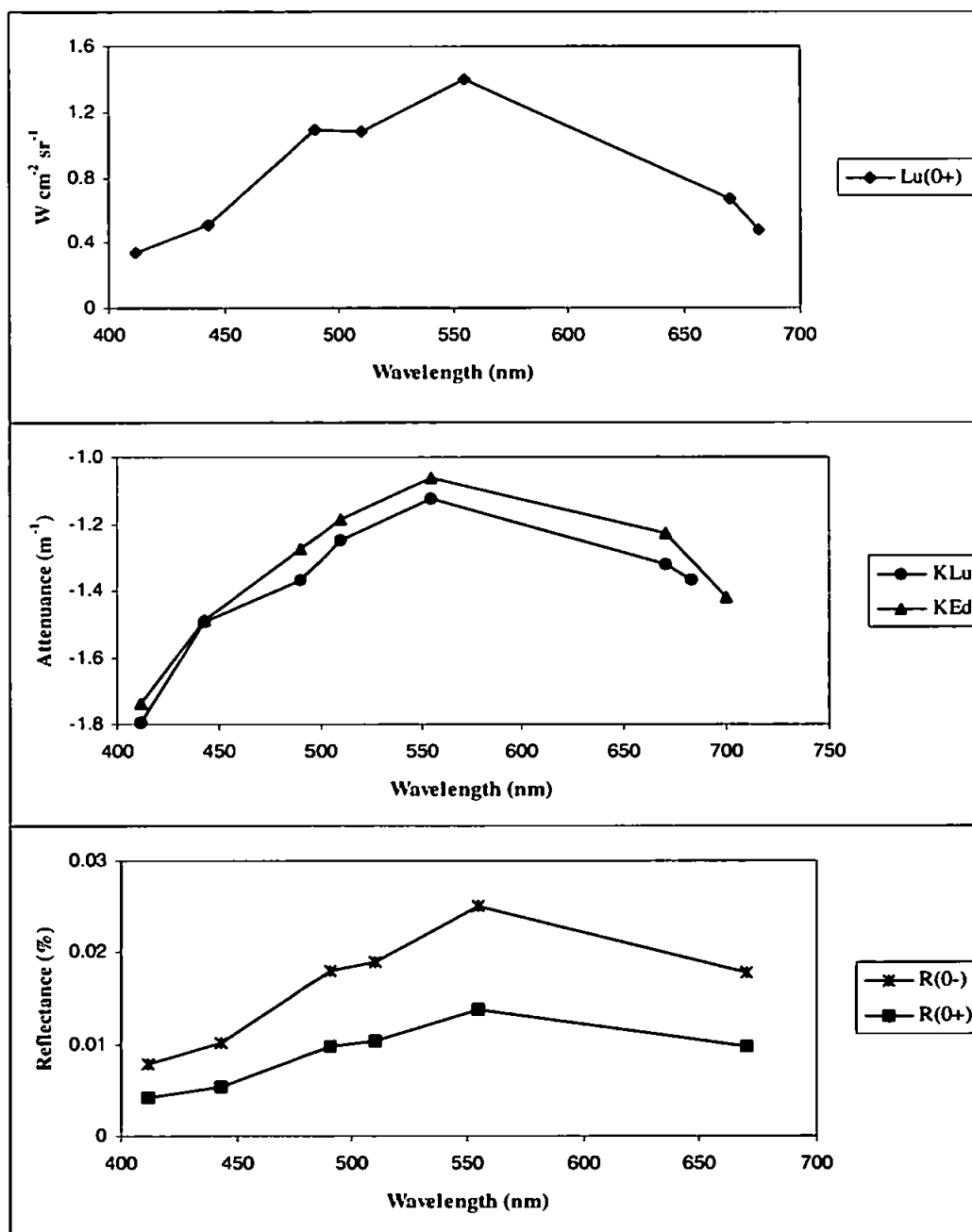
21 April 1995 (CH118b), 10:22 GMT

$\lambda$	$L_u(0^-)$	$L_u(0^+)$	$K_{Lu}$	$E_d(0^-)$	$K_{Ed}$	$R(0^-)$	$R(0^+)$	$z_{90}$
412	0.3816	0.2054	-0.3207	81.3178	-0.3178	0.0047	0.0025	-3.1463
443	0.4669	0.2523	-0.2609	93.7384	-0.2657	0.0050	0.0026	-3.7636
490	0.6927	0.3759	-0.1852	103.4157	-0.1929	0.0067	0.0035	-5.1831
510	0.7016	0.3813	-0.1732	100.2583	-0.1839	0.0070	0.0037	-5.4364
555	0.6668	0.3634	-0.1691	95.2213	-0.1759	0.0070	0.0037	-5.6861
670	0.0344	0.0188	-0.2000	52.0361	-0.5392	0.0007	0.0003	-1.8547
683	0.0347	0.0190	-0.1699					
700				49.6409	-0.6517			-1.5345



23 April 1995 (CH118b), 10:36 GMT

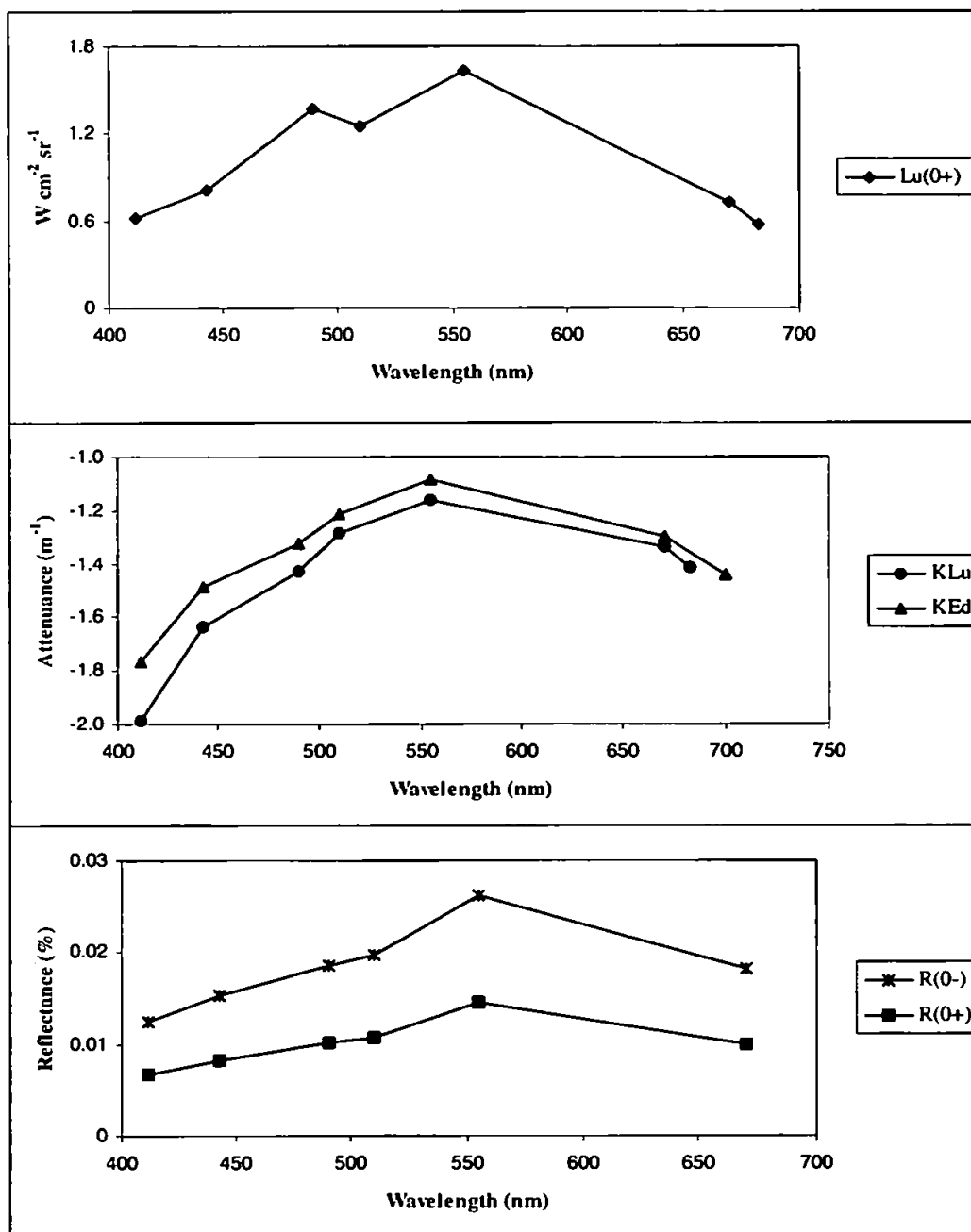
$\lambda$	$L_u(0^-)$	$L_u(0^+)$	$K_{Lu}$	$E_d(0^-)$	$K_{Ed}$	$R(0^-)$	$R(0^+)$	$z_{90}$
412	0.6344	0.3415	-1.7944	81.6949	-1.7379	0.0078	0.0041	-0.5754
443	0.9483	0.5124	-1.4914	93.2199	-1.4895	0.0102	0.0054	-0.6714
490	2.0160	1.0939	-1.3707	112.0884	-1.2742	0.0180	0.0098	-0.7848
510	1.9875	1.0801	-1.2492	105.5022	-1.1866	0.0188	0.0102	-0.8428
555	2.5647	1.3977	-1.1262	102.8050	-1.0618	0.0249	0.0138	-0.9418
670	1.2230	0.6699	-1.3207	68.5820	-1.2309	0.0178	0.0097	-0.8124
683	0.8723	0.4781	-1.3700					
700				71.4930	-1.4201			-0.7042





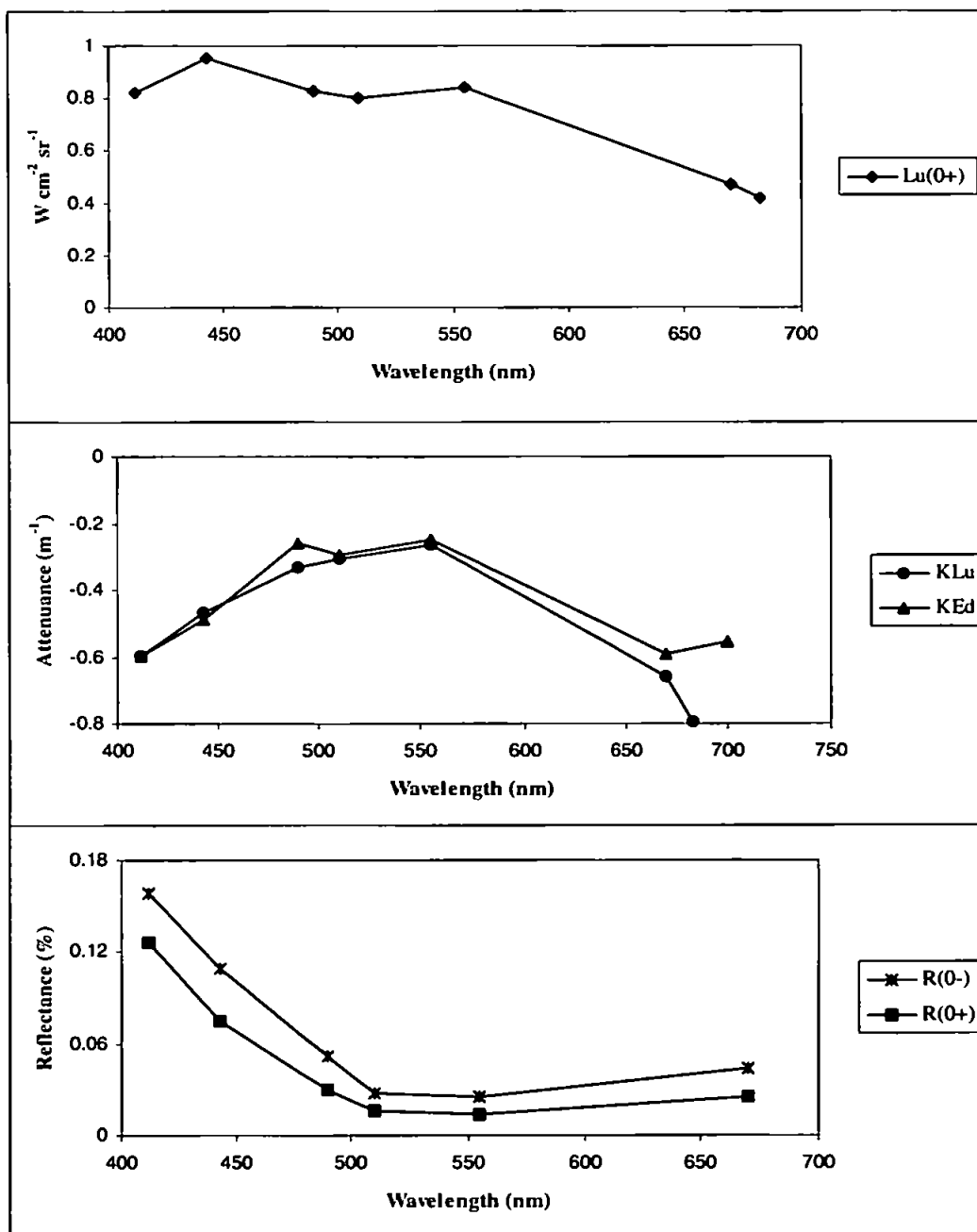
23 April 1995 (CH118b), 10:42 GMT

$\lambda$	$L_u(0^-)$	$L_u(0^+)$	$K_{Lu}$	$E_d(0^-)$	$K_{Ed}$	$R(0^-)$	$R(0^+)$	$z_{90}$
412	1.1588	0.6239	-1.9872	93.9423	-1.7634	0.0123	0.0066	-0.5671
443	1.5068	0.8142	-1.6390	98.7680	-1.4901	0.0153	0.0082	-0.6711
490	2.5293	1.3725	-1.4264	136.8194	-1.3265	0.0185	0.0100	-0.7539
510	2.3137	1.2574	-1.2862	118.1153	-1.2133	0.0196	0.0107	-0.8242
555	2.9866	1.6277	-1.1634	114.3278	-1.0870	0.0261	0.0144	-0.9200
670	1.3314	0.7293	-1.3408	73.2792	-1.2959	0.0182	0.0099	-0.7717
683	1.0500	0.5754	-1.4188					
700				77.4100	-1.4390			-0.6949381



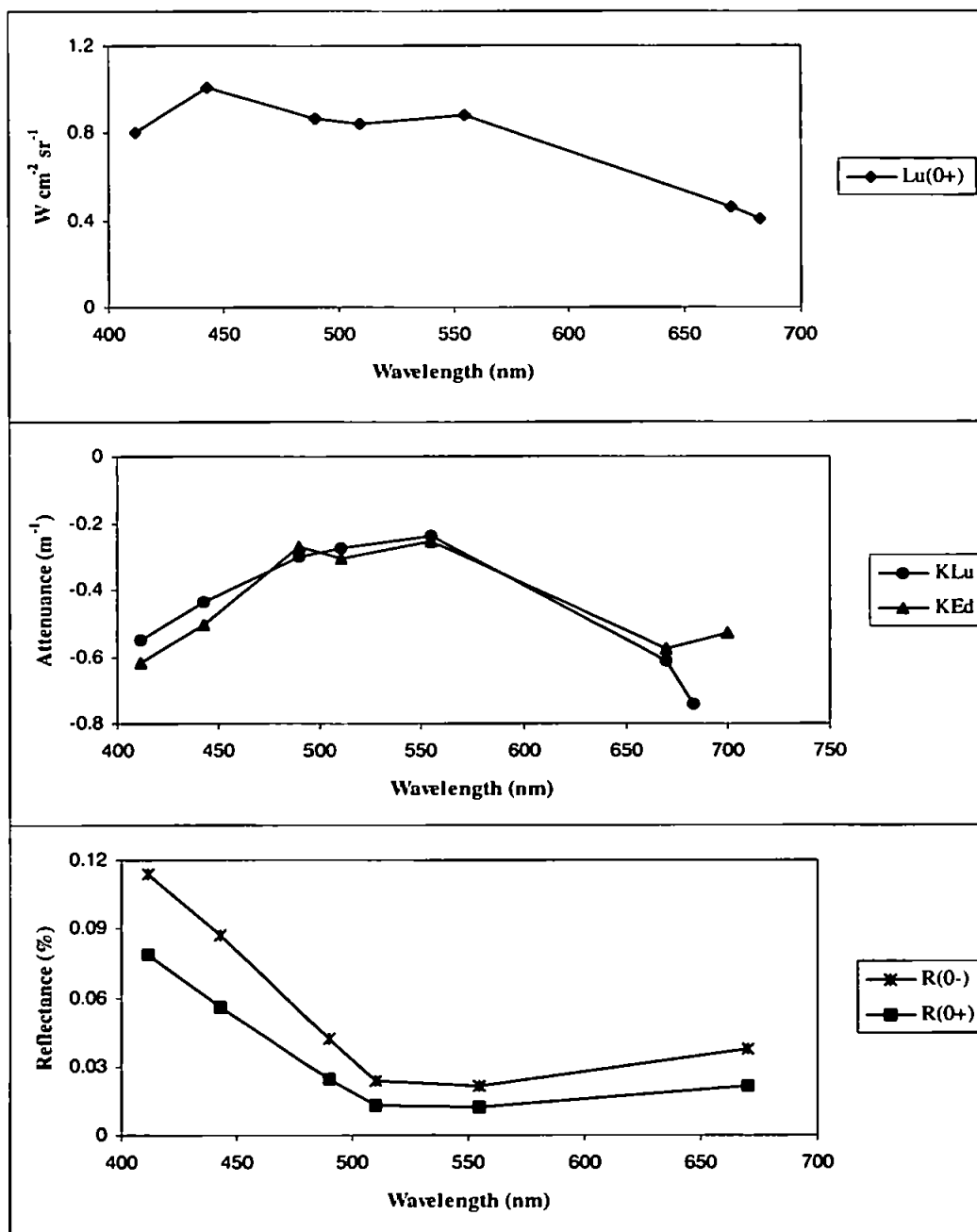
22 August 1995 (SV24), 13:31 GMT

$\lambda$	$L_u(0^-)$	$L_u(0^+)$	$K_{Lu}$	$E_d(0^-)$	$K_{Ed}$	$R(0^-)$	$R(0^+)$	$z_{90}$
412	1.5262	0.8217	-0.5991	9.6276	-0.5986	0.1585	0.1258	-1.6706
443	1.7652	0.9537	-0.4660	16.2199	-0.4899	0.1088	0.0742	-2.0414
490	1.5199	0.8247	-0.3317	29.3910	-0.2622	0.0517	0.0304	-3.8144
510	1.4793	0.8039	-0.3054	52.9208	-0.2958	0.0280	0.0155	-3.3804
555	1.5433	0.8411	-0.2646	60.9084	-0.2487	0.0253	0.0140	-4.0209
670	0.8599	0.4710	-0.6614	19.5215	-0.5943	0.0440	0.0254	-1.6826
683	0.7624	0.4178	-0.7938					
700				20.8484	-0.5567			-1.7962



22 August 1995 (SV24), 13:57 GMT

$\lambda$	$L_u(0^-)$	$L_u(0^+)$	$K_{Lu}$	$E_d(0^-)$	$K_{Ed}$	$R(0^-)$	$R(0^+)$	$z_{90}$
412	1.4977	0.8063	-0.5486	13.1862	-0.6196	0.1136	0.0785	-1.6140
443	1.8661	1.0083	-0.4347	21.4909	-0.5017	0.0868	0.0558	-1.9932
490	1.5899	0.8627	-0.3027	37.7641	-0.2714	0.0421	0.0242	-3.6846
510	1.5500	0.8423	-0.2766	65.9680	-0.3045	0.0235	0.0129	-3.2844
555	1.6230	0.8845	-0.2368	74.6450	-0.2537	0.0217	0.0119	-3.9423
670	0.8465	0.4637	-0.6142	22.6708	-0.5754	0.0373	0.0212	-1.7379
683	0.7447	0.4081	-0.7424					
700				24.0938	-0.5288			-1.8912



29 June 1995

## LW - 0.23h to LW + 0.1h

	x	s	f	v	z	ln(x)	ln(s)	ln(f)	ln(v)	ln(z)
x	1.00									
s	0.52	1.00								
f	-0.50	-0.86	1.00							
v	-0.02	0.55	-0.38	1.00						
z	-0.06	0.42	-0.22	0.89	1.00					
ln(x)	0.89	0.45	-0.46	-0.05	-0.09	1.00				
ln(s)	0.31	0.75	-0.68	0.86	0.69	0.33	1.00			
ln(f)	0.37	0.65	-0.78	0.56	0.39	0.42	0.84	1.00		
ln(v)	0.00	-0.47	0.17	-0.88	-0.88	0.04	-0.70	-0.23	1.00	
ln(z)	-0.07	0.42	-0.27	0.90	0.98	-0.10	0.72	0.48	-0.82	1.00

## LW - 0.23h

	x	s	f	v	z	ln(x)	ln(s)	ln(f)	ln(v)	ln(z)
x	1.00									
s	0.58	1.00								
f	-0.53	-0.90	1.00							
v	0.02	0.51	-0.43	1.00						
z	-0.02	0.38	-0.26	0.90	1.00					
ln(x)	0.87	0.49	-0.50	-0.06	-0.07	1.00				
ln(s)	0.34	0.72	-0.71	0.87	0.71	0.34	1.00			
ln(f)	0.37	0.67	-0.77	0.70	0.53	0.41	0.93	1.00		
ln(v)	-0.06	-0.46	0.27	-0.91	-0.90	0.02	-0.74	-0.46	1.00	
ln(z)	-0.03	0.38	-0.30	0.91	0.98	-0.09	0.73	0.60	-0.84	1.00

## LW - 0.1h

	x	s	f	v	z	ln(x)	ln(s)	ln(f)	ln(v)	ln(z)
x	1.00									
s	0.50	1.00								
f	-0.50	-0.83	1.00							
v	-0.02	0.61	-0.44	1.00						
z	-0.05	0.47	-0.26	0.89	1.00					
ln(x)	0.91	0.45	-0.49	-0.04	-0.07	1.00				
ln(s)	0.31	0.79	-0.73	0.87	0.69	0.35	1.00			
ln(f)	0.38	0.67	-0.84	0.59	0.40	0.45	0.86	1.00		
ln(v)	0.00	-0.54	0.22	-0.90	-0.89	0.03	-0.72	-0.28	1.00	
ln(z)	-0.06	0.47	-0.31	0.90	0.98	-0.07	0.72	0.49	-0.83	1.00

x = patch size, s = within-patch total SPM concentration, f = within-patch total SPM flux,  
v = within-patch averaged surface velocity & z = within-patch averaged water depth

LW + 0.1h										
	x	s	f	v	z	ln(x)	ln(s)	ln(f)	ln(v)	ln(z)
x	1.00									
s	0.45	1.00								
f	-0.50	-0.82	1.00							
v	-0.10	0.60	-0.33	1.00						
z	-0.14	0.45	-0.15	0.90	1.00					
ln(x)	0.91	0.42	-0.45	-0.11	-0.14	1.00				
ln(s)	0.27	0.80	-0.64	0.85	0.69	0.31	1.00			
ln(f)	0.37	0.60	-0.78	0.41	0.22	0.45	0.74	1.00		
ln(v)	0.09	-0.49	0.07	-0.87	-0.88	0.10	-0.67	-0.02	1.00	
ln(z)	-0.15	0.45	-0.21	0.90	0.98	-0.15	0.71	0.33	-0.82	1.00

10 August 1995

## LW + 1.38h to LW + 3.33h

	x	s	f	v	z	ln(x)	ln(s)	ln(f)	ln(v)	ln(z)
x	1.00									
s	0.82	1.00								
f	0.69	0.85	1.00							
v	0.02	-0.04	0.31	1.00						
z	0.11	0.03	0.18	0.02	1.00					
ln(x)	0.88	0.62	0.45	0.03	0.06	1.00				
ln(s)	0.77	0.72	0.48	-0.11	-0.07	0.86	1.00			
ln(f)	0.49	0.39	0.56	0.68	0.26	0.53	0.45	1.00		
ln(v)	0.03	-0.03	0.28	0.85	0.03	0.03	-0.11	0.80	1.00	
ln(z)	0.10	0.00	0.18	0.08	0.99	0.06	-0.12	0.27	0.07	1.00

## LW + 1.38h

	x	s	f	v	z	ln(x)	ln(s)	ln(f)	ln(v)	ln(z)
x	1.00									
s	0.90	1.00								
f	0.10	0.14	1.00							
v	0.01	0.05	0.80	1.00						
z	0.03	0.06	0.68	0.79	1.00					
ln(x)	0.94	0.84	0.08	-0.01	0.02	1.00				
ln(s)	0.87	0.93	0.15	0.06	0.09	0.92	1.00			
ln(f)	0.46	0.52	0.37	0.20	0.20	0.48	0.58	1.00		
ln(v)	-0.03	0.02	0.07	-0.13	-0.22	-0.02	0.03	0.76	1.00	
ln(z)	0.02	0.01	0.68	0.83	0.99	0.02	0.05	0.14	-0.27	1.00

## LW + 1.58h

	x	s	f	v	z	ln(x)	ln(s)	ln(f)	ln(v)	ln(z)
x	1.00									
s	0.87	1.00								
f	0.26	0.21	1.00							
v	0.00	0.00	0.65	1.00						
z	-0.01	-0.08	0.62	0.43	1.00					
ln(x)	0.95	0.82	0.27	0.02	0.01	1.00				
ln(s)	0.87	0.93	0.25	0.04	-0.06	0.91	1.00			
ln(f)	0.41	0.39	0.65	0.78	0.54	0.46	0.46	1.00		
ln(v)	0.02	0.00	0.48	0.87	0.38	0.06	0.04	0.86	1.00	
ln(z)	0.00	-0.11	0.63	0.43	0.99	0.02	-0.08	0.53	0.37	1.00

x = patch size, s = within-patch total SPM concentration, f = within-patch total SPM flux,  
v = within-patch averaged surface velocity & z = within-patch averaged water depth

**LW + 1.85h**

	x	s	f	v	z	ln(x)	ln(s)	ln(f)	ln(v)	ln(z)
x	1.00									
s	0.82	1.00								
f	0.67	0.53	1.00							
v	-0.09	-0.22	0.47	1.00						
z	0.09	-0.20	0.37	0.39	1.00					
ln(x)	0.91	0.78	0.67	-0.06	0.04	1.00				
ln(s)	0.80	0.89	0.55	-0.23	-0.25	0.90	1.00			
ln(f)	0.57	0.42	0.85	0.66	0.43	0.64	0.48	1.00		
ln(v)	-0.09	-0.23	0.42	0.94	0.34	-0.06	-0.24	0.67	1.00	
ln(z)	0.08	-0.24	0.37	0.47	0.99	0.03	-0.28	0.46	0.41	1.00

**LW + 2.07h**

	x	s	f	v	z	ln(x)	ln(s)	ln(f)	ln(v)	ln(z)
x	1.00									
s	0.76	1.00								
f	0.75	0.70	1.00							
v	-0.09	-0.01	0.39	1.00						
z	0.04	-0.34	0.04	-0.20	1.00					
ln(x)	0.93	0.70	0.75	-0.01	0.01	1.00				
ln(s)	0.78	0.89	0.73	0.06	-0.38	0.84	1.00			
ln(f)	0.69	0.64	0.90	0.52	-0.03	0.79	0.78	1.00		
ln(v)	-0.10	-0.02	0.35	0.96	-0.29	-0.02	0.07	0.51	1.00	
ln(z)	0.03	-0.39	0.04	-0.10	0.99	0.00	-0.42	-0.01	-0.19	1.00

**LW + 2.35h**

	x	s	f	v	z	ln(x)	ln(s)	ln(f)	ln(v)	ln(z)
x	1.00									
s	0.77	1.00								
f	0.85	0.81	1.00							
v	-0.24	-0.22	0.07	1.00						
z	0.19	-0.07	0.13	-0.42	1.00					
ln(x)	0.93	0.72	0.82	-0.16	0.12	1.00				
ln(s)	0.75	0.90	0.80	-0.12	-0.22	0.82	1.00			
ln(f)	0.78	0.74	0.92	0.16	0.08	0.85	0.85	1.00		
ln(v)	-0.24	-0.29	0.02	0.95	-0.44	-0.17	-0.17	0.12	1.00	
ln(z)	0.18	-0.13	0.12	-0.33	0.99	0.12	-0.26	0.08	-0.36	1.00

**LW + 2.62h**

	x	s	f	v	z	ln(x)	ln(s)	ln(f)	ln(v)	ln(z)
x	1.00									
s	0.82	1.00								
f	0.78	0.92	1.00							
v	-0.13	-0.09	0.04	1.00						
z	0.11	0.03	0.13	-0.66	1.00					
ln(x)	0.92	0.72	0.71	-0.08	0.05	1.00				
ln(s)	0.78	0.88	0.81	-0.08	-0.03	0.84	1.00			
ln(f)	0.75	0.80	0.87	0.16	0.08	0.81	0.90	1.00		
ln(v)	-0.12	-0.11	0.04	0.95	-0.64	-0.07	-0.11	0.17	1.00	
ln(z)	0.09	-0.03	0.10	-0.59	0.99	0.04	-0.09	0.05	-0.57	1.00

**LW + 2.83h**

	x	s	f	v	z	ln(x)	ln(s)	ln(f)	ln(v)	ln(z)
x	1.00									
s	0.88	1.00								
f	0.86	0.98	1.00							
v	-0.22	-0.21	-0.16	1.00						
z	0.18	0.16	0.19	-0.66	1.00					
ln(x)	0.86	0.64	0.62	-0.15	0.11	1.00				
ln(s)	0.81	0.73	0.70	-0.22	0.05	0.88	1.00			
ln(f)	0.79	0.71	0.72	-0.01	0.12	0.86	0.93	1.00		
ln(v)	-0.18	-0.16	-0.10	0.95	-0.62	-0.13	-0.17	0.08	1.00	
ln(z)	0.17	0.14	0.18	-0.59	0.99	0.10	0.00	0.11	-0.56	1.00

**LW + 3.08h**

	x	s	f	v	z	ln(x)	ln(s)	ln(f)	ln(v)	ln(z)
x	1.00									
s	0.89	1.00								
f	0.88	0.99	1.00							
v	-0.16	-0.18	-0.12	1.00						
z	0.17	0.12	0.14	-0.72	1.00					
ln(x)	0.83	0.59	0.59	-0.10	0.15	1.00				
ln(s)	0.78	0.67	0.65	-0.22	0.09	0.90	1.00			
ln(f)	0.78	0.64	0.67	-0.03	0.17	0.90	0.92	1.00		
ln(v)	-0.15	-0.16	-0.08	0.96	-0.66	-0.11	-0.21	0.02	1.00	
ln(z)	0.17	0.11	0.14	-0.68	0.99	0.14	0.06	0.16	-0.61	1.00



LW + 3.33h										
	x	s	f	v	z	ln(x)	ln(s)	ln(f)	ln(v)	ln(z)
x	1.00									
s	0.86	1.00								
f	0.83	0.93	1.00							
v	-0.09	-0.28	-0.10	1.00						
z	0.01	0.10	0.19	-0.60	1.00					
ln(x)	0.91	0.73	0.72	-0.05	-0.04	1.00				
ln(s)	0.84	0.85	0.77	-0.28	0.04	0.90	1.00			
ln(f)	0.81	0.75	0.83	0.04	0.15	0.86	0.86	1.00		
ln(v)	-0.07	-0.24	-0.04	0.97	-0.53	-0.04	-0.26	0.12	1.00	
ln(z)	0.00	0.07	0.19	-0.52	0.99	-0.05	0.00	0.16	-0.44	1.00

11 August 1995

## LW - 0.15h to LW + 0.08h

	x	s	f	v	z	ln(x)	ln(s)	ln(f)	ln(v)	ln(z)
x	1.00									
s	0.44	1.00								
f	0.29	0.42	1.00							
v	0.00	0.00	0.66	1.00						
z	-0.01	-0.16	-0.02	-0.15	1.00					
ln(x)	0.59	0.69	0.51	-0.04	0.14	1.00				
ln(s)	0.37	0.80	0.54	0.07	-0.24	0.84	1.00			
ln(f)	0.17	0.30	0.75	0.77	0.02	0.35	0.44	1.00		
ln(v)	0.00	-0.03	0.58	0.86	-0.05	-0.05	0.05	0.90	1.00	
ln(z)	-0.03	-0.18	-0.01	-0.13	0.99	0.13	-0.25	0.02	-0.04	1.00

## LW - 0.15h

	x	s	f	v	z	ln(x)	ln(s)	ln(f)	ln(v)	ln(z)
x	1.00									
s	0.72	1.00								
f	-0.76	-0.71	1.00							
v	0.04	0.48	-0.12	1.00						
z	0.04	0.39	-0.06	0.91	1.00					
ln(x)	0.92	0.61	-0.72	0.02	0.01	1.00				
ln(s)	0.65	0.82	-0.69	0.59	0.47	0.70	1.00			
ln(f)	0.52	0.40	-0.78	-0.13	-0.20	0.57	0.46	1.00		
ln(v)	-0.06	-0.39	-0.11	-0.83	-0.83	-0.05	-0.48	0.51	1.00	
ln(z)	0.04	0.38	-0.09	0.92	0.98	0.01	0.44	-0.14	-0.76	1.00

## LW + 0.08h

	x	s	f	v	z	ln(x)	ln(s)	ln(f)	ln(v)	ln(z)
x	1.00									
s	0.69	1.00								
f	-0.83	-0.64	1.00							
v	0.05	-0.45	0.03	1.00						
z	-0.02	0.41	0.00	-0.83	1.00					
ln(x)	0.90	0.61	-0.79	0.08	-0.02	1.00				
ln(s)	0.58	0.83	-0.67	-0.52	0.39	0.64	1.00			
ln(f)	0.70	0.55	-0.87	0.01	-0.06	0.79	0.67	1.00		
ln(v)	-0.02	-0.53	-0.02	0.85	-0.84	-0.01	-0.58	0.14	1.00	
ln(z)	-0.03	0.35	0.01	-0.83	0.98	-0.04	0.33	-0.06	-0.79	1.00

x = patch size, s = within-patch total SPM concentration, f = within-patch total SPM flux,  
v = within-patch averaged surface velocity & z = within-patch averaged water depth

15 August 1995

LW - 3.33h to LW - 2.17h

	x	s	f	v	z	ln(x)	ln(s)	ln(f)	ln(v)	ln(z)
x	1.00									
s	0.64	1.00								
f	-0.78	-0.90	1.00							
v	0.00	0.33	-0.16	1.00						
z	0.07	0.06	-0.18	0.52	1.00					
ln(x)	0.90	0.58	-0.70	-0.02	0.05	1.00				
ln(s)	0.63	0.84	-0.81	0.36	0.06	0.71	1.00			
ln(f)	0.69	0.74	-0.85	0.10	0.23	0.77	0.89	1.00		
ln(v)	-0.01	-0.36	0.16	-0.97	-0.49	0.01	-0.39	-0.10	1.00	
ln(z)	0.06	0.08	-0.21	0.51	0.99	0.05	0.09	0.28	-0.47	1.00

LW - 3.33h

	x	s	f	v	z	ln(x)	ln(s)	ln(f)	ln(v)	ln(z)
x	1.00									
s	0.89	1.00								
f	-0.89	-0.94	1.00							
v	0.09	0.09	0.06	1.00						
z	0.03	-0.12	0.07	0.75	1.00					
ln(x)	0.90	0.82	-0.82	0.08	0.02	1.00				
ln(s)	0.80	0.88	-0.84	0.07	-0.17	0.90	1.00			
ln(f)	0.77	0.81	-0.88	-0.13	-0.12	0.87	0.92	1.00		
ln(v)	-0.09	-0.08	-0.09	-0.97	-0.71	-0.09	-0.05	0.18	1.00	
ln(z)	0.03	-0.11	0.05	0.73	0.99	0.02	-0.16	-0.08	-0.68	1.00

LW - 3.18h

	x	s	f	v	z	ln(x)	ln(s)	ln(f)	ln(v)	ln(z)
x	1.00									
s	0.86	1.00								
f	-0.90	-0.94	1.00							
v	-0.01	0.07	0.08	1.00						
z	0.05	-0.08	0.01	0.69	1.00					
ln(x)	0.92	0.81	-0.84	-0.04	0.04	1.00				
ln(s)	0.79	0.91	-0.86	0.02	-0.14	0.87	1.00			
ln(f)	0.79	0.82	-0.90	-0.19	-0.04	0.86	0.91	1.00		
ln(v)	0.00	-0.05	-0.12	-0.98	-0.66	0.02	0.00	0.24	1.00	
ln(z)	0.05	-0.06	-0.02	0.67	0.99	0.04	-0.12	0.01	-0.61	1.00

x = patch size, s = within-patch total SPM concentration, f = within-patch total SPM flux,  
v = within-patch averaged surface velocity & z = within-patch averaged water depth

**LW - 2.93h**

	x	s	f	v	z	ln(x)	ln(s)	ln(f)	ln(v)	ln(z)
x	1.00									
s	0.82	1.00								
f	-0.86	-0.95	1.00							
v	0.06	0.26	-0.16	1.00						
z	0.04	0.03	-0.12	0.70	1.00					
ln(x)	0.89	0.73	-0.77	0.03	0.02	1.00				
ln(s)	0.75	0.86	-0.83	0.27	0.03	0.85	1.00			
ln(f)	0.75	0.79	-0.85	0.12	0.14	0.86	0.92	1.00		
ln(v)	-0.07	-0.24	0.13	-0.97	-0.67	-0.03	-0.25	-0.05	1.00	
ln(z)	0.04	0.06	-0.15	0.69	0.99	0.02	0.06	0.19	-0.64	1.00

**LW - 2.7h**

	x	s	f	v	z	ln(x)	ln(s)	ln(f)	ln(v)	ln(z)
x	1.00									
s	0.71	1.00								
f	-0.77	-0.96	1.00							
v	0.02	0.31	-0.25	1.00						
z	0.06	0.10	-0.21	0.64	1.00					
ln(x)	0.91	0.60	-0.67	-0.02	0.05	1.00				
ln(s)	0.67	0.83	-0.83	0.39	0.18	0.73	1.00			
ln(f)	0.68	0.75	-0.82	0.22	0.33	0.76	0.92	1.00		
ln(v)	-0.01	-0.28	0.21	-0.97	-0.56	0.03	-0.35	-0.13	1.00	
ln(z)	0.06	0.13	-0.24	0.63	0.99	0.05	0.22	0.39	-0.53	1.00

**LW - 2.43h**

	x	s	f	v	z	ln(x)	ln(s)	ln(f)	ln(v)	ln(z)
x	1.00									
s	0.71	1.00								
f	-0.79	-0.94	1.00							
v	0.08	0.42	-0.35	1.00						
z	0.11	0.19	-0.33	0.65	1.00					
ln(x)	0.87	0.66	-0.69	0.05	0.05	1.00				
ln(s)	0.61	0.88	-0.83	0.49	0.24	0.69	1.00			
ln(f)	0.63	0.83	-0.86	0.40	0.40	0.71	0.95	1.00		
ln(v)	-0.10	-0.45	0.37	-0.98	-0.65	-0.07	-0.52	-0.42	1.00	
ln(z)	0.09	0.22	-0.34	0.67	0.99	0.04	0.27	0.43	-0.65	1.00

LW - 2.17h

	x	s	f	v	z	ln(x)	ln(s)	ln(f)	ln(v)	ln(z)
x	1.00									
s	0.67	1.00								
f	-0.67	-0.91	1.00							
v	0.04	0.37	-0.29	1.00						
z	0.02	0.20	-0.39	0.60	1.00					
ln(x)	0.92	0.60	-0.62	0.05	0.02	1.00				
ln(s)	0.62	0.83	-0.81	0.48	0.32	0.67	1.00			
ln(f)	0.62	0.77	-0.86	0.35	0.49	0.67	0.93	1.00		
ln(v)	-0.03	-0.41	0.30	-0.98	-0.58	-0.04	-0.53	-0.38	1.00	
ln(z)	0.02	0.23	-0.40	0.64	0.99	0.02	0.35	0.51	-0.62	1.00

21 August 1995

LW + 3.27h to LW + 4.7h

	x	s	f	v	z	ln(x)	ln(s)	ln(f)	ln(v)	ln(z)
x	1.00									
s	0.84	1.00								
f	0.50	0.57	1.00							
v	-0.05	0.06	0.67	1.00						
z	0.21	-0.14	-0.01	-0.14	1.00					
ln(x)	0.91	0.79	0.50	-0.04	0.18	1.00				
ln(s)	0.77	0.90	0.56	0.11	-0.22	0.85	1.00			
ln(f)	0.31	0.40	0.76	0.79	0.02	0.36	0.47	1.00		
ln(v)	-0.07	0.05	0.60	0.87	-0.06	-0.04	0.09	0.91	1.00	
ln(z)	0.21	-0.15	0.01	-0.12	0.98	0.18	-0.22	0.03	-0.05	1.00

LW + 3.27h

	x	s	f	v	z	ln(x)	ln(s)	ln(f)	ln(v)	ln(z)
x	1.00									
s	0.84	1.00								
f	-0.60	-0.71	1.00							
v	0.33	0.17	0.27	1.00						
z	0.35	-0.02	0.14	0.70	1.00					
ln(x)	0.87	0.74	-0.72	0.26	0.32	1.00				
ln(s)	0.72	0.87	-0.79	0.09	-0.12	0.83	1.00			
ln(f)	0.51	0.61	-0.89	-0.47	-0.28	0.67	0.77	1.00		
ln(v)	-0.34	-0.21	-0.27	-0.98	-0.64	-0.25	-0.12	0.48	1.00	
ln(z)	0.33	-0.06	0.14	0.64	0.99	0.31	-0.16	-0.27	-0.58	1.00

LW + 3.48h

	x	s	f	v	z	ln(x)	ln(s)	ln(f)	ln(v)	ln(z)
x	1.00									
s	0.79	1.00								
f	0.83	0.96	1.00							
v	-0.25	0.01	0.09	1.00						
z	0.22	-0.18	-0.13	-0.79	1.00					
ln(x)	0.93	0.74	0.80	-0.23	0.18	1.00				
ln(s)	0.77	0.90	0.89	0.02	-0.22	0.83	1.00			
ln(f)	0.80	0.86	0.92	0.13	-0.15	0.87	0.95	1.00		
ln(v)	-0.25	-0.02	0.08	0.98	-0.75	-0.22	-0.02	0.12	1.00	
ln(z)	0.20	-0.22	-0.16	-0.77	0.99	0.16	-0.26	-0.19	-0.72	1.00

x = patch size, s = within-patch total SPM concentration, f = within-patch total SPM flux,  
v = within-patch averaged surface velocity & z = within-patch averaged water depth

**LW + 3.72h**

	x	s	f	v	z	ln(x)	ln(s)	ln(f)	ln(v)	ln(z)
x	1.00									
s	0.91	1.00								
f	0.90	0.94	1.00							
v	-0.16	0.00	0.11	1.00						
z	0.16	-0.11	-0.07	-0.83	1.00					
ln(x)	0.91	0.87	0.87	-0.13	0.11	1.00				
ln(s)	0.82	0.92	0.87	0.07	-0.21	0.91	1.00			
ln(f)	0.80	0.87	0.91	0.22	-0.18	0.90	0.94	1.00		
ln(v)	-0.16	-0.01	0.13	0.97	-0.78	-0.12	0.06	0.25	1.00	
ln(z)	0.15	-0.12	-0.06	-0.80	0.99	0.11	-0.21	-0.16	-0.75	1.00

**LW + 3.98h**

	x	s	f	v	z	ln(x)	ln(s)	ln(f)	ln(v)	ln(z)
x	1.00									
s	0.88	1.00								
f	0.87	0.93	1.00							
v	-0.14	0.13	0.22	1.00						
z	0.11	-0.20	-0.16	-0.79	1.00					
ln(x)	0.92	0.83	0.84	-0.13	0.08	1.00				
ln(s)	0.81	0.92	0.90	0.22	-0.27	0.88	1.00			
ln(f)	0.79	0.88	0.93	0.32	-0.25	0.86	0.97	1.00		
ln(v)	-0.15	0.13	0.23	0.97	-0.71	-0.14	0.23	0.35	1.00	
ln(z)	0.10	-0.16	-0.11	-0.61	0.94	0.06	-0.19	-0.15	-0.47	1.00

**LW + 4.25h**

	x	s	f	v	z	ln(x)	ln(s)	ln(f)	ln(v)	ln(z)
x	1.00									
s	0.85	1.00								
f	0.82	0.93	1.00							
v	-0.23	0.08	0.19	1.00						
z	0.23	-0.13	-0.11	-0.86	1.00					
ln(x)	0.91	0.80	0.83	-0.17	0.20	1.00				
ln(s)	0.79	0.90	0.90	0.19	-0.21	0.87	1.00			
ln(f)	0.76	0.84	0.92	0.28	-0.18	0.87	0.96	1.00		
ln(v)	-0.24	0.05	0.18	0.98	-0.85	-0.17	0.18	0.29	1.00	
ln(z)	0.24	-0.14	-0.10	-0.83	0.99	0.21	-0.21	-0.16	-0.81	1.00

**LW + 4.48h**

	x	s	f	v	z	ln(x)	ln(s)	ln(f)	ln(v)	ln(z)
x	1.00									
s	0.87	1.00								
f	0.85	0.95	1.00							
v	-0.15	0.16	0.25	1.00						
z	0.17	-0.19	-0.17	-0.88	1.00					
ln(x)	0.93	0.83	0.83	-0.13	0.15	1.00				
ln(s)	0.79	0.91	0.89	0.27	-0.30	0.87	1.00			
ln(f)	0.77	0.87	0.91	0.38	-0.30	0.85	0.96	1.00		
ln(v)	-0.13	0.16	0.26	0.98	-0.85	-0.09	0.27	0.40	1.00	
ln(z)	0.20	-0.18	-0.14	-0.85	0.99	0.18	-0.29	-0.26	-0.82	1.00

**LW + 4.7h**

	x	s	f	v	z	ln(x)	ln(s)	ln(f)	ln(v)	ln(z)
x	1.00									
s	0.82	1.00								
f	0.75	0.94	1.00							
v	-0.27	0.16	0.28	1.00						
z	0.25	-0.19	-0.19	-0.85	1.00					
ln(x)	0.92	0.78	0.76	-0.22	0.21	1.00				
ln(s)	0.75	0.91	0.89	0.26	-0.29	0.83	1.00			
ln(f)	0.70	0.86	0.91	0.39	-0.30	0.79	0.96	1.00		
ln(v)	-0.26	0.12	0.26	0.98	-0.83	-0.20	0.23	0.38	1.00	
ln(z)	0.25	-0.21	-0.18	-0.83	0.99	0.22	-0.30	-0.29	-0.80	1.00



## **Appendix F : Published papers**

Robinson, M-C., Morris, K.P. & Dyer, K.R., 1998, *Deriving Fluxes of Suspended Particulate Matter in the Humber Estuary using Airborne Remote Sensing*, Marine Pollution Bulletin, **37(3-7)**, 155-1163

Uncles, R.J., Morris, K.P., Stephens, J.A., Robinson, M-C. & Murphy, R.J., 1999, *Aircraft and Sea-truth Observations of Salinity and Temperature within the Tweed Estuary and Coastal-zone Frontal System*, International Journal of Remote Sensing, **20(3)**, 609-625



# Deriving Fluxes of Suspended Particulate Matter in the Humber Estuary, UK, Using Airborne Remote Sensing

M.-C. ROBINSON<sup>+</sup>\*, K. P. MORRIS<sup>+</sup> and K. R. DYER<sup>‡</sup>

<sup>+</sup>Centre for Coastal Marine Science, Plymouth Marine Laboratory, Prospect Place, West Hoe, Plymouth PL1 3DH, UK

<sup>‡</sup>Institute of Marine Studies, University of Plymouth, Drake Circus, Plymouth PL4 8AA, UK

This study exploits the use of airborne remote sensing for the assessment of coastal and estuarine environments, in particular the Humber Estuary. A Compact Airborne Spectrographic Imager was used to acquire a series of flightlines across the mouth of the Humber estuary during the flood on 10 August 1995. The flightlines encompassed the *flux curtain*, which consists of five moorings set out across the estuary to monitor flux of Suspended Particulate Matter (SPM). The images were radiometrically, atmospherically and geometrically corrected and SPM concentrations in surface waters derived. SPM flux was assessed by incorporating image-derived SPM concentration values with velocity results from a hydrodynamic model. These results were integrated over depth and an estimate of total flux determined for a 2-h section of the flood. © 1999 Elsevier Science Ltd. All rights reserved

## Introduction

The work presented here forms a core part of the Land-Ocean Interaction Study (LOIS), a Natural Environment Research Council (NERC) funded Thematic Programme. An important part of the LOIS campaign is the characterization, monitoring and modelling of fluxes within the coastal zone, which forms an integral part of the RACS(C) (Rivers, Atmospheres, Estuaries and Coasts Study (Coasts and Estuaries)) component of LOIS.

The accurate estimation of flux is important for a number of reasons (Jay *et al.*, 1997). These include:

- the calculation of residence time for the classification of estuaries and their ecosystems,
- the prediction of long-term changes in estuaries and the mechanisms behind such changes,
- assessment of the impacts of anthropogenic influences on estuarine environments.

- analysis of the origin of sedimentary sequences and the geological evolution of estuaries,
- improved management of the coastal zone, from both environmental and socio-economic perspectives.

Traditional approaches by oceanographic, estuarine and riverine monitoring projects incorporate *in situ* point source measurements. As Allan (1983) observed, 'the worst place from which to study the sea is the sea surface'. Point source monitoring does not provide a synoptic view of the area in question and may, in fact, be misleading in cases where a localized anomaly occurs. Jay *et al.* (1997) suggest that estimates of flux derived from direct measurements are generally inadequate and prone to error, and further that fluxes should be estimated using knowledge of the two-dimensional spatial distribution, in conjunction with variations in depth and time.

This paper attempts to approach the question of flux estimation multi-dimensionally. Remote sensing provides the two-dimensional synoptic coverage of an area and repeatedly flying an aircraft across a target provides a unique and invaluable time-series of image data. The modelling of in-water parameters with depth introduces a third dimension and, when incorporated with information gained through hydrodynamic modelling, provides a comprehensive multi-dimensional description of an area.

Airborne remote sensing within LOIS has acted as a unifying technology by providing synoptic parameterization of the areas of study. The main LOIS RACS(C) coastal study area (Fig. 1) comprises a section of the East Coast of England from Great Yarmouth to Berwick-upon-Tweed. This area is highly dynamic and susceptible to change, particularly in response to any rise in sea level. Acute coastal erosion of up to 2 m p.a. is prevalent along the Holderness coast, to the north of the Humber Estuary (Valentin, 1971). The Humber Estuary is one of the UK's largest and most economically influential estuaries, with a catchment area spanning

\*Corresponding author.

**TABLE 1**  
CASI bandset definition for RACS(C) and their associated SeaWiFS band relations.

CASI Band No.	SeaWiFS Band No.	Wavelength Range		Purpose
		Min (nm)	Max (nm)	
1	1	408	422	Gelbstoffe & chlorophyll
2	2	438	454	Chlorophyll & gelbstoffe
3	3	484	500	Gelbstoffe, chlorophyll and accessory pigment
4	4	504	519	SPM & accessory pigment
5	5	548	564	Accessory pigment and chlorophyll
6	6	612	631	MERIS compatible
7		662	678	Chlorophyll, SPM & chlorophyll fluorescence
8		680	687	SPM & chlorophyll fluorescence
9		707	718	Chlorophyll fluorescence & MERIS
10	7a	748	755	SPM & atmospheric aerosols
11	7b	757	784	SPM & atmospheric aerosols
12	8	817	831	Atmospheric water vapour band
13		848	884	SPM & atmospheric aerosols
14		888	902	Atmospheric aerosols & sediment

one-fifth of the surface area of England and with a port that handles 15000 ship movements and 500 000 passengers every year. The estuary has to be constantly dredged to maintain the shipping lanes that are so important for the economy of the region. Sediment fluxes into and out of the Humber Estuary, therefore, have great economic as well as environmental influence and importance.

The remote sensing platform used in this study was the NERC Piper Navajo Chieftain aircraft. On board was an ITRES Compact Airborne Spectrographic Imager (CASI), alongside a Daedalus AADS-1268 Airborne Thematic Mapper (ATM) and a Wild RC-10 camera. The CASI is a programmable, high spectral and spatial resolution, imaging spectrometer (Anger *et al.*, 1990). It has the analytical potential of a spectrometer, with the ability to record up to 288 spectral channels in the visible and near infrared. However, there is a trade-off between spectral and spatial resolutions on the CASI instrument, and at full spatial resolution it was only possible to resolve 14 spectral channels. These were acquired for the specific scientific application of water quality and atmospheric correction (Table 1). Suspended Particulate Matter (SPM) concentrations were derived from the CASI image data after a number of image calibration and correction steps. This enabled the calculation of sediment fluxes into and out of the estuary.

### Data Acquisition

The objective behind CASI overflights of the Humber Estuary was the acquisition of a sequential time-series of data throughout a significant fraction of the tide for the purposes of estimating sediment fluxes and providing sediment distributions for modelling. This was achieved by repeatedly flying transects across the mouth of the Humber Estuary from Spurn Head to Tetney Haven (Figs. 1 and 2). These data were then used to derive the SPM concentrations that were evolving over this time

scale. The SPM concentration varied in relation to tidal strength and exhibited spatial patterns that were related to bathymetry and bedform type.

This study focuses on a series of flightlines acquired on 10 August 1995, when low water was at 11:08 GMT (at Spurn Head) and high water at 17:25 GMT. The tides were rising springs and the tidal range was 5.9 m. The mean tidal range at Spurn Head is 4.8 m. ATM and CASI images were acquired over the mouth of the estuary. The transect encompassed a series of five fixed moorings (Fig. 2), the so-called *flux curtain* (Hardisty *et al.*, 1995). This sampled the top 0.2 m of water for SPM.



Fig. 1 LOIS RACS(C) study area.

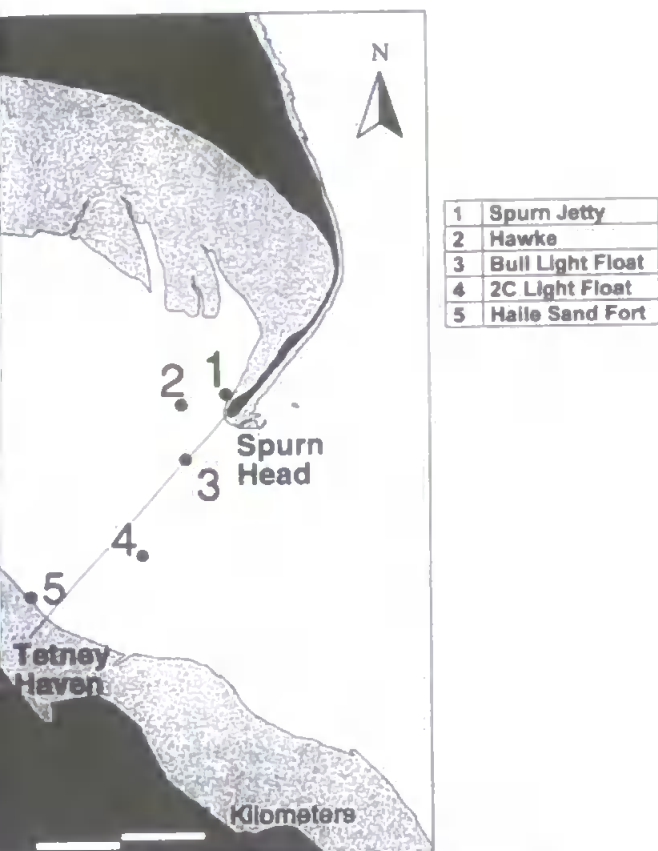


Fig. 2 Location of the transaxial CASI flightline across the Humber mouth and the flux curtain moorings.

tidal velocity, temperature and salinity at hourly intervals throughout the day and at 15-min intervals throughout the period coincident with the overflights (Fig. 3). This period covered the section of flooding tide from 12:27 GMT to 14:31 GMT.

## Data Processing

There are a number of image calibration and correction steps that need to be followed in order to accurately estimate SPM from image radiance values. These include radiometric calibration, atmospheric correction,

geometric correction and derivation and validation of the SPM algorithm itself.

### Radiometric calibration

The images were radiometrically calibrated using a suite of software developed for the NERC Airborne Remote Sensing Facility (ARSF) (Wilson *et al.*, 1997). Spectral calibration of the sensor was carried out at regular intervals. This information was used to calibrate each spectral band and applied to the dataset on a per pixel basis.

### Atmospheric correction

The useful remotely sensed information about an area of sea is contained within the physical properties of the radiation leaving that target, i.e. the water-leaving radiance. This signal is difficult to quantify due to interactions between absorption, scattering and reflection of light by in-water constituents. This is a considerable problem in coastal waters, whose optical properties are determined by resuspended organic and/or inorganic sediments and terrigenous particles (Gordon and Morel, 1983). Compounding this problem is the fact that radiative flux arriving at the sensor has travelled some distance through the atmosphere and has therefore suffered scattering, attenuation and possibly augmentation from surrounding light fields. The atmospheric contribution to remotely sensed data at optical wavelengths is over 50% and may approach 80–90% of the radiance received at the sensor towards the blue end of the spectrum, leaving only 10% of the signal containing useful information regarding the condition of the water (Cracknell and Hayes, 1991). The atmospheric component is not constant throughout an image, particularly in airborne data where the target-sensor path length is variable across the image. Atmospheric correction is therefore imperative. The CASI bandset (Table 1) was chosen to allow the detection and quantification of atmospheric aerosols, which represent a key input to the atmospheric correction procedure over coastal, SPM-dominated waters.

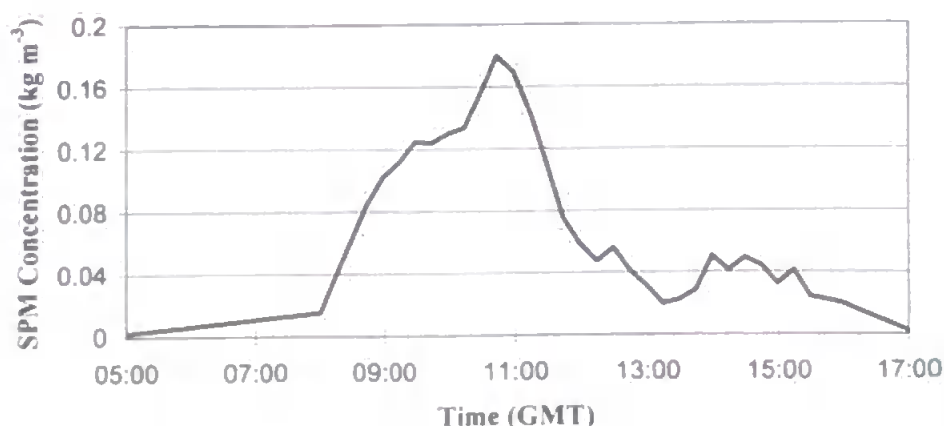


Fig. 3 SPM concentration measured from the Bull light Float on 10 August 1995.

The atmospheric correction algorithms used in this study (Moore *et al.*, 1998) assume that in waters with a significant SPM concentration, as is the case in the Humber Estuary, there is significant water-leaving radiance at near-infrared (NIR) wavelengths. Such areas are flagged within the atmospheric correction procedure and an iterative approach is employed, using a constrained fit of aerosol optical thickness values in the NIR and water-leaving reflectance against sediment concentrations. In clearer waters it is assumed that all radiance in the NIR has originated from the atmosphere, because water absorbs all energy at these wavelengths (Gordon and Wang, 1994). Values from the NIR are then used to correct bands in the visible part of the spectrum.

#### Geometric correction

Airborne images can suffer from a number of geometric distortions due to the instability of the aircraft. With the addition of the CASI to the NERC aircraft, the NERC ARSF took the important step of designing an Integrated Data System which synchronized the collection of ATM, CASI, and Global Positioning Satellite (GPS) data (Wilson, 1997). The GPS system consists of four separate antennae fitted in a rigid cross-shape on the aircraft roof. This provides measurements of local position and, by using the relative output of each antenna, allows the accurate measurement of the attitude of the aircraft in roll, pitch and yaw (Mockridge *et al.*, 1997).

#### SPM algorithm determination

SPM was derived from the CASI data using a simple band ratio algorithm that employed two visible wavebands covering the green (509 nm; band 4) and red (668 nm; band 7) parts of the electromagnetic spectrum. These wavelengths correspond to channels 4 and 6 of SeaWiFS (Sea viewing Wide Field-of-View Sensor; Hooker *et al.*, 1992) and were chosen to highlight the red clay sediments, which dominate the particulates found in the Humber mouth. Little, or no, chlorophyll was found in the area at this time. The signal from the green waveband, therefore, is dominated by SPM, justifying its use in the algorithm ratio. The algorithm takes the form:

$$\text{SPM}(\text{mg l}^{-1}) = a \left( \frac{\lambda_{509}}{\lambda_{668}} \right)^b$$

where  $\lambda_n$  is radiance at wavelength  $n$  and  $a$  and  $b$  are constants of 3.505 and  $-2.726$ , respectively.

The coefficients  $a$  and  $b$  were derived from the comparison of *in situ* SPM measurements, taken from the Bull Light Float (one of the *flux curtain* moorings; Fig. 2) and the corresponding image spectral ratios. The algorithm was applied to the suite of CASI images acquired on 10 August 1995 in order to obtain SPM information for that portion of the tidal cycle moni-

tored. Fig. 4 shows examples of image-derived SPM, acquired 2 h after Low Water (LW + 2h) and at LW + 3h.

### Interpretation of Image Features

Profiles across the mouth of the Humber, which encompassed the Bull Light Float (Fig. 2), were assessed for each SPM image. The results, displayed in Fig. 5, show the SPM concentrations throughout the 2-h section of the flood tide monitored for this exercise. The left-hand side of each plot represents Spurn Head with the  $x$ -axis defining distance along the profile (in metres). The dark lines represent SPM concentration in units of  $\text{kg m}^{-3}$ . On each profile, the location of the Bull Light Float can be identified as the  $0 \text{ kg m}^{-3}$  SPM feature at approximately 1300 m.

The asymmetric nature of the concentration field across the Humber is clear from the cross-sectional profiles in Fig. 5. Higher SPM concentrations were evident in the deeper northern channels during the flooding tide and lower concentrations in the south. SPM in the uppermost layers of the estuarine waters were mainly fine grained. Median particle sizes were in the range 70–110  $\mu\text{m}$  in the top few metres of the water column and probably comprised flocs of silt and clay and very fine sand (Uncles, R.J., pers. comm.).

During the flood tide, fine particulate matter was re-suspended as flow velocities increased. Sharp increases in the SPM concentrations at various points across the profile occurred from LW + 2.3h onwards (Fig. 5). The patterns of resuspension were streaky in nature at this stage of the flood tide (Fig. 4b and Fig. 5) and were probably influenced by the seabed distribution of sediment and by bedforms. Other surface features, such as the stirring up of large quantities of SPM in the wake of a ship, can be distinguished (Fig. 4b and Fig. 5). A small section of the ship was incorporated in the profile at LW + 3h and subsequently identified and masked out (as  $0 \text{ kg m}^{-3}$  SPM concentration) at a distance of approximately 2000 m across the profile. The sharp peak that immediately followed the ship's passage reached concentrations in excess of  $0.1 \text{ kg m}^{-3}$  (i.e. over twice the local background level) as water was stirred up from deeper in the water column. This exemplifies the stratified nature of these waters and identifies the complex problem of modelling their sediment dynamics.

### Calculation of SPM Flux

Previous studies have been largely limited by single-point flux calculations due to the limited spatial coverage of most surface-based monitoring exercises. Lane *et al.* (1997) identify that 'accurate flux calculations require consistently high spatial and temporal resolution across the cross section'. The use of remote sensing provides the temporally instantaneous spatial resolution, but direct velocity measurements are normally



Fig. 4 SPM concentrations derived from CASI images acquired at (a) (left) LW = 2h (b) (right) LW = 3h.

sparse. Assessment of SPM fluxes can be made through the incorporation of hydrodynamic models, which estimate flow velocities and direction. This is an important application for operational coastal remote sensing, as it reduces the need for costly and time-consuming surface-based monitoring.

The calculation of SPM flux needs to take into account the hydrological dynamics of flow in three dimensions. The Depth Integrated Velocities And Solute Transport (DIVAST) hydrological model (Falconer and

Owens, 1990) has been used here to model the depth-averaged flows in the Humber. The north and east velocity components from the DIVAST model were used to derive depth-averaged velocity vectors perpendicular to the profile across the Humber mouth. Surface velocities were then estimated from the Van-Veen profile (Fig. 6a) determined from the following equation:

$$u_1 = \frac{u}{\int_0^1 \eta^{0.19} \partial \eta} = 1.19 \bar{u}$$

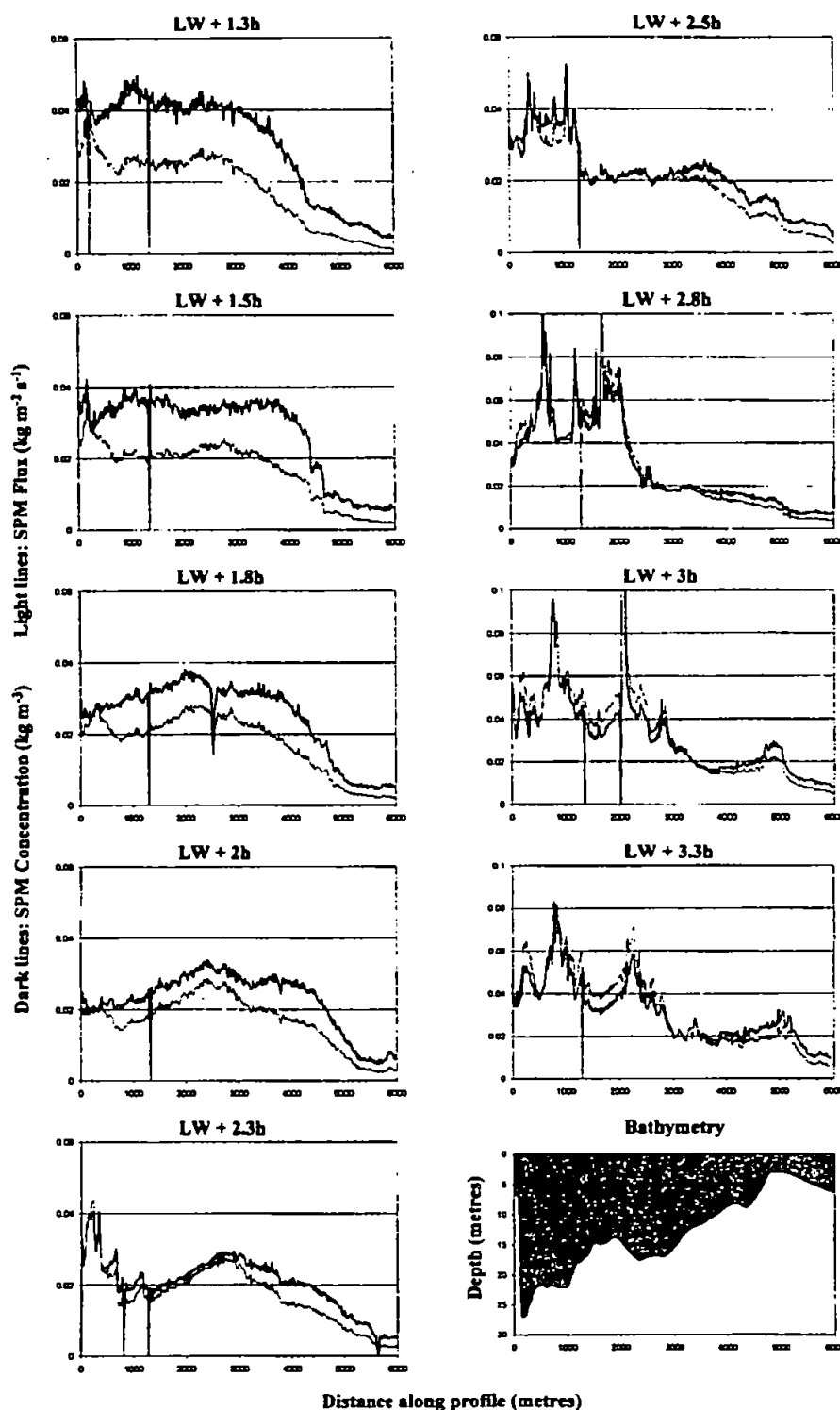


Fig. 5 Cross-sectional profiles derived from the CASI images acquired between LW + 1.3h and LW + 3.3h. The left-hand side of each plot represents Spurn Head with the  $x$ -axis defining distance along the profile. The dark lines represent SPM concentration; the light grey lines represent SPM flux. On each profile the location of the Bull Light Float can be identified as the  $0 \text{ kg m}^{-3}$  SPM feature at approximately 1300 m.

where  $\bar{u}$  is depth averaged velocity,  $u_1$  the velocity at the surface and  $\eta$  is the relative depth:

$$\eta = \frac{z}{d}$$

where  $z$  is height above the bed and  $d$  the total depth (e.g. Uncles and Jordan, 1994).

The product of the resultant surface velocities and image-derived SPM concentrations then provided an estimate of SPM flux for each 2.5 m pixel along the profile. Fig. 5 shows SPM fluxes in  $\text{kg m}^{-2} \text{ s}^{-1}$  as a light grey line. At LW + 1.3h, velocities ranged from 0.3 to 0.7  $\text{m s}^{-1}$ . Velocities gradually increased to LW + 2.5h,



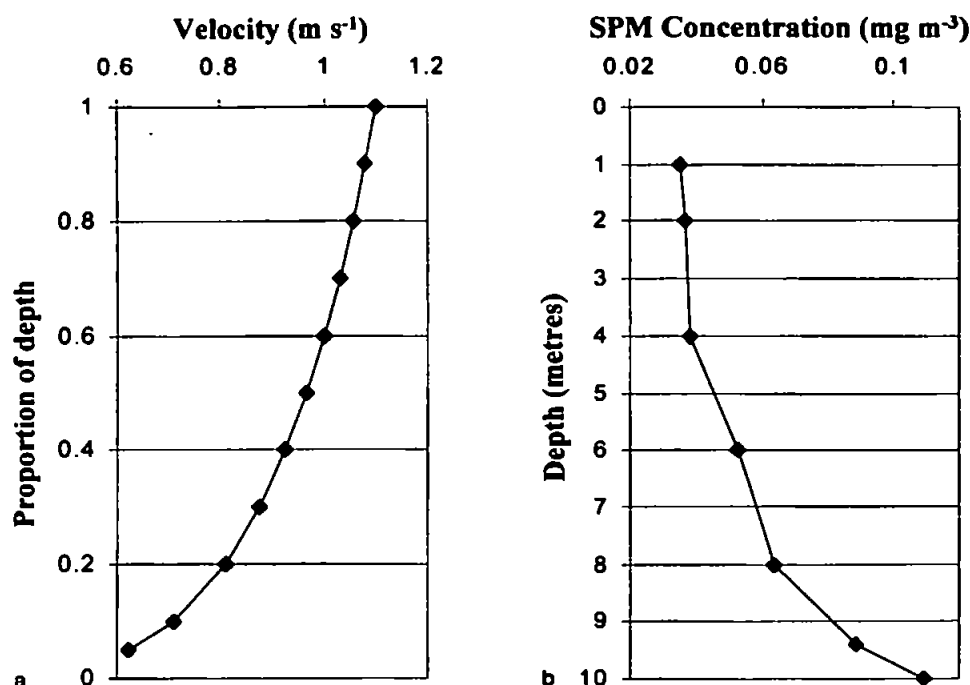


Fig. 6 (a) (left) The Van-Veen profile showing the variation of water velocity with depth. (b) (right) A typical depth profile of SPM concentrations acquired approximately 600 m to the west of Spurn Head at Hawke.

where an average of 1 m s<sup>-1</sup> was reached. Following this, velocities exceeded 1 m s<sup>-1</sup> in the northern channels, which coincided with the resuspension of sediment in these deeper channels.

Field measurements acquired in the region of the Humber mouth have shown that SPM concentrations increase with depth. Fig. 6b shows a depth profile of SPM concentrations taken approximately 600 m to the west of Spurn Head (Uncles, R.J., pers. comm.). This increase with depth corresponds inversely to the Van-Veen profile (Fig. 6a), where water velocities are shown to decrease characteristically towards the bed as SPM concentrations increase. SPM depth profiles will also vary with sediment and bedform type and slope and current speed. The Rouse equation (from Dyer, 1986) was fitted to the measured SPM depth profile. The equation describes concentration with depth and is defined as:

$$\frac{C_z}{C_a} = \left(\frac{a}{z}\right)^B$$

where  $C_z$  and  $C_a$  are SPM concentration at a height  $z$  and at a reference height  $a$ , respectively, and:

$$B = \frac{w_s}{\beta \kappa u_*}$$

where  $\beta$  is the ratio of the eddy diffusion coefficient for the sediment to that for the fluid (assumed to be 1; Dyer, 1986),  $\kappa$  is von Karman's constant (taken to be 0.4; Dyer, 1986),  $w_s$  is the settling velocity and  $u_*$  is the friction velocity.

In the case of the Humber Estuary,  $w_s/u_*$  will be small, due to the dominance of fine silts and clays in a fast flowing environment. An initial estimate of 0.1 for

$w_s/u_*$  was taken and then iteratively changed to fit the Rouse equation to the measured SPM profile. A final value of 0.5 was derived for  $B$ . Using this value in the equation, the measured SPM concentrations were integrated with depth and a total concentration for the profile of 0.471 mg m<sup>-3</sup> derived. If the surface SPM concentration value is assumed as a uniform measure throughout the profile, a total concentration of 0.315 mg m<sup>-3</sup> is obtained. Therefore, by assuming uniform concentration with depth, one can expect a 33% error when calculating total concentration throughout the profile. However, in the absence of reliable models that describe SPM concentrations down through the water column during the measurement period and over the study site, a uniform concentration with depth has been assumed here. The limitations of this assumption must be recognized and the possible errors in the calculation of fluxes appreciated.

Using bathymetric data of the estuary (derived from Hydrographic Office charts), it was possible to integrate SPM flux with depth. By additionally integrating throughout the observed time sequence, an estimate of SPM flux for the 2-h section of the flood tide was obtained (Fig. 7). This figure illustrates the larger influx of SPM to the estuary through the northern channels during a flood tide. The total SPM flux for this time period was  $8.8 \times 10^6$  kg.

## Conclusions

Surface-based measurements are largely limited to single point studies. Remote sensing provides informa-



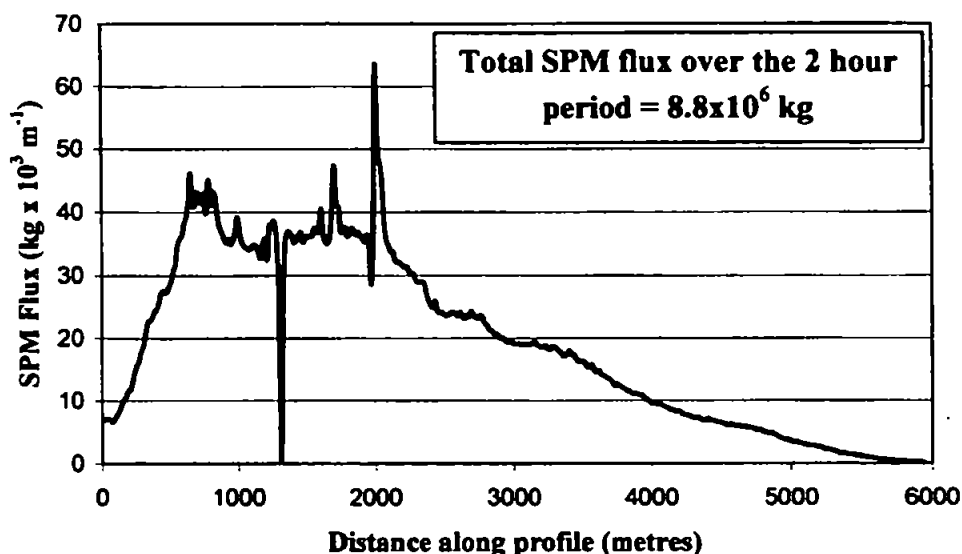


Fig. 7 Total SPM flux for the transaxial cross-section of the Humber mouth over the 2-h section of the flood tide spanning LW + 1.3h to LW + 3.3h. The left-hand side of the plot represents Spurn Head with the x-axis defining distance along the profile.

tion on the two-dimensional, surface structure of the water. Bathymetric analysis extends this to three dimensions and hydrodynamic models add the temporal element. A vast quantity of remotely sensed data has been acquired within the LOIS project and the future holds much potential, with studies over a more complete tidal cycle possible.

The work presented here has examined the use of remotely sensed data to estimate SPM fluxes across a section of the flood tide. This study has successfully tested new approaches to SPM flux evaluation and has estimated SPM flux across the mouth of the Humber Estuary over a 2-h section of the flood tide. Although the assumption that SPM concentration is uniform with depth had to be made due to model and *in situ* data limitations, the results provide some insight into the feasibility of such studies.

Of great importance are the hydrodynamic models themselves and an increase in the spatial resolution of their output would be of benefit. A hydrodynamic model has been developed within LOIS for use in the Humber Estuary (Wood *et al.*, 1996) and this should enable the more accurate determination of flow regimes within the estuary. In addition to this, a modelled depth profile of velocity and SPM would increase the accuracy in three dimensions.

It is hoped that future work will examine the type and distribution of bedforms to the SPM concentration and flux measurements derived using the procedures reported here. It may then be possible to attempt to describe the sources of the SPM entering the estuary and any resuspension which takes place. Studies such as these will enable the progression of our understanding of the fluxes into and out of the Humber Estuary and so fulfil one of the main aims of the LOIS project.

This study was executed as part of the NERC LOIS project and is LOIS Publication Number No. 430. The CASI data were acquired and distributed by the NERC ARSF. We would like to thank Dr R.J. Uncles at Plymouth Marine Laboratory for his advice and assistance, and Prof. J. Hardisty and N. Hughes at the Humber Observatory, Hull University, for provision of the *in situ* data.

- Allan, T. D. (1983) Oceanography from Space. In *Remote Sensing Applications in Marine Science and Technology*, ed. A. P. Cracknell. Reidel, Dordrecht, Holland, pp. 1–16.
- Anger, C. D., Babey, S. K. and Adamson, R. J. (1990) A new approach to imaging spectroscopy. In *Imaging Spectroscopy of the Terrestrial Environment* pp. 72–86, ed. G. Vane, Proc. SPIE 1298.
- Cracknell, A. P. and Hayes, L. W. B. (1991) *Introduction to Remote Sensing*, eds. Taylor and Francis, London, p. 150.
- Dyer, K. R. (1986) *Coastal and Estuarine Sediment Dynamics*, eds. John Wiley, Chichester, UK, p. 160.
- Falconer, R. A. and Owens, P. H. (1990) Numerical modelling of suspended sediment fluxes in estuarine waters. *Estuarine, Coastal and Shelf Science* 31, 745–762.
- Gordon, H. R. and Morel, A. Y. (1983) *Remote Assessment of Ocean Color for Interpretation of Satellite Visible Imagery. Lecture Notes on Coastal and Estuarine Studies*, Springer, Berlin, p. 27.
- Gordon, H. R. and Wang, M. (1994) Retrieval of water-leaving radiance and aerosol optical thickness over the oceans with SeaWiFS: a preliminary algorithm. *Applied Optics* 33(3), 443–452.
- Hardisty, J., Huntley, D. A., Metcalfe, S. E., Marsden, T. K. and Rouse, H. L. (1995) Modelling and *in situ* measurement of sediment flux in the lower Humber with particular reference to freshwater controls, tidal and storm forcing. In: *LOIS RACS(C) Second Annual Workshop*, LOIS publication No. 54, Bristol, UK, 8–4, 27–29 September 1995.
- Hooker, S. B., Esaias, W. E., Feldman, G. C., Gregg, W. W. and McClain, C. R. (1992) An overview of SeaWiFS and ocean color. NASA Technical Memorandum 104566, Vol. 1, p. 1.
- Jay, D. A., Geyer, W. R., Uncles, R. J., Vallino, J., Largier, J. and Boynton, W. R. (1997) A review of recent developments in estuarine scalar flux estimation. *Estuaries* 20, 262–280.
- Lane, A., Prandle, D., Harrison, A. J., Jones, P. D. and Jarvis, C. J. (1997) Measuring fluxes in tidal estuaries: sensitivity to instrumentation and associated data analyses. *Estuarine, Coastal and Shelf Science* 45, 433–451.
- Mockridge, W., Leach, M. and Wilson, A. K. (1997) Integrating a Daedalus 1268 ATM, attitude GPS and AHRS to achieve scan rate geometric correction. *Proceedings of the Third International Airborne Remote Sensing conference and exhibition*, 7–10 July 1997, Copenhagen, Denmark, 1-158-1-165.

- Moore, G. F., Aiken, J. and Lavender, S. J. (1998) The atmospheric correction of water colour and the quantity retrieval of suspended particulate matter in Case II waters. Application to MERIS. *International Journal of Remote Sensing*, Special Issue, in press.
- Uncles, R. J. and Jordan, M. B. (1994) Measurements of tidal currents and estimated energy fluxes in the Bristol Channel. In *Mixing and Transport in the Environment*, ed. K. J. Beven. John Wiley, Chichester, UK, pp. 221-245.
- Valentin, H. (1971) Land loss at Holderness. *Applied Coastal Geomorphology*, ed. J. A. Steers. MacMillan, UK, pp. 116-137.
- Wilson, A. K. (1997) An integrated data system for airborne remote sensing. *International Journal of Remote Sensing* 18(9), 1889-1901.
- Wilson, A. K., Mockridge, W. and Robinson, M.-C. (1997) Post-processing to achieve radiometric and geometric correction of ATM and CASI data. In *Proceedings of the Third International Airborne Remote Sensing conference and exhibition*, 7-10 July 1997, Copenhagen, Denmark, 1-447-1-454.
- Wood, R., Gorley, R and Harris, J. (1996) Estuarine and coastal flux modelling. In *Land-Ocean Interaction Study first annual meeting*, 26-28 March 1996, Plymouth, LOIS Publication No. 106, pp. 109-110.
-

## Aircraft and sea-truth observations of salinity and temperature within the Tweed Estuary and coastal-zone frontal system

R. J. UNCLES, K. P. MORRIS, J. A. STEPHENS,  
M.-C. ROBINSON† and R. J. MURPHY‡

NERC, Centre for Coastal and Marine Sciences, Plymouth Marine Laboratory,  
Plymouth PL1 3DH, England, UK; e-mail: rju@pml.ac.uk

†Institute of Marine Studies, University of Plymouth, Plymouth PL4 8AA,  
England, UK

‡National Institute of Water and Atmospheric Research, PO Box 14-901,  
Kilbirnie, Wellington, New Zealand

**Abstract.** Results are presented of frontal phenomena in the Tweed Estuary, UK. Salinity distributions in the lower estuary were particularly complex and salinity stratification was strong. Large areas of high salinity waters abutted waters of much lower salinity with the formation of distinct frontal systems. These systems were largely controlled by the bathymetry of the region, especially the shoal and inlet morphologies. Sea-truth and remote sensing observations allowed the high-resolution, spatial determination of surface temperature and salinity fields within the frontal regions.

### 1. Introduction

The River Tweed and Tweed Estuary are located on the English-Scottish border (figure 1(a)). Early research within the estuary concentrated on its chemistry (Gardner and Ravenscroft 1991) and little information on circulation and salinity was available until recently (Uncles and Stephens 1996, Uncles *et al.* 1997). These later studies showed that the Tweed was a rapidly flushed, highly stratified estuary in which frontal systems were ubiquitous. In this article we present high-resolution surface salinity and temperature distributions that delineate frontal phenomena within the Tweed. Data were derived from aircraft and sea-truth measurements made during May 1995.

Remotely sensed data have become increasingly important in our attempts to understand the fine-scale behaviour of both estuarine circulation (Anderson *et al.* 1992, Ferrier *et al.* 1996, Ferrier and Anderson 1997a,b) and estuarine and coastal wastewater dispersal (Ferrier and Anderson 1996, Davies *et al.* 1997). The focus of this article is on the use of thermal and photographic observations from aircraft and sea-based monitoring to estimate the high-resolution surface temperature and salinity fields that were associated with a tidal intrusion front that propagated through the Tweed's inlet on a flooding, mean-range tide (Uncles *et al.* 1997, and also Simpson and Britter 1979, Simpson and Nunes 1981, Largier 1992). Previous work showed that the inlet neck (region of minimal cross-section) appeared to act as a control

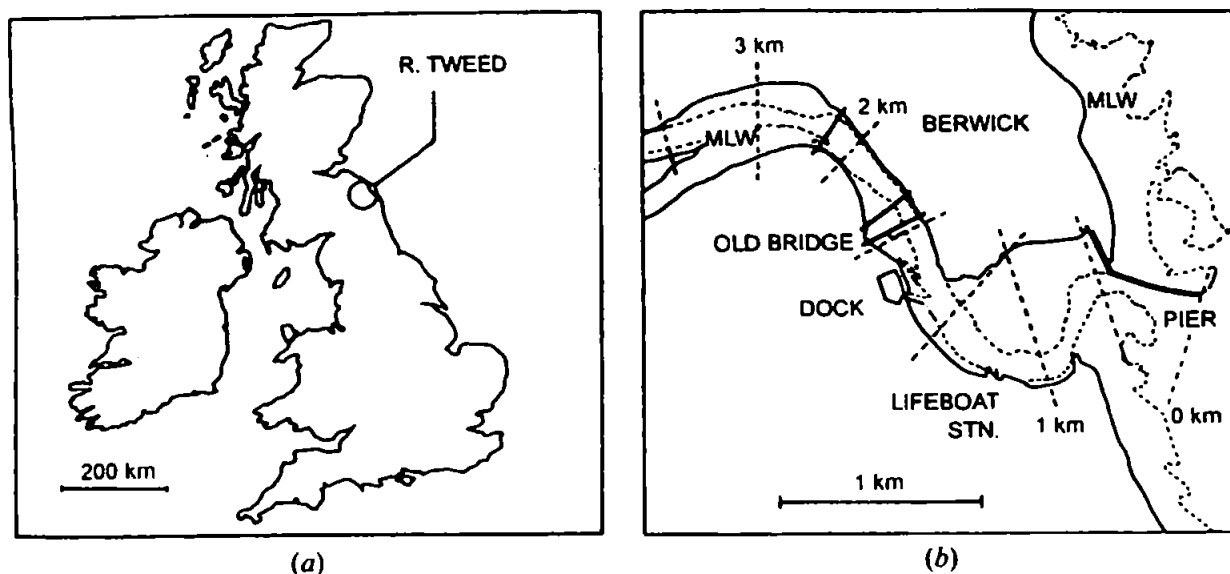


Figure 1. The Lower Tweed Estuary and its location within the British Isles. (a) Location of the Tweed Estuary. (b) The Lower Tweed. Distances along the estuary are marked off in 0.5 km intervals from the Pier Head at the seaward end of the Harbour Pier.

section for the inflow of high-salinity coastal waters during the flood portion of spring tides (Armi and Farmer 1986, Stigebrandt 1988, Largier and Taljaard 1991, Uncles *et al.* 1997). The objectives here are to: (i) investigate near-surface stratification in the outer Tweed Estuary, (ii) follow the evolution of surface frontal systems during a flooding tide, and (iii) map the surface distributions of salinity and temperature.

The Tweed is particularly important as a fishery for trout and salmon (The Tweed Foundation 1989 and 1992). It is a fairly steeply rising and shallow estuary. The tidal limit is located approximately 13 km from the mouth (Fox, personal communication). The mouth of the estuary is located between the coastal towns of Berwick-upon-Tweed (Berwick) and Tweedmouth. Depths at high water are typically a few metres. The width at the tidal limit is about 100 m and the width near the old Berwick Bridge, at 2 km from the mouth, is about 300 m (figure 1(b)). The width increases to about 700 m in the lower estuary, between the Old Bridge and the Harbour Pier. The mouth (a tidal inlet at low water levels) is confined between the Harbour Pier and a sand spit. The spit is dry at low water and is covered at high water. The width at the inlet neck is about 50 m at low water.

## 2. Observations and methods

Near-surface salinity and temperature were measured during a flooding tide along transverse tracks in the lower estuary on 4 May 1995 in order to delineate frontal features there. An inflatable boat was fitted with salinity-temperature sensors at 0.10, 0.45 and 0.55 m beneath surface and steered between navigational turning stations. Data at 0.1 m were recorded at 30-sec. intervals and those at 0.45 and 0.50 m at 3-sec. intervals. During these measurements, repeated aircraft over-flights were undertaken to acquire photographs and thermal images of the region.

The aircraft deployed for this study was the NERC Airborne Remote Sensing Facility's Piper Navajo Chieftain PA31-350. Mounted onboard this craft was a suite of instrumentation that included a Daedalus-AADS-1268 Airborne Thematic Mapper (ATM) and a Wild-RC-10 metric survey camera. No other approach could have provided the near-synoptic, contiguous acquisition of salinity and temperature data

that are essential for the quantitative delineation of rapidly changing frontal systems within estuaries and the coastal zone.

Remotely sensed data were acquired every 5–10 minutes throughout two portions of a flood tide on 4 May 1995. Data acquisition commenced at 1055 GMT (low water, i.e. LW) and continued until LW+0.66h, and then from LW+2.51h to LW+5.21h (1608 GMT). This coincided with the monitoring exercise in place at the water's surface. The work presented here comprises a description of the series of images taken between LW and LW+4.1h (1500 GMT).

### 3. Environmental data

Tides at Berwick are semidiurnal with mean spring and neap ranges of 4.1 and 2.5 m, respectively. Mean high water and low water spring tide water levels are 4.7 and 0.6 m, relative to local chart datum (Hydrographic Office 1992 and 1993). Mean high-water and low-water neap tide water levels are 3.8 and 1.3 m. The tidal range was decreasing from 4.0 m spring tides on 29 April to 3.5 m on 4 May, slightly greater than the mean tidal range of 3.3 m (figure 2(a)).

Freshwater inflow to the Tweed Estuary is the sum of run-off from the Tweed and Whiteadder Rivers. The long-term averaged inflow from the Whiteadder is about 8% of that from the Tweed. The long-term, monthly-averaged inflow to the estuary varies from about  $140 \text{ m}^3 \text{ s}^{-1}$  during January to about  $30 \text{ m}^3 \text{ s}^{-1}$  during July. The freshwater inflows from the Tweed and Whiteadder Rivers were steadily decreasing over the 12 day period before the measurements and amounted to  $27 \text{ m}^3 \text{ s}^{-1}$  on 4 May, compared with the long-term annual mean of  $84 \text{ m}^3 \text{ s}^{-1}$  (figure 2(b)).

### 4. Physical background

Data from an earlier field study are used to illustrate physical behaviour in the lower Tweed Estuary and inside the inlet region during a flood tide.

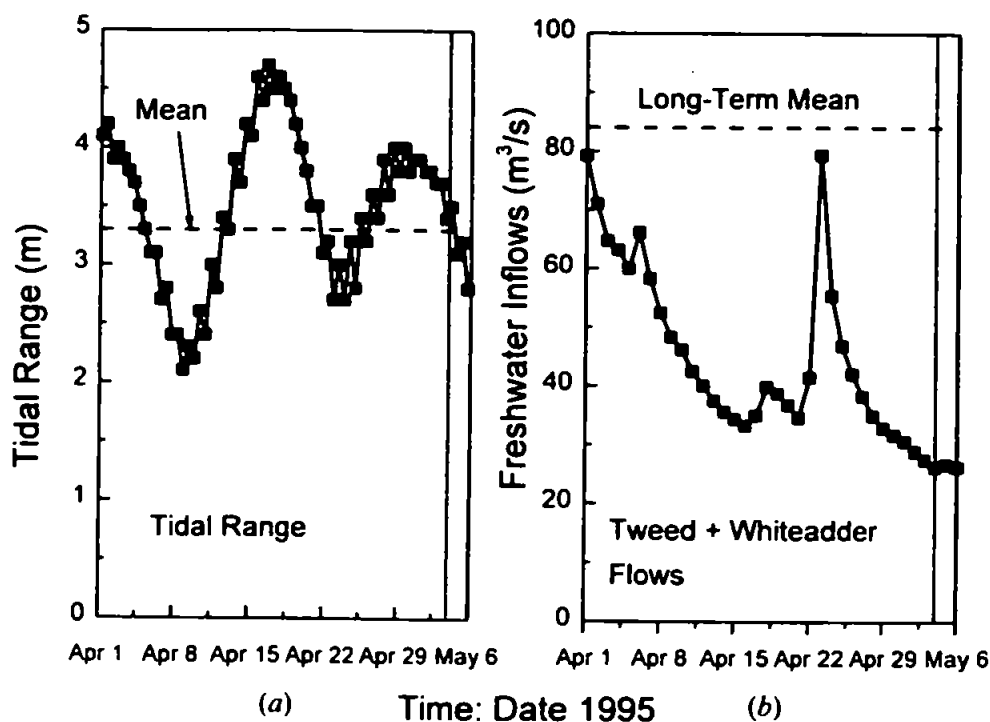


Figure 2. Environmental data during 1 April to 6 May 1995. (a) Predicted tidal range at Berwick (m). (b) Freshwater inflow from the Tweed and Whiteadder Rivers ( $\text{m}^3 \text{ s}^{-1}$ ).

#### 4.1. Longitudinal salinity distributions

Main-channel salinity distributions are strong functions of intratidal phase, tidal range and freshwater inflow (e.g. Fischer *et al.* 1979, Dyer and New 1986). The flood behaviour observed on 20 September 1993 is relevant to the behaviour of tidal intrusion fronts (figure 3). High-water (HW) level at Berwick was 4.7 m (mean springs) and the freshwater inflow was fairly low ( $35 \text{ m}^3 \text{ s}^{-1}$ ). The salt wedge (salinity  $>30$ ) had moved  $>1 \text{ km}$  up-estuary by 2.6 h after low-water (LW + 2.6 h). The halocline which separated upper and lower layers (salinities  $<5$  and  $>30$ , respectively) was about 1 m thick (figure 3(a)). By LW + 3.3 h the salt wedge had moved  $>2 \text{ km}$  into the estuary and the halocline thickness had increased to 1.5 m. In the lower reaches the halocline had mixed to the surface, so that the water column comprised a two-section system with high salinity waters overlain by a highly stratified upper layer of about 2 m thickness. Frontal systems were evident inside the inlet ( $<0.5 \text{ km}$  from the Pier Head) at LW + 2.8 h (figure 3(a)) and in the main channel of the estuary ( $>0.5 \text{ km}$ ) at LW + 3.5 h (figure 3(b)).

#### 4.2. Currents

Measurements in the neck of the inlet on 28 September 1993 illustrate the early flood dynamics of the flow there (figure 4). Tides were small springs (4.4 m HW level at Berwick) and freshwater inflows were low ( $25 \text{ m}^3 \text{ s}^{-1}$ ). A vertical profiling station was occupied close to the Harbour Pier wall and in shallow water to the side of the main channel. At LW + 0.2 h the water column was homogeneous (salinity  $\sim 5$  over a depth of 1.2 m) and the ebb-directed current profile was approximately linear with depth. Speeds increased from bed to surface (figures 4(a,b)). By LW + 0.9 h a near-bed, high salinity current was observed to be moving up-estuary. This current probably occurred earlier in the deep channel ( $\sim 4 \text{ m}$ ) but required a greater depth of flooding water before spreading onto the shallower parts of the section. The upper 1 m still had low salinities ( $<7$ ). By LW + 1.4 h the flooding, high salinity basal current had become thicker and the low salinity ( $<5$ ) upper layer was  $<0.7 \text{ m}$  thick (figures 4(a,b)).

A classical gravitational circulation (e.g. Turner 1973) therefore occurred within

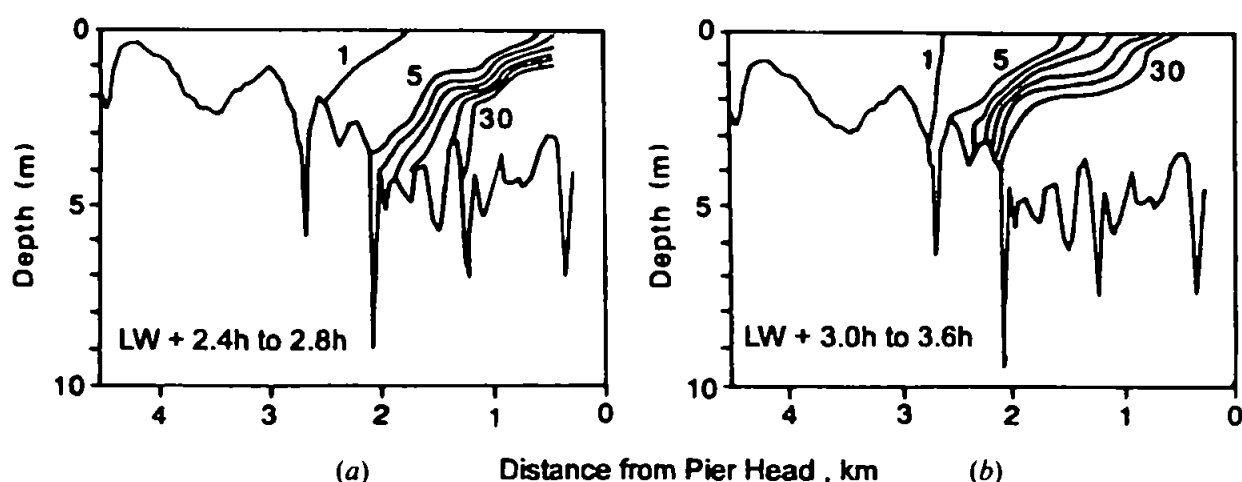


Figure 3. Salinity from longitudinal transects of the Tweed during a flooding spring tide on 20 September 1993. The HW level at Berwick was 4.7 m and the daily-averaged freshwater inflow was  $35 \text{ m}^3 \text{ s}^{-1}$ . (a) Transect between LW + 2.4 h and 2.8 h. (b) Transect between LW + 3.0 h and 3.6 h.

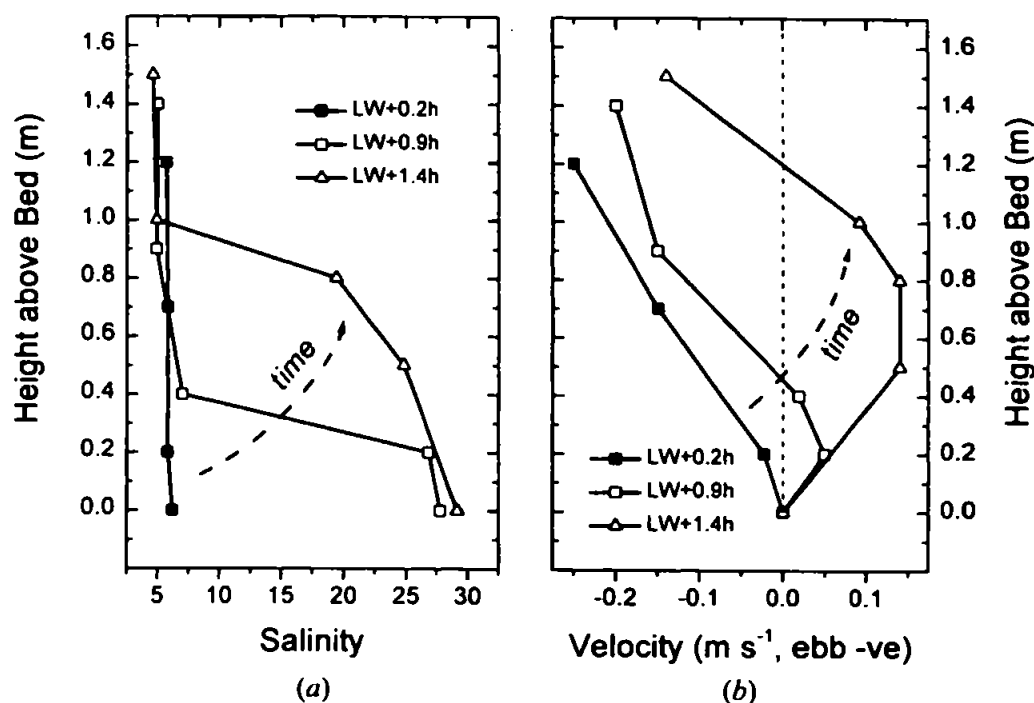


Figure 4. Vertical profiles of currents and salinity at the inlet neck on a flooding spring tide during 28 September 1993. Profiles are at LW + 0.2, 0.9 and 1.4 h. (a) Salinity. (b) Velocity.

the inlet during the early flood period of this low freshwater inflow, small spring tide. The surface layer thinned while ebbing and decelerating (figure 4(b)) and the flooding basal current increased in speed.

## 5. Results

### 5.1. Remotely sensed time-series images

Remotely sensed, thermal (band 11, i.e.  $8.4\text{ }\mu\text{m}$ – $11.5\text{ }\mu\text{m}$ ) ATM images of the estuary mouth were used to track the intrusion of saltwater into the Tweed during the afternoon flood tide of 4 May 1995. The raw digital thermal data were processed to provide apparent surface temperatures. In-flight calibration consisted of two controllable black bodies that acted as maximum and minimum infrared references (Wilson 1988). The calibrated radiance was converted to brightness temperature by inverting the Planck function equation (Callison 1985). The water surface was assumed to have a constant emissivity of 0.98, which is an average value for clear water bodies (Wilson, personal communication). A further step of atmospheric correction would be required to derive actual sea surface kinetic temperature (Callison *et al.* 1987), but this was not done here.

Between LW and LW + 0.6 h there was little thermal structure evident in the low salinity surface waters of the lower Tweed and in the adjacent coastal zone (figure 5). By LW + 2.5 h the flooding tide of high salinity coastal waters had developed a frontal boundary that defined the margins of the out-flowing, low-salinity surface waters (figure 5). The 'V'-shaped tidal intrusion front of high-salinity coastal waters formed within the inlet between LW + 2.7 h and LW + 3.0 h (figure 6) at around the time of peak flood currents. The 'V'-shaped front remained within the inlet between LW + 3.0 and LW + 3.6 h (figures 6 and 7) but had migrated into the main channel of the estuary by LW + 4.0 h (figure 7). The maximum rate of frontal migration was about  $0.1\text{ m s}^{-1}$ , compared with tidal current speeds of  $>0.5\text{ m s}^{-1}$ . Denser saline waters had already progressed further into the estuary beneath the low-salinity

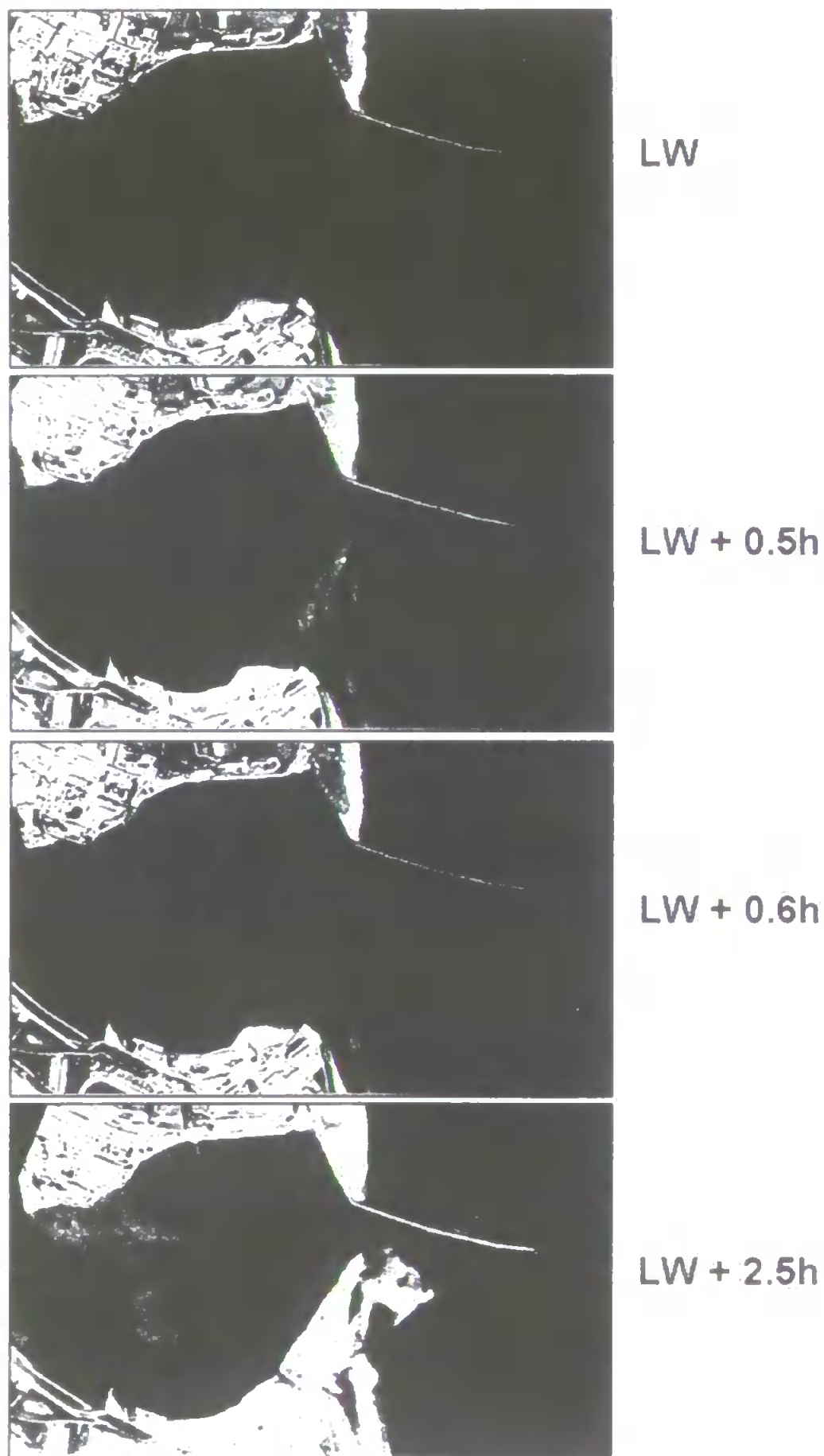


Figure 5. ATM thermal (band 11) image acquired at LW, LW+0.5h, LW+0.6h and LW+2.5h on 4 May 1995 and scaled to display and highlight the frontal features within the water surface. The lighter grey shading delineates the warmer, fresher waters in the estuary and the darker grey and black shading the colder seawater.



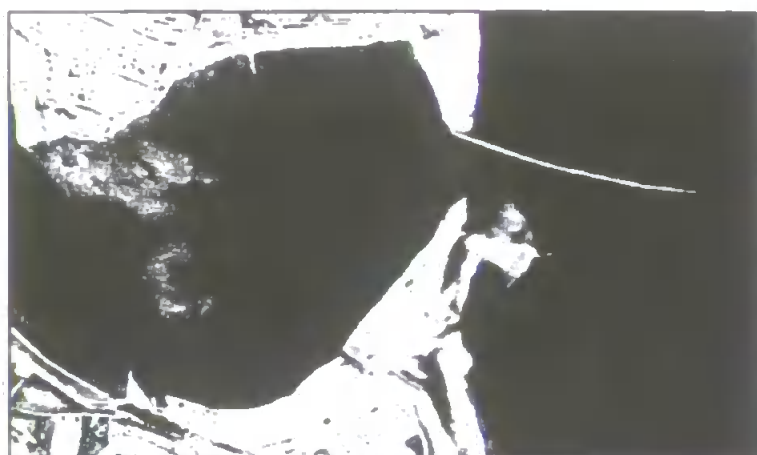
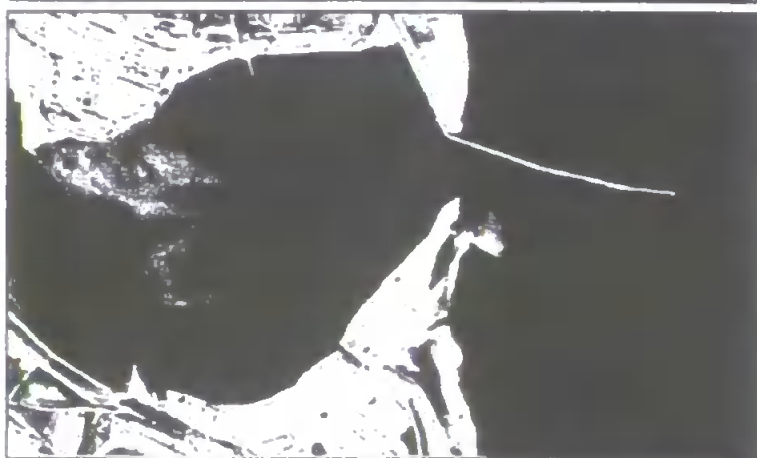
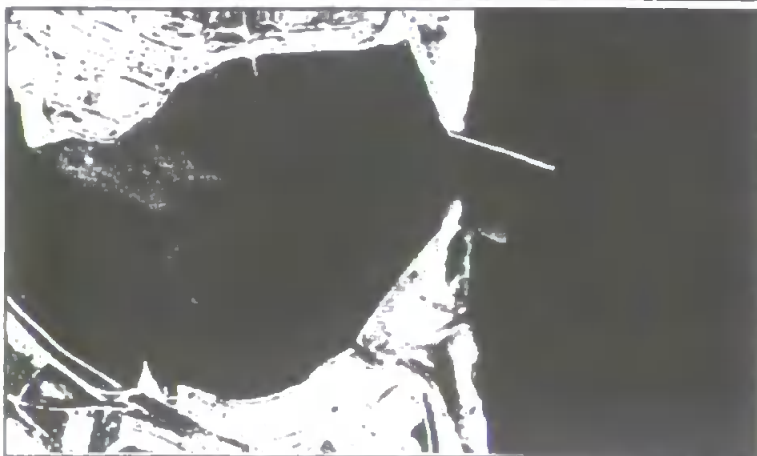
**LW + 2.7h****LW + 3.0h****LW + 3.1h****LW + 3.2h**

Figure 6. ATM thermal (band 11) image acquired at LW + 2.7 h, LW + 3.0 h, LW + 3.1 h and LW + 3.2 h on 4 May 1995 and scaled to display and highlight the frontal features within the water surface. The lighter grey shading delineates the warmer, fresher waters in the estuary and the darker grey and black shading the colder seawater.

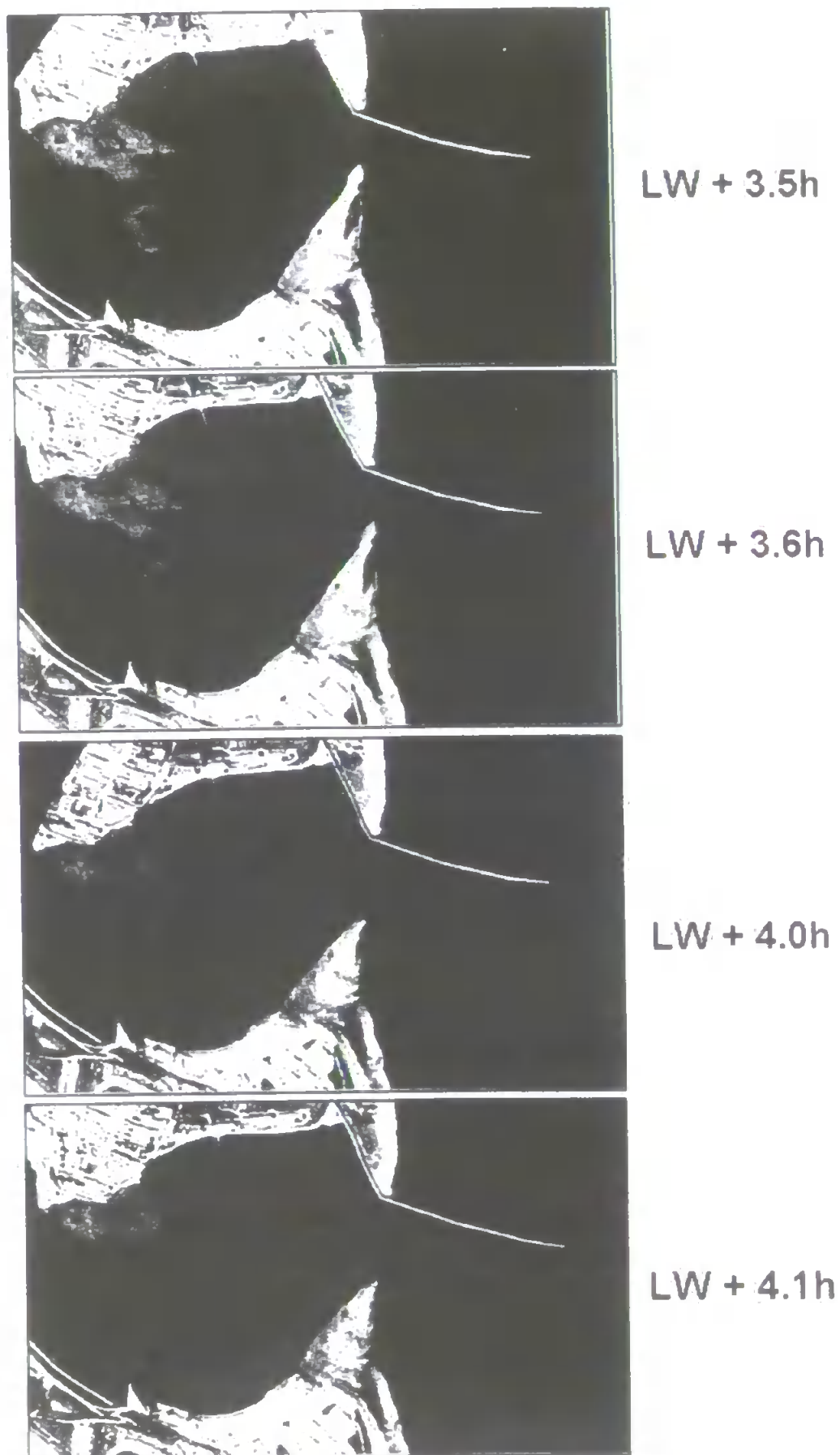


Figure 7. ATM thermal (band 11) image acquired at LW + 3.5 h, LW + 3.6 h, LW + 4.0 h and LW + 4.1 h on 4 May 1995 and scaled to display and highlight the frontal features within the water surface. The lighter grey shading delineates the warmer, fresher waters in the estuary and the darker grey and black shading the colder seawater.

surface layers by the time that the 'V'-shaped front was first observed within the inlet (LW + 3.0 h, figure 6). The small patch of cooler waters that had up-welled to the west of the sandspit, on the inner shoals and near the water's edge evidences this (LW + 3.0 h, figure 6). The cool patch gradually increased in size through to LW + 3.2 h (figure 6) and was associated with some slight mixing of cooler waters to the surface that occurred between itself and the intrusion front. The cool, saline basal current eventually mixed upwards at LW + 3.5 h when the intrusion front at the inlet neck finally migrated into the main channel of the estuary. A second intrusion front formed between LW + 3.5 h and LW + 4.0 h that slowly moved up-channel. At LW + 4.1 h the high-salinity waters had trapped a body of freshwater adjacent to the sandspit. Another, small patch of cooler waters had appeared near the southern-most point of the southern bank by LW + 4.1 h (figure 7). This was again due to the upwelling of denser, saline waters that comprised the basal current that flowed up-channel beneath the lighter, near-surface fresher waters.

### 5.2. Sea-truth tracks

Intense stratification was a feature of the near-surface salinity and temperature fields during the early flood, as expected from previous field data (figures 3 and 4). Between LW + 1.3 h and LW + 1.7 h the salinity differences between 0.1 and 0.55 m beneath surface were  $>20$  throughout the sea-truth grid and were strongest in the coastal zone immediately outside the inlet (station 1, figure 8). Near-surface salinity at 0.1 m was low throughout the inlet and estuary ( $<10$ ). However, elevated salinity and greatly reduced stratification were observed at station 2. This is consistent with the higher surface salinities (cooler waters) observed in the ATM images somewhat later in the flood, at LW + 2.5 h (figure 5).

Reduced, but nevertheless pronounced, salinity stratification persisted throughout the mid-flood (figure 9). Salinity between stations 12 and 17 at LW + 4.2 h to LW + 4.5 h was similar at 0.4 and 0.55 m beneath surface, but exceeded the 0.1-m salinity by about 10. The strongest feature of these data was the existence of pronounced salinity peaks on the outside of the main-channel bends (figures 1 and 9). These peaks can be attributed to an upward tilting of the near-surface isohalines that resulted from centrifugal forcing of the tidal currents (Proudman 1953) at channel bends (denoted by 'C' on figure 9). The marked decrease in near-surface

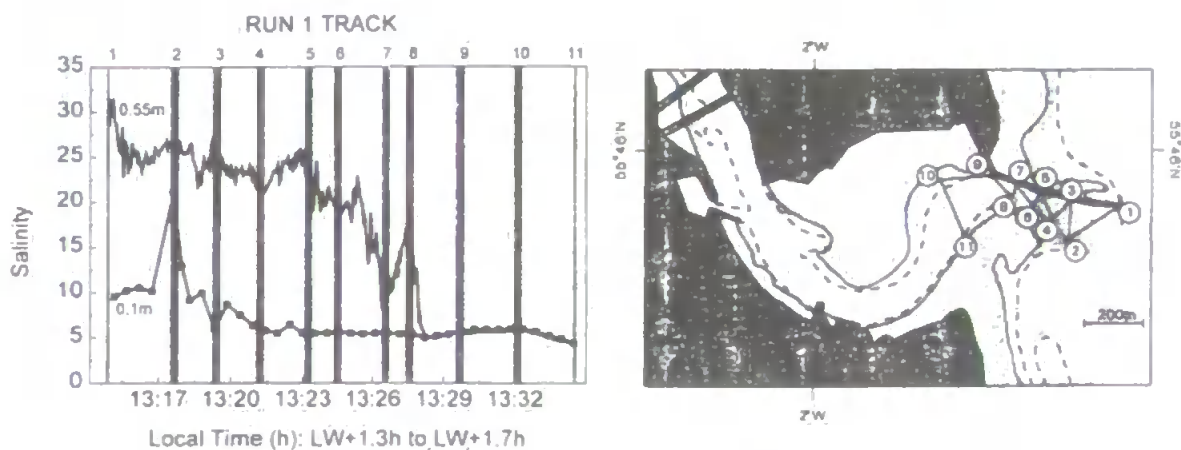


Figure 8: Salinity at 0.1 and 0.55 m beneath surface along sea-truth-track run 1 over the period LW + 1.3 h to LW + 1.7 h. Turning stations 1 to 11 and the water-line (continuous line) and LW-line (dashed line) are superimposed on a chart of the Tweed.

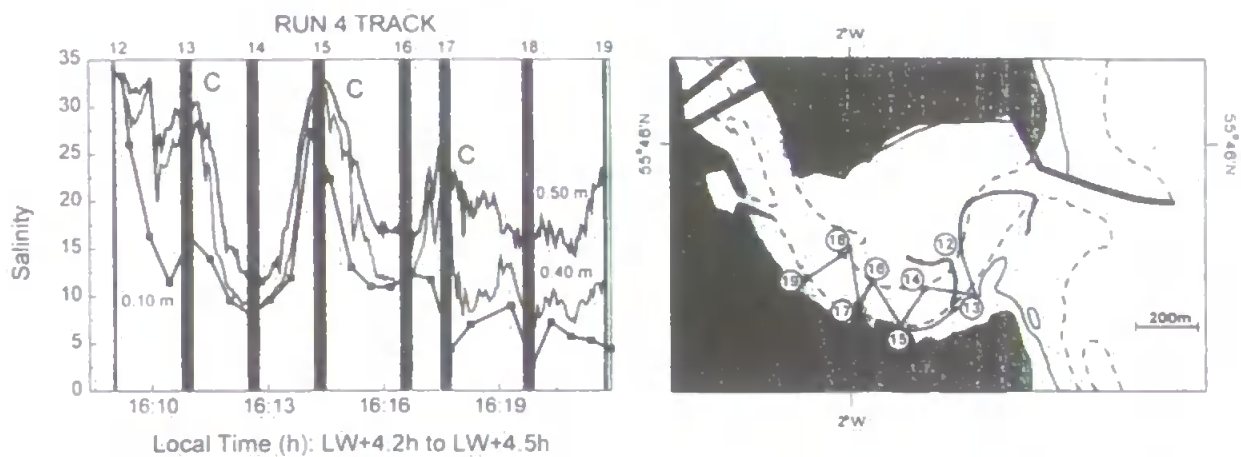


Figure 9. Salinity at 0.1, 0.4 and 0.5 m beneath surface along sea-truth-track run 4 over the period LW + 4.2 h to LW + 4.5 h. Turning stations 12 to 19 and the water-line (continuous line) and LW-line (dashed line) are superimposed on a chart of the Tweed.

stratification between turning stations 13 and 14 was associated with the boat's passage across a foam line.

Salinity stratification was greatly reduced on the late flood approaching high water, between LW + 5.6 h to LW + 6.1 h (figure 10). Vertically homogeneous coastal saltwater had intruded up-channel to station 15 and displaced fresher surface waters further into the estuary. Isohaline tilting and associated salinity peaks were still evident on the outside of channel bends at turning stations 15, 17 and 19 ('C' on figure 10).

### 5.3. Temperature-salinity plots

Large quantities of simultaneous, near-surface salinity and temperature data were derived from the sea-truth tracks (runs 1, 2, 3, 4, 5a, 5b and 6) throughout the flood tide. Scatterplots of salinity versus temperature exhibited strong linearity over the entire salinity range for each individual sea-truth run. These linear relations varied slightly and consistently throughout the afternoon flood tide. Coastal saltwater maintained a constant temperature of 7.5°C, whereas the freshwater, river end-member temperature increased from 16.5 to 18°C during the afternoon, presumably in response to solar heating of in-flowing and near-surface, fresher waters. The last

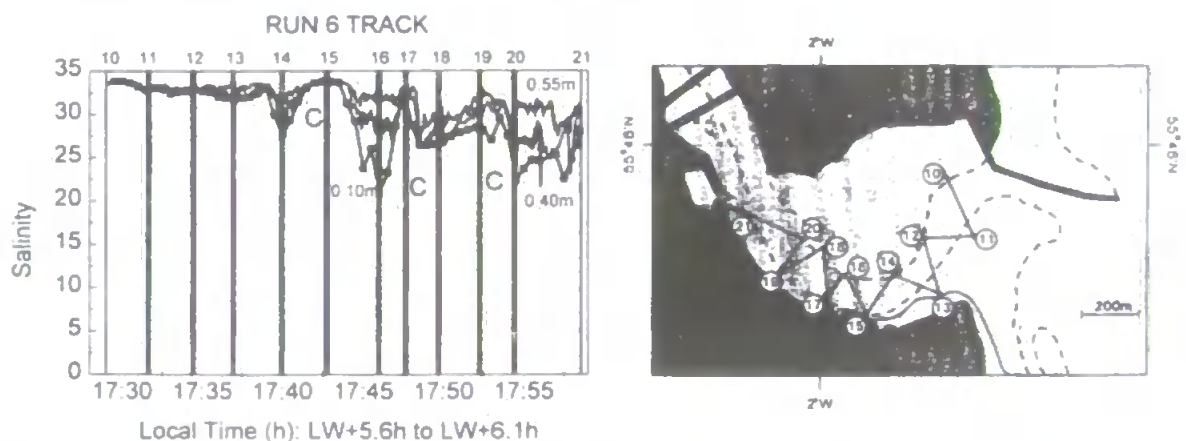


Figure 10. Salinity at 0.1, 0.40 and 0.55 m beneath surface along sea-truth-track run 6 over the period LW + 5.6 h to LW + 6.1 h. Turning stations 10 to 21 and the water-line (continuous line) and LW-line (dashed line) are superimposed on a chart of the Tweed.



three sea-truth runs of the flood tide measured relatively few low-salinity data throughout the tracks, but the temperature-salinity plots remained essentially linear (figure 11). A scatterplot of all data measured during all runs maintains linearity (figure 11); most of the scatter about the regression line can be attributed to the slight heating of near-surface, fresher waters during the course of the flood tide.

#### 5.4. Remotely-sensed salinity distributions

The strong linearity of these scatterplots indicates that mixing between waters of differing salinities was essentially conservative; i.e. that mixing occurred with negligible loss or gain of heat during a single sea-truth run. These linear salinity-temperature plots and their associated least-squares regression lines, derived from sea-truth measurements, enabled salinity data to be derived from temperature data acquired from ATM thermal images. In order to deduce temperatures from thermal images, calibration was performed for those images that were acquired at times coincident with sea-truth measurements. In each image, the inflatable boat was identified and the pixels around its location were interrogated. Means and standard deviations for each set of apparent temperature values were found. These have been compared with the sea-truth data (figure 12) and a least squares regression fitted to the data. The regression achieved a 0.952 coefficient of determination.

The temperature derived from the ATM was, on average,  $1.2^{\circ}\text{C}$  higher than that measured at the water's surface. This can be accounted for by the fact that the boat measurements were taken subsurface ( $>0.1\text{ m}$ ) whereas the ATM results relate to the surface, where heating from the Sun increases the 'skin' temperature by up to  $2^{\circ}\text{C}$  (Wilson, personal communication). The atmosphere can also influence the ATM-derived apparent surface temperature. Weather conditions and altitude of aircraft could have a positive, negative or neutral effect on the derived data. The most effective way of overcoming any atmospheric influence is to move to a minimum-two channel thermal instrument, to allow 'split window' atmospheric corrections to be performed (Wilson, personal communication).

Calibrated temperatures were derived from the ATM thermal images using boat data to provide true surface temperature images. Using the temperature-salinity

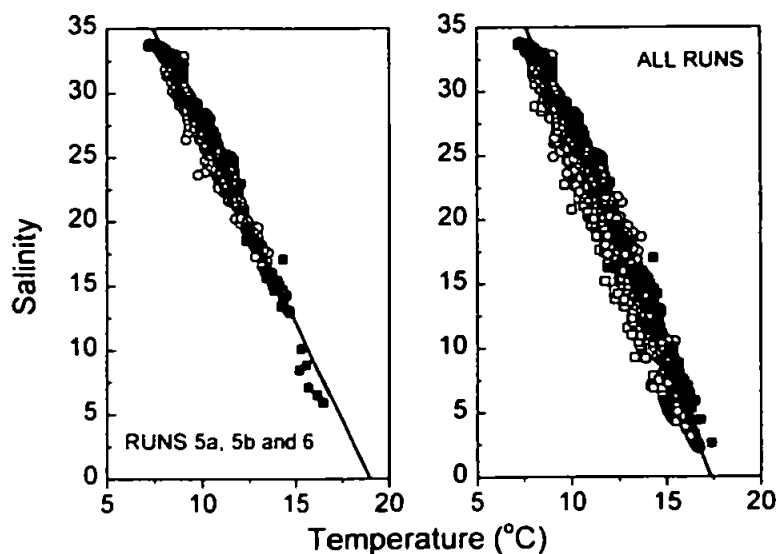


Figure 11. Salinity-temperature scatterplots for sea-truth tracks 5a, 5b and 6 and for all tracks, runs 1 to 6, combined. Data have been used from the two instruments nearest the surface (0.1 and 0.4 m) in order to reduce the number of plotted data points.

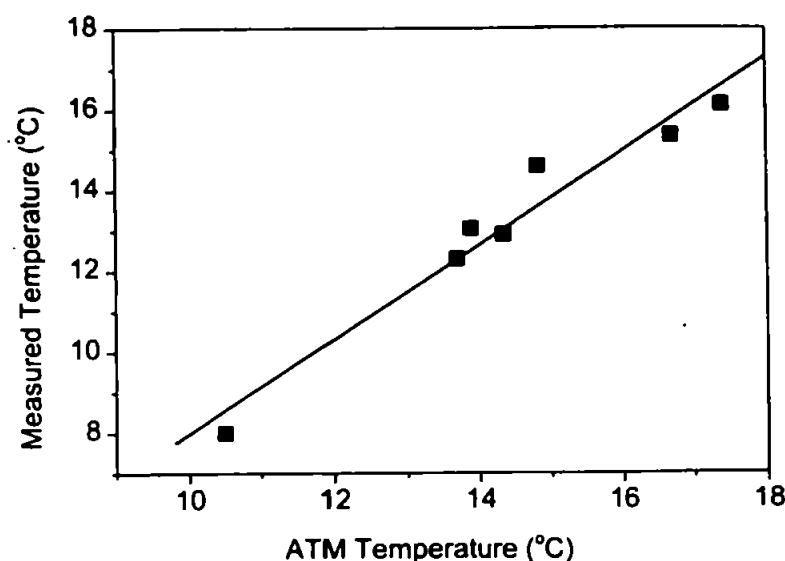


Figure 12. Comparison of ATM-derived temperatures with sea-truth data and the least squares regression line (0.952 coefficient of determination).

regressions derived from sea-truth measurements, ATM-based salinity images were constructed for the entire set of ATM scenes. The surface salinity and temperature fields within the Tweed's lower estuary and coastal zone exhibited complex and remarkable structures. The 'V'-shaped intrusion front within the Tweed's inlet at LW + 3.1 h was sharply defined by the margin between saltwater of coastal salinity ( $> 33$ , yellow on figure 13, top panel) and intermediate waters of salinity  $< 20$ . Slight vertical mixing of the plunging, flooding coastal flow with the overlying estuarine waters generated these intermediate-salinity waters. Incompletely mixed surface waters were traceable through the main inlet channel, into the estuarine channel and onto the shoals. Centrifugal-induced up-welling on the outside, western side, of the main channel bend also led to somewhat higher salinity waters at the surface (figure 13). Topographically induced upwelling was also evident on the shoal to the west of the main channel. A higher-salinity patch of waters to the west of the main channel (figure 13) appeared to result from up-welling due to topographic blocking of the high salinity basal flow as it moved onto the shoal. Additional, coastal-zone features in the surface-salinity field were the movements of intermediate-salinity plume waters to the north of the inlet's mouth and the trapping of intermediate-salinity waters on the shallow, recently covered intertidal areas (figure 13). These features were, of course, also evident in the temperature field at LW + 3.1 h (lower panel, figure 13).

By LW + 4.0 h the intrusion front (salinity  $> 30$ ) had moved into the estuary's main channel and collapsed as a result of intense mixing (figure 14). The front was then transferred up-channel. Waters of salinity  $> 30$  plunged beneath waters of salinity  $< 15$ . Salinity was high over the shoals. Surface salinity was  $< 10$  further up-channel. Lower salinity ( $< 30$ ) waters remained trapped close to the coast. Despite pronounced mixing of the remnants of the Tweed's ebb-tide plume, a frontal boundary nevertheless remained between these mixed waters and high-salinity North Sea waters (figure 14). These features were also evident in the temperature field, which covered the range 6.4 to 18°C.

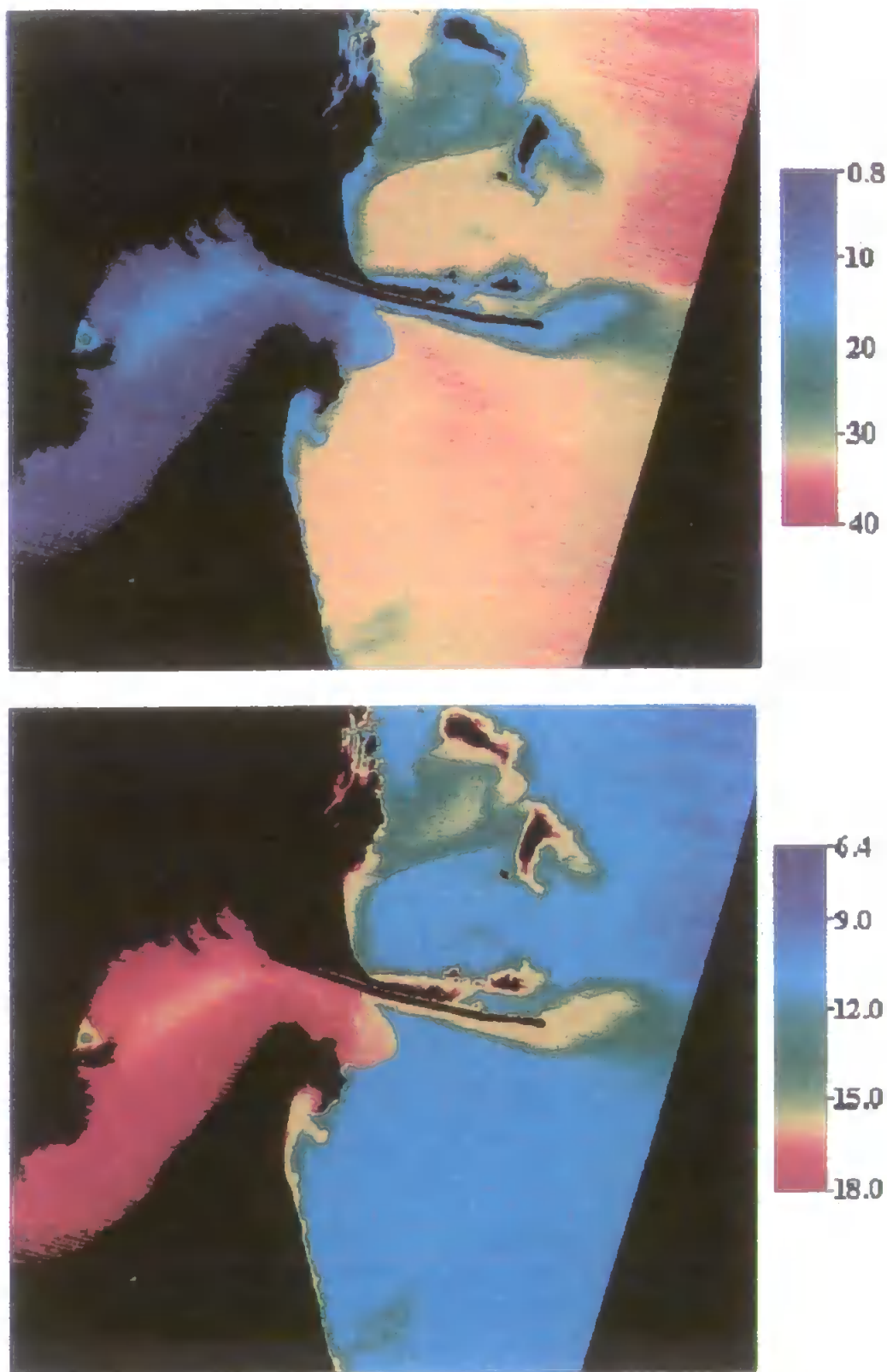


Figure 13. Temperature (lower panel) and salinity (upper panel) of the Tweed Estuary at LW + 3.1 h. Acquired 4 May 1995 and derived from the ATM thermal band 11 image.

## 6. Discussion and conclusions

Previous measurements in the Tweed have shown that frontal systems occur both inside the inlet at around mid-water and in the main channel of the estuary later into the flood tide during spring tides and at fairly low inflows (Uncles *et al.* 1997).

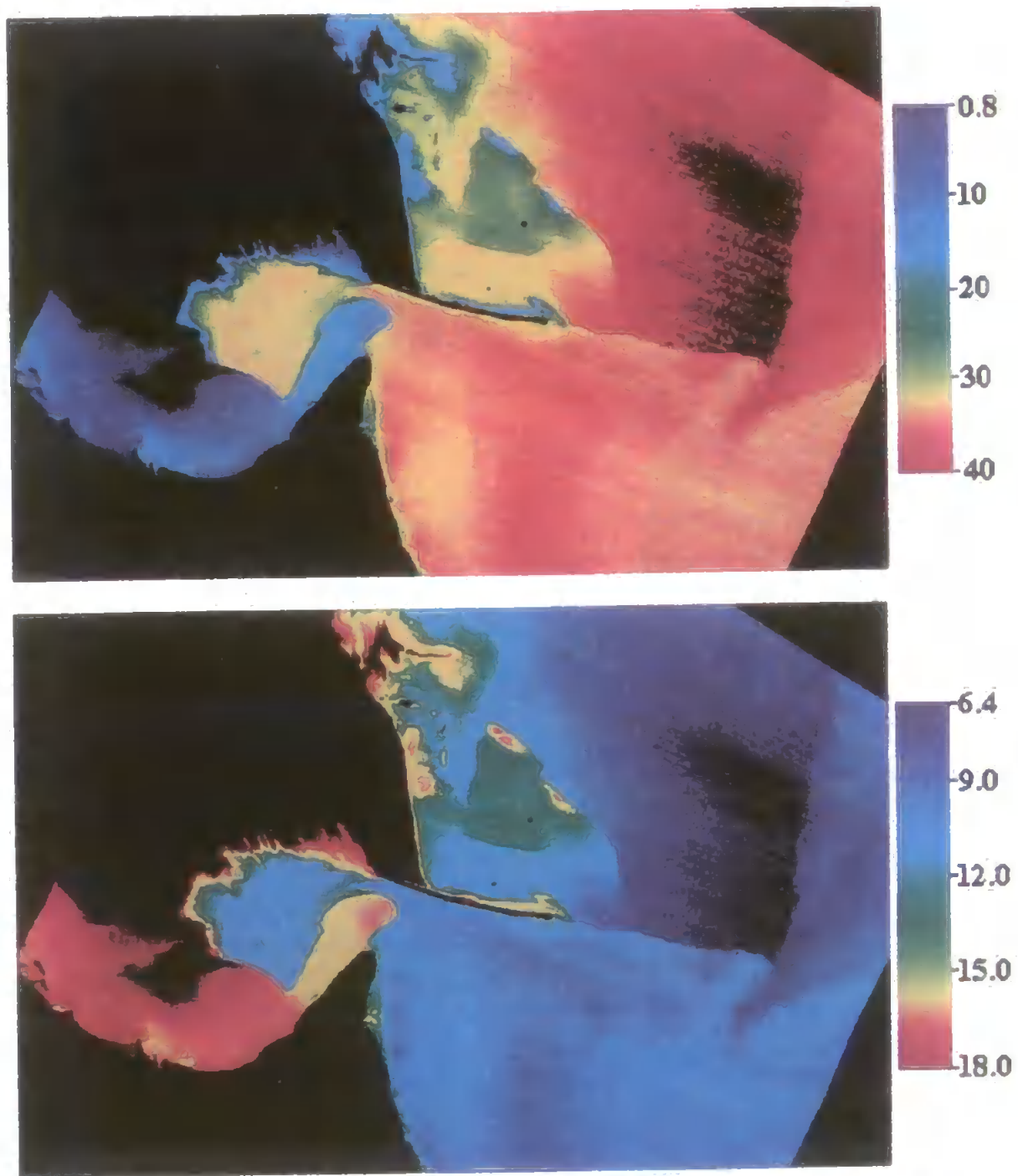


Figure 14. Temperature (upper panel) and salinity (lower panel) of the Tweed Estuary at LW+4.0h. Acquired 4 May 1995 and derived from the ATM thermal band 11 image.

The data presented here demonstrate that similar behaviour also occurs during lower, mean tidal-range tides. Additionally, the salinity and temperature fields within these frontal systems have been defined with both temporal and spatial resolutions that far exceed previous studies in this and, to our knowledge, any other estuarine study.

The 'V' shaped front that formed in the neck of the inlet was particularly well developed around mid-flood. Previous, vertical-profiling measurements illustrated the early flood dynamics of the flow in the inlet. A gravitational circulation occurred.



during the early flood period. The flooding basal current increased in speed and the upper layer thinned while it ebbed seawards.

The tidal intrusion front that was observed at the constricted neck of the inlet was similar to those described and reviewed by Largier (1992). In particular, an inflow Froude-number criterion (Uncles *et al.* 1997) when applied to the inlet's neck, appeared to control the timing and shape of the plunge line within the inlet (where high salinity waters plunged beneath lower salinity estuarine waters). The intrusion front was observed to occur at the inlet neck around mid-water. At that time, and earlier in the flood, the neck acted as a constriction to the flow. The observed apparent migration speed of the front through the inlet was about  $0.1 \text{ m s}^{-1}$ , which was much slower than the tidal currents.

According to the review by Largier (1992), on the early flood tide the outflowing surface waters from the estuary to the coastal zone are blocked when the inflow Froude number at the inlet neck lies within a critical range of values. These surface waters are then pushed back towards the neck as the flood currents increase. Plunging occurs at the neck when the Froude Number is unity. Observations presented here demonstrate that blocking of surface waters occurred by LW + 2.5 h, roughly 0.5 h before peak flood current speeds (figure 5). During peak current speeds, the intrusion front was located within the inlet's neck. Subsequently, plunging would be expected to occur up-estuary of the neck.

On the early flood, vertical profiling in the inlet showed that high salinity coastal waters entered the inlet as a basal density current. This current was topographically steered into the lower estuary along the deep channel and transverse salinity gradients occurred due to centrifugal, cross-channel tilting of the isohalines (Proudman 1953). Less saline waters were forced onto the edges of the flanking intertidal shoals, sometimes with the formation of long, buoyancy-induced and shear-induced frontal systems (Huzzey 1988, Huzzey and Brubaker 1988). When an intrusion front occurred inside the inlet, the high salinity waters plunged beneath estuarine waters. With rising water levels, the basal current bifurcated as it left the inlet and entered the estuary. One branch turned into the main channel while the other branch retained its course and flooded the shoals. Weak vertical mixing between the high-salinity basal current and the fresher surface waters led to elevated surface salinities that were evident in the remotely sensed images.

The experiment reported here was undertaken at a time when it was known that particularly strong temperature contrasts would be observed between in-flowing freshwater to the Tweed and coastal saltwater. These contrasting temperatures led to straightforward identification of water masses from the sea-truth measurements. The effective flushing of the Tweed over the course of an ebb tide (Uncles and Stephens 1996) generated an essentially homogeneous body of low-salinity waters at low water. The introduction of essentially 'new', high-salinity North Sea waters on the flood led to extremely well defined and linear salinity-temperature scatterplots. These plots enabled salinity to be defined in terms of temperature from the ATM images. While the methodology could be applied in other estuarine areas the ATM is most effective at examining relative changes and thermal gradients. Therefore, it has most value at those times of the year for which strong temperature differences exist between in-fluxing and receiving waters.

### Acknowledgments

We are grateful to I. A. Fox, Tweed River Purification Board, for supplying hourly freshwater inflow data for the Tweed and Whiteadder Rivers. We appreciate

the kind assistance and hospitality extended to us by Captain Jenkinson, Queen's Harbourmaster, Berwick-Upon-Tweed. We would also like to thank the NERC Airborne Remote Sensing Facility for acquisition of remotely sensed images. This work forms part of the Plymouth Marine Laboratory's contribution to the Land Ocean Interaction Study, Community Research Project of the NERC (LOIS contribution No. 350).

## References

- ANDERSON, J. M., DUCK, R. W., MCMANUS, J., and DIEZ GONZALEZ, M. J., 1992, Recognition of an overspill-induced estuarine frontal system in the Ria do Barqueiro, north-west Spain, using remote sensing techniques. *International Journal of Remote Sensing*, **13**, 1903–1911.
- ARMI, L., and FARMER, D. M., 1986, Maximal two-layer exchange through a contraction with barotropic net flow. *Journal of Fluid Mechanics*, **164**, 27–51.
- CALLISON, R. D., 1985, Sea surface temperatures from Daedalus ATM data—preliminary results. *International Journal of Remote Sensing*, **6**, 1671–1680.
- CALLISON, R. D., BLAKE, P., and ANDERSON, J. M., 1987, The quantitative use of Airborne Thematic Mapper thermal infrared data. *International Journal of Remote Sensing*, **8**, 113–126.
- DAVIES, P. A., MOFOR, L. A., VALENTE NEVES, M. J., 1997, Comparison of remotely sensed observations with modelling prediction for the behaviour of wastewater plumes for coastal discharges. *International Journal of Remote Sensing*, **18**, 1987–2020.
- DYER, K. R., and NEW, A. L., 1986, Intermittency in estuarine mixing. In *Estuarine Variability*, edited by D. A. Wolfe (Orlando: Academic Press), pp. 321–339.
- FERRIER, G., and ANDERSON, J. M., 1996, The application of remote sensing data in the study of effluent dispersal in the Tay Estuary, Scotland. *International Journal of Remote Sensing*, **17**, 3541–3566.
- FERRIER, G., and ANDERSON, J. M., 1997a, A multidisciplinary study of frontal systems in the Tay Estuary, Scotland. *Estuarine, Coastal and Shelf Science*, **45**, 317–336.
- FERRIER, G., and ANDERSON, J. M., 1997b, The application of remotely sensed data in the study of frontal systems in the Tay Estuary. *International Journal of Remote Sensing*, **18**, 2035–2065.
- FERRIER, G., DAVIES, P. A., and ANDERSON, J. M., 1996, Remote sensing observations of a vortex street downstream of an obstacle in an estuarine flow. *International Journal of Remote Sensing*, **17**, 1–8.
- FISCHER, H. B., LIST, E. J., KOH, R. C. Y., IMBERGER, J., and BROOKS, N. H., 1979, *Mixing in Inland and Coastal Waters* (New York: Academic Press).
- GARDNER, M. J., and RAVENSCROFT, J. E., 1991, The range of copper-complexing ligands in the Tweed Estuary. *Chemical Speciation and Bioavailability*, **3**, 22–29.
- HUZZEY, L. M., 1988, The lateral density distribution in a partially mixed estuary. *Estuarine, Coastal and Shelf Science*, **9**, 351–358.
- HUZZEY, L. M., and BRUBAKER, J. M., 1988, The formation of longitudinal fronts in a coastal plain estuary. *Journal of Geophysical Research*, **93**, 1329–1334.
- HYDROGRAPHIC OFFICE, 1992, *Admiralty Chart no. 1612*. Hydrographer of the Navy, Taunton, Somerset, England, UK.
- HYDROGRAPHIC OFFICE, 1993, *Admiralty Tide Tables, Vol. 1*, Hydrographer of the Navy, Taunton, Somerset, England, UK, pp. 65 and 307.
- LARGIER, J. L., 1992, Tidal intrusion fronts. *Estuaries*, **15**, 26–39.
- LARGIER, J. L., and TALJAARD, S., 1991, The dynamics of tidal intrusion, retention, and removal of seawater in a bar-built estuary. *Estuarine, Coastal and Shelf Science*, **33**, 325–338.
- PROUDMAN, J., 1953, *Dynamical Oceanography* (London: Methuen).
- SIMPSON, J. H., and NUNES, R. A., 1981, The tidal intrusion front: an estuarine convergence zone. *Estuarine, Coastal and Shelf Science*, **13**, 257–266.
- SIMPSON, J. E., and BRITTER, R. E., 1979, The dynamics of the head of a gravity current advancing over a horizontal surface. *Journal of Fluid Mechanics*, **94**, 477–495.
- STIGEBRANDT, A., 1988, Dynamic control by topography in estuaries. In *Hydrodynamics of*

- Estuaries, Volume 1 (Estuarine Physics)*, edited by B. Kjerfve (Boca Raton, Florida: CRC Press), pp. 17-25.
- TURNER, J. S., 1973, *Buoyancy Effects in Fluids*, Cambridge Monographs on Mechanics and Applied Mathematics (Cambridge: Cambridge University Press).
- TWEED FOUNDATION, 1989, Tweed towards 2000. In *Tweed towards 2000 (A Symposium on the Future Management of the Tweed Fisheries)*, edited by D. Mills, published by the Tweed Foundation, 27 Main Street, Tweedmouth, Berwick-upon-Tweed TD15 2AB, UK.
- TWEED FOUNDATION, 1992, *Review and Progress Report*, published by the Tweed Foundation, 27 Main Street, Tweedmouth, Berwick-upon-Tweed TD15 2AB, UK.
- UNCLES, R. J., and STEPHENS, J. A., 1996, Salt intrusion in the Tweed Estuary. *Estuarine, Coastal and Shelf Science*, **43**, 271-294.
- UNCLES, R. J., STEPHENS, J. A., and MURPHY, R. J., 1997, Aircraft and sea-truth observations of a small-scale estuarine intrusion front. *Journal of Marine Systems*, **12**, 199-219.
- WILSON, A. K., 1988, Calibration of thermal data. NERC, Airborne Campaign Workshop, I.H. Wallingford, 24 February 1988, NERC, 219-231.